# Computational Design of Biomimetic Nanopores: A Molecular Dynamics Study


**Jemma Louise Trick**

Department of Biochemistry

University of Oxford

A thesis submitted in partial fulfilment of the requirements for the degree of Doctor of Philosophy at the University of Oxford.

St. Cross College

Trinity 2015

# Acknowledgements

Firstly I'd like to thank my supervisors, Prof. Mark Sansom for being continually helpful throughout this project. Also my other "nanopore" supervisors Prof. Hagan Bayley and Dr. Jayne Wallace.

To my family and friends, my parents who have always supported throughout my Oxford years. My friend Steph and fellow PhD-er, and also the "Welshies" whose ridiculousness has kept me laughing. Hilaritus - you know who you are. Also Jemma and Min - my fellow Oxford DPhil-ers for the whining.

Everyone who has helped me in the SBCB, David "**Blank Space**" Shorthouse, GB "**Red**" Morris, & Jo "**Fearless**" Lee. Also previous and past members such as Erin, Nat, Phill S, Phil F, Lukas, Greg, Maria, Rouse, Craig, Jerome and Syma for helping me throughout the many years I have been here.

Also to my internet distractions, be they Spotify, BBC Sport & Netflix for maintaining my sanity.

# Publications

The following publications are mentioned in this thesis

- J. L. Trick, E. J. Wallace, H. Bayley and M. S. P. Sansom. "Designing a Hydrophobic Barrier within Biomimetic Nanopores," *ACS Nano,* vol 8, pp. 11268-11279, 2014.

- J. L. Trick, P. Aryal, S. Tucker and M. S. P. Sansom. "Molecular simulation studies of hydrophobic gating in nanopores and ion channels," *Biochemical Society Transactions,* vol 43, pp. 146-150, 2014.

- J. L. Trick, C. Song, E. J. Wallace, H. Bayley and M. S. P. Sansom. "Electrowetting of a Hydrophobic Gate: Computational Electrophysiology of Voltage-Gating in a Biomimetic Nanopore", *in prep.*

- J. L. Trick, E. J. Wallace, H. Bayley and M. S. P. Sansom. "Conformational State of the Ligand Gated Serotonin Receptor, A Simulation Study," *in prep.*

# Abstract

Molecular dynamics simulations are used to study the function of hydrophobic gates within models of biomimetic nanopores and in ligand-gated ion channels. A computational approach to building and simulating model $\beta$-barrel nanopores has been established to explore the effects of changing the shape and polarity of amino acids lining the pore lumen. Changing the position of such residues resulted in different water conductive states. In 14 $\beta$-strand pores, a computationally transplanted hydrophobic barrier to water and ions has been demonstrated and characterised in detail using free energy calculations. Electrowetting of such a hydrophobic gate within a model $\beta$-barrel nanopore is demonstrated in simulation, using two different methods to apply a transmembrane electric field. An increase in the transmembrane voltage results in breakdown of the hydrophobic barrier, resulting in the flow of water and ions. The effect (electrowetting) is shown to be reversed upon the removal of the transmembrane voltage. An investigation into the possible hydrophobic gate of the 5-$HT_3$ receptor channel via free energy calculations and simulations confirmed that the crystal structure is in a closed conformation with respect to the flow of ions. This demonstrates that simulations and free energy calculations may be used to functionally annotate crystal structures of ion channels.

# List of Abbreviations

| | |
|---|---|
| $\alpha$HL | alpha-Hemolysin |
| ABF | adaptive biasing force |
| CG | coarse grained |
| c.o.m | centre of mass |
| DNA | deoxyribonucleic acid |
| dsDNA | double stranded DNA |
| ECD | extracellular domain |
| EM | electron microscopy |
| ENM | elastic network model |
| GNM | Gaussian network model |
| HG | hour glass |
| LGIC | ligand gated ion channel |
| LLL | STLLLTS Nanopore |
| LJ | Lennard-Jones |
| N | number of $\beta$ strands |
| NLLN | STNLLNT nanopore |
| NLL | STNLLTS nanopore |
| NMR | nuclear magnetic resonance |
| MD | moleclar dynamics |
| nAChR | nicotinic acetylcholine receptor |
| OMP | outer membrane protein |
| pLGIC | pentameric ligand gated ion channel |

| | |
|---|---|
| PBC | periodic boundary conditions |
| PME | particle mesh Ewald |
| PMF | potential of mean force |
| QM | quantum mechanics |
| $S$ | shear |
| SCNT | silicon carbide nanotube |
| ssDNA | single stranded DNA |
| TM | transmembrane |
| TMD | transmembrane domain |
| VdW | Van der Waals |
| WHAM | weighted histogram analysis method |
| WT | wild type |

# Table of contents

# List of figures

# List of tables

# Chapter 1

# Introduction

*"Are we out of the woods"*

---

Taylor Swift

## 1.1 Cellular Domains

All life as we know it is cellular based, with the compartmentalisation of chemical reactions defining the cell, enabling a range of diverse functions. There are three domains with this cellular base, eukaryotes, prokaryotes, and archaea. This last domain are a minor group in our consideration and are defined mainly from prokaryotes by ether linkages in their cellular lipids. They will not be considered in the rest of this thesis.

Eukaryotes differ to prokaryotes fundamentally due to their enclosed nucleus within the cell and deoxyribonucleic acid (DNA) organisation. Eukaryotes have multiple internal compartmentalised organelles such as mitochondria, the nucleus, plastids (if plant based) but also many others (such as the golgi apparatus, chloroplasts, endoplasmic reticulum). The remainder of the cell volume is occupied by the cytosol. Also differing are the cytoskeletal elements; microtubules, composed mainly of tubulin and

microfilaments which are actin based. These exist within the cell to support shape and functions. A major differing factor between eukaryotes and prokaryotes is their size, with generally eukaryotes being much larger (with average cell size of 10 -100 $\mu$m compared to a standard prokaryote. *i.e.* a bacteria 1-5 $\mu$m). A diagram of both, of a standard cell of each are in figure 1.1*.

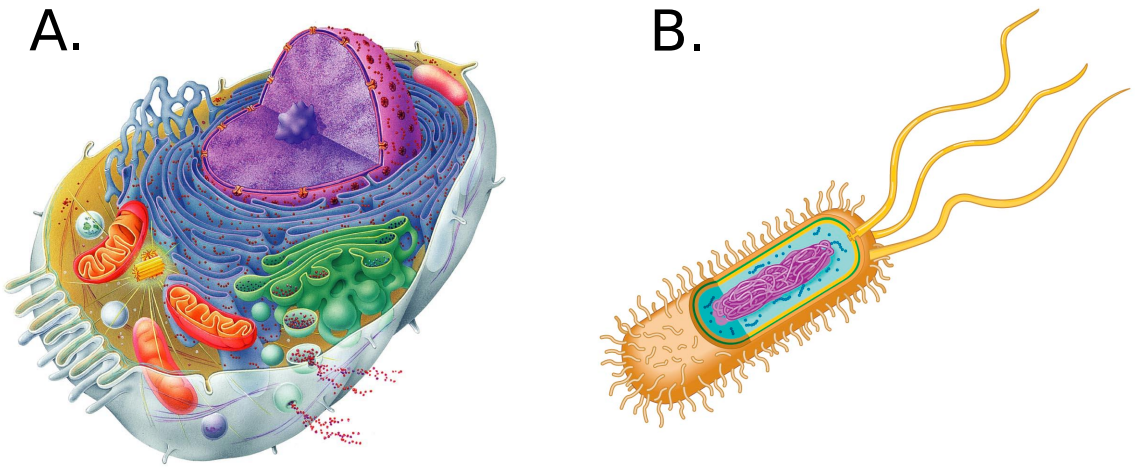


**Fig. 1.1:** Eukaryotic and prokaryotic cells. Cell sizes range from 10-100 $\mu$m for the eukaryotic cell (A.) and 1-5 $\mu$m for the bacterial cell, B. Images are not to scale. Copyright of Pearson Education.

*source of images, lassconnection.s3.amazonaws.com/327/flashcards/1031327/jpg/cell -structure1334774434699.jpg & www.fullfrontalanatomy.com/Bio3/Standard$_{d}$ocs/$Resources/Campbell/Chapter_{0}4/B_{J}peg_{I}mages/04_{U}nlabeled_{I}mages/04_{0}4aProkaryoticArt - U.jpg$

## 1.2 Biological Membranes

Cells are surrounded by a semi permeable biological membrane. Examples are the membrane which defines the cytoplasms to the extracellular matrix, but are also used intracellularly to define the organelles. Our description of the membrane is based on the fluid mosaic model first proposed in 1972 where the membrane is described as a two-dimensional liquid in which the lipid, such as phospholipids and proteins can diffuse [1]. This is regulated in permeability, with control of what can go through the membrane. Both eukaryotes and prokaryotes are based on the same bilayer model, however, with differing lipid compositions. A lipid is characterised by their hydrocarbon tail, in number and length, the saturation of mentioned tail, and functional head group [2]. In a typical arrangement, a membrane is formed from two leaflets of the phospholipids and sphingolipids, with the head groups facing away from another and the hydrocarbon tails in contact. This creates a hydrophobic core surrounded by polar head groups [3]; an example of the cellular membrane arrangement is shown in figure 1.2. The presence of such a structure permits a high energy barrier of ~50 kJ $mol^{-1}$ to ions [4].

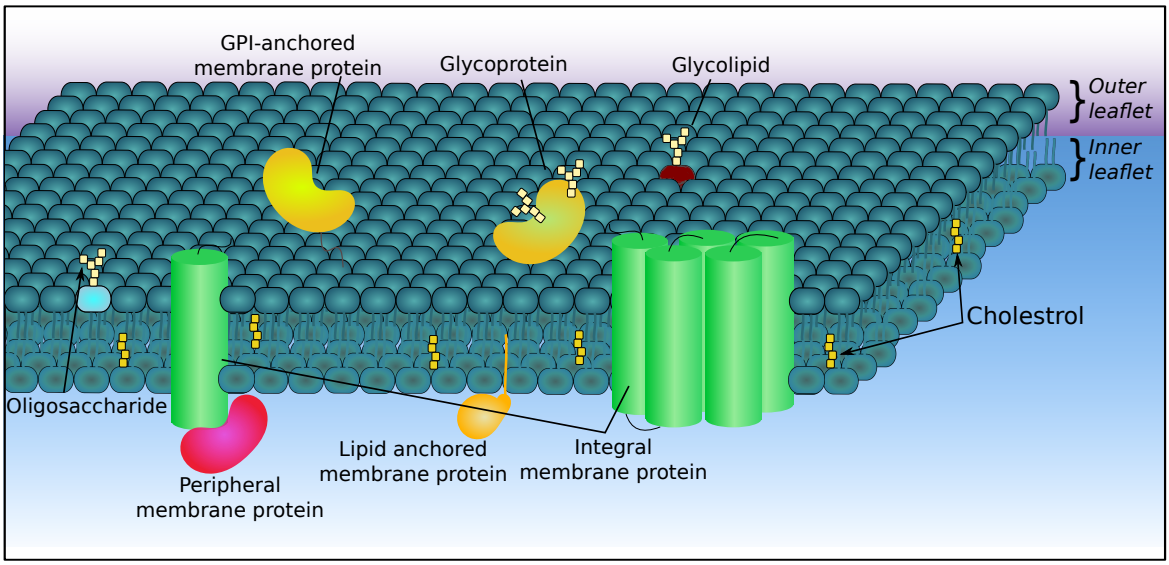


**Fig. 1.2:** Schematic of eukaryote cell plasma membrane. Lipids are indicated as dark green, with schematic proteins (green cylinders, pink and yellow adapted circles). It is estimated 50 % of the bilayer is protein, which is not represented accurately in this figure. Not shown are lipid rafts, membrane curvature or cytoskeletal elements.

The three major classes of lipid within the eukaryotic bilayer are phospholipids, sphingolipids and sterols (in the form of cholesterol); all of which are amphipathic in chemical nature. Prokaryotes (bacterial bilayers for this thesis) contain a more varied class of lipids with there being two defined classes, Gram-negative and Gram-positive. This is based on their different colours under gram stain [5], indicating the presence of peptidoglycan at the surface of the bacterium. A basic representation of the Gram-negative bacterial bilayer structure (both inner and outer leaflets) is shown in figure 1.3.

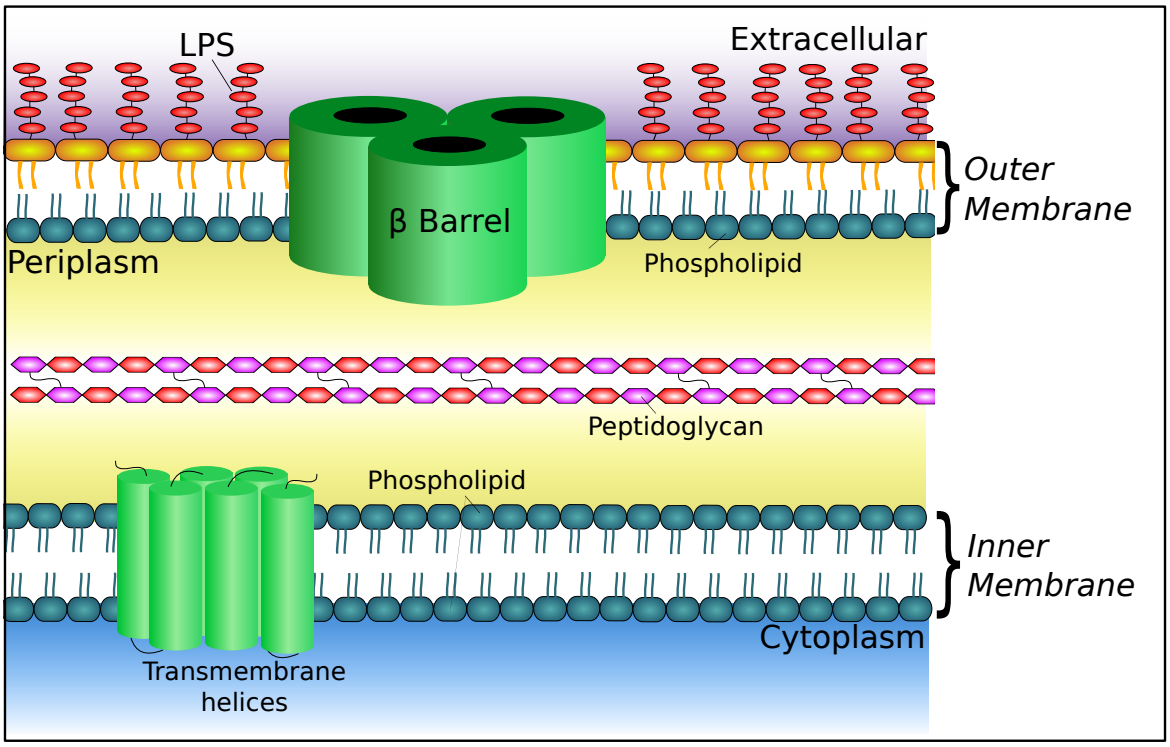


**Fig. 1.3:** Schematic of the cell envelope of a Gram-negative bacteria. Shown are both the inner and outer membranes with dark green lipids indicating phospholipids, orange lipid A and the red circles being the remainder of the LPS. Also shown are schematic proteins within both membranes (green). Image is not to scale and adapted from [6].

The most common lipid in biological membranes are phospholipids whose backbone is a *L* isomer *sn*-glycerol-3-phosphate. The acyl chains vary in length from 10 to 24 hydrocarbon tails (and always an even number) and are attached to an alcohol group via a glycerol linkage, resulting in many possibe phospholipids. The main ones to consider are phosphatidylethalonamine (PE), phosphatidylcholine (PC), phosphatidylserine (PS), phosphatidylglycerol (PG), and phosphatidylinositol (PI) lipids. An example of a phospholipid structure is shown in figure 1.4.

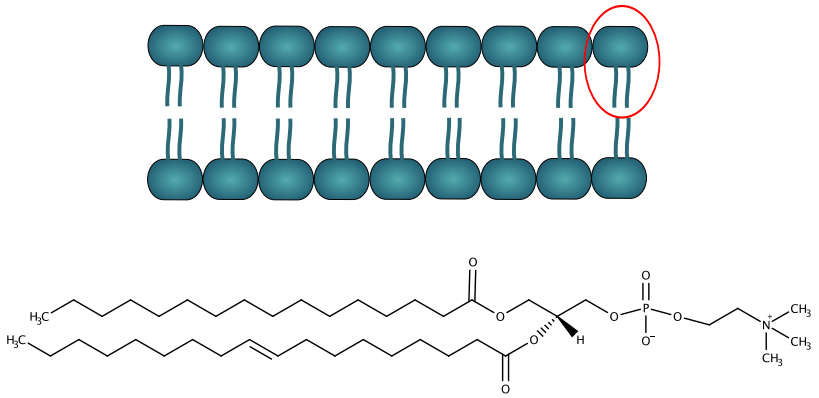


**Fig. 1.4:** POPC lipid structure. Above, schematic of a cell membrane, in which each sphere and two tails represents a phospholipid. Below, chemically drawn structure of POPC.

Simulated in this thesis are 1,2-dipalmitoylphosphatidylcholine (DPPC) and 1-palmitoyl-2-oleoylphosphatidylcholine (POPC) lipids, who have the same choline head group but different lipid tails. DPPC has two 16 carbon saturated chains, however POPC has one saturated 16 carbon, and one 18 carbon chain with one double bond. The chain saturation and its length are important in the shape and thickness of the membrane. Also found in bilayers are glycolipids and sterol based lipids which also contribute to the properties of the bilayer, with interplay between protein and lipid determining ultimate membrane curvature [7, 8].

Within the Gram-negative species, the unusual lipid, lipid A is present. It is a

moiety of outer lipopolysaccharide (LPS) layer, with the lipid having ~6 acyl chains between 10 and 16 carbons in length [9] and ester linked to two glucosamine sugars which bond to the other components of the LPS. Also present are phospholipids and some species have hapnoids which act in the same way as sterols to modulate membrane ordering. The outer membrane (OM) is asymmetric, with ~70-80% PE, 20-30% PG, and cardiolipin present on the inner leaflet and lipid-A containing LPS on the outer. As well as a lipid A molecule, the OM contains an inner core, outer core of oligosaccharide components such as the acidic and negatively charged heptose, galactose, mannose (to name a few), and an outer most O antigen of a repeating glycan polymer with variation species to species [10]. Calcium ions are known to associate with the OM and stabilise the structure of the membrane [11]. The OM provides the region in which passive transport occurs, with substrates and solutes coming from external sources, such as sugars, amino acids, and metal co-factors via the $\beta$-barrel porins. Most metabolic functions are carried out by the inner membrane, using $\alpha$-helical proteins [12]. The inner membrane is thought to be phospholipid containing, however composition is species dependent (table 1, [13]).

## 1.3 Membrane Proteins & Function

Approximately 20 to 30 % of eukaryotic genes expressed encode for transmembrane proteins [14] with some playing vital roles through the bilayer such as transport, cell signalling via a membrane receptor, cellular adhesion in an immune response and as membrane enzymes to regulate the bilayer.

Membrane proteins can be classed into two groups, peripheral proteins (which attached to the surface of the bilayer) such as a PH (pleckstrin homology) domain and integral proteins be they monotopic, who span part way through the membrane or fully transmembrane (TM) with basic examples shown in figure 1.2. Within this

thesis, the focus will be in the TM integral proteins which come in two main structural types, $\alpha$-helices & $\beta$-barrels.

### $\alpha$ helices & $\beta$ barrels

Most transmembrane proteins are $\alpha$-helical [15], with $\beta$-barrels being found on the outer membrane of Gram-negative bacteria, *e.g.* porins, some bacterial secreted toxins and on the mitochondrial outer membrane (the 19 $\beta$ stranded voltage dependent anion channel-VDAC) (figure 1.5). $\alpha$-helices are found on the inner membrane of Gram-negative bacteria and in the membranes of eukaryotes. Diversity of $\alpha$-helical protein is apparent, with variation on the helical assembly within the bilayer, the number of helices, their oligomeric state, and also presence and structure of extracellular and intracellular domains. The TM regions are considered stable domains that do not unfold completely in denaturation due to the hydrophobicity of the membrane. They are translocated and inserted into the inner membrane of bacteria and the endoplasmic reticulum membrane of eukaryotes by the Sec61$\alpha$ $\beta$ $\gamma$ [16] and SecYEG (bacteria) translocase.

In this thesis, simulations are conducted on the $\alpha$-helical cys loop receptor proteins which will be discussed in more detail further on in this chapter.

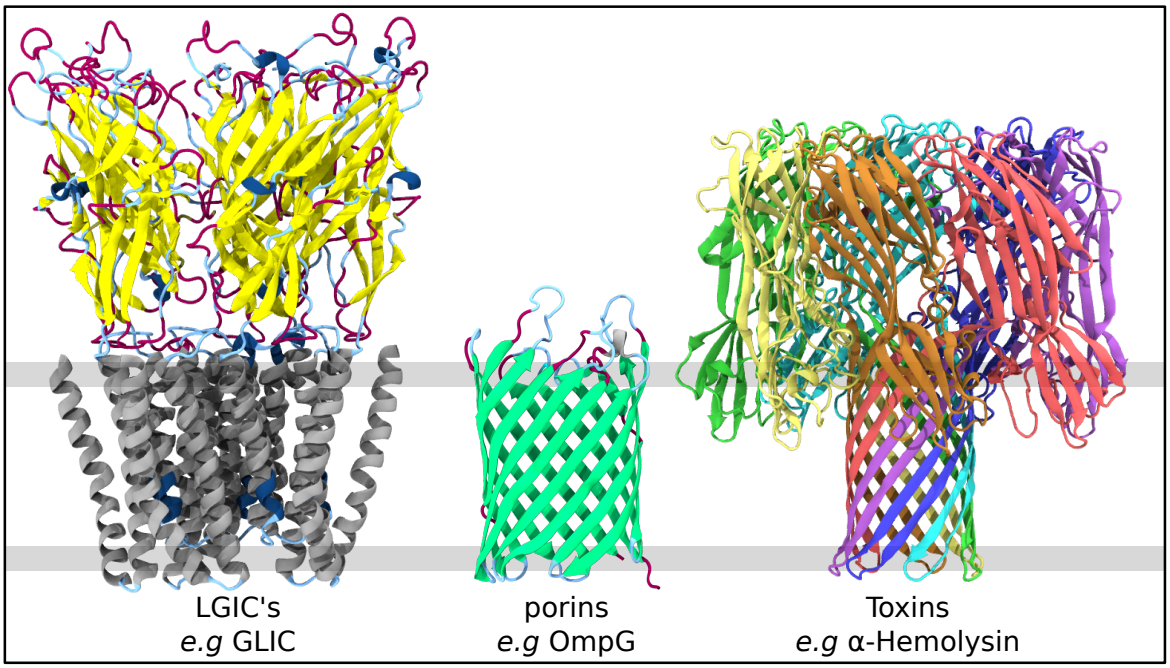


**Fig. 1.5:** Structures of membrane proteins. Shown (from left to right) pentameric ligand gated ion channel (GLIC), a porin (OmpG) and a lytic, toxin protein $\alpha$-Hemolysin). Grey line indicates bilayer regions.

Beta-barrels are membrane proteins consisting of a large $\beta$-sheet of intra-hydrogen bonds within, to form a barrel like structure known as a porin [17, 18], and are involved in the permeability of the OM [19]. Within these barrels, the hydrogen bonding pattern is usually anti-parallel, and are encoded by ~3 % of the genes within Gram-negative species [20]. The structure of the barrels are defined by a shear number ($S$) and by the number of strands. Shear number is the number of hydrogen bonds which have been "jumped" from the first strand to the last, and effectively introduce torque to the barrel which can influence the height of the strands and the diameter of the barrel. Thus a barrel can have the same number, and length of strands but have different dimensions in height and width due to the shear number. Porins are structured in this way and also have long flexible loops connecting the strands, with typically the longer loops facing the extracellular region for recognition and selectivity. Within the larger porins (~16 strands or more), the loops are known to fold back within to the barrel lumen

to provide moderate substrate recognition regions [12, 21, 22]. Strand number can range from 8-22 and is always even (apart from the eukaryotic porin VDAC [23, 24]). They can be general [25–27] or substrate specific in their conduction [28, 29], with some of the larger porins also having a plug-type region for coupled transport events, *e.g.* BtuB which transports cobalamin within *E. coli*. Gating within these pores are varied with voltage gating [30], based on the charge distributions at their construction (OmpC, [31] and the hydrogen bonding network [32]), or the position of key loops such as L3 (RcP porin, [33]) or L6 loops (OmpG, [34]) affecting the pore conduction directly.

Structurally, porins can exists as monomers, or higher order states such as trimers (examples shown in figure 1.6) and have shown to be highly stable to unfolding over a wide range of temperatures and perturbing conditions *in vitro* [35]. There are also non-constitutive $\beta$-barrel membrane proteins produced by bacteria as toxins, which have a higher order oligomeric state (such as $\alpha$-hemolysin which is a heptamer, and $\gamma$-hemolysin which is octameric).

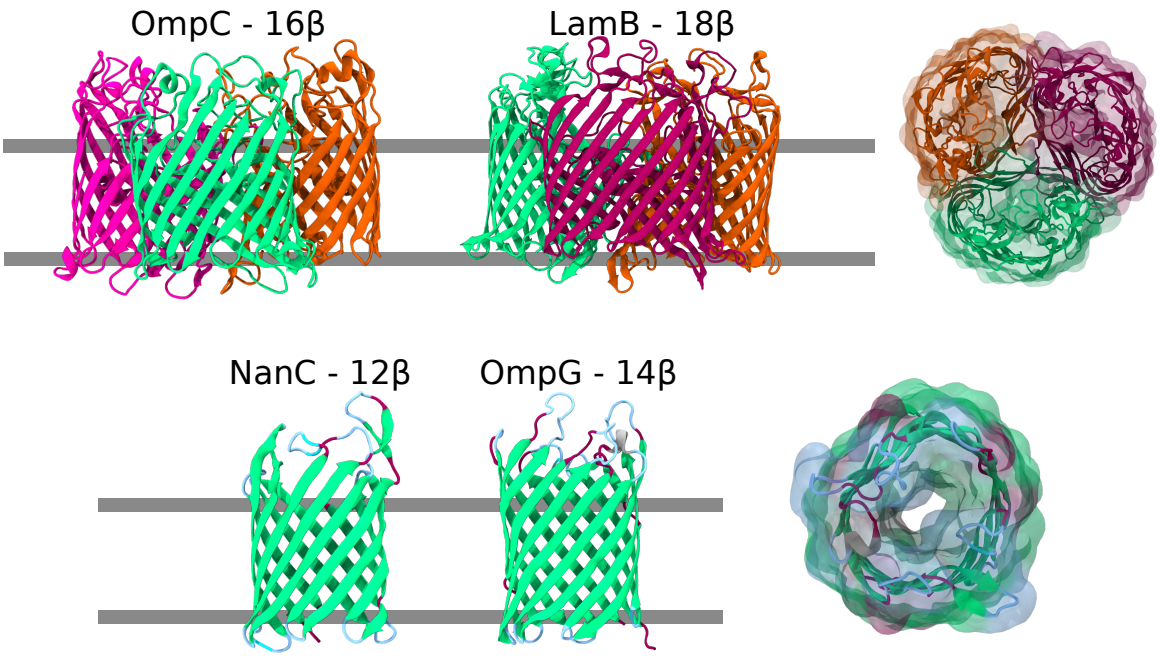


**Fig. 1.6:** Structures of outer membrane proteins found in Gram-negative bacteria. Trimeric pores shown of the cation selective OmpC pore, and the maltose specific LamB. Monomeric pores of NanC, which is specific for acidic saccharides and OmpG, for non-specific large oligosaccharides. Face down images are of LamB and OmpG. All pores are shown in the same orientation to which the top reflects the extracellular regions, and bottom the periplasm. Represented with the extracellular region being the top side for all 4 proteins.

To this month (September 2015), there are a total of 551 unique membrane protein structures [36], out of a total of 36,141 number of unique structures within the protein data bank (~1.5 %). This low number in comparison is due to the difficulties of structure determination of such types of protein especially with over-expression, purification and crystallisation of such proteins [37] as in most cases, these proteins are expressed at low levels within the native cell [38]. Many methods are utilised to improve the crystallisation of membrane proteins such as detergents, antibody fragments and recently, lipidic mesophases for gaining x-ray crystal structures [39], in which the proteins are highly concentrated within a continuous cubic lipid phase. In recent years structure determination methods have advanced significantly, especially with advances

in cryo-electron microscopy (cryo-em). This was used to determine the structure of complex I of the respiratory chain [40], which has 44 subunits with a combined mass of 1 MDa and most recently, different conformational states of the glycine receptor (GlyR) have been defined via this method [41]. Improved computational techniques and algorithms have allowed this method of structure determination to be used for larger proteins, of which some are membrane proteins. Porins are known to be flexible (in their loop regions), thus improvement in structure determination which also has the ability to give dynamic information is also a consideration, such as nuclear magnetic resonance (NMR). The use of solid state magic-angle spinning NMR has allowed information on flexibility, consequently the dynamics, on what is usually considered a static protein by other methods [42] such as the structure by solid state NMR methods of the eukaryotic VDAC barrel [43]. The reconstitution of an integral membrane protein from its hydrophobic bilayer into a solvent is thought to change the structure, thus to prevent this and mimic a membrane environment within NMR, nanodiscs can also be used. This method has been used to study OM proteins, such as OmpX [44].

To note, there are many different types of TM proteins with examples of $\alpha$-helical and $\beta$-barrels:

- *Membrane enzymes.* Prostoglandin $H_2$ synthase and OmpLA
- *Receptors.* GPCR or neurotranmitters receptors such as GluA2 and GluCl
- *Transporters.* Secondary LacY, GlpT, FucP, LeuT. Also the ABC class of BtuCD-F and TonB and the drug effluxers of ErmE, ArcB, TolC
- *Channels and pores.* Aqp and GlpP, Potassium, CLC, Mechanosensitve, Porins
- Membrane proteins of the electron transport chain. Complexes I-V, $bc_i$

of which, only a subset will be discussed and considered for the remainder of this thesis.

### Channels & Pores

Three major classes of TM protein exists for substrate movement through a membrane. Channels, which enable passive substrate flow down the concentration gradient at near diffusional rates. Pumps, which use energy in the form of ATP and its subsequent hydrolysis to transport against the substrates concentration gradient, and transporters, which can couple substrate movement against its concentration gradient to that of another, *e.g.* protons, such as LacY, which transports lactose against its concentration gradient by using a favourable proton gradient.

It is known that ion channels can be regulated by a variety of mechanisms, such as voltage, current rectification, light, mechanosensivitity, and ligand binding. This allows passive ion conduction events via the binding of a chemical, such as a neurotransmitter or drug. A subgroup of these ligand gated ion channels (LGIC's) are the cys-loop receptors [45, 46]. The structure of nAChR was first determined by low resolution EM (electron microscopy) [47], followed by a higher resolution (4 Å) 8 years later [48], and further refined structures the same year [49]. Based on the nAChR structure being the only pentameric ligand gated ion channel (pLGIC) structure available for a long period of time, other structures were initially based on homology models of it. Initially thought to be in an open conformation, the nAChR structure has shown to be functionally closed [50], showing that observation of a crystal structure and its dimensions cannot present a definitive answer into the conformational state of a channel. The first non-nAChR structure (23 years after the initial nAChR structure) was the bacterial GLIC channel in an open state (3.1 Å followed by a higher resolution structure [51] and closed at neutral pH [52]) and the ELIC channel (closed) [53]. Another pLGIC, the glutamate gated chloride channel (GluCl) was crystallised in an open state and with agonist ivermectin [54] and lipid (POPC) bound GluCl, [55] and most recently, the $GABA_A$ receptor [56]. A new structure, the 5-$HT_{3A}$ receptor will

be investigated in this thesis (chapter 6).

All ion transport events have to be regulated so cellular events can happen in the correct time and place, *e.g.* the action potential. This can be done by three main ion current gating mechanisms shown in figure 1.7.

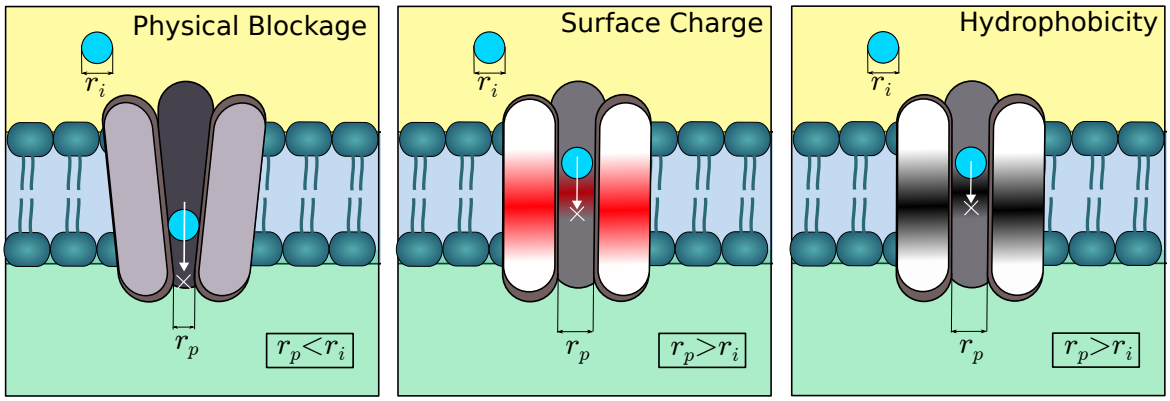


**Fig. 1.7:** Ionic current gating mechanisms. Shown are three representations , with the protein indicated in the center in grey. In the middle figure, charge is shown in red, and in the right hand image, hydrophobic bands are shown in black on the protein. Bilayer is indicated with dark green circles and lines, blue sphere indicates a figurative ion. Ion radius ($r_i$) and pore radius ($r_i$) are indicated.

Via a conformational change, the structure of a membrane protein can change to accommodate the needed conductive state. The passage of substrate will not occur due to the physical presence of the channel protein within the conductive pathway. This is indicated in figure 1.7 as a physical blockage, in which a change such as a "helical" movement changes the conductive pathway creating a region smaller than that of the translocating substrate. An example of this is the mechanism of KcsA with a gating state of the cation being dependent on the helix bundle crossing on the intracellular side therefore being regulated by a physical blockage to all solute species [57].

Protein gating and selectivity of ions via surface charge is done so by surface charge on the protein being able to exclude ions of the same charge, while ions (or molecules) of the opposite charge or neutral can conduct through, with the role of

surface charges also contributing to general sensing [58]. An example of this is also in KcsA's selectivity filter [59] and a crystal structure of the closed form [57], in which, carbonyl groups of the p2 loop form the selectivity filter for potassium ions, thus begin cation selective from the charge association.

Ionic current gating via hydrophobicity is based on the unusual behaviour of water in confined hydrophobic regions and is a well studied gating mechanism.

### Hydrophobic Gating

Within a protein pore with a hydrophobic chemical nature, be it a channel or theoretical model, there is a change in the density of water within the pore, dependent of the radius of the hydrophobic region. Therefore, with a change in radius as seen in conformational change of channels there is a drying or wetting transition within the hydrophobic protein region (within TM the protein pore). The radius and hydrophobicity of the channel is able to regulate the water, hence ion or substrate flow through. This was first observed in molecular dynamics (MD) simulations of model nanopores and also within hydrophobic carbon nanotubes of a certain radius [60, 61], with initial models showing bulk water transitions below a radius of 4.5 to 5.5 Å [50, 62] and general bulk water transitions modelled in hydrophobic pores [63, 64] (and sometimes conceptualised as the formation of nanoscopic bubbles [65]).

The diameter of a water molecule is ~3.5 Å, thus assumed in a crystal structure if the region was at least this in diameter, a water molecule would in theory be present. However, in hydrophobic regions with radius less than ~7 Å, the bulk behaviour of water changes to varying degrees of liquid-vapour transitions. The most prominent transitions occur between a radius of 4 to 7 Å, with only a 1 Å change in radius changing the water state of a pore (observed in the TWIK potassium channel [66]), thus a small change in radius form a conformational change can result in a different

conductive states [50]. A graphical representation is shown in figure 1.8.

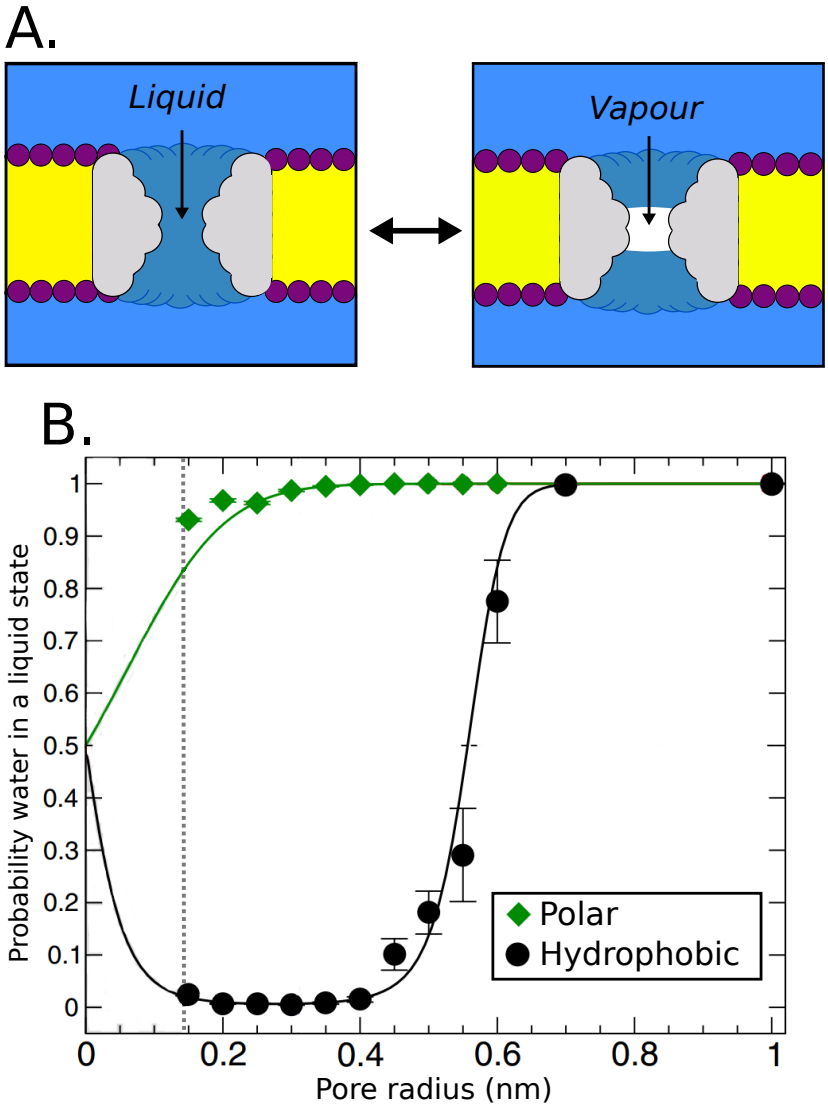


**Fig. 1.8:** Probability of water based on hydrophobicity. A. Representation of a pore (grey) in a bilayer (yellow and purple), radius and chemical nature of the pore can result in a dry-vapour region indicated. B Probability of water within the pore for a polar nanopore model and that of a hydrophobic one. The fully polar, hydrophilic pore remains wet. Once radius increases from 4 Å, a change in water within the pore occurs with saturation at 7 Å radius. dotted line represents the radius of a water molecule. Images adapted from [62, 67].

Simulation tells that these are true gates in the form of free energy calculations [68], not just to water but also to various ion species. In simulation, these barriers have

been overcome with the application of a constant electric field [69]. Experimentally, hydrophobic nanopores have been investigated in solid state nanopores, in which an applied voltage can cause wetting in an otherwise dry pore [70].

Within this thesis, hydrophobicity will be investigated via the building (chapter 3), free energy calculations (chapter 4) and voltage breaking (chapter 5) of such gating motifs.

With the diversity of ion channels, many have pore dimensions which correlate to the radius of water transition events and also have the hydrophobic residues to do so.

This has been proposed for a number of ion channel gates (review [67, 71]) with experimental investigations and simulations on the nicotinic acetylcholine receptor (nAChR) [48, 72, 73], also other pentameric ligand gated ion channels (pLGIC), [74–76] and MscL [62, 77–80] with all using hydrophobic leucine residues. MD studies and free energy calculations into the nAChR receptor [72] demonstrated that the hydrophobic region of the pore, and the liquid-vapour state is indeed a true energetic barrier.

Hydrophobic gating was also noted in voltage gated potassium channel [81, 82] and the TWIK potassium channel experimentally and via simulation [66], and with many other channels such as GLIC, and MscS (summarised in [67]). Also recently in the magnesium channel CorA [83], which has a key leucine residue (L294) within the dry region of the pore

## 1.4 Nanopores

Protein engineering has been an expanding field in recent years with two strategies; rational design and directed evolution to design such proteins. With the improvement of protein structures and the use of computational tools, rational design of proteins can be used for nanoprotein assembly [84], enzymatic improvement for industry [85],

membrane protein design [86] particularly within the nanopore field.

Nanopores have many potential uses within single molecule chemistry [87] such as stochastic biosensors [88, 89], electrical devices [90, 91], water filtration [92–95], separation of gases, ions, and biomolecules [96–98], and also in DNA sequencing [99–101] which is the basis of the sequencing by Oxford Nanopores MiniION. This has been successfully used to identify bacterial antibiotic resistance islands [102] as part of the movement into next-generation sequencing with continual improvements [103].

They can be constructed from different biological and non biological materials, with an overview of the most familiar nanopores in figure 1.9, which shall be discussed further and will be a focal point of this thesis.

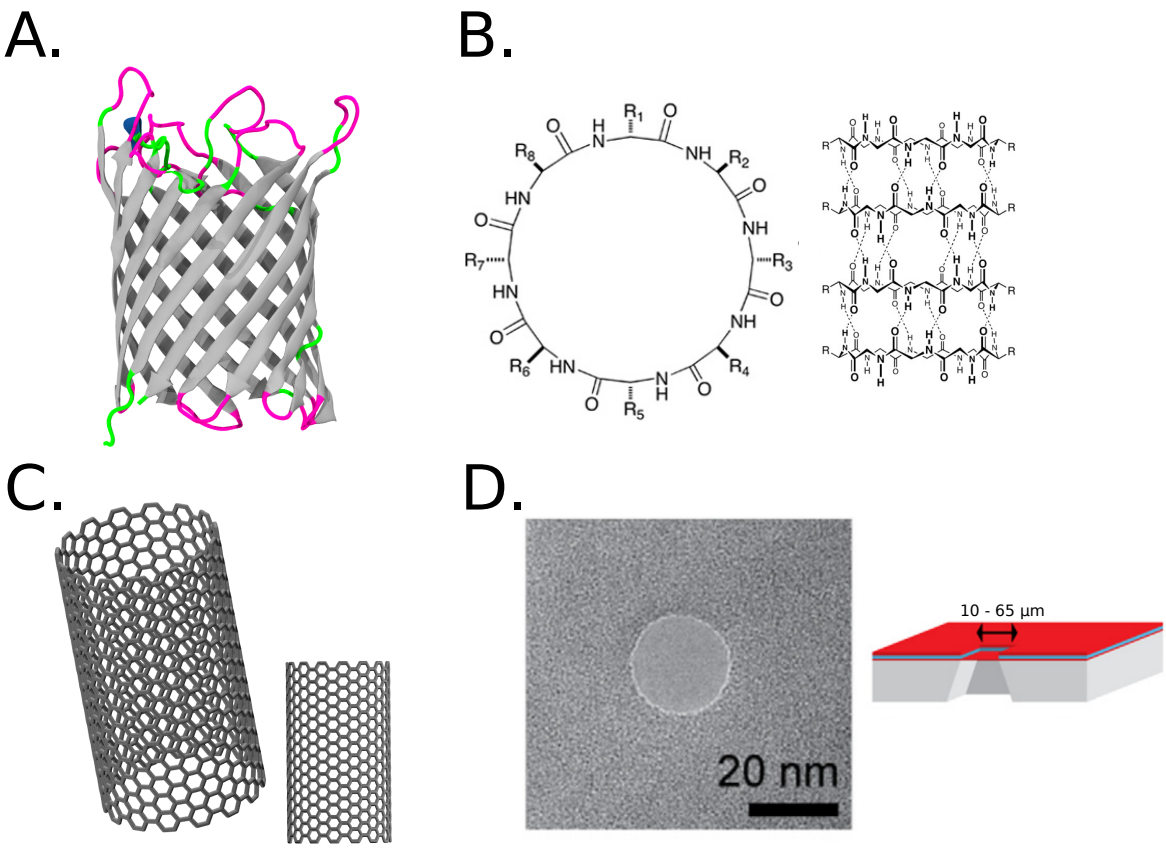


**Fig. 1.9:** Various types of nanopores. A. Biologically based monomeric porin OmpG. B. Cyclic peptide nanopore of D,L-$\alpha$-peptide, with a pore formed via stacking (image from [104]. C. Carbon Nanotube. D. Solid state nanopore and a typical scaffold and dimensions (image from [105]).

### 1.4.1 Types of Nanopore

To date, many reviews are available on the various types of nanopore [106–109], with the basis that there are three main types of nanopores: protein, artificial and solid state.

#### 1.4.1.1 Protein

Protein nanopores were based initially on the lytic, pore forming protein, $\alpha$-Hemolysin ($\alpha$-HL) expressed by the *Streptococcus* bacterial genus, which as a pathogen, punctures

red blood cells. As a protein, it contains a barrel domain and a cap domain (figure 1.10 on page 22) and after association of the heptameric units, it spontaneously inserts itself into a lipid bilayer.

With the structure determined for $\alpha$-HL [110], a zinc binding site (using 4 histidine residues) was integrated into the pore which in turn turned the channel into a $Zn^{2+}$ sensor [88, 111] with the basis it could be used for various other detection processes [89] such as protein [112], organic molecules [113], TNT [114] and also detection of different chemical enantiomers through the pore [115].

A recent development of the nanopore of $\alpha$-HL is its ability to sequence DNA [116] and RNA [117]. The pore itself ($\alpha$-HL) has a constriction of 1.4 nm (present at the barrier cap region at residue M113), which is larger than the diameter of a single stranded DNA (ssDNA), but smaller than that of the double helix, thus the single strand DNA can be threaded through the pore. Mutagenesis of $\alpha$-HL [118] has allowed more manipulation, with enhanced translocation and sequencing of DNA [119] through via manipulation of the internal charge of the pore [120] to allow faster translocation and also the opposite, slowing down of DNA translocation through such a pore with the site directed mutagenesis of positive charges within the constriction [121]. Additionally adaptors [113] such as $\beta$-cyclodextrin (and others of interest [122]) have been used to improve stand recognition and gating events into the pore.

Another nanopore of interest is the MspA pore [123] (figure 1.10 on page 22) which, like $\alpha$-HL has been shown to detect and translocate ssDNA with recognition of all 4 bases [124]. Unlike $\alpha$-HL, it is a member of the porin family produced by the *Mycobacteria* genus, allowing hydrophilic substrates into the bacterium. In comparison to $\alpha$-HL, it has a smaller constriction (of 1.2 nm) which is present at the base of the protein, near the periplasm entrance.

Other DNA sequencing pores for consideration are the mechanosensitve channel,

MscL [125] and also the phi29 protein. This protein is a DNA-packaging motor from bacteriophage, which allows double stranded DNA (dsDNA) to enter the virus [126, 127]. It has also been combined with MspA to improve DNA sequencing [100]and is being used as the next-generation DNA sequencing device [128, 129] and the basis of many biotech companies for such purpose.

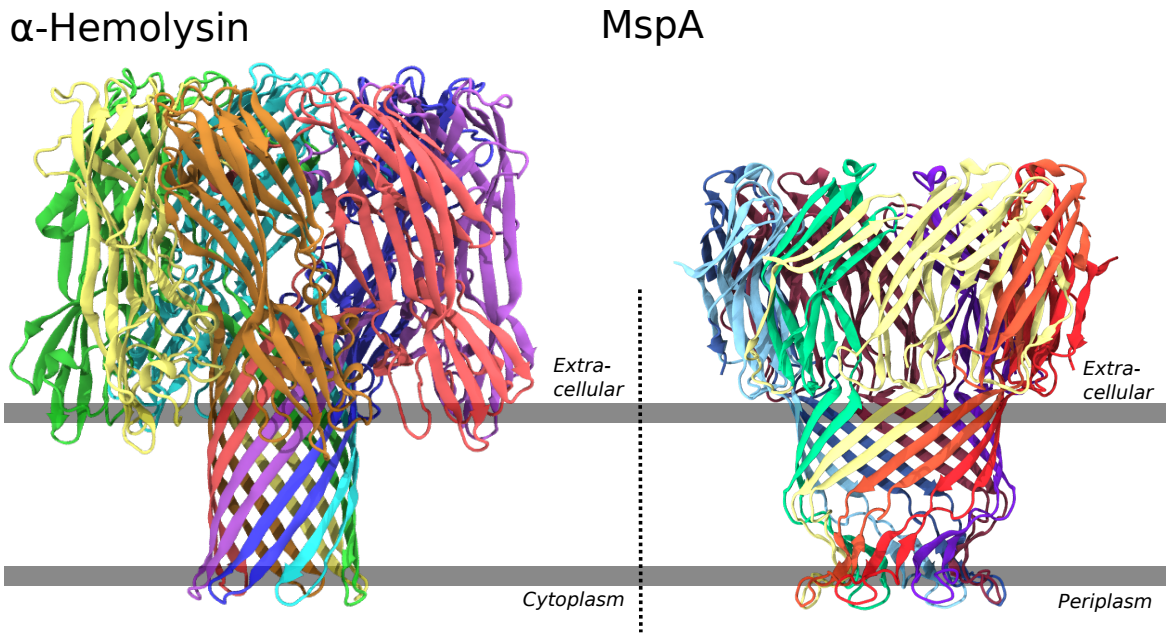


**Fig. 1.10:** Protein pores for DNA sequencing. $\alpha$-HL & MspA. $\alpha$-HL consists of 7 subunits with a transmembrane $\beta$-barrel domain and a cap domain which is present as shown, between the cytoplasm and extracellular region in an eukaryotic membrane. MspA is an octameric porin with each subunit containing a $\beta$-sandwich and a beta ribbon. This is present physiologically on the OM of the bacterium.

The sensing of analyte and DNA above is based on stochastic sensing (figure 1.11). With the addition of an applied potential, a normalised current is present due to the flow of ions on either side of the bilayer through the pore. A native or engineered binding site for the analyte is present in the pore (or the presence of a DNA strand). Each time an analyte binds, or a specific base of DNA is present within the constriction/pore region, the current is modulated - and its unique to the analyte and pore, from which concentration of the analyte can also be calculated based on the lifetimes

of bound/unbound state.

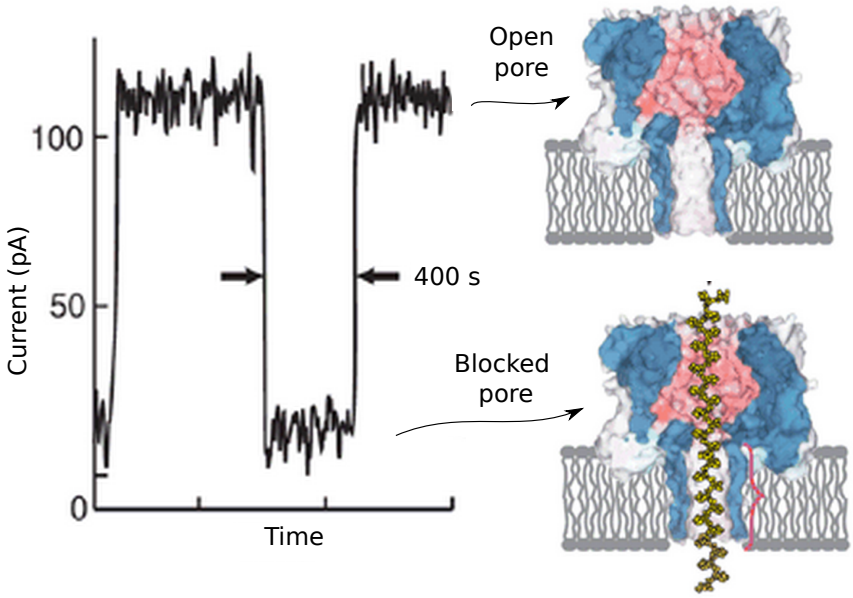


**Fig. 1.11:** Stochastic biosensing of DNA. A time-current trace is shown from a theoretical binding event, in this figure it is the presence of a polymer (DNA) strand through the pore. The open pore has a higher current than that of a modulated, DNA-present pore, with DNA sequencing each base (A,T,C, or G) has its own current level. The change in current is dependent of the base present, and from the values, the sequence can be determined. Image adapted from [116].

Other biological pores mimicry and biosensing are also the similar to $\alpha$-HL such as the anthrax pore (has a much longer barrel domain) [130]. But also the porins such as OmpF [131], FhuA [132–134] & OmpG [34, 135] which have all been mutagenised to improve function as DNA sequencing pores or biosensors. It is also possible to modify the general activity of nanopores, such as MscL via various chemical biology modifications to become light activated [136].

#### 1.4.1.2 Artificial & Peptide (including Graphene)

**Artificial**

These nanopores are much small in size than biological pores and come in a variety of constructs and chemical motifs [137–139]. Originally, these pores were made out of a central crown ethers, which are three amphipathic macrocyles on each side of the membrane, making the wall of the nanopore, which in turn produces a hydrophilic channel [140] and the basis of many synthetic channels available in a wide range of channel motifs [141]. They can be formed out of metal-organic chemicals, from $\pi$-$\pi$ stacking, based on these macrocycles (with variable inward and outward pointing functional groups) and are shown to be ion selective and also water permeable [142].

An example of a recent artificial channel is that constructed from hydrazine-appended pillar-[5]-arene derivatives which have been shown via an x-ray crystal structure to adopt tubular, pore structure which have been shown to insert into the membrane of lipid vesicles and conductive to water [143]. The structure design for this synthetic pore is mimicked from the single pore features of aquaporins [144].

A number of artificial systems for transmembrane transport exist with transport of ions and neutral organic solutes [145, 146] and water transport [147] through many artificial channels [148].

**Peptide**

Peptide nanopores can be formed from artificial $\beta$-barrels with varying structural motifs based on the strand [149]. Synthetic $\alpha$-helices are also functional, constructed from leucine and serine residues in a heptad repeat to form a helix. The arrangement places all leucines membrane facing and all hydrophilic serine residues lumen facing to create a conductive channel, and self assemble into a helix bundle [150]. Based on this structure, it is possible to build such a pore in which selectivity and functionality

can be represented through lumen pointing amino acids.

Cyclic peptide nanotubes [137, 151, 152] composed of $\alpha$ amino acids (example in figure 1.9, B. on page 20) are also functional pores, with alternative stereochemistry can be used to form pores creating a structure known as $\beta$-helices.

Most recently, nanopores have been constructed out of DNA [153] and also DNA origami constructs [154].

### Graphene

This well known material made from an allotrope of carbon which can exist in the 2D, as graphene sheets or within the 3D as buckminsterfullerene [155] or carbon nanotubes (CNT's) [156] (figure 1.10, C. on page 20). In the 2D form, it can be used as a nanopore, with functional conductive pores from 3 Å in diameter [157]. The 2D graphene pores have also been shown to translocate DNA [158–162] with investigations into its hydrophobicity for such purpose [163]. Computationally, the pores have been modelled with a biomimetic ammonia switch within a theorised synthetic channel [164] and as bioinspired pores with selectivity for $Na^+$ and $K^+$ [165].

CNTs can form functional pores and has been simulated as water conductive [60, 166], with the addition of charges used to modulate selectivity through a model CNT pore [167]. Recently, this stochastic transport through these CNT in lipid bilayers and live cell membranes has been experimentally noted[168]. However, these pores are difficult to insert into bilayers unless externally modified [169] due to the hydrophobic nature of the nanotube and their interaction with the hydrophobic lipid tails.

Both carbon forms can act as general pores (with CNT being radius dependent), however specificity is difficult introduce in the water-conductive lumen of both via specific chemical modification due to the size and the ubiquitous nature of the material. External modification of both is well characterised (in CNT at the end of the tubes)

and could have useful medical implications [170, 171].

#### 1.4.1.3 Solid State

First fabricated in ~1991 as a polymer nanopore (overview in [172, 173]), they were designed initially as a scaffold for biological applications. Initially pores were created with ion beam sculpting on $Si_3N_4$ membranes which created pores, with diameters of ~60 nm. With the use of ion-track etching, pores with much smaller diameters of up to 2 nm were constructed on silicon nitride (SiN) membranes [174] with the development of such method for thinner membranes [175], with recent electron beam methods being used to create pores which can be visually inspected [176].

Solid state nanopores have been used in the detection of many biological species, be they DNA [177–180], RNA [181], proteins [182–184], CNTs [185], and also the recognition of DNA structures [180, 186]. They have also been modified for the sensing of small molecules, such as potassium in the form of a DNA switching event (within the lining of the pore) with the binding of $K^+$, to these DNA strands and changing the diamater of the pore and modulating pore current [187]. Also implementation of zinc finger motifs which have been immobilised on the channel walls, changing configuration with $Zn^{2+}$ binding [188], With the same principle being applied to $F^-$ binding and recognition [189].

Variations to the standard solid state pore have been applied with chemical modification of pores allowing for regulation via pH & voltage [190] and development into voltage gated pores [191]. Based on immobilisation with (trimethylsily)diazomethane [70] which incorporates hydrophobicity into the newer polyethylene terephthalate (PET) nanopores. This type of modulation brings about much interest into the use of such mechanisms for nano-electronics and voltage gated nanopores [192]. Such pores have also been lipid coated [193], based on insect olfactory systems, which trap

odourants within lipid pores on their skin. This nanopore system has been shown to act in the same manner, with concentration of such molecules within the lipid-lined solid state pore.

More variations have been applied in the replication of the nuclear pore complex within a solid state system [108, 194] with recent example in which a solid state pore has been functionalised with an FG strand mimicking polyisopropylacrylamide (pNIPAM), where faster single stranded DNA translocation was noted through the functionalised pore [194]. Pores have also been demonstrated for their DNA sequencing ability [159] with comparisons between both solid state and biological sequencing pores being made [195].

The solid state scaffold can also be hybridised with protein nanopores such as gramicidin A [196] and $\alpha$-HL [197].

## 1.5 Utility of Simulation

Simulations can be performed using many or few levels of detail, from the computationally demanding quantum mechanics to the continuum based models of simulation (figure 1.12, A.).

Generally, the more detail in a simulation the longer it will need to be simulated, therefore one needs to consider a balance between level of detail and efficiency. Within this thesis, only atomistic (AT) and coarse grained (CG) simulations will be used, with the main detailed focus of this thesis on the AT simulations with an approximation of accessible time scales shown (figure 1.12, B.).

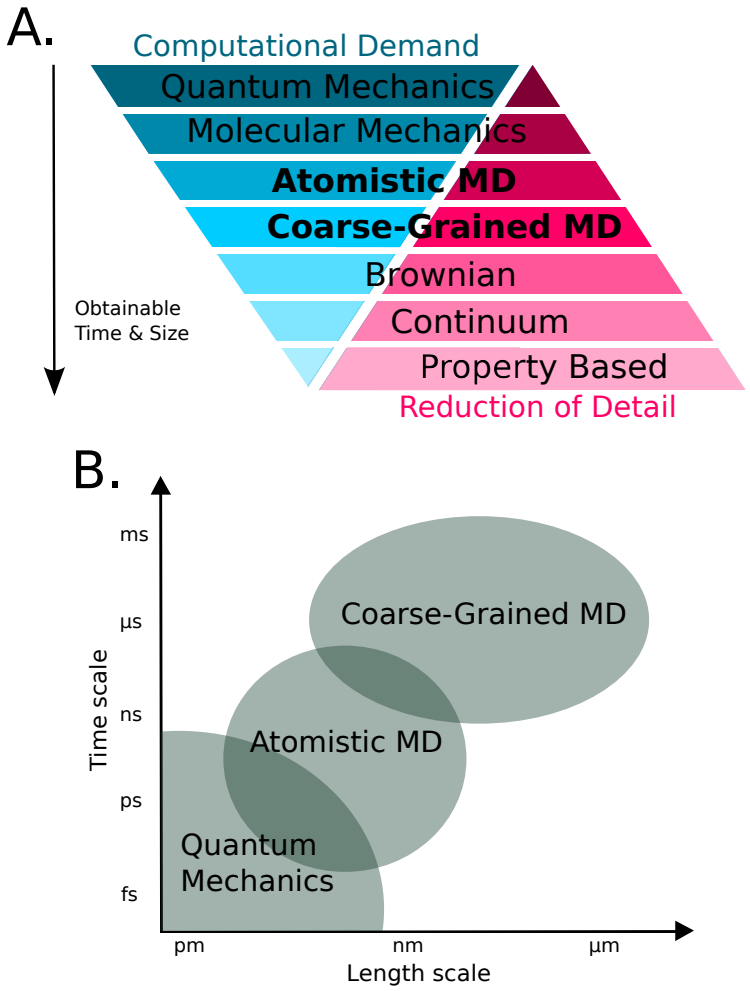


**Fig. 1.12:** Compromise between computational details and demands and computational methods time scales. A. Comparison of details and demands. QM methods require a higher computational demand with comparably the least reduction in detail whereas property based methods are the opposite. Methods used in this thesis are indicated in bold. B. The circles indicate an estimate of the boundaries of the possible time and length scales feasible. Figure adopted from Dr. Jochen Klingelhoefer.

## 1.6 Work Presented in this Thesis

Based on the increasing number of nanopores, numerous biomimicry available, and increasing number of protein structures, this thesis will be based on the design and implementation of biological motifs into a computational nanopore model.

Within chapter 3, the question of whether a hydrophobic gate can be computationally transplanted into a simple nanopore model will be addressed, based on the known structure and simulation of other $\beta$-barrel proteins [198–201]. The functionally of such a motif will be added in the form of hydrophobicity and polarity of amino acids, and analysed by water flow through the pore and compared with many previous simulations of water within hydrophobic nanopores [60, 64, 202–206] to investigate the hydrophobic gate, and validate the theoretical model's stability and shape.

Based on previous free energy calculations [207–210], ion conduction through hydrophobic pores [211, 212] and in combination with nanopore design in pores [167, 213, 214], the validity of the gate from the previous chapter will be assessed via free energy calculations. This will be conducted on some of the more interesting model pores (ability to change water conductance through) with the aim to address the way in which the hydrophobic region regulates ions and water through the pore.

Simulation under voltage has also been extensively simulated, be it membrane only [215–218] or with protein incorporated [200, 219–221]. Therefore, models will be simulated under voltage, as it is known that it can indeed break a hydrophobic barrier within a solid state pore [70]. Therefore, can such a transplanted barrier within the model nanopores be broken in the same manner? The simulation will be analysed based on previous simulations of hydrophobic pores and their water behaviour [222, 223] within nanopores [69, 203, 224–226] as an assessment of the affect of voltage upon these models and the hydrophobic barriers.

The function of the biomimetic hydrophobic gates shall be compared to a new serotonin receptor (5-$HT_3$) which is presumed to be in a closed state and gated in a similar manner. It will also be investigated via free energy calculations based on previously known gating mechanisms of pLGIC's [227] with combined theory and simulation into their ion conduction events [228, 229]. Previous simulation of the

drying transition in the hydrophobic gate of GLIC [75], nAChR [72] channels, as well as equilibrium MD [230, 231] and conformational states simulations [232, 233] on other ligand gated ion channels allow a full overview and comparison to the new channels conductive state.

Chapter 7 will present an overview of the findings of the previous chapters highlighting their significance with future direction discussion.

# Chapter 2

# Methods

*"All We Know, Is Don't Let Go"*

Taylor Swift

The findings presented in this thesis are based on the use of molecular dynamics (MD) simulations to study nanopore design and hydrophobicity. The methods used are described in the following section, with a more detailed discussion in *A. R. Leach* [234] and the GROMACS manual [235] where appropriate.

## 2.1 Classical Molecular Dynamics Simulations

The behaviour of biological molecules can be described by the interactions between the nuclei and electrons. Via simulation, this complete representation using quantum mechanics is a computationally demanding process, limiting the use of this type of simulation technique to relatively a small number of atoms (<1000) *e.g. enzyme substrate binding sites* [236, 237]. To efficiently simulate large molecules, be they biological in nature or not, using MD requires the effective ignoring of these nuclear elements, and thus the formation of classical MD simulations [234]. In classical MD simulations, the "force field" is a interpretation of the interactions between all the

atoms within the system [238]. The field is a potential energy function, $V(\mathbf{p}^N)$, where $\mathbf{p}$ is the position of such particle and N is the their number. The potential energy is generally calculated from the sum of the bonded and non bonded interactions.

$$V(\mathbf{p}^N) = \sum V_{bonded} + \sum V_{non-bonded} \tag{2.1}$$

### 2.1.1 Bonded Interactions

These interactions are composed of bond stretching ($V_{bonds}$), bond angle bending ($V_{angles}$), and bond torsion described as the rotation of dihedral angles, ($V_{torsions}$). To preserve stereochemistry, improper diheadral angles can be incorporated ($V_{improper}$). These interactions are shown diagrammatically in figure 2.1 on page 33.

$$\sum V_{bonded} = \sum_{bonds} \frac{k_B}{2}(l_i - l_{i,0})^2 + \sum_{angles} \frac{k_\theta}{2}(\theta_i - \theta_{i,0})^2 + \sum_{torsions} \frac{V_n}{2}(1 + cos(n\omega - \gamma)) \tag{2.2}$$

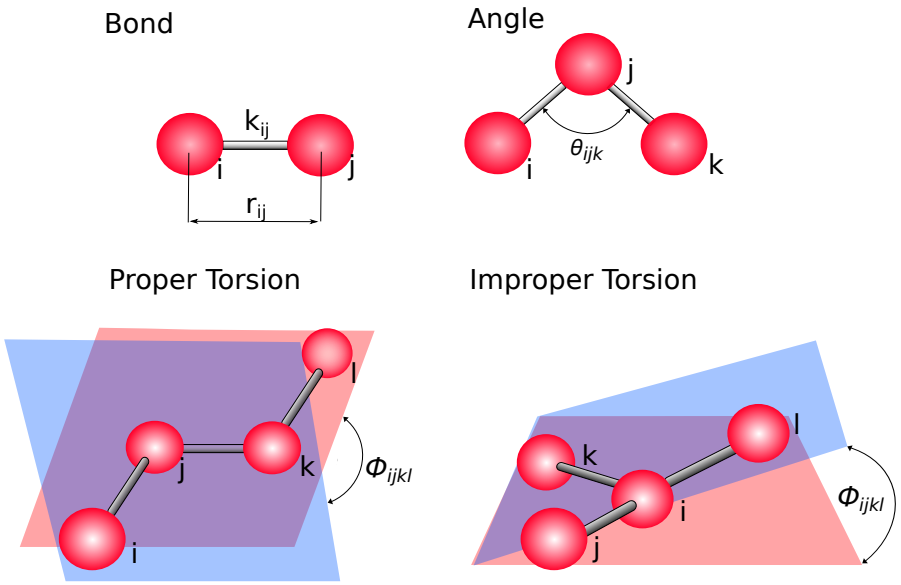


**Fig. 2.1:** Bonded interactions. Atoms are represented as red spheres with bonds being shown as grey rods. Figure is adapted from http://cbio.bmt.tue.nl/pumma/index.php/Theory/Potentials.

The potential energy for a bond stretching and angle terms can be described via Hooke's law, in which the energy varies with the square of the displacement from the reference bond length ($b_0$) or angle ($\theta_0$). Force constants are also implemented (atom set specific) to govern the penalty resulting from bond stretching and angle bending. These values are hard to deform from their high values, thus most of the energetic and conformational changes encountered during simulation are a result of non bonded and torsional effects [234].

Torsional angle interactions differ to those previously mentioned with internal rotational barriers lower compared to the other interactions and are also periodic in nature. This can be represented in the conversion between states of alkane chains, such as butane which exists through the "high" (eclipsed) and "lower" (staggered, gauche or anti) energy states [239].

### 2.1.2 Non-Bonded Interactions

Non bonded terms can be grouped into Van der Waals (VdW) and Coulombic, electrostatic interactions

$$\sum V_{non-bonded} = \sum V_{VDW} + \sum V_{electro} \tag{2.3}$$

$$\sum V_{non-bonded} = \sum_{i=1}^{N} \sum_{j=i+1}^{N} \left( 4\epsilon_{ij} \left[ \left( \frac{\sigma_{ij}}{r_{ij}} \right)^{12} - \left( \frac{\sigma_{ij}}{r_{ij}} \right)^{6} \right] + \frac{q_i q_j}{4\pi\epsilon_0 r_{ij}} \right) \tag{2.4}$$

#### 2.1.2.1 Van der Waals Interactions (Lennard-Jones Potential)

The Lennard-Jones (LJ) potential is used to approximate the interaction between a pair of neutral atoms, thus the VdW term mentioned here. Included in the potential is the strong repulsive term ($r^{12}$) (Pauli repulsion), present due to overlapping electron orbitals and long attractive long term ranges ($r^6$), originating from short ranged instantaneous dipoles (London dispersion) [234]. The potential has the following form:

$$V_{LJ}(r_{ij}) = 4\epsilon_{ij} \left( \left[ \frac{\sigma_{ij}}{r_{ij}} \right]^{12} - \left[ \frac{\sigma_{ij}}{r_{ij}} \right]^{6} \right) \tag{2.5}$$

in which $\sigma_{ij}$ indicates the distance at which the energy between the two atoms in the system is zero, $\epsilon_{ij}$ describing the strength of the interaction. Both parameters are dependent on the species of $i$ & $j$.

An artifact of the LJ potential is that it has an infinite range, with the force becoming infinitely weak at long distances. Computationally, this is highly demanding as the force must be calculated for every pair of particles within simulation. Thus, a cut-off is introduced to reduce this number of calculations. In this thesis, a cut-off is placed at 12 Å and a smoothing of the potential from 9 Å to reduce complications from a straight cut off.

#### 2.1.2.2 Coulombic Interactions

Dipoles, based on unequal electron positioning exist due to electronegativity differences resulting in a "charge" in a molecule. In the classical MD model this can be replicated by the placement of partial charges within an atom [235]. The Coulombic interaction between partially charged particles can be calculated using Coulomb's law which includes the particles ($i$ & $j$), their partial charges ($q_i$ & $q_j$), the distance between them ($r_{ij}$), and the produce of permittivity of free space ($\epsilon_0$).

$$V_C(r_{ij}) = \frac{q_i q_j}{4\pi\epsilon_0 r_{ij}} \tag{2.6}$$

With a scaling of $r^1$, unlike the $r^6$ within the LJ potential, the decay to zero is much slower in this form of non bonder interaction. Therefore, more consideration is needed in MD for this long range type of interaction [238].

### 2.1.3 Pair Exclusions

The non bonded interactions only apply to atoms pairs ($i$ & $j$) that are within the same molecule (but separated by at least 3 covalent bonds) or part of different molecules. The first and second atoms are excluded completely, with the third using modified scaling LJ parameters, and being force field dependent.

### 2.1.4 The Particle-Mesh Ewald method

Long range electrostatics are calculated with particle-mesh Ewald (PME) method [240, 241] based on the initial Ewald sum method [242] originally used to compute the long range electrostatic energies of a crystal system. This method utilises the periodicity of simulation and is based on infinite latticing a volume within the simulation, of which all interactions are summed. Primarily, PME separates electrostatic

interaction calculation into a short-range component which converges quickly within real space, and a long-range component that converges quickly in the Fourier space. The separation allows a quicker conversion of both (with the rate dependent on the cancelling Gaussian distributions of the point charges conversion), and the application of a cut-off for the real space with a limited number of modes for the Fourier. The implementation via this method reduces the scaling from $N^2$ to $N\log(N)$, where N is the number of particles in the system. PME is used in all simulations of this thesis.

### 2.1.5 Force-Field Parametrisation

Force fields are parametrised to quantum mechanical and experimental data [234] with each based on their own initial data sets. For example electrostatic potential fitting (EPF), to calculate accurate partial charges from a QM model and infrared spectroscopy and crystal structures used for the validation of bond strengths and lengths. With the recent increase in simulation time scales and protein folding, these force fields are possibly unsuitable for such purposes with re-parameterisation needed for such an event [243, 244].

In a force field, a way to reduce the number of particles (and thus the number of calculations performed in the simulation and saving time), is to alter the treatment of non polar hydrogen atoms, *e.g.* those on the hydrocarbon lipid tails such as DPPC. They are combined with the carbon "atom" to form a single interaction site, defined as an united atom (figure 2.2). This may cause difficulties in chiral centres and unsaturated bonds however defined improper dihedrals cease this from occuring [234]. A number of force fields include the implementation of a united atom, the two being used in this thesis are the OPLS-UA [245] and GROMOS [246, 247].

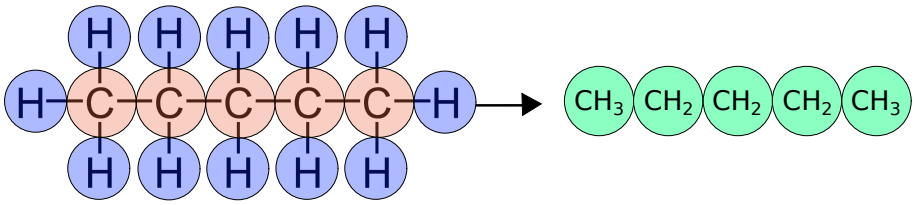


**Fig. 2.2:** United atom representation. Figure shows chemical structure of pentane (atomistic) and its united atom representation as green circles, in which hydrogen atoms are not modelled.

Many other force fields are available for biological simulations of protein and phospholipid bilayers be they CHARMM [248], AMBER [249], and the Berger lipid set [250] based on united atom with elements from the OPLS, AMBER and GROMOS force fields.

## 2.2 Simulation Techniques

Shown in figure 2.3 is the basic MD algorithm by which a simulation is conducted.

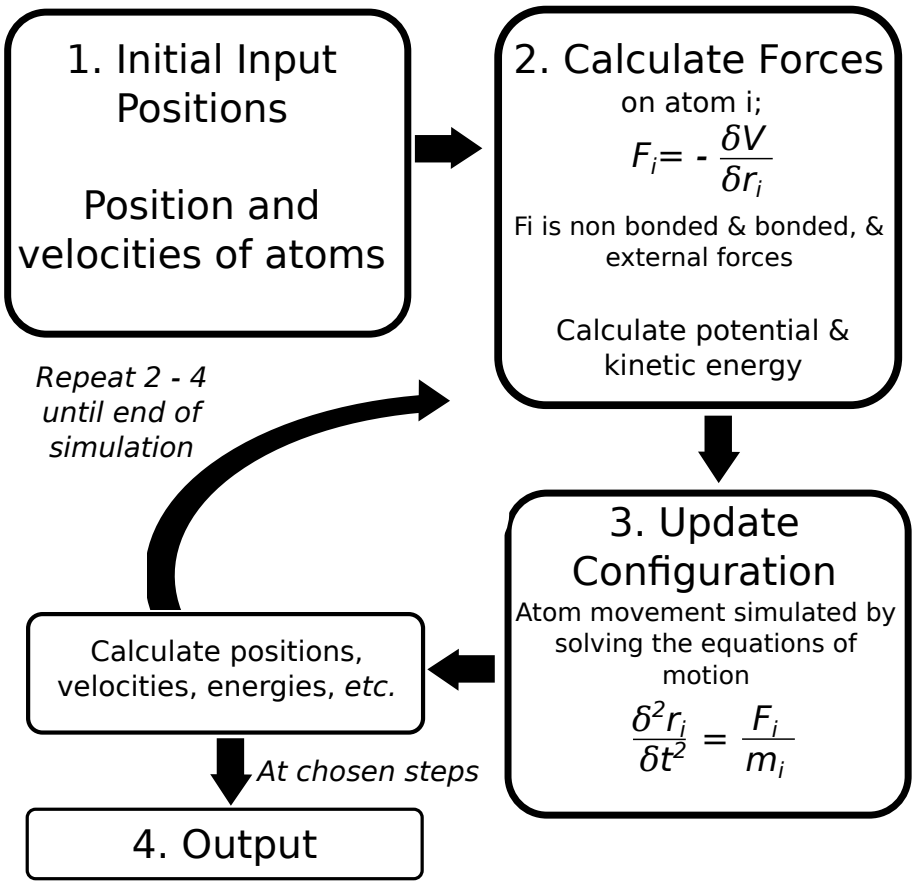


**Fig. 2.3:** MD algorithm. Based on a figure in [235].

Summarised, the change in position and velocity of a particle within simulation can be calculated from their previous, initial state. If no velocity is inserted, they are obtained from a Maxwell-Boltzmann distribution.

### 2.2.1 Equations of Motion

In molecular dynamics simulations, the trajectory of the particles is calculated by solving Newtons 2$^{nd}$ law *(F=ma)*, giving the particles' motion, $m_i$ along the coordinate

($z_i$) with the force $F_{zi}$ acting in in the z direction.

$$\frac{d^2x_i}{dt^2} = \frac{F_{z_i}}{m_i} \tag{2.7}$$

Within simulation, it is not possible to analytically describe motion due to the coupled nature of the particles' motion due to the force being dependent to the position relative to the other particles. Therefore a finite difference method must be used [234].

Finite difference methods are used to generate trajectories within MD. In essence, the integration is broken down into multiple small stages, with each separated in time (by a fixed time). The force on each particle at time, $t$, is calculated as a vector sum of its interactions with the other particles. From the force calculated, the acceleration on each can be gained, and then combined with the position and velocity at $t$, to calculated at $t$ $+\delta t$, with a constant force assumption [234].

Multiple algorithms can be used for this, with the GROMACS package using a modification of the Verlet algorithm based on two Taylor expansions (forward and backward), the leap frog algorithm [251]. Verlet uses the accelerations and positions at time $t$, and positions from the previous step, $\mathbf{r}(t$ $-\delta t)$, to calculate the next position at $t$ $+$ $\delta t$, $\mathbf{r}(t$ $+$ $\delta t)$. The GROMACS package uses the following terms for the leap frog:

$$\begin{aligned} r(t+\Delta t) &= r(t) + v(t+\frac{\Delta t}{2})\Delta t \\ v(t+\frac{\Delta t}{2}) &= v(t-\frac{\Delta t}{2}) + a(t)\Delta t \\ v(t) &= \frac{1}{2}\left[v(t+\frac{\Delta t}{2}) + v(t-\frac{\Delta t}{2})\right] \end{aligned} \tag{2.8}$$

The leap frog is advantageous over the Verlet as it includes explicitly the velocity to calculate the kinetic properties. Within this, the velocities are calculated at the mid point of the position evaluation and *vice versa*.

### 2.2.2 Choice of Timestep

Choice of a time step is not a definite value of a MD simulation. If the value is too small, the trajectory will only cover a limited region of the phase space, if too large there may be integration problems due to the high energy atom overlap, leaving to the non-conservation of momentum. The time step should be a $10^{\text{th}}$ of the time of the fastest motion (corresponding to the C-H bond vibration of ~10 fs) [234]. In all atomistic simulations of this thesis, a time step of 2 fs is used.

### 2.2.3 Bond Constraints

With use of a small time step, to maximise its efficiency it is common to restrain the bond lengths of the fastest bonds, in terms of their vibration (and hydrogen containing). Luckily, these are the least interesting in terms of chemistry to the systems simulated in this thesis. Two methods used are the SHAKE [252] & LINCS [253] restraints. For both GROMOS and OPLS-UA forcefields used in this thesis, the faster LINCS method is used.

### 2.2.4 Periodic Boundary Conditions

The use of periodic boundary conditions (PBC) in simulation allows for a small number of particles to be simulated. It also eliminates a known artifact of simulation, *e.g.* a box of water in which the edges would be in contact with a vacuum, which is rather unphysiological. PBC impose infinite copies of the simulation box in all three directions so that none of the dimensions are exposed to an effective vacuum (example, figure 2.4). This also imposes a constant number of particles within the simulation box.

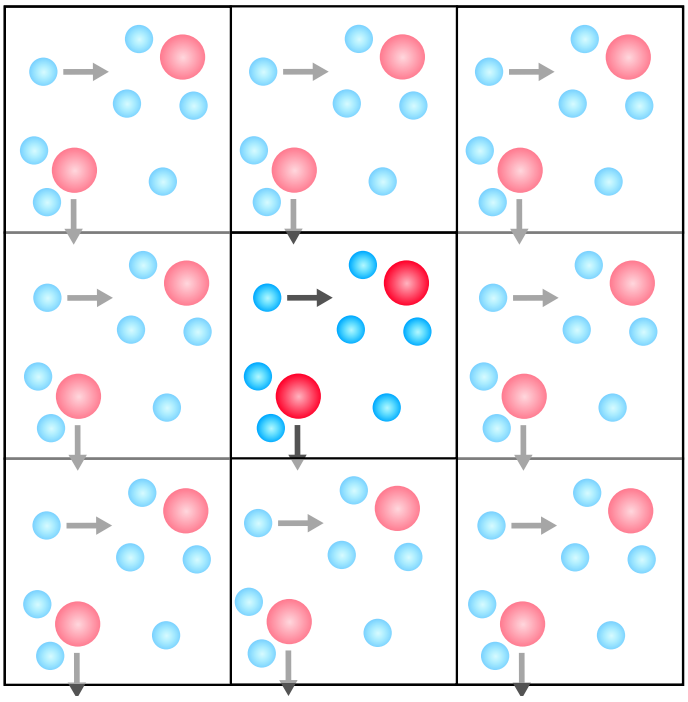

**Fig. 2.4:** Periodic boundary conditions. The simulation box (center, unshaded) is duplicated periodically in all directions (shaded boxes), creating an infinite system, avoiding convergence problems associated with the box edges. If a particle were to leave the box, *e.g.* the red sphere, it will be replaced by an image particle entering from the opposite side. Shown is a 2D extension, in simulation this would be in all x, y, & z directions.

A complication associated with PBC is an unwanted, increased ordering of the system [238] and also problems in regards to "unphysiological" membrane fluctuations [254] which need to be considered in simulation. With the cut-offs mentioned previously, GROMACS uses a boundary condition with a minimum image convention. Thus only the particles closest to an interacting box are considered for short range interactions.

### 2.2.5 Pressure and Temperature Control

In a "standard" MD protocol, a constant *NVE* approach is used which controls the number of particles $N$, the volume $V$ and the energy of the system, $E$ at a constant.

Within biological simulation, it is more ideal to maintain the pressure $P$ and temperature $T$ of the system, therefore a $NPT$ approach is used instead. To maintain the systems at physiological temperatures and pressures, multiple algorithms are used by fundamentally applying a barostat and thermostat to produce constant $NVT$ & $NVP$ systems. In this thesis, the Parrinello-Rahman barostat [255] and the V-rescale themostat [256] is used. Other algorithms are available for coupling (*e.g.* for temperature, the Berendsen, Nose-Hoover, Anderson etc. for pressure, also the Berendsen).

#### 2.2.5.1 The Parrinello-Rahman Barostat

A method to keep a constant pressure on a system is to change the volume of a system (based on Boyle's law). This is done by coupling the system to a pressure bath, with the change in pressure represented as:

$$\frac{dP(t)}{dt} = \frac{1}{\tau_p}(P_{bath} - P(t)) \tag{2.9}$$

in which *P(t)* is the pressure of the component at time *t*. $P_{bath}$ is the pressure of the pressure bath & $\tau_p$ the coupling constant. For this, the box volume is scaled to allow the constant pressure.

In systems containing a bilayer, full pressure coupling diminishes the surface area of lipids within the simulation, therefore semi-isotropic coupling is used, which allows pressure changes along the x-y bilayer to vary, while the z component is varied independently. Pressure chosen in this thesis is the reference, 1 bar [238].

#### 2.2.5.2 The V-rescale Thermostat

In MD, the systems temperature is related to the kinetic energy of the particles:

$$K_{NVT} = \frac{1}{2}\sum m_i v_i^2 = \frac{3}{2}Nk_BT \tag{2.10}$$

where $K$ is the kinetic component, $k_B$ the Boltzmann constant, $m$ is molecular mass, $v$ is the velocity & $N$ the number of molecules. Based on the system, the simplest way to control the temperature is to scale the velocities. In the V-rescale thermostat, the system is coupled to an external heat-bath that is fixed at the chosen temperature $T_{bath}$. The velocities of each particle are scaled proportionally to the change in temperature of the $T_{bath}$ and the system.

$$\frac{dT(t)}{dt} = \frac{1}{\tau_t}(T_{bath} - T(t)) \tag{2.11}$$

where $T$ is the temperature of the system at time $t$ and $\tau_{\mathrm{t}}$ is the coupling parameter of the system to the bath. The V-rescale is very similar to the more commonly known Berendesen thermostat, however with the implementation of a stochastic term which ensures that correct canonical ensemble is generated [235]. Within this thesis, all atomistic simulations are conducted as 310 K, with all coarse-grained at a higher 323 K.

### 2.2.6 Water Models

Multiple water models are possible within an atomistic force field [257] with a trade off between the models' accuracy and complexity. Simple models can be simulated in larger, longer simulations but the more accurate within shorter, smaller systems. Each model is developed to fit well into a particular structure or parameter (be it density or rdf) of water. Within this thesis, the SPC model [258] is used within the GROMOS force field, in which there is no representation of the lone electron pairs on the oxygen, just a negative atom type with the assumption of point charge (this gives an incorrect dipole moment which is altered by changing the bond angle to 109.42°, from the accurate 104.5°) and TIP4P [259] (which has an inward pointing negative charge to try and replicate the lone pair) within the OPLS-UA simulations.

## 2.3 Energy Minimisation

Energy Minimisation (EM) is essential for the start of a MD simulation. This is initially used to find a low-energy structure by reducing steric clashes in the system giving a more stable starting configuration, which is especially needed for coarse grain to atomistic conversion (explained later in this chapter). Two main methods by which this is performed are the steepest decent and conjugate gradient. Both of these methods involve a gradual change in the Cartesian coordinates, reducing the energy of the system to a minimum. As a method, the steepest descent looks for minima using a line-search approach which is independent of the previous step, thus most effective when the system is far away from the energy minima. The CG-MD simulations used the steepest descent method. For AT-MD systems, a minimum of 5000 steps of steepest descent was used. The conjugate method is based on the next step which is dependent on the previous, and is most effective when the system is at its minima [234].

## 2.4 Coarse Grained Simulations

Coarse graining allows for a decreased complexity of a system (therefore allowing longer time scales to be simulated). Multiple coarse grained (CG) models & force fields have been built by many groups in recent years with varying degrees of "coarse-graining" be it the Martini force field [260], with the approximate 4:1 mapping of atoms of amino acid residues, 1 residue to 1 bead mapping [261] or approximate shape mapping [262]. Recently, CG has been applied to the 4:1 mapping of DNA [263]. Reducing the system in this parameter results in fewer calculations and longer time steps (20 fs for CG) with an increase up to 1000 fold speed up in simulations compared with an atomistic system.

Within this thesis, CG simulations are used exclusively for protein insertion into a bilayer via a self assembly method (due to the speed up for the CG versus AT method) and a relavitly quick simulation for protein stability. This is done via the Martini model [260] for the channels (chapter 6) and a version of the Martini - the Bond force field [264] for the $\beta$-barrel simulations. The bond force field has been used extensively in simulations of membrane proteins with successes, especially to those of porins, which are to be replicated in this thesis. An application of a harmonic restraint to maintain protein secondary structure between residues $i$ and $i + 4$ (except a proline) is applied in the Bond force field, however, in the Martini, a form of dihedral angle restraints on the protein backbone is used.

Even with the advantages mentioned to this simulation method, many disadvantages also follow which makes this an unsuitable model for this thesis. Be it the absence of hydrogen bonding within the protein but also in the CG water model (4 water molecules to 1 water "bead"). Key hydrophobic interactions and hydrogen bonding are noted in water flow and interactions with proteins and its behaviour with itself and hydrophobic surfaces, thus this is not a suitable model. Possibly with the polarisable CG water model [265] these interactions could be compared.

### 2.4.1 Multiscale Simulations

As described, CG MD is a system in which there a low amount of detail (compared to AT). A CG system can be converted to that of an AT one by mapping the configurations of the AT molecule *e.g.* a lipid to each corresponding CG, choosing the closest fit [266]. Recently, this can be effectively automated into the "CG2AT" method which involves the fragment based fitting approach, of lipid but also protein leading to a fast conversion process [267] using PULCHRA [268] to fit the AT (protein crystal structure) to that of the CG bead. An example of the conversion is shown in figure

2.5.

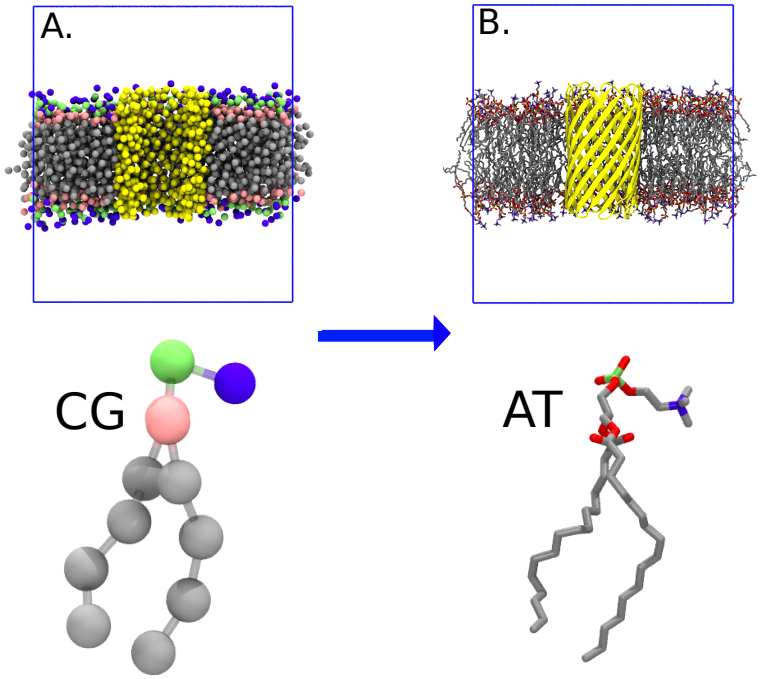


**Fig. 2.5:** Conversion of CG to an AT system. A. Equilibrated system in the CG format, below is shown a DPPC lipid in the CG form. B. Conversion allows representation of CG system in an AT resolution for further investigation. Protein is shown in yellow, bilayer hydrocarbon tails in grey, phosphate group in purple, choline group in green and glycerol linkage in pink of a DPPC lipid. Atomistic colours are consistent with oxygen in red.

## 2.5 Non Equilibrium Methods

A limitation of Classical Molecular Dynamics is the timescale in which simulations relate to biological events. Within general MD, simulation is in the equilibrium states, however for *e.g.* a conformational change or permeation event to occur (where for OmpF permeation is $10^8$ ions per second [219], thus 1 translocation event every 10 ns), long simulations are needed which (based on the assumption that is the system is sampled for long enough, all states will be sampled) in turn require longer amounts of time to simulate the "rare" events. To overcome this, non-equilibrium methods are

used to simulate these events.

### Steered Molecular Dynamics (SMD)

In steered MD (SMD) an external force is applied, driving a system to non equilibrium [269] with the addition of a virtual harmonic spring to two groups of the system (be it the center of mass (c.o.m) of an atom or an entire protein region). A force is applied to the spring, overcoming energy barriers thus driving them towards ion permeation events or apart i.e. protein dissociation events. The force needed is:

$$F = -k(x - vt) \tag{2.12}$$

where $k$ is the spring constant, $x$ is the coordinate of the pulling group, and $v$ is the velocity.

### Potential of Mean Force (PMF)

Potential of Mean Force (PMF) is an enhanced sampling method which can determine a change in system energy via a reaction coordinate. It based on the the following, with a PMF being defined as:

$$W(R) = -kTlnP(R) \tag{2.13}$$

To overcome incomplete sampling, a method used to calculated the PMF is umbrella sampling where the potential function is modified to sample unfavourable states. The system is simulated with a biasing window potential, *U(R'R)* which is used to confine the coordinates of R to a small interval window [270], *e.g.* a small variation of the z coordinate in this thesis to allow sufficient sampling. The modification of the

potential function;

$$W^{biased}(R') = -kTlnP^{biased}(R) + U(R, R') + C \tag{2.14}$$

where U(R,R') is the umbrella potential component of a harmonic function;

$$U(R') = \frac{1}{2}k(R - R)^2 \tag{2.15}$$

For a full profile, many simulations are needed, each with a differently sampled $R$ region, with the unbiased windows being combined into a PMF profile [270]. Each window is determined by change of the free energy constant ($C$) by the weighted histogram analysis method (WHAM) [271]. This algorithm effectively "guesses" the free energy constant to estimate a probability. This is then repeated until the guessed constant matches the actual value giving a correct energy profile. Bootstrapping is used to gain a statistical error on the calculated value. Considered in this method is the coordinate $R$, in which sufficient overlap of windows is needed for an accurate energy estimate and also the length of simulation. Other free energy methods are available, including free energy perturbation [272], thermodynamic integration [273], SMD [274], umbrella sampling [275], metadynamics [276], adaptive biasing force [277] & markov state modelling [278]. In this thesis, as mentioned, umbrella sampling is used.

## 2.6 Modelling Protein Pores

Beta-barrel protein pores were built on the idealised $\alpha$ carbon positions of theorised pores [279]. The carbon coordinates were feed into MODELLER [280] to build 50-100 models with the correct anti-parallel beta strands (calculated via hand drawn models) and small loops. Modeller converts the template structure (C$\alpha$ template)

and the sequence of the desired pore to give a set of spatial restraints for the protein. The backbone and loop structures are minimised via conjugate gradient methods. Following this, side chain atoms are added and optimised. The resulting structures are scored, with lowest chosen as the model pore.

## 2.7 Software & Analysis

All the simulations performed in this thesis were done so using the GROMACS biomolecular simulation package [246]. Analysis was conducted either using gromacs or locally written code. Visulisastion and graphics were performed with VMD [281] or PyMOL [282]. Radius profiles were calculated with HOLE [283] and MDAnalysis [284, 285]. Graphs were plotted using matplotlib [286]. Free energy calculations were done so via WHAM method [271].

# Chapter 3

# Designing and Simulating Nanopores

This chapter is based on the first half of the following publication; Designing a Hydrophobic Barrier within Biomimetic Nanopores. Trick et al, (2014) ACS Nano. 8 11268-79.

*"I don't know about you, But I'm feeling 22"*

Taylor Swift

## 3.1 Introduction

As mentioned previously in chapter 1, nanopores in membranes have a wide range of potential applications, and can be derived from *e.g.* existing biological nanopores, formed by stacks of synthetic cyclic peptides, or non-biological synthetic pores [137–139].

In designing nanopores, one approach is to mimic key features of biological pores (*e.g.* those of ion channels and bacterial porins) of known structure and function

such as bacterial porins, which provide a wide range of conductances and selectivities to inorganic ions, and also to small polar and/or charged solutes such as sugars and antibiotics. Porins, and related outer membrane proteins from Gram negative bacteria have the potential to provide design motifs for biomimetic nanopores, and to act as templates for generation of functional pores, as mentioned previously in the porin OprP and OmpG.

Molecular dynamics (MD) simulations (methods, chapter 2) play a key role in allowing us to understand the physical basis of nanopore function, both for biological pores such as general porins, OpdK and OmpF, $\alpha$-HL and for models based on CNT's or theoretical model pores, where simulations are used to explore more general models of pore selectivity and gating. An example being that of the selectivity in OprP, where simulation identified the key phosphate binding sites and residues [207, 209, 210] therefore allowing biomimicry of such features into a nanopore model pore [213].

In order to design a biomimetic pore, one may wish to transplant a key structural and functional feature from a more complex ion channel into a simple $\beta$-barrel template such as a hydrophobic gate, which has not been found in a $\beta$-barrel nanopore (OmpW is a hydrophobic $\beta$-barrel, however this is very narrow and binds detergent molecules [287]). Therefore, one may wish to test whether a hydrophobic barrier formed by consecutive rings of hydrophobic sidechains in the pore lining (as seen in the nicotinic acetylcholine receptor and related channels) can be designed into a "bland" (no selectivity or gated) high conductance $\beta$-barrel in order to control the conductance of the resultant nanopore.

In this results chapter, I designed $\beta$-barrel nanopores that contain a hydrophobic barrier. I use MD simulations to explore the function of such nanopores, initially using water flux as a proxy for ionic conductance. I explore the behaviour of these pores as a function of the size (in terms of number of strands) and hydrophobicity of the amino

acid sidechains forming the designed hydrophobic barrier. These studies provide a detailed example of the use of MD simulation to design and evaluate simple model nanopores based on a $\beta$-barrel template, with a prospect of their further development for biotechnological applications.

## 3.2 Methods

### 3.2.1 Building Protein Models

Atomic coordinates for the initial models were generated using idealized models for transmembrane $\beta$ barrels [279], allowing for the mapping of the C$\alpha$ positions of a desired barrel template as a function of number of strands, shear, and length of the barrel. The resultant C$\alpha$ templates were used as inputs for MODELLER [280] in conjunction with designed sequences in FASTA format (figure 3.1). Pore radius profiles of the resultant models were calculated using HOLE [283].

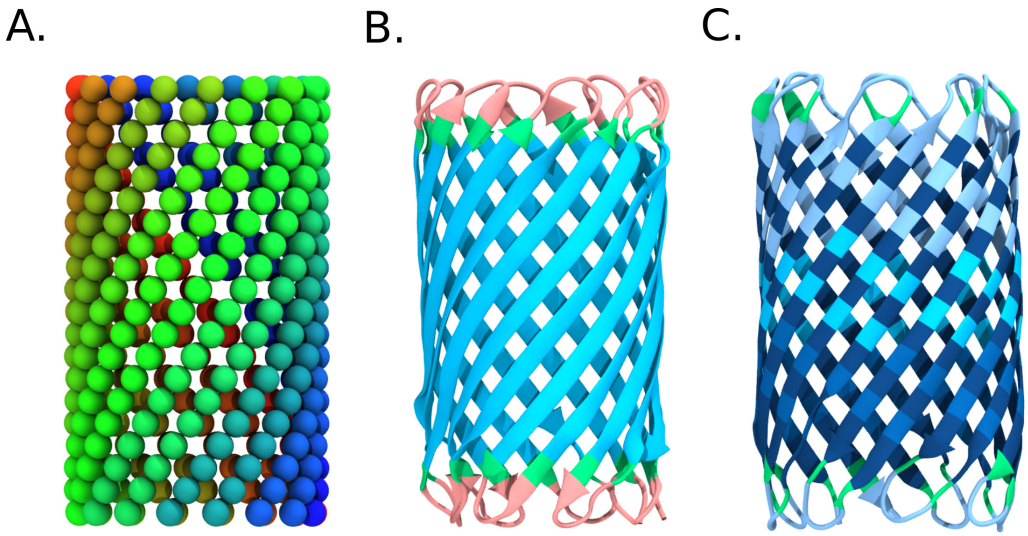


**Fig. 3.1:** Building a protein pore from the C$\alpha$ backbone (16$\beta$ example). A. C$\alpha$ backbone model output (from [279]). B. Initial modeller design with basic protein backbone (blue and green strands) to implement the correct strand hydrogen bonding and loop (pink) length. C. Final protein build for this model of 16$\beta$ funnel hydrophobic pore. Ranging blue colours indicated modelled lumen pointing residue positions.

### 3.2.2 Simulation Protocol

Atomistic models of designed pores were converted to a coarse grained (CG) representation using a locally modified version of the widely used MARTINI forcefield [264]. CG MD simulations of duration 1 $\mu$s were used to position the nanopores within a DPPC phospholipid bilayer (figure 3.2). At the end of the simulation, the orientated pore-bilayer system was converted back to an atomistic representation using a CG2AT protocol [267].

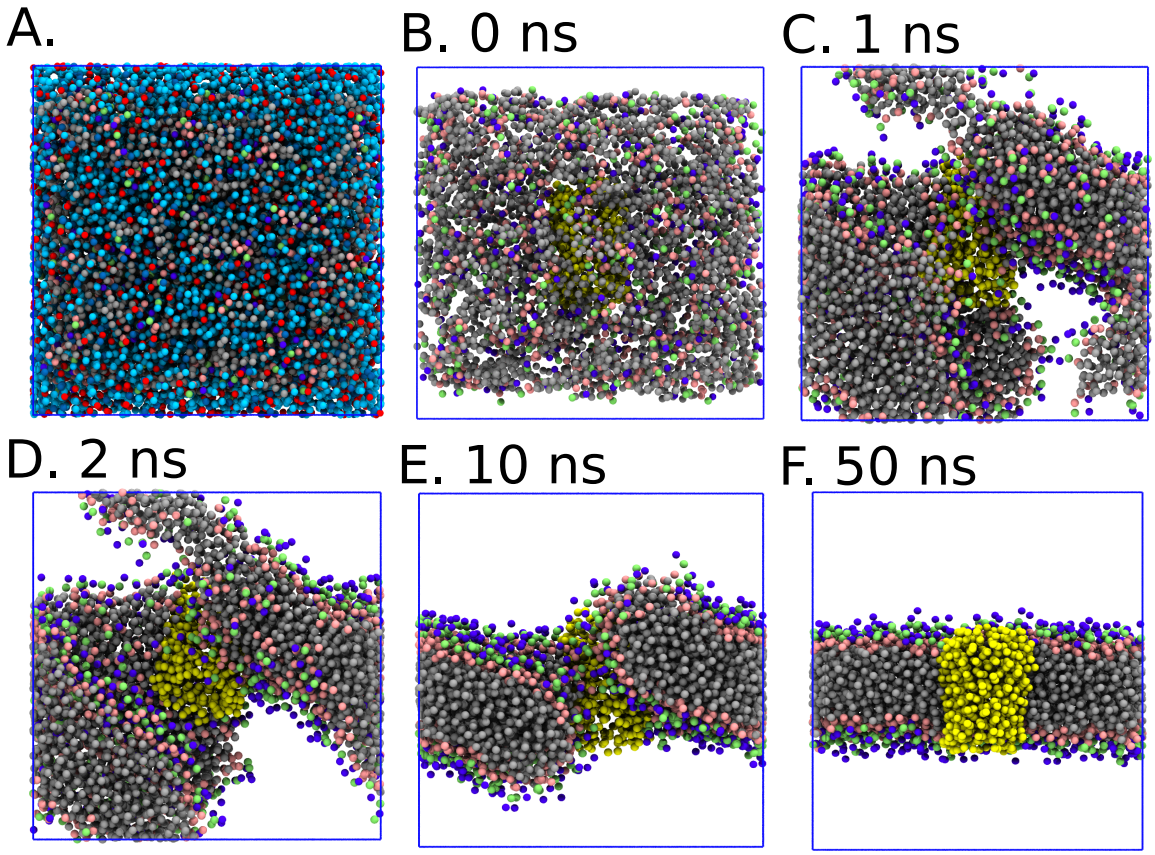


**Fig. 3.2:** Coarse grained self assembly of protein pore in DPPC lipid. A. All CG particles in the system are shown including lipid and head groups (grey tails, pink/green/blue head groups), sodium (red) chloride (dark blue) ions, water (cyan) and protein (yellow). B. As A, however for clarity, only protein and lipid are shown using previous colours at the starting configuration. C. to F. Progress through simulation with time noted above.

Atomistic simulations were performed using GROMACS version 4.5.5 [288] (www.gromacs.org) and using the GROMOS96 43a1 forcefield [246, 247]. Long range electrostatic interactions were treated with the Particle Mesh Ewald method with a short range cut off of 1 nm, a Fourier spacing of 0.12 nm [240, 241], and the SPC water model was used [258]. Simulations were performed in the NPT ensemble with the temperature being maintained at 310 K with a V-rescale thermostat [256] and a coupling constant of $\tau_t = 0.1$ ps. Pressure was maintained semi-isotropically using the Parrinello-Rahman [255] algorithm at 1 bar coupled at $\tau_p = 1$ ps. The time step for

integration was 2 fs with bonds constrained using the LINCS algorithm [253]. Analysis was conducted with GROMACS routines, MD Analysis [284], and locally written code. I performed an initial equilibration of each system containing ~330 DPPC lipids and ~50,000 water molecules for 1 ns during which the protein was restrained. Water flux was calculated by counting water molecules crossing through the centred protein (on x and y) within a 20 Å diameter shell from this centre. Water crossings were counted as upwards (positive) if parallel to z and downwards (negative) if anti-parallel (figure 3.3). Water fluxes were evaluated over the full length of the simulations and shown as the sum of the flux. In most cases this did not lead to a major change in estimated flux compared to evaluating the flux, *e.g.* the latter half of the simulation. Pore radii with error estimate for a simulation was calculated using MDAnalysis. Molecular graphic images were produced with visual molecular dynamics (VMD) [281].

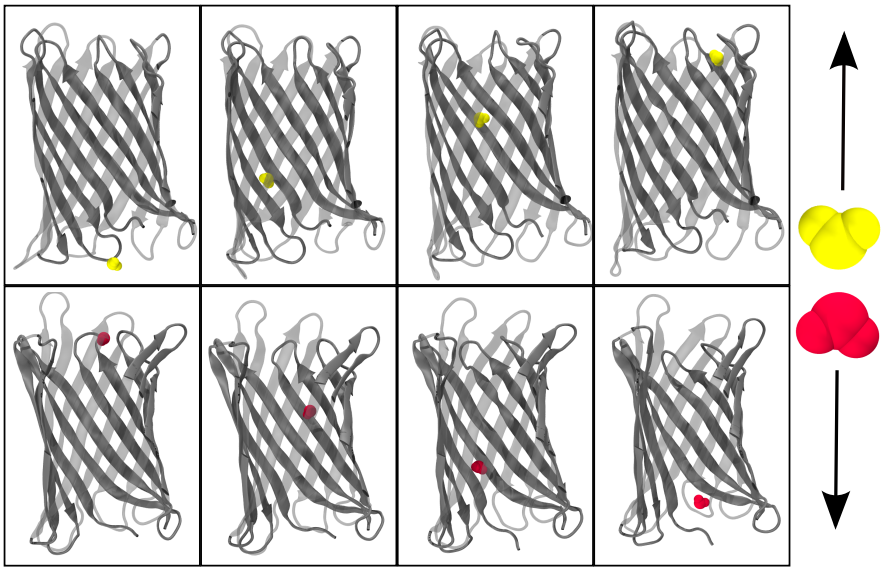

**Fig. 3.3:** Example of water flux calculation through a nanopore. Diagram to represent the calculation of water flux through a nanopore. When 'yellow water' passes through the pore center of mass (not shown) in an upward, parallel (yellow water) or downward, anti parallel manner (red water) it will be considered a conductive event in simulation.

## 3.3 Results and Discussion

### 3.3.1 Biomimicry and Barrel Design

#### 3.3.1.1 Modelling $\beta$-Barrel Nanopores

Based on detailed visual inspection of the known structures of bacterial $\beta$-barrel membrane proteins, I set out to design biomimetic model nanopores with 12, 14 or 16 strands per $\beta$-barrel. Such pores are seen within naturally occurring $\beta$-barrel proteins, for example the porin NanC (pdb: 2WJQ [289]) of 12$\beta$ strands, and the lytic toxins $\alpha$-HL (pdb: 7AHL [110]), and $\gamma$-hemolysin (pdb: 3B07 [290]) of 14 and 16 $\beta$-strands respectively.

To generate and evaluate these models I used the following workflow. The initial C$\alpha$ template was generated based on the idealized geometry of a transmembrane $\beta$-barrel pore (figure 3.1). The strand lengths (of 20 residues per strand) were used to generate nanopores of ~40-42 Å in length, sufficient to span a lipid bilayer. These templates were converted to protein models and then embedded in a phospholipid bilayer for evaluation in terms of stability and permeation properties by use of atomistic MD simulations.

To generate minimalist biomimetic $\beta$-barrel nanopores which would sit stably within a lipid bilayer, the outer surface of the barrel was covered with hydrophobic leucine sidechains (figure 3.4) which interact with the hydrophobic core of DPPC. The $\beta$-strands were connected via short flexible loops of glycine residues (2 to 3 residues) with a band of tryptophan residues included on the outer surface at each end of the barrel. These amphipathic aromatic sidechains are known to 'lock' membrane proteins into place in a lipid bilayer by forming hydrogen bonds to lipid headgroups [291, 292]. Together these features were designed to form a stable, bilayer spanning nanopore and allowing the nature of the inwards, lumen facing pore-lining sidechains to be designed

in order to control water and ion permeation events.

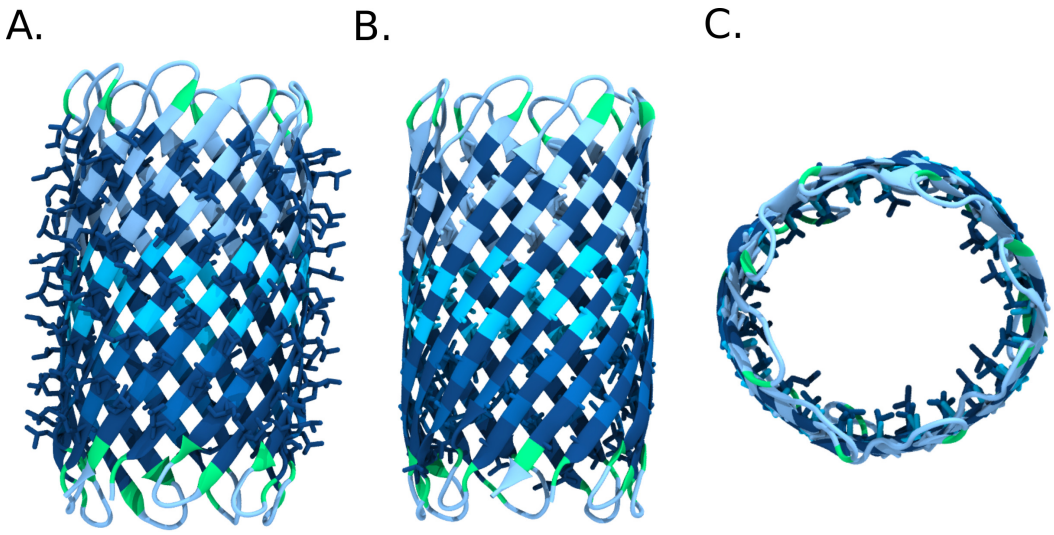


**Fig. 3.4:** Residue Positions on a 16$\beta$ pore. Shown is that of the funnel-hydrophoboic pore. A. All external, lipid-facing leucine residues (dark blue) shown in stick form. B. Internal lumen water-facing residues shown through backbone cartoon (shades of blue). C. Image of B rotated 90° looking through the conductive pore axis with inward pointing residues in stick form. Functional residues are always built to be lumen facing.

In order to evaluate these models, atomistic MD simulations (of duration from 40 to 100 ns, see table 3.1 for a full list of simulations in this chapter) were performed for each nanopore embedded in a DPPC bilayer with a NaCl solution of 1M. Models were assessed in terms of conformational stability of the protein, dimensions of the transbilayer pore, and the flow of water and ions through the pore. Due to timescales of simulation, water conduction will be used as a proxy for ion conduction for this series of simulations.

### Design Principles

In our initial exploration of possible designs, I explored both funnel (F) and hourglass (HG) shaped pores (Figure 3.5). The latter have a central constriction which mimics

porins, as many have a central constriction [293–295]. The overall size of the nanopores was determined by the number of $\beta$-strands (N) in the barrel (where N=12, 14, or 16 $\beta$ strands) whilst the shape (F or HG) was determined by the sizes and positions of the residues lining the pore. The nature of the pore-lining sidechains was varied to yield either a hydrophobic (lined by glycine, alanine, valine or leucine residues) or hydrophilic (lined by serine, threonine, asparagine and glutamine residues) model pore (figure 3.6). Thus each pore design may be described by the number of $\beta$-strands in the barrel template, the overall shape of the pore, and by specification of the rings of sidechains lining the pore. An example of a pore, as a 2D sheet representation is shown (figure 3.7).

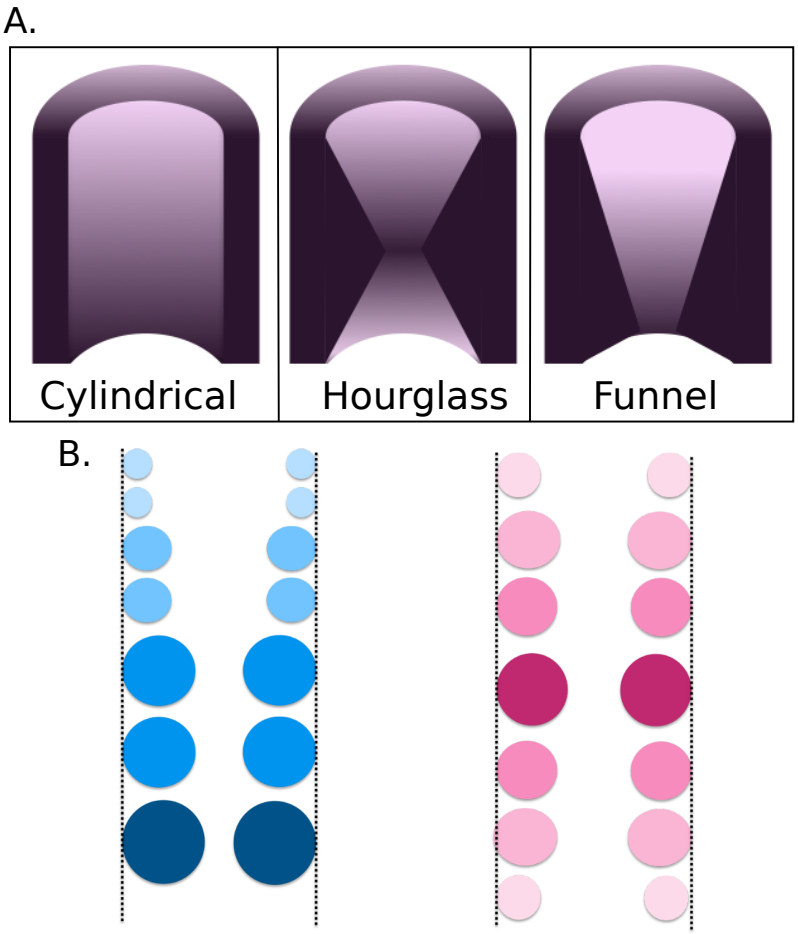


**Fig. 3.5:** Theoretical pore concept shape and residue design. A. Concept of nanopore lumen shapes to be implemented into designed pore. B. Implementation of dimensions can acquired by using different residue R groups (shown here in beads according to proposed R group volume).

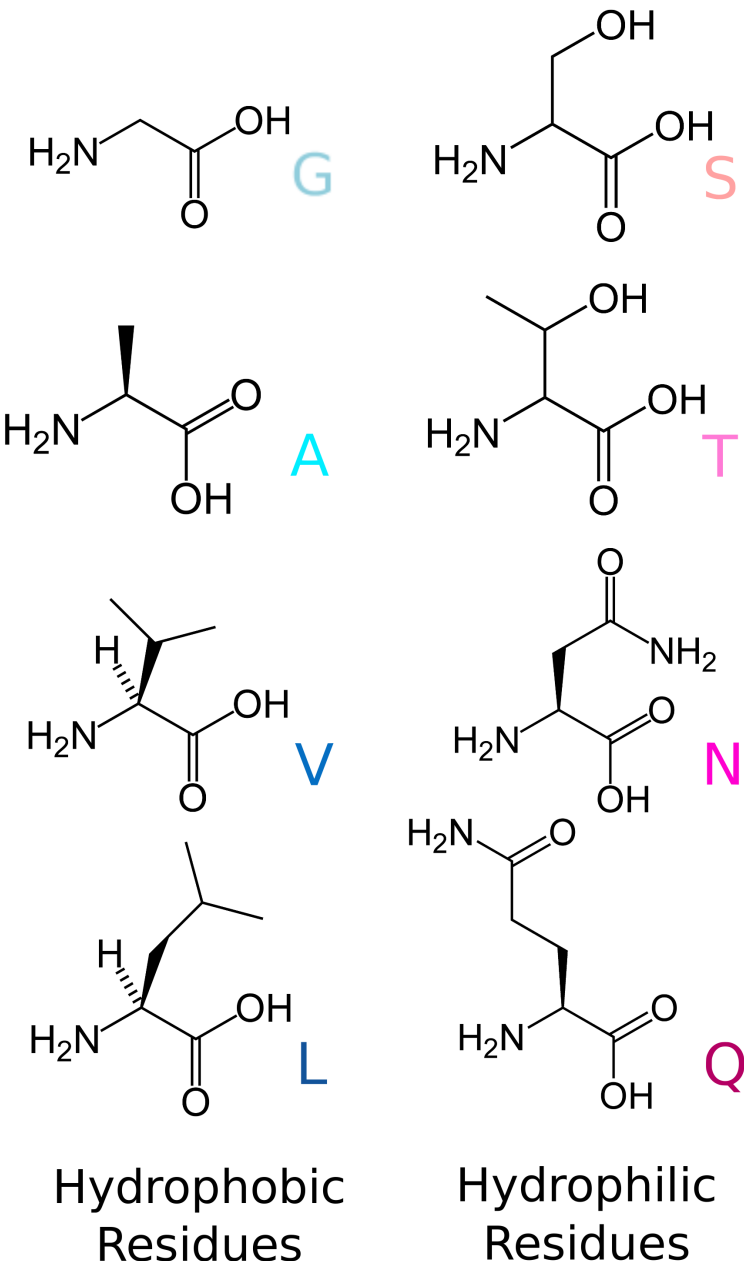


**Fig. 3.6:** Polar and non-polar amino acids. Amino acids which will be used impose shape and functionality within model nanopores. Grouped on polarity and size of increasing R group, with the largest at the bottom. Residue names are coloured by polarity which will be used throughout this thesis (pink - hydrophilic, blue - hydrophobic).

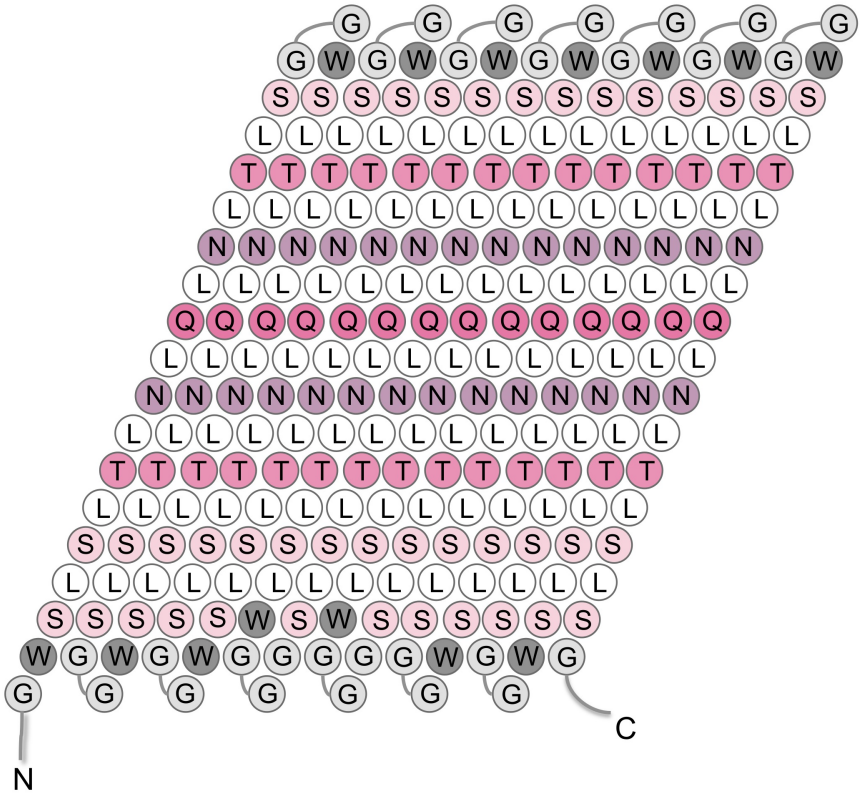


**Fig. 3.7:** Theoretical $\beta$ strand concept and residue placement. A 2D sheet of a model protein pore, where each residue is shown as a circle with residue as a one letter code. Due to the hydrogen bonding pattern (shear), residues will be staggered in the folded form. Minor adjustments made after modelling ensures no pore occlusion by excess tryptophan residues or glycine loops. Hydrophilic residues coloured to polarity. N and C termini are indicated.

The overall conformational stability of these pore models was evaluated by measurement of the root mean square deviation (RMSD) of both the protein and C$\alpha$ carbons from the initial pore model over the course of the atomistic MD simulation. An example, the *N=12*, funnel (F), STNQNTS model shows that the overall C$\alpha$ RMSD plateaus at ca. 4 Å (figure 3.9), just a little higher than would be the case for comparable simulations of native porin structures [33, 296]. The conformational fluctuations are higher for the inter-strand loops, again as expected (figure 3.9, E.). Thus, the *de novo* designed nanopores behave in a similar manner to porins in MD simulations in a

bilayer on a ~100 ns timescale. Calculation of the pore radius profile at selected time points during the simulation suggests that the initial model structure of the pore does indeed "relax" to adopt a more clearly, hourglass or funnel profile shape as expected from the initial model structure. Comparable changes in pore radius profiles have also been seen in simulations of porins [297, 298] and confirm the importance of relaxing initial pore models by MD simulation before evaluating them in terms of pore radius and permeability properties.

Having established an overall methodology, I use this to explore three generations of nanopore design. The 1$^{st}$ generation, as described in the next section provides an overall exploration of pore size, shape, and hydrophobicity of the pore lining residues. The 2$^{nd}$ generation models explored further refinements of the stable *N=14*, HG 1$^{st}$ generation models. Both *N=14*, HG STNQNTS and *N=14*, HG GAVLVAG were used as 'host' pores for a central ring of "guest" residues, yielding "hydrophilic-x" and "hydrophobic-x" models respectively. This involved the replacement of the central, constricting residues of either the hydrophobic or hydrophilic pore with the opposite polarity residue, such as the hydrophobic leucine was introduced into the central ring of the hydrophilic STNQNTS pore or a hydrophilic glutamine residue, was introduced into the central ring of the otherwise hydrophobic GAVLVAG pore. In the 3$^{rd}$ generation of models, *N=14*, HG models were explored further, combining an overall hydrophilic pore lining with 1, 2 or 3 rings of L sidechains to yield a central hydrophobic constriction of increasing thickness.

**Table 3.1:** Table of nanopore simulations in chapter 3.

| *N* | Shape | Pore lining rings | Time (ns) | Cα RMSD (Å) | Minimum radius (Å) | Mean water flux ($ns^{-1}$) | Generation |
|---|---|---|---|---|---|---|---|
| 12 | F | GGAAVVL | 100 | 4.6 | 1.0 | 0.1 | 1st |
| | | SSTTNNQ | 100 | 3.6 | 3.2 | 13 | 1st |
| | | | | | | | |
| 12 | HG | GAVLVAG | 100 | 4.5 | 1.0 | 0.1 | 1st |
| | | GAVQVAG | 2 x 40 | 5.1 | 1.6 | 3.0 | 2nd |
| | | STNQNTS | 100 | 5.0 | 3.3 | 13 | 1st |
| | | STNFNTS | 40 | 3.8 | 2.9 | 12 | 2nd |
| | | STNLNTS | 40 | 5.5 | 3.9 | 18 | 2nd |
| | | | | | | | |
| 14 | F | GGAAVVL | 2 x 100 | 3.7 | 4.9 | 0.2 | 1st |
| | | SSTTNNQ | 100 | 3.5 | 4.5 | 29 | 1st |
| | | | | | | | |
| 14 | HG | GAVLVAG | 3 x 100 | 4.1 | 4.5 | 0.4 | 1st |
| | | GAVQVAG | 3 x 40 | 3.8 | 4.4 | 35 | 2nd |
| | | STNQNTS | 2 x 100 | 3.7 | 4.5 | 32 | 1st |
| | | STNFNTS | 40 | 4.3 | 4.0 | 26 | 2nd |
| | | STNINTS | 40 | 3.2 | 5.1 | 34 | 2nd |
| | | STNLNTS | 100 | 4.2 | 5.2 | 37 | 2nd |
| | | STNWNTS | 40 | 3.4 | 3.2 | 23 | 2nd |
| | | STNYNTS | 40 | 3.8 | 2.6 | 12 | 2nd |
| | | TNLLLNT | 100 | 3.8 | 5.5 | 0.5 | 3rd |
| | | TNNLLNT | 100 | 5.1 | 5.1 | 34 | 3rd |
| | | STNIINT | 100 | 4.3 | 5.4 | 45 | 3rd |
| | | STLLLTS | 2 x 100; & 40 | 4.7 | 5.4 | 0.3 | 3rd |
| | | STNLLTS | 3 x 100; & 40 | 4.8 | 5.1 | 26 | 3rd |
| | | STNLLNT | 3 x 100 | 4.1 | 5.2 | 23 | 3rd |
| | | | | | | | |
| 16 | F | GGAAVVL | 100 | 4.7 | 6.3 | 80 | 1st |
| | | SSTTNNQ | 100 | 3.9 | 4.8 | 50 | 1st |
| | | | | | | | |
| 16 | HG | GAVLVAG | 100 | 4.1 | 4.6 | 55 | 1st |
| | | STNQNTS | 2 x 100 | 4.2 | 6.2 | 64 | 1st |
| | | STNFNTS | 40 | 4.4 | 6.3 | 63 | 2nd |
| | | STNLNTS | 40 | 3.8 | 7.1 | 61 | 2nd |
| | | STNWNTS | 40 | 3.4 | 5.2 | 48 | 2nd |
| | | STNYNTS | 40 | 3.6 | 5.8 | 51 | 2nd |

*Residues are coloured as depicted before with hydrophobic residues in blue, and hydrophilic in pink. W and Y residues are in purple.

### 3.3.2 First Generation Pores

Focus will be placed on the pores based on their size, of 12, 14 or 16 $\beta$ strands and secondly, on the polarity of the residues within the lumen of the hydrophobic or hydrophilic pores.

I first examined water flux as a proxy for ionic conductance, *i.e.* as a simple measure of pore 'openness'. This was used due to the time scales for ion conduction events, requiring substantially longer simulation times in order to detect these rare events [61] in conductance through proteins of the 1$^{st}$ generation of pore models. Stability and cumulative water fluxes (either 'upwards' or 'downwards' dependent on whether the direction of flow is measured in a positive or negative z direction) were evaluated for these models over the course of the simulations, with water flux scaling approximately with the cross-sectional area of the central constriction of the pore [299].

#### 3.3.2.1 12 $\beta$ Models: Stability and Conduction

These series of pores were modelled theoretically on the backbone structure of the bacterial OMP NanC (*N = 12, S = 12*) in figure 3.8 (A). For this pore, 4 models are built;

i 12$\beta$ Funnel (F) Hydrophobic

ii 12$\beta$ Hourglass (HG) Hydrophobic

iii 12$\beta$ F Hydrophilic

iv 12$\beta$ HG Hydrophilic

To assess the stability of the pore in the bilayer during a 100 ns AT MD simulation, RMSD, hydrogen bonding between the main chain of the protein pore, root mean square fluctuations (RMSF), and radii profiles are analysed from the simulation. To

assess the (as previously mentioned) 'openness' of the pore, water flux profiles are calculated for water movement through the pore (see figures 3.9 and 3.10).

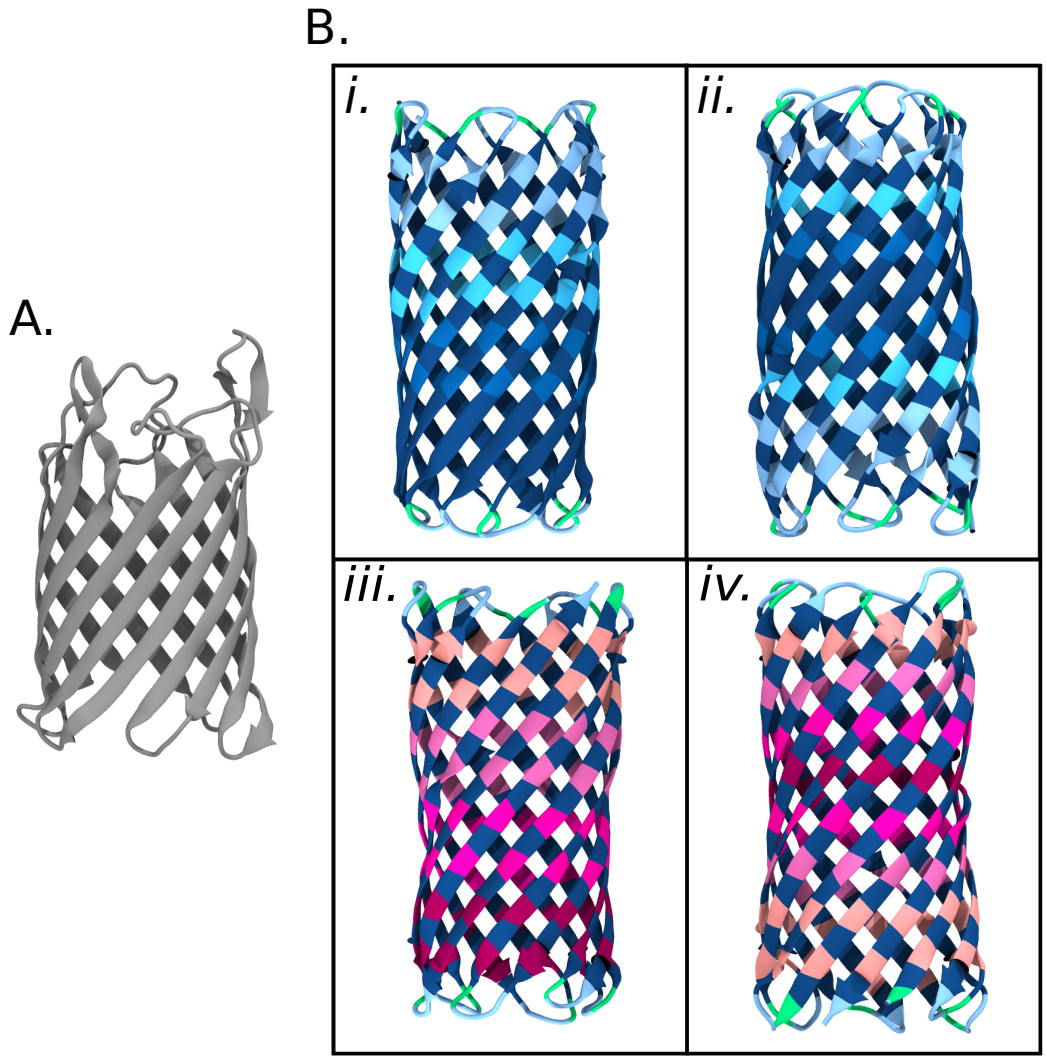


**Fig. 3.8:** NanC porin and 1st generation N=12, 12$\beta$ pores. A. Silver cartoon of the bacterial porin shown, perpendicular to the membrane plane, with a $\beta$ strand height of ~25 Å and including loops ~52 Å . B. Funnel and hourglass hydrophobic pores with the same numbers as in the text. Residue colouring is consistent to polarity of residues shown before. Model pore strand length is ~38 Å, and when including loops is ~45 Å.

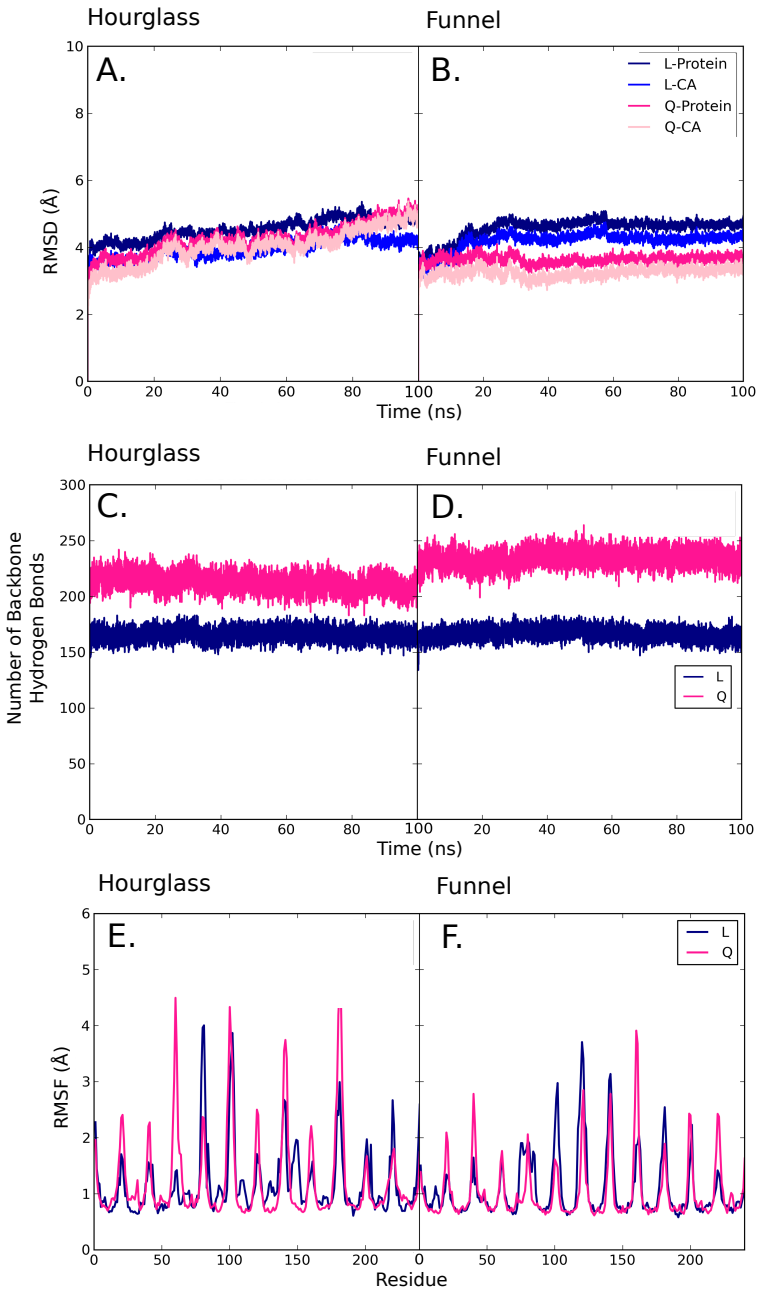


**Fig. 3.9:** RMSD, backbone hydrogen count and RMSF for *N=12*, 12$\beta$ model pores. A and B. RMSD for both HG and F pores (pink (Q) - hydrophilic, blue (L) - hydrophobic pore) for C$\alpha$ and protein. C and D. Backbone hydrogen bond count with consistent colours as A. and B. E and F. RMSF.

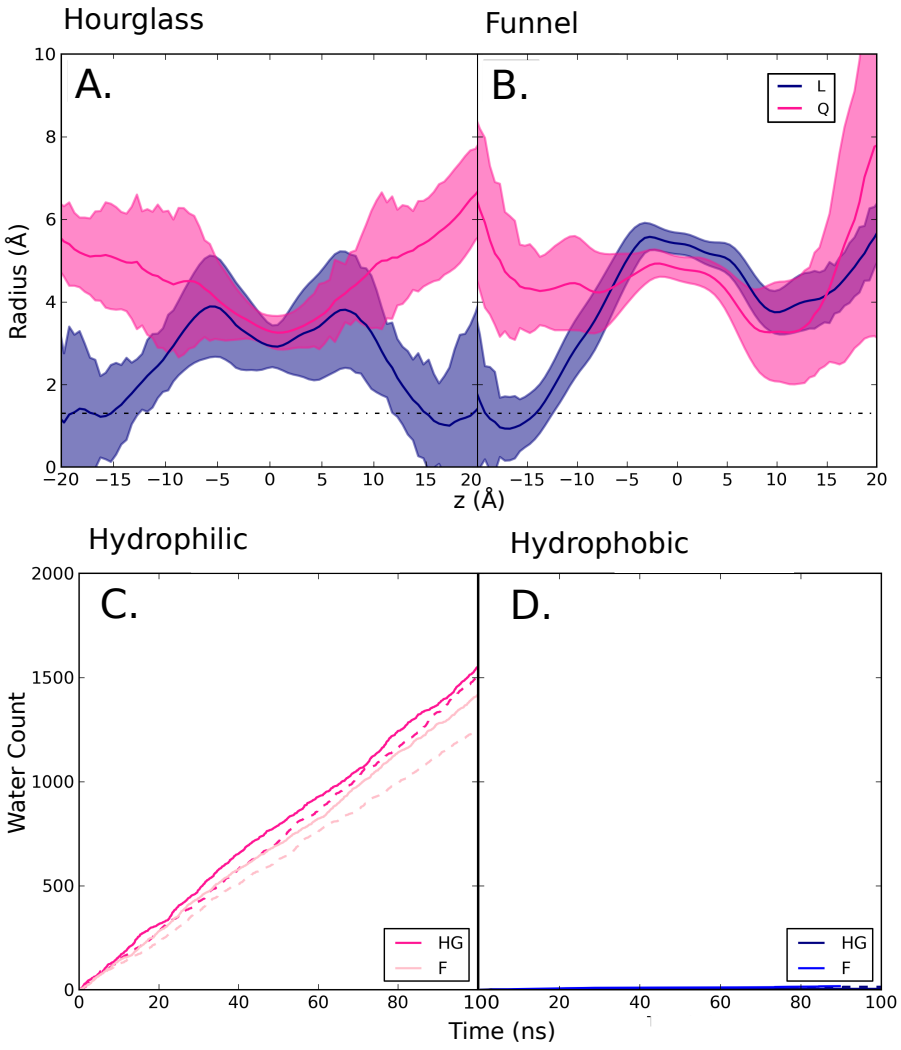


**Fig. 3.10:** Radii profile and water flux measurement of *N=12*, 12$\beta$ pores. A and B. Radii profile of all 4 pores, with the x axis representing the z axis going through the lumen of the pore and radius on y. Dotted line on plot at ~1.9 Å indicates the radius of a water molecule which will be considered as the radius of a pore being open or closed. C and D. Water flux profiles of water conduction through the pores. Solid line indicates an upward flux, and dashed, downward.

From the previous assessments of the *N=12* models, it can be noted that *de novo* protein design, in the manner presented in this thesis, is a feasible method to build and simulate nanopores. In terms of stability, all four of the pores of this size and chemical character are stable in terms of the plateau, and also rational RMSD profile with a maxima at ~4 - 5 Å (a exception from figure 3.9 A., is the hydrophilic hourglass

pore which required a longer simulation time to maintain stability). The hydrogen bond contacts within 3.5 Å of the barrel backbone (which are considered to assess the stability of the pore, if the protein is unstable and "fall apart" one would expect a decrease in the number of hydrogen bonds over time) are at a constant level throughout the simulation suggesting protein backbone stability for this non-physiological pore. Throughout all simulations, hydrophilic pores exhibit on average a higher number of hydrogen bond contacts than their hydrophobic counterparts (which could be due to the excessive presence hydrophobicity of residues, exhibiting partial intrinsic stability in terms of backbone bonding). All pores show an expected RMSF profile based on simulations of other pore and porin proteins, with high RMSF peaks depicting more mobile loop regions of the protein.

In terms of relating stability to conduction, interestingly in the previous figure (3.10), even though exhibiting details showing a stable pore, the 12$\beta$ hydrophobic HG and F models are both functionally closed in terms of radii (*i.e.* narrower than the radius of a water molecule) and in water flux (figure 3.10 A,B and D). Therefore, analysis of the protein structure (as in figure 3.9) alone is not sufficient to assess the functionality of these pores, with further investigation needed. Both hydrophilic forms of these 12$\beta$ pores exhibit a water flux and are thus considered to be "open" pores in this case.

#### 3.3.2.2 14 $\beta$ Models: Stability and Conduction

The next series of pores are modelled on the transmembrane domain of $\alpha$-Hemolysin ($\alpha$HL) which has *N=14* and *S=14*. As before, four protein models are constructed and modelled;

i 14$\beta$ F Hydrophobic

ii 14$\beta$ HG Hydrophobic

iii $14\beta$ F Hydrophilic

iv $14\beta$ HG Hydrophilic

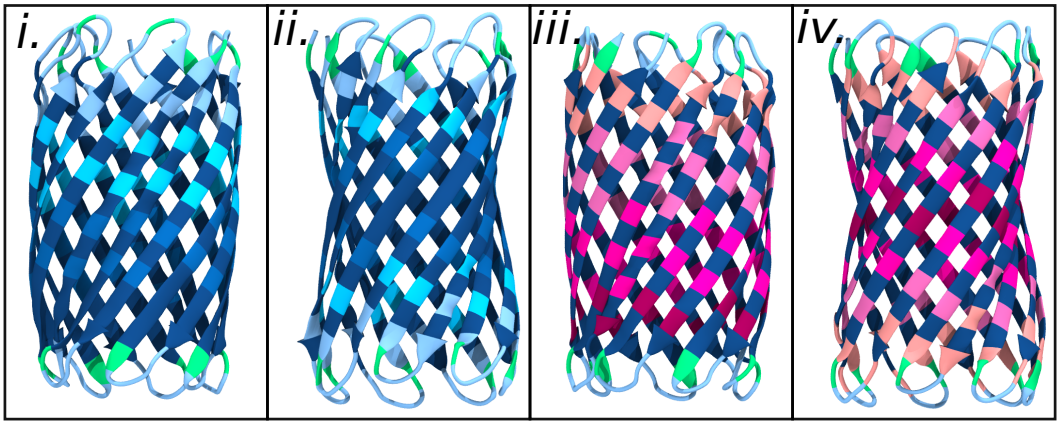


**Fig. 3.11:** First generation *N=14*, $14\beta$ pores. Boxes show the funnel and hourglass hydrophobic pores with same roman numbering as shown in the text previously. Residue colouring is consistent to polarity of residues previously.

Stability and openness of the pore is assessed in the same manner as *N=12* pores, shown in figures 3.12 and 3.13.

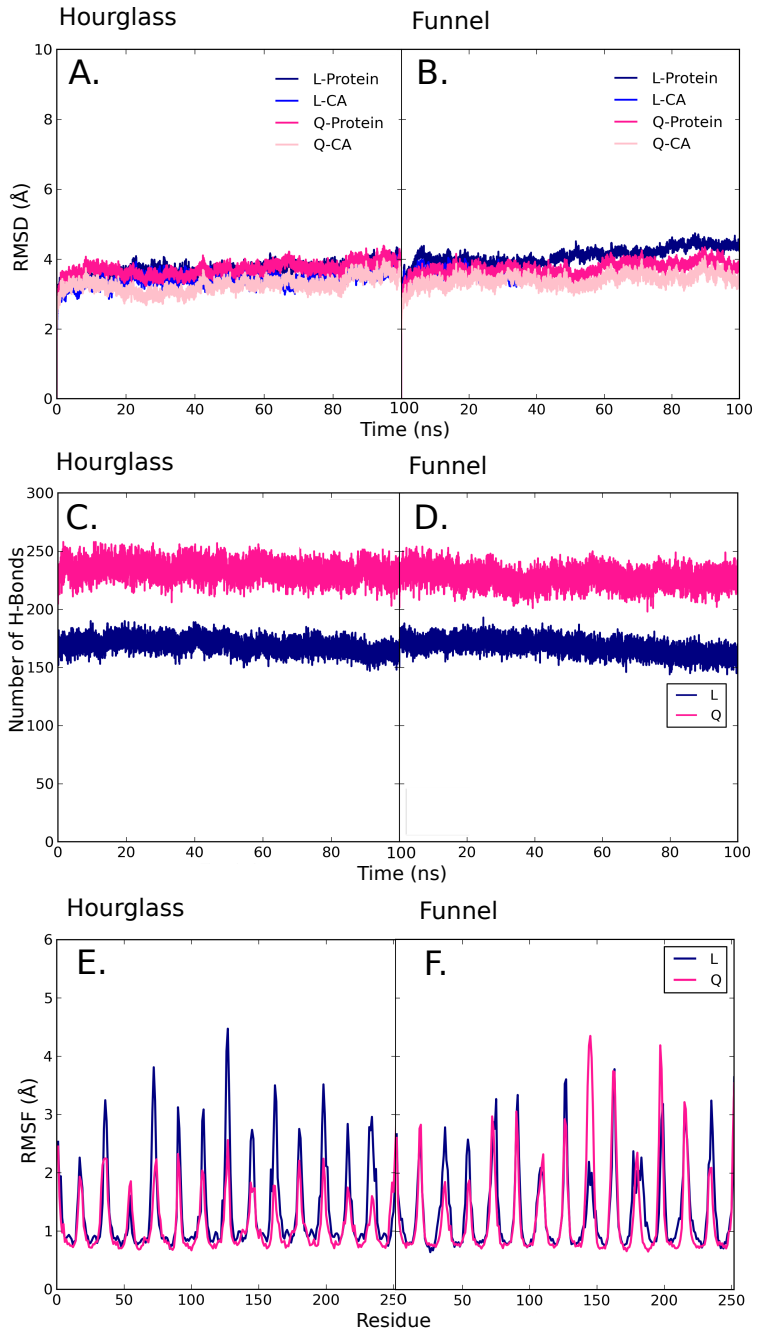


**Fig. 3.12:** RMSD, backbone hydrogen count and RMSF for *N=14*, 14$\beta$ model pores. A and B. RMSD for both HG and F pores (pink (Q) - hydrophilic, blue (L) - hydrophobic pore) for C$\alpha$ and protein. C and D. Backbone hydrogen bond count with consistent colours as A. and B. E and F. RMSF.

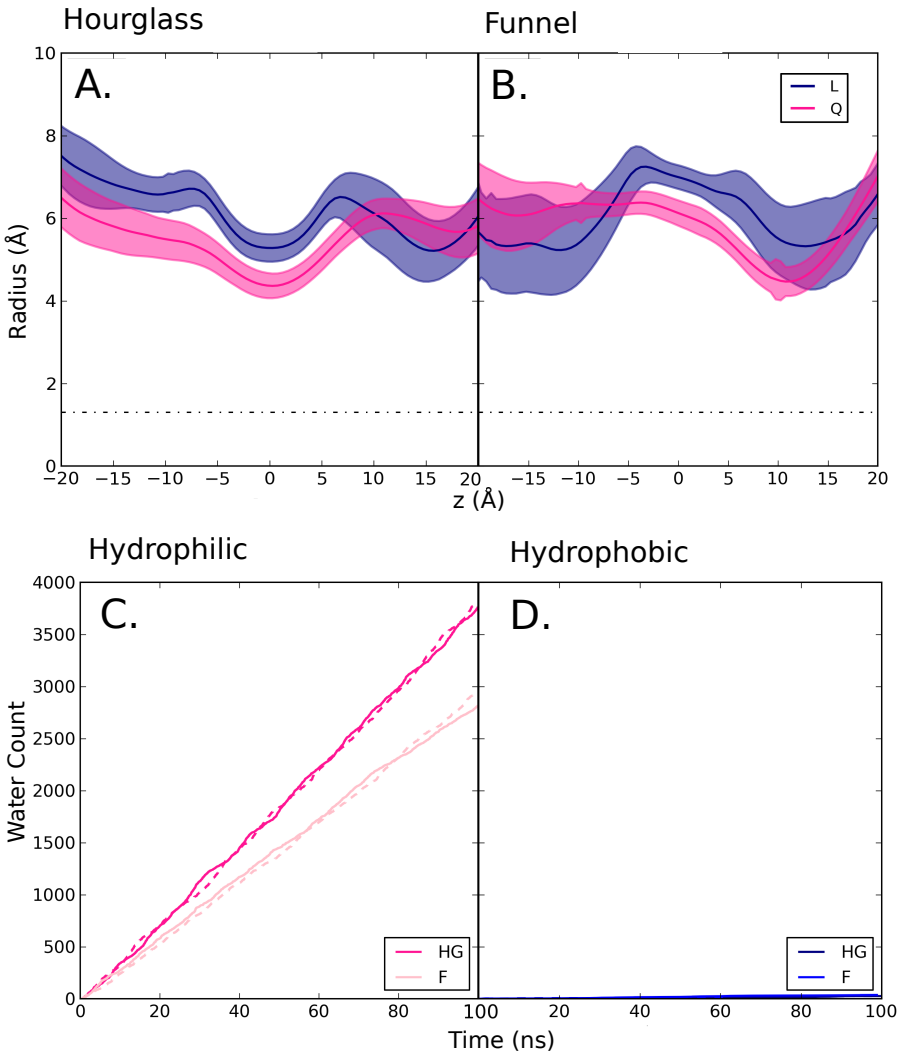


**Fig. 3.13:** Radii profile and water flux measurement of *N=14*, 14$\beta$ pores. A and B. Radii profile of all 4 pores, with the x axis representing the z axis going through the lumen of the pore and radius on y. Dotted line on plot at ~1.9 Å indicates the radius of a water molecule which will be considered as the radius of the pore being open or closed. C and D. Water flux profiles of water conduction through the pores. Solid line indicates an upward flux, and dashed, downward.

Similar structural trends between these model pores and the previous pores can be noted from the profiles in figure 3.12. Again, all four exhibit RMSD stability and plateau during the simulation (except the hydrophobic, funnel pore) between values of 4 - 5 Å. RMSF profiles for all indicate a fluctuations in structure akin to a native porin, and to that of the *N=12* pore. Also noted are a stable number of backbone hydrogen

bonds with a hydrophobic and hydrophilic pore trend seen previously. Precise values are noted in table 3.2.

| Pore | Hydrogen Bond Count |
|---|---|
| Hydrophilic HG | 233 ± 7 |
| Hydrophilic F | 227 ± 7 |
| Hydrophobic HG | 169 ± 6 |
| Hydrophobic F | 168 ± 6 |

**Table 3.2:** Hydrogen bond contacts of *N=14*, 14$\beta$ 1$^{st}$ generation pores

Unlike the previous smaller model pores, this series of model pores and simulations exhibit the initial desired structure, such as the hourglass models maintaining a central constriction and the funnel pores maintaining their end restriction (figure 3.13). All are shown to be functionally open pores in terms of their radii to that of a water molecule (indicated on figure as black line, figure 3.13, A and B) which can also be seen in simulation. To investigate the "functionally open" hydrophobic pores further, even larger pores shall be modelled to gain insight into their stability and water conduction.

#### 3.3.2.3 16 $\beta$ Models: Stability and Conduction

Finally, simulated and modelled as part of the series of the 1$^{st}$ generation pores are those modelled on the octameric protein (and also lytic) $\gamma$-Hemolysin with a *S=16* and *N=16*. Structurally, $\gamma$-HL is identical to that of $\alpha$HL, (barrel and cap domain), however it is formed from 8 monomers rather than 7. Four models are modelled on the TMD and shown (figure 3.14);

i 16$\beta$ Funnel (F) Hydrophobic

ii 16$\beta$ Hourglass (HG) Hydrophobic

iii 16$\beta$ F Hydrophilic

iv $16\beta$ HG Hydrophilic

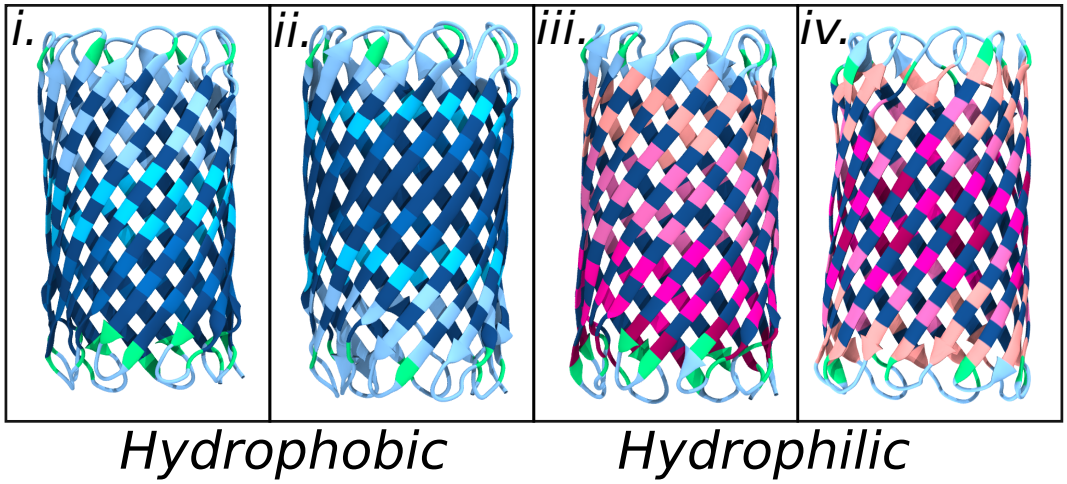


**Fig. 3.14:** First generation *N=16*, $16\beta$ pores. Boxes show the funnel and hourglass hydrophobic pores with same roman numbering as shown in the text previously. Residue colouring is consistent to polarity of residues.

Stability and openness of the pore is assessed in the same manner for *N=12* and *N=14* pores, shown in figures 3.15 and 3.16.

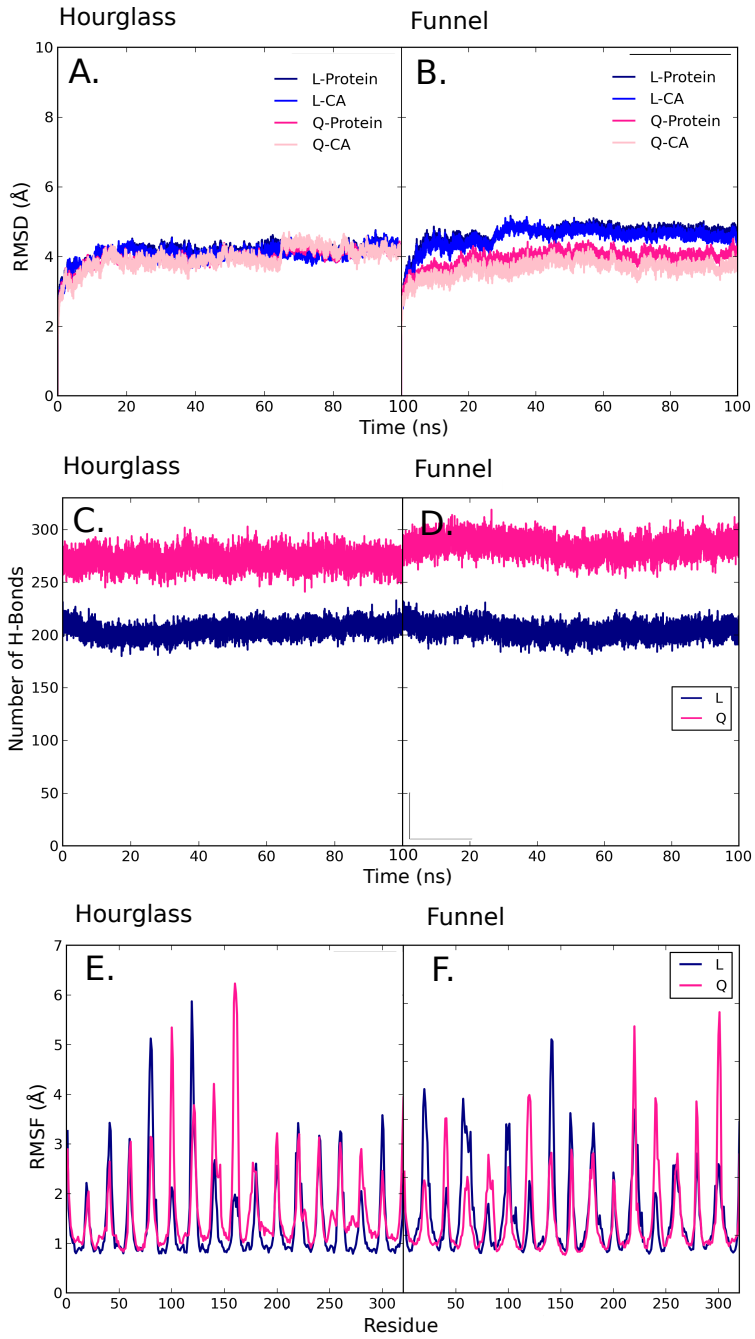


**Fig. 3.15:** RMSD, backbone hydrogen count and RMSF for *N=16*, 16$\beta$ model pores. A and B. RMSD for both HG and F pores (pink (Q) - hydrophilic, blue (L) - hydrophobic pore) for C$\alpha$ and protein. C and D. Backbone hydrogen bond count with consistent colours as A. and B. E and F. RMSF.

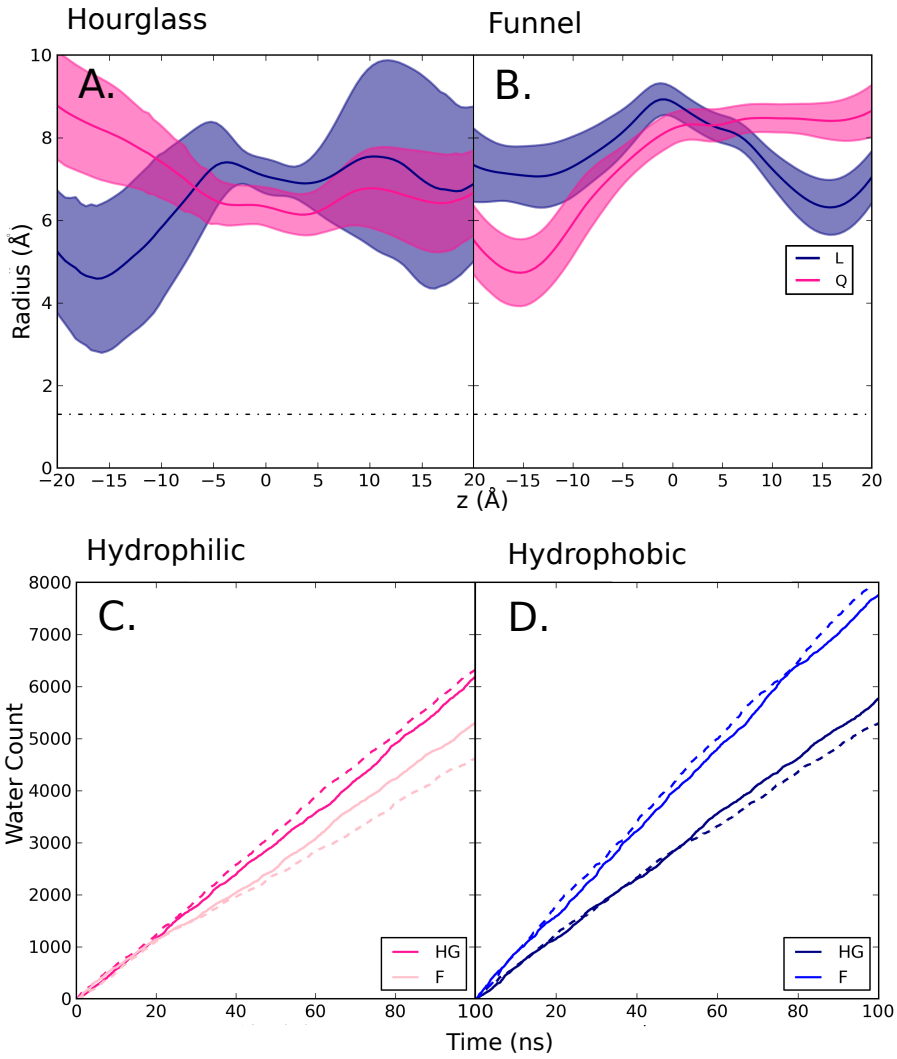


**Fig. 3.16:** Radii profile and water flux measurement of *N=16*, 16$\beta$ pores. A and B. Radii profile of all 4 pores, with the x axis representing the z axis going through the lumen of the pore and radius on y. Dotted line on plot at ~1.9 Å indicates the radius of a water molecule which will be considered as the radius of a pore being open or closed. C and D. Water flux profiles of water conduction through the pores. Solid line indicates an upward flux, and dashed, downward.

Similarly to the previously modelled and simulated pores, the RMSD, RMSF, and hydrogen bond contacts indicate that these larger model protein pores are structurally stable. Following the trend of the smaller *N=12*, to the *N=14* barrel, this *N=16* is the largest pore in terms of number of residue numbers and radius, therefore in comparison to the other pores, it has a higher number of hydrogen bond contacts and follows

the trend of having fewer contacts in the hydrophobic barrels than their hydrophilic counterpart. As with the *N=14* pores, all are functionally open in regards to the radii (and water diameter) but differ in water flux. All *N=16* pores have a considerably higher water flux, unseen in the other models (figure 3.16). Both hydrophilic pore models have maintained their initial desired shape, however there is more deviation within the hourglass models. Therefore this raises a possible question regarding the stability induced by the position of lumen facing residues and also residue polarity, especially those hydrophobic in nature.

Overall, within the simulations of 1$^{st}$ generation models, an interesting characteristic has arisen from this series of simulations. We can see that the *N=14*, HG models form stable pores which conduct water, however they are sufficiently narrow to be functionally sensitive (in terms of water flux) to the nature (hydrophilic vs. hydrophobic) of the pore lining residues (with a flux of 31.9 ns$^{-1}$ and and 0.4 ns$^{-1}$ for the HG hydrophilic and HG hydrophobic pores respectively). Also, in simulation of the 1$^{st}$ generation pores, the hourglass pores maintained their desired initial shape more consistently than the funnel shaped pore models, thus leading into a continuation in pore modelling in which functionality will be 'mutated ' into the *N=14*, 14-$\beta$ HG pore to switch functionality between the hydrophobic and hydrophilic pores.

### 3.3.3 Second Generation Pores

#### Switching Functionality

In the 2$^{nd}$ generation of models I either introduced a central ring of hydrophobic residues into a hydrophilic HG pore (by replacement of the central glutamine ring by a hydrophobic residue 'X' to give the hydrophilic-x models. *i.e* STNQNTS to become STNLNTS), or I incorporated a central ring of glutamine residues into the hydrophobic HG pore, to give a hydrophobic-Q model (GAVLVAG to GAVQVAG),

depicted in figure 3.17.

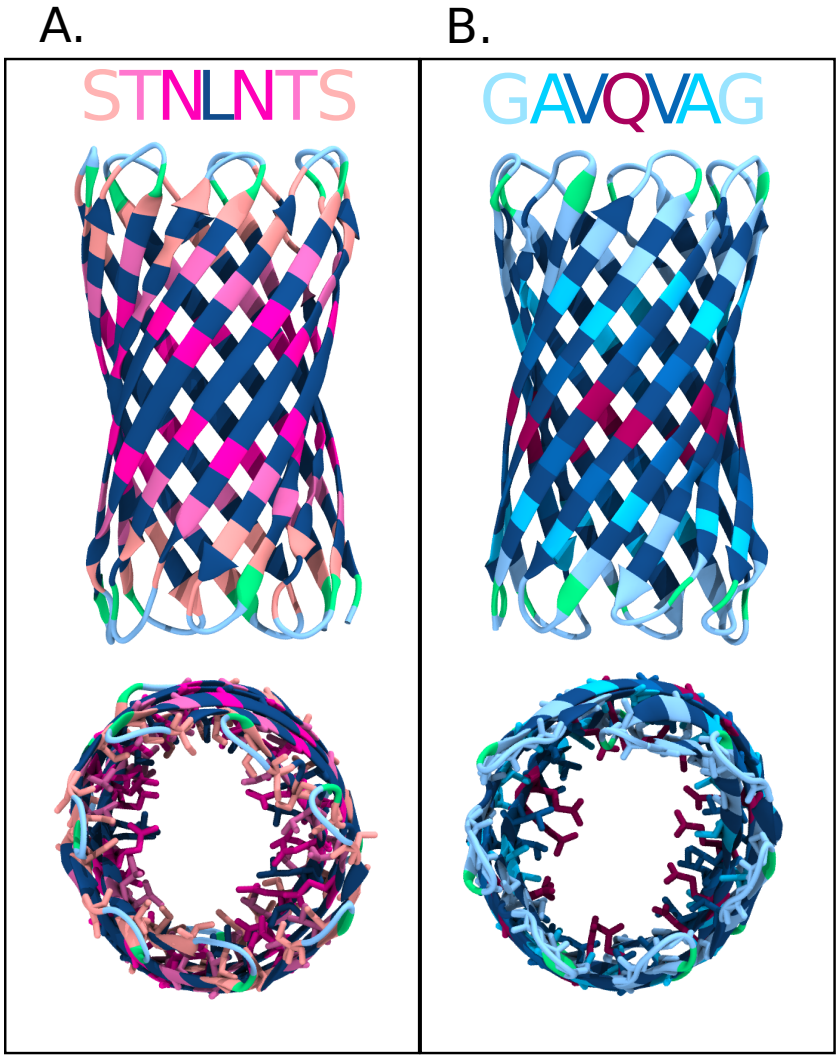


**Fig. 3.17:** Second generation model pores. A. Hydrophilic hybrid pore STNLNTS (previously STNQNTS). B. Hydrophobic hybrid pore GAVLVAG (previously GAVLVAG). Colour of residues is consistent with previous models.

### Stability and Conduction

It is instructive to compare the details of the original models with their 2$^{nd}$ generation counterparts, with mutation of the central ring giving the pores a more heterogeneous chemical lumen. These new 2$^{nd}$ generation pores are stable (figure 3.18), as seen with the 1$^{st}$ generation models. Observation of conductance, in terms of radii is similar both

for the hydrophobic-Q and hydrophilic-L pores, and the hydrophobic-Q model radius is equal to its sole-hydrophobic 1st generation parent (radii, GAVQ ~4.4 Å and GAVL ~4.5 Å). Interestingly, this small change in radius from the original pore, resulted in an ~40 fold increase in flux of water through the pore (figures 3.19 and 3.20).

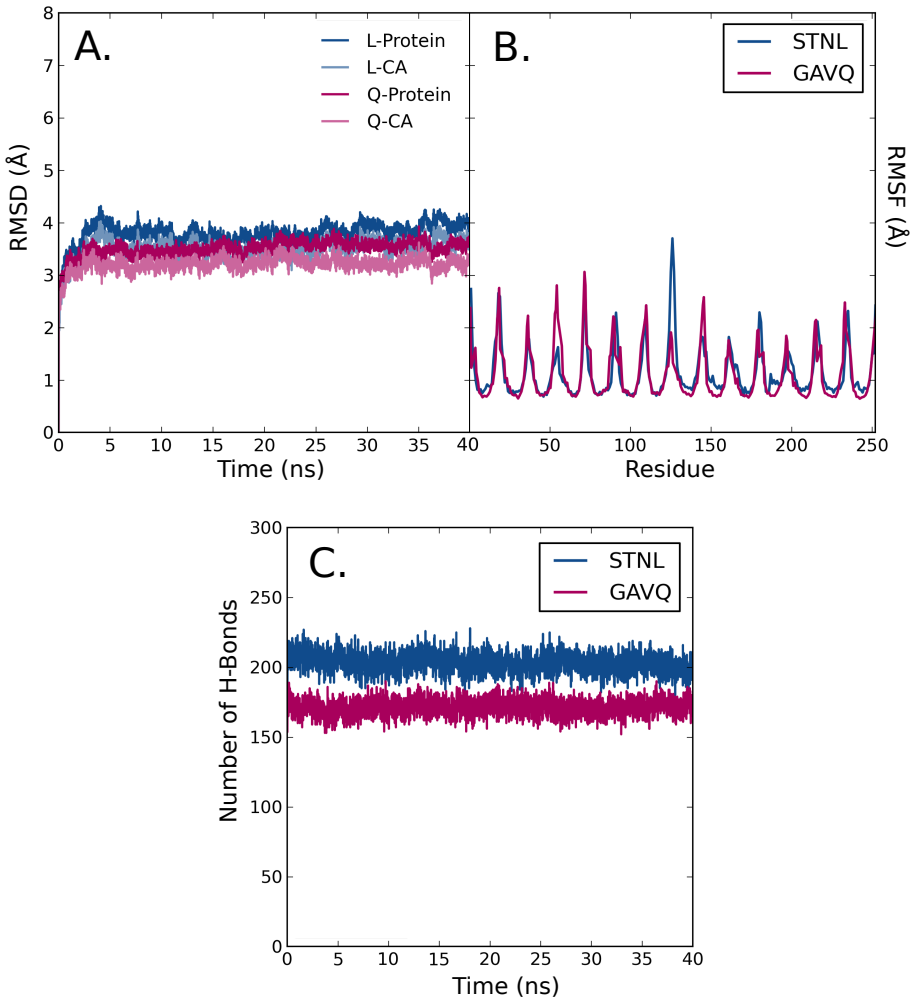


**Fig. 3.18:** RMSD, RMSF, and backbone hydrogen count of*N=14*, 2nd generation pores. A. RMSD for both hybrid pores (pink hues, GAVQVAG and blue - STNLNTS pore) for C$\alpha$ and protein. B. RMSF for both model pores, same y scale as A.. C. Backbone hydrogen bond count for both pores (within 3.5 Å ), colours are consistent with B.

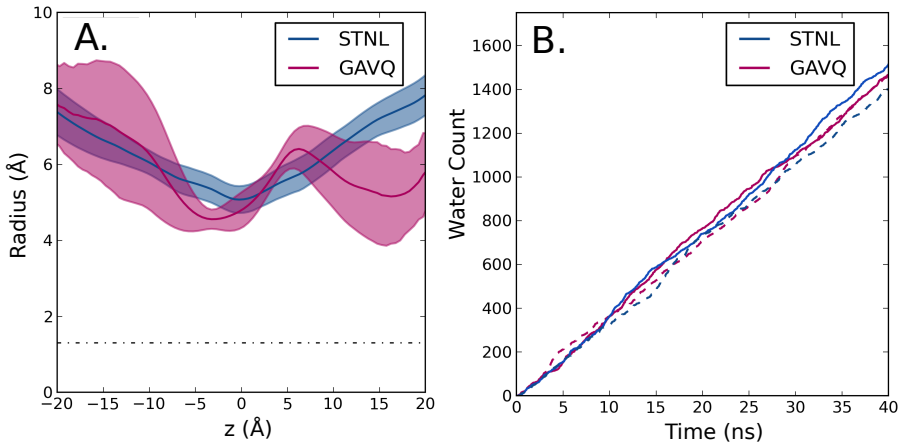


**Fig. 3.19:** Radii profile and water flux of *N=14*, 2nd generation pores. A. Radii profile for both hybrid pores, with the x axis representing the z axis going through the lumen of the pore and radius on y. Dotted line on the plot at ~1.9 Å indicates the radius of water a molecule. B. Water flux profiles of water conduction through the pores. Solid line indicates an 'upward' flux, dashed indicates downward.

In previous observations of the 1st generation pores, I note that the water conductance of the hydrophobic GAVLVAG *N=14* pore is ~0.5 $ns^{-1}$ and is less than that of the single file conductance of water (ca. 3 $ns^{-1}$) in the aquaporin channel [300, 301]. Modelling and simulation of the 2nd generation pores, where leucine was replaced with glutamine at the constriction of an otherwise hydrophobic pore, has enabled a "hydrophobic barrier" to be breached with a flux increase to ~35 $ns^{-1}$. This change in conductance is due to the ability of polar, hydrogen bonding sidechains to stabilise water within a hydrophobic barrier region, demonstrated both in earlier simulation studies of simple models of nanopores [61] and in more recent combined experimental and computations studies of ion channels, such as the TWIK-1 potassium channel [66].

I also examined a series of hydrophilic-x models (STN-X) in which a central hydrophobic ring was introduced into a hydrophilic, HG pore. All of the hydrophilic-x pores showed significant water conductance (figure 3.20 A. and C.). However, as the size of the residue R group that forms the hydrophobic constriction ring were

increased a reduction in water conduction was observed. It is interesting to note that there is a greater increased conductance in the hydrophilic-W model than in the smaller hydrophilic-Y pore, even though the tryptophan sidechain is larger than tyrosine. This seemed to reflect a change in conformation via rotation of the smaller Y sidechains, which resulted in local pore deformation, thus resulting in a narrower pore and a smaller water flux.

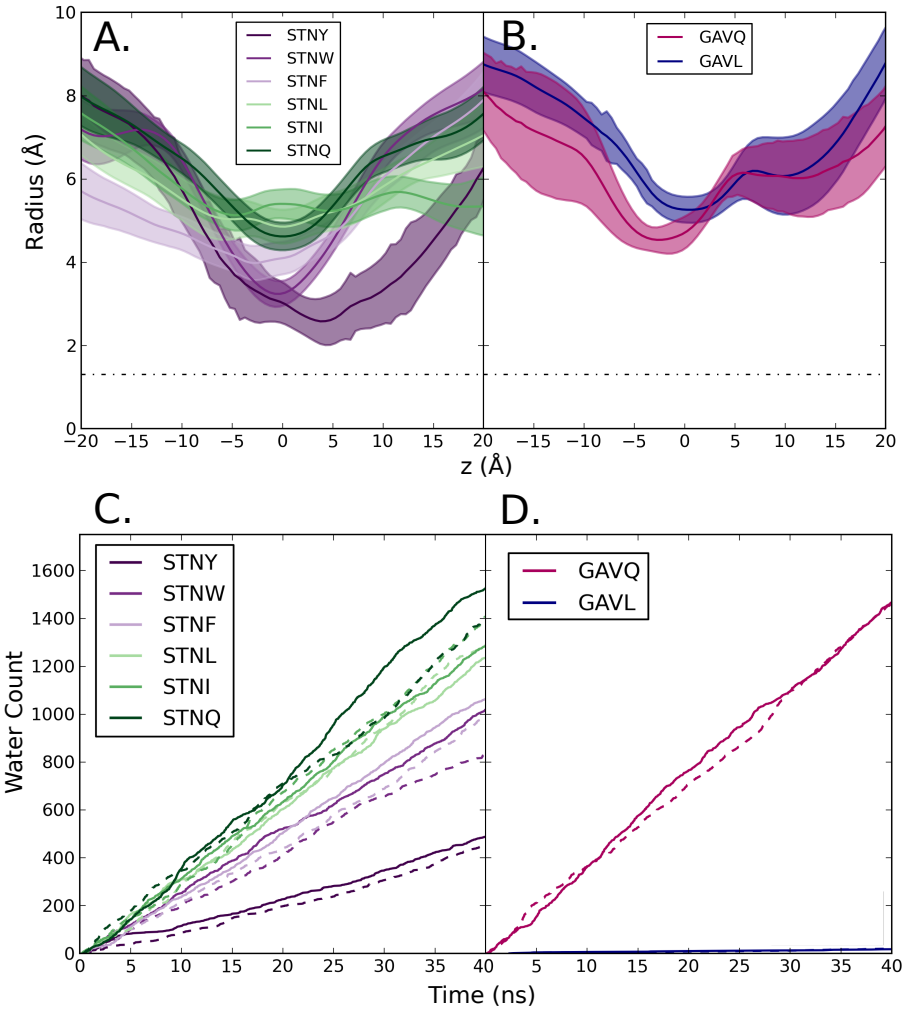


**Fig. 3.20:** Radii profile and water flux of other *N=14*, 2nd generation pores. A and B. Radii profile of both pores, STN-X in which X is a hydrophobic residue and GAV-Z pores. x axis is the z axis going through the lumen of the pore with radii shown on the y. C and D. Water flux profiles of water conduction through the pores. Solid line indicates an 'upward' flux, dashed indicates downward. GAVL line is present along the x axis.

Based on these 2nd generation models, I have observed that the functional 'openness' of the pores can be successfully modulated by changing the nature of the central constriction, and that this is most sensitive when a central hydrophobic barrier is implented into a hydrophilic pore. This was then explored in further detail within the 3rd generation models.

### 3.3.4 Third Generation Pores

The 2nd generation hydrophilic-x (STNX) models revealed that the introduction of a single ring of leucine residues is not sufficient to functionally close the pore, Therefore, I will now move on to the 3rd generation L-gate models, where I will examine the effect of increasing the thickness of the central hydrophobic constriction by introducing either two or three rings of leucines producing STNLLNT, STNLLTS, and STLLLTS pore models (figure 3.21) for further investigations into water flux.

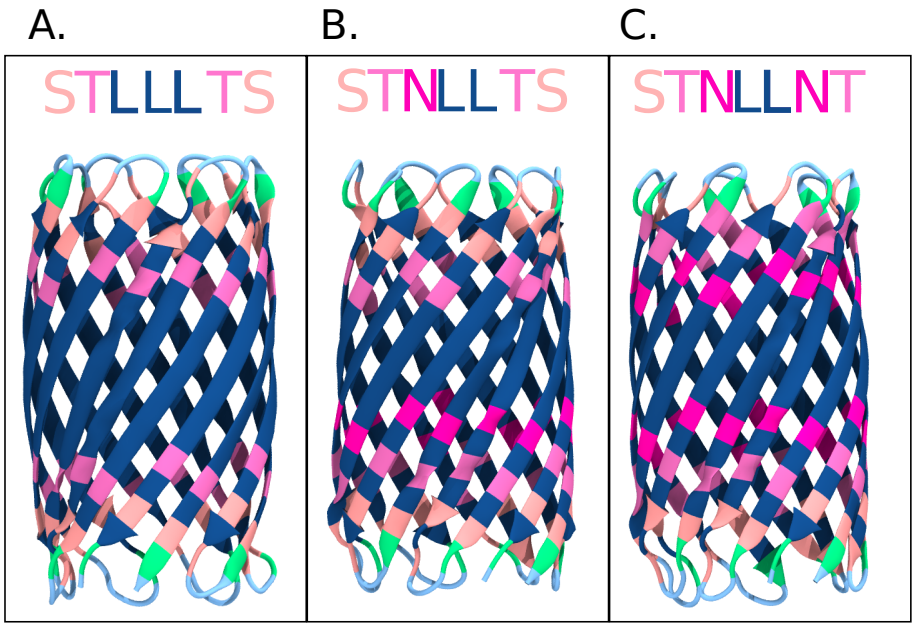


**Fig. 3.21:** Third generation *N=14* model pores. Shown in cartoon, with consistent residue colours are A. STLLLTS pore, B. STNLLTS pore, and lastly, C. STNLLNT pores. All are a hybrid model of 1st generation hydrophilic STNQNTS pore.

Each of these models has a minimum radius of ~5.5 to 6 Å (figure 3.22) and is comparable in this aspect to values which result in hydrophobic gating (chapter 1, introduction) of simplified models of nanopores [61], with dynamic changes in water seen between 4 and 7 Å. Significantly, for all three models dynamic wetting/dewetting is observed within our simulations, seen as stochastic steps in the cumulative water flux plot (figure 3.23). Visualisation of the simulations reveals that, as anticipated,

the dewetting occurs in the vicinity of the central rings of the hydrophobic leucine sidechains. In terms of water conductances this ranges from ~30 $ns^{-1}$ for the STNLLTS, ~6 $ns^{-1}$ for the STNLLNT, to ~0.2 $ns^{-1}$ for the STLLLTS pore, akin to the initial full hydrophobic pore model and also an order of magnitude less than aquaporin water flux [300, 301]. The amphipathic pore of aquaporin is continuously occupied by water and so does not exhibit dewetting events. For all simulated pores, as in previous simulations, protein pore stability was monitored during the simulation which is shown in figure 3.24.

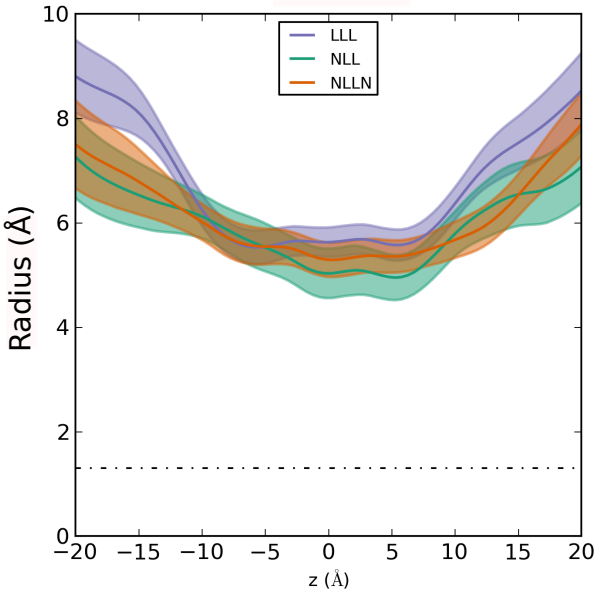


**Fig. 3.22:** Radii profiles for N=14, 3rd generation pores. LLL denotes STLLLTS, NLL is STNLLTS, and NLLN is the STNLLNT pore. This abbreviation is used throughout this thesis. x axis is the z axis going through the lumen of the pore with radii shown on the y.

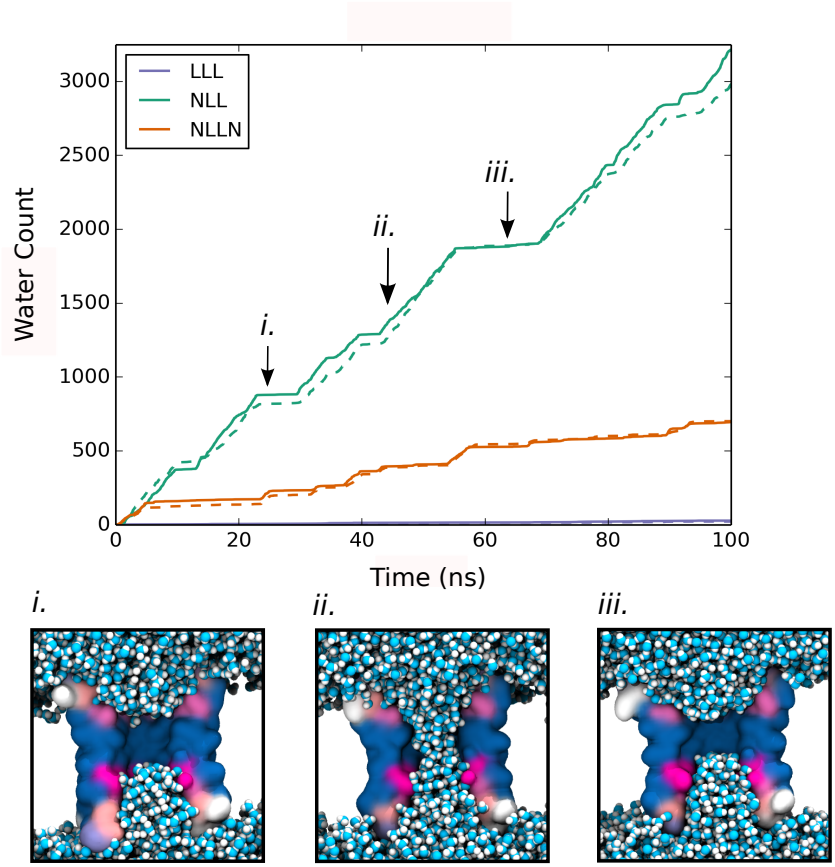


**Fig. 3.23:** Water flux through the *N=14* 3rd generation pores. Water Flux profiles of water conduction through pores. Solid line indicates an 'upward' flux, dashed indicates "downward". Colour of pores is consistent across these figures. Shown in i, ii, and iii are simulation snapshots of stochastic dewettting, wetting and dewetting of the NLL nanopore at 22, 46, and 63 ns intervals.

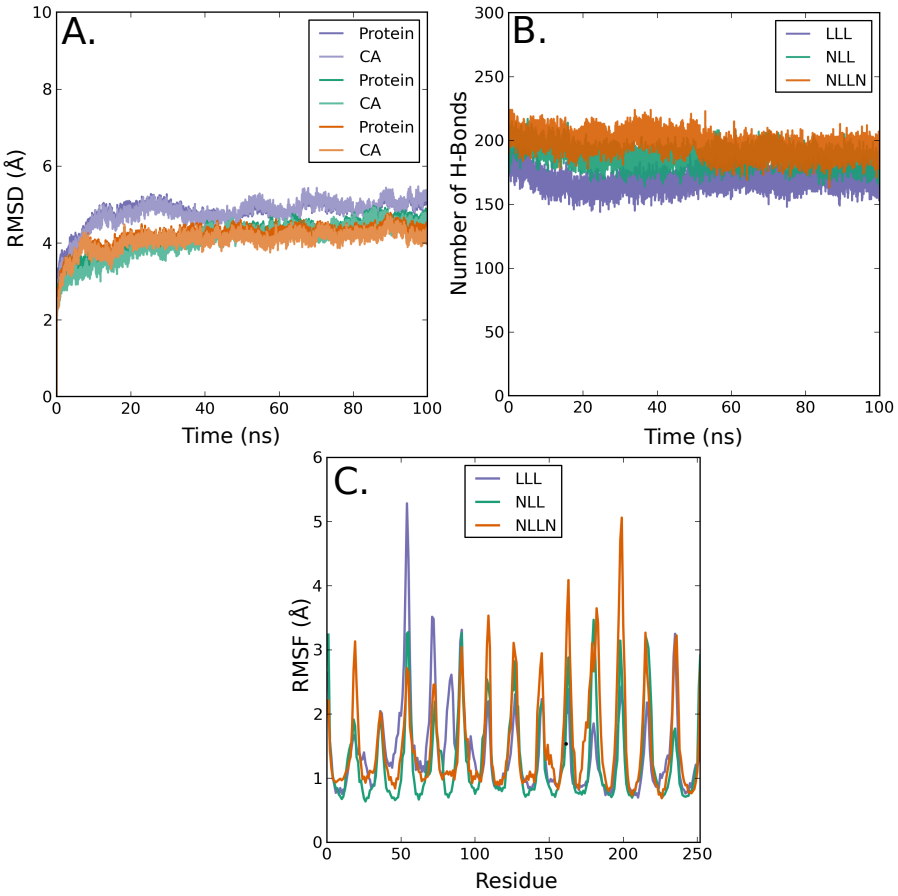


**Fig. 3.24:** RMSD, RMSF, and backbone hydrogen count of the *N=14*, 3rd generation 14$\beta$ pores. A. RMSD for all three models (colors of models consistent as before and in this figure) for C$\alpha$ (CA) and protein. C. RMSF of all three pores. C. Backbone hydrogen bond count.

### 3.3.5 Implementing Barriers into $\alpha$-Hemolysin

A further extension of the hydrophobic barriers implement via a leucine ring constriction is used to computationally model the motif back into the native protein, that the pore is modelled upon ($\alpha$-Hemolysin). The TM region of the protein was mutated using modeller to create a triple leucine ring within the pore (figure 3.25). Six residues were mutated on the 2$\beta$ strands on each monomer (of the heptamer) to leucine (T117L, G119L, N121L, G137L, N139L and S141L). Two other residues were mutated

to smaller residues to emphasise the leucine band as a potential barrier (N123A and L135A). Simulation protocol was identical to that of the model pores mentioned previously in this chapter, however the cap domain was not simulated and the protein region was restrained using positional restraints.

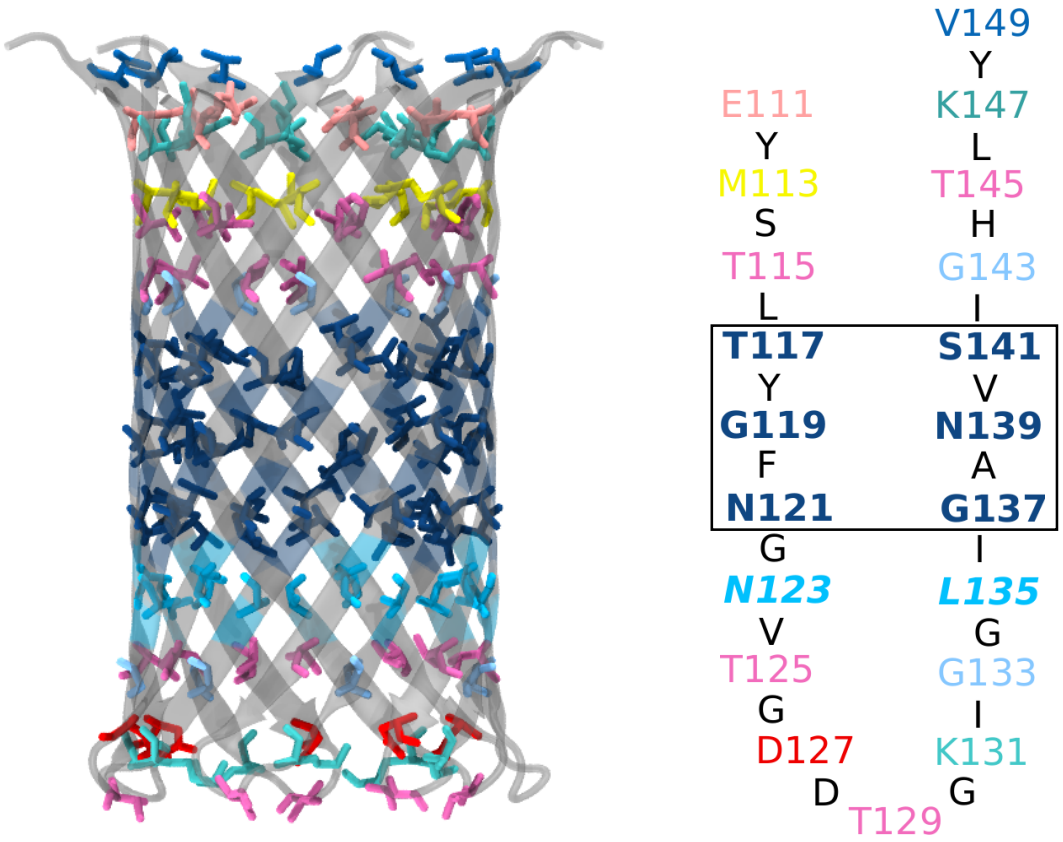


**Fig. 3.25:** $\alpha$-Hemolysin mutated transmembrane $\beta$-barrel region. Left. $\alpha$-HL barrel with residues coloured to the right hand sequence. Only inward, lumen pointing residues are shown. Right. Residues of the barrel, residues in colour are lumen facing. One letter code indicates membrane facing residues. Boxed are the six residues that are mutated to leucine, with the residues in bold cyan indicating the two residues mutated to alanine.

Within simulation, akin to the 3$^{rd}$ generation pores, a "3L" motif in this protein pore was sufficient to exclude water from that pore region (figure 3.26, C.). The introduction of the leucine ring has not decrease the constriction radius of the pore, however has moved it further down the barrel and increased it in height (mutation

of L135) and is within the upper cut-off of hydrophobicity affecting confined water. Related this to flux, the $\alpha$HL-LLL pore has a flux indistinguishable to the LLL 3$^{rd}$ generation pore (~0.2 ns$^{-1}$ for both 3L pores). For $\alpha$-HL wild type (WT) the flux is ~19 ns$^{-1}$, which is comparable to other nanotube simulations (single walled CNT) of 17 ns$^{-1}$ [60], but is lower than other simulated $\alpha$-HL fluxes (66 ns$^{-1}$, [302]) in which the entire pore was modelled. This suggest that this method of forming a hydrophobic barrier could actually be transplanted into a WT $\alpha$HL pore (provided that key mutations would not affect the folding of the protein) therefore modulating its activity and flux without the use of an external adaptor protein.

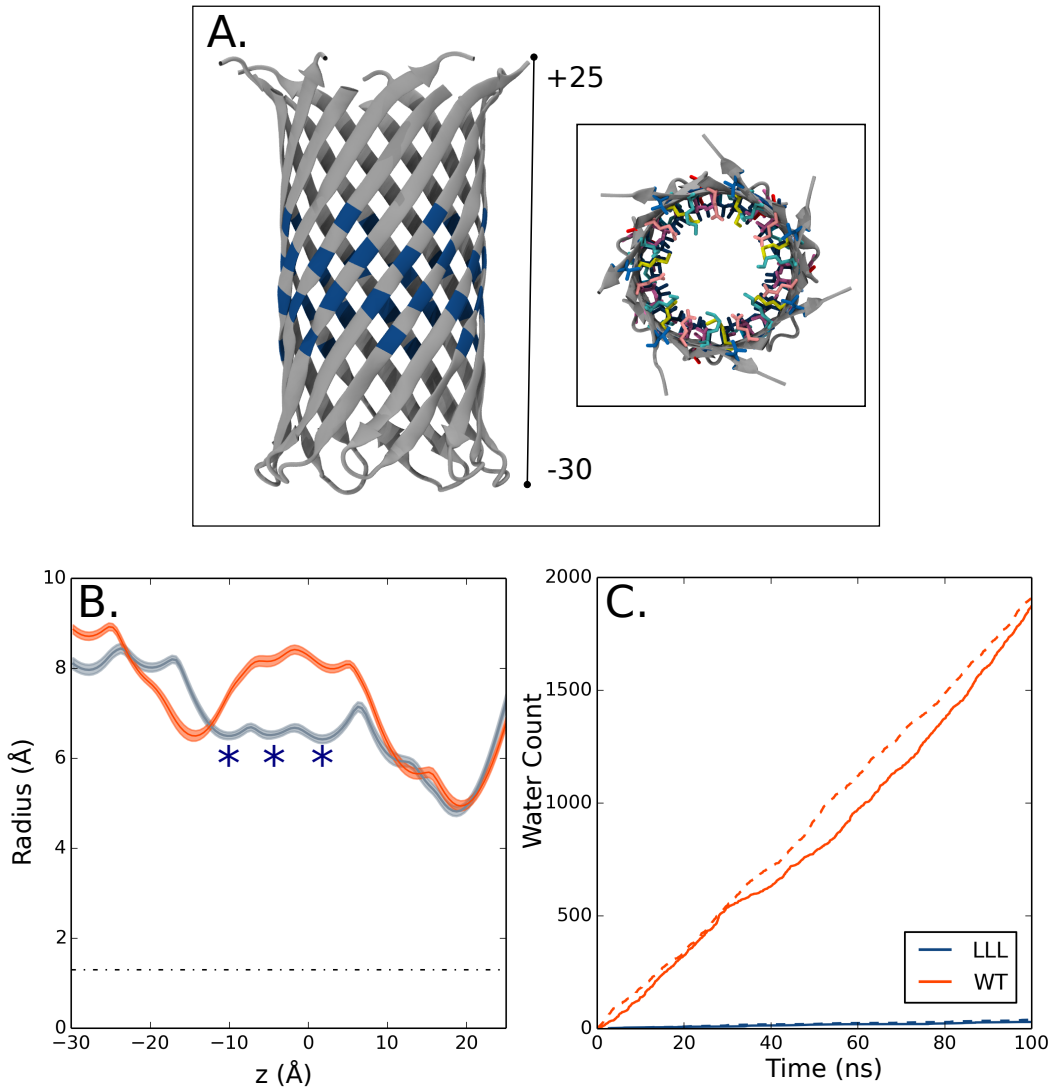


**Fig. 3.26:** $\alpha$-Hemolysin transmembrane barrel, radii profile, and water flux of WT and LLL region. A. $\alpha$HL TM region indicating leucine residues (blue) and lumen. Numbers indicate the orientation of the protein in B. B. Radii profile of WT $\alpha$-HL and LLL model. Navy stars indicate the region in which 3 leucine mutation is present. C. Water flux profiles of water conduction through pores represented in B. Solid line indicates an 'upward' flux, dashed indicates "downward".

## 3.4 Conclusion

In this chapter, I have computationally designed and simulated biomimetic protein nanopores of a stable and conductive nature akin to the biological protein pores they are based upon in a lipid bilayer. From these pores, I have also computationally transplanted a hydrophobic barrier to water and ion flux (derived from gating mechanisms in the nicotinic acetylcholine receptor and in the bacterial MscS mechanosensitive channel [72, 303]) into this family of nanopores. Simulated was the transplantation of such a barrier into a biological protein pore. Thus leading to an argument that this method is a suitable method for design of motifs for protein nanopores. The designed nanopores mimic the template proteins in terms of overall nanopore stability in ca. 100 ns MD simulations in a simple phospholipid bilayer. Using these models, I have investigated the effect of size, shape, and of the hydrophobicity/hydrophilicty of the pore lining residues on water flux through the nanopores (in part using water as a proxy for ionic currents). A number of clear trends have emerged, in particular the generation of a hydrophobic barrier (along with associated stochastic wetting/dewetting behaviour [69, 224]) when a central constriction lined by successive rings of leucine residues is engineered into the pore. To investigate this barrier in more detail, more analysis of permeation free energy landscapes will be conducted in the next chapter.

Inevitably, there are methodological limitations to this study. In particular, I have not explored for all models simulated the water model employed. With the forcefield used, the SPC model was employed, however there are other water models of differing polarisability which could be used [257]. It could be of interest to examine how the use of polarisable force fields [304] for water and protein could affect the behaviour of a conduction in these pores. Also it will be of interest to study the effect of the aliphatic hydrogen atoms on non-polar amino acids (which are excluded in the GROMOS forcefield used). One may also wish to question the timescale in which

these simulations were conducted in relation to structure and conductivity. Based on previous simulation papers, this is a widely used simulation length on which to observe the stability of protein pores and porins. However as noted in this chapter, the possibility of instability induced by a highly-hydrophobic pore may raise the issue of whether 100 ns is long enough to observe protein stability. Regarding conduction, as previously mentioned water flux is used as a proxy for ion conduction due to the timescale and high number of simulations completed in this chapter. For these series of proteins, ion conduction does occur with a water conduction event (however in much lower numbers, ~1-5 per 100 ns simulation (data not shown), compared to the ~30 per 100 ns for OmpF [219]) which is consistent with time scales of ion conduction events, thus water observation allows for a shorter simulation to observe if a pore is conductive. Also there have been studies on the computation of transport within nanopores which suggests that a change in the neighbour-list within the gromacs code is needed for accurate solute translocation [305]. This was tested for a simulation in this chapter, however the decrease in neighbour-list from 10 to 1 (as suggested) resulted in ~10 fold increase in computation time.

Furthermore a difficultly arising from such pores simulated in this chapter would be (in the event of synthesising the protein pore in wet lab) protein folding due firstly, to the multiple mutations in the native protein and secondly, the introduction of a high degree of hydrophobicity to the protein itself which is known to be a driving force of globular protein folding [306].

It would also be of interest to explore possible sensitivity to the nature of the lipid bilayer in which the pore is embedded. The porin group of proteins (which the $12\beta$ barrel pores are based upon) are mainly present in the outer membrane of gram negative bacteria, which consists of an LPS bilayer (not that of the phospholipid one simulated here) which is known to affect the gating and conduction of these porins

[307]. Thus in further studies it may be of interest to investigate the influence of bilayer composition. Also relating to this area is the membrane in which the industrial sponsor uses (Oxford Nanopore Technologies) which is known to insert stable pores. However details of such membrane composition are not in the public domain.

# Chapter 4

# Free Energy Landscapes for Permeation in Designed Pores

This chapter is based on the latter half of the following publication;
Designing a Hydrophobic Barrier within Biomimetic Nanopores. Trick et al, (2014) ACS Nano. 8 11268-79.

*"And the Haters Gonna Hate, Hate, Hate, Hate, Hate"*

Taylor Swift

## 4.1 Introduction

Nanofluidics, the study of the behaviour, manipulation and control of fluids within the nanoscale has become a major field recently due to the biotechnological uses of water manipulation via ionic and water flow for water desalination,[214, 308–311], electronics [312, 313], analytical separation of biological molecules [314] and lab-on-a-chip structures [315] with the use of synthetic and biological based nanopores. Based

on the wide use of such pores and interest in water control, it is of interest to investigate the full permeation properties of such pores created in the previous chapter.

As mentioned previously, when designing nanopores, one approach is to mimic key features of biological nanopores to act as templates and mimics for the development of such model pores. Throughout this thesis and in the work of others, MD simulations play a key role in allowing us to understand the physical basis of nanopore function and conductance. Following on form the previous chapter, here I use to use free energy simulations do determine if transplantation of a hydrophobic ring into a biomimetic model ($3^{rd}$ generation pore) is a true hydrophobic barrier (and not just an unfortunate case of a too short a timescale of simulation).

MD simulations and free energy calculations have been used to investigated hydrophobicity in a number of constructs such as protein channels of pLGICs, nAChR, GluCl, and GLIC [72, 75, 233, 316], potassium channels [66, 317, 318], also within theoretical models and CNT [60, 319, 320] (along with the hydrophilic version, boron nitride nanopores [91, 321, 322]). Additionally, MD simulations and free energy calculations have been used to look at ion conduction [204, 323], which would be of interest to the model pores studied here.

In this study, I use the previously designed $\beta$-barrel nanopores (figure 4.1) that contain a possible hydrophobic barrier based on the chemical nature and radius of the pores (which lie within the hydrophobic transition radius). Equilibrium and non-equilibrium MD simulations are used to explore the barrier present in the nanopores using various molecule types. To quantify the barriers, potential of mean force (PMF) calculations are used to reveal 1D energy landscapes of permeation. These studies provide a detailed example of the use of MD simulation to design and evaluate simple model nanopores based on a $\beta$-barrel template, with a prospect of their further development.

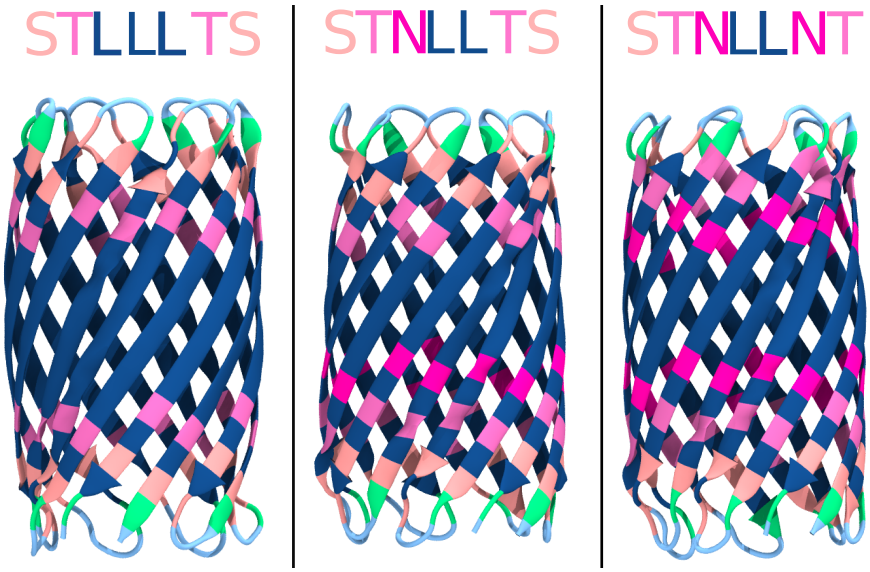


**Fig. 4.1:** Model Pores in which permeation will be investigated via free energy methods. Shown in cartoon are the pores which were designed and simulated in the previous chapter.

## 4.2 Methods

### 4.2.1 System Preparation

The hydrophobic nanopores were embedded in a self assembled DPPC bilayer using methods from the previous section. After AT conversion, water molecules (SPC) and counter ions were present in the system (ionic concentration of 1M). For the equilibrium simulations, I initially restrained the protein and the ion (with the ion being placed in the center of the leucine band) with a force constant of 1000 $kJmol^{-1}nm^{-2}$ for 2.5 ns. After the time elapsed, the restraints were removed and the system was simulated for another 2.5 ns. For the steered MD (SMD) simulations, the ion was placed just above the lumen facing leucine residues of a STLLLTS nanopore (in initial simulations I tried placing the ion further above the leucine residues however all runs were unsuccessful) at a pulling rate of 2 Å $ns^{-1}$ with a spring constant of 350

$kJmol^{-1}nm^{-2}$. For the umbrella sampling simulations the molecule was placed at the center of mass (c.o.m) position of the protein (x and y) in the center of the pore lumen, with the z coordinate being varied. Particles which overlapped with the molecule were repositioned via energy minimization before simulation. Energy minimisation (steepest decent algorithm) was run for 5000 steps. All simulations were carried out with GROMACS version 4.5.5 [288, 324] with the united atom GROMOS96 43a1 forcefield [246, 247].

### 4.2.2 Umbrella Sampling

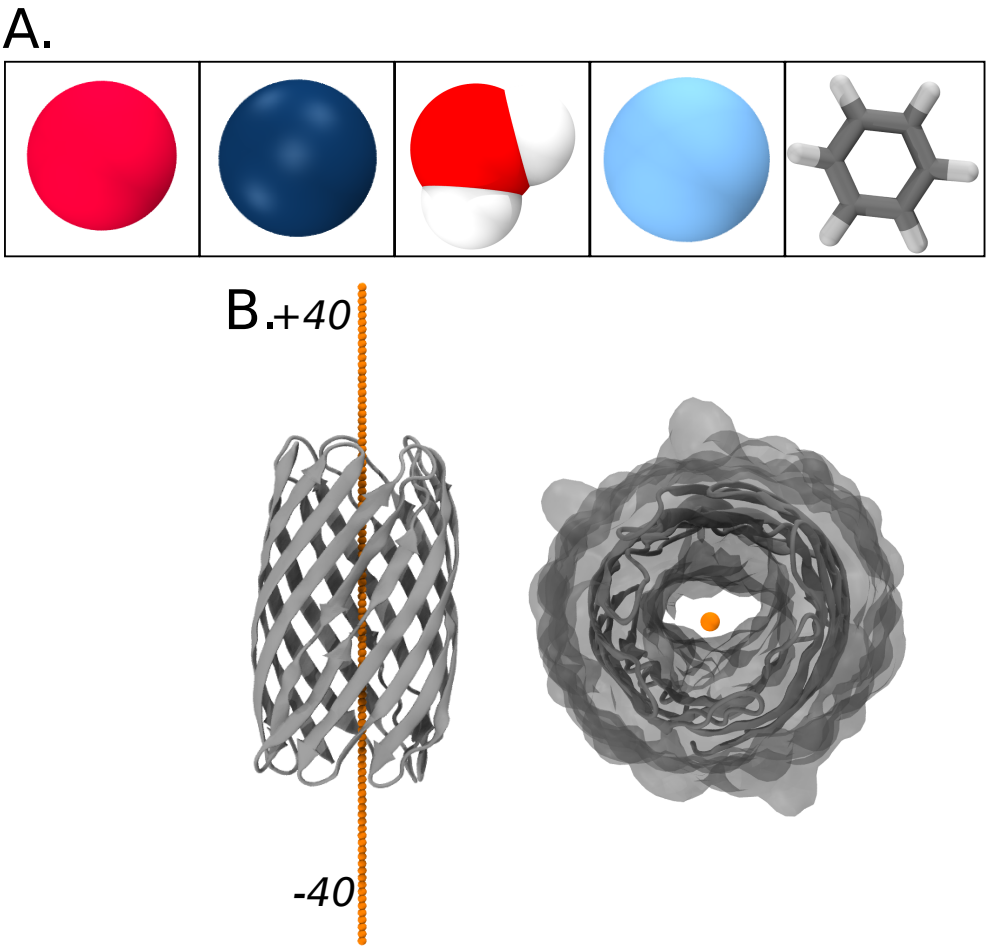


**Fig. 4.2:** Simulated molecules and pore axis for umbrella sampling. A. Molecules in which free energy profiles will be calculated for in this chapter. From the left, $Na^+$ ion, $Cl^-$ ion, water molecule, methane and benzene. Images are not to scale. B. Cartoon representation of protein with spheres (orange) indicating the PMF pathway through the pore lumen. right - 90° rotation of figure with surf representation of the surface.

The initial system for the umbrella sampling simulations were obtained from a 60 ns equilibration simulation of the nanopore model in a lipid bilayer. The reaction coordinate was defined as the z/pore axis, ranging from ±40 Å with the bilayer and protein centre at z = 0 Å (figure 4.2). This defined ~80 windows along the z axis, with spacing of 1 Å between successive windows. A harmonic biasing potential was

applied to the z coordinate of one atom of the molecule (ion and methane, main bead. Benzene CD2 and water OW atom types) with a force constant of 1000 kJ $mol^{-1}nm^{-2}$ acting on the z coordinate only. Each window was simulated for 2 ns for both ion and water windows, 4 ns for methane, and 10 ns for benzene. Convergence for water and ion was analyzed by calculating the height of the central barrier as a function of time intervals for consecutive 0.1 ns segments from each 2 ns window. Methane convergence was calculated for every 0.5 ns, and benzene for every 1 ns. PMF profiles were computed using the weighted histogram analysis method (WHAM) [271]. PMF profiles were tethered and errors were calculated by the bootstrapping method.

## 4.3 Results and Discussion

### 4.3.1 Landscape of Various Molecules

As mentioned, vaying types of molecular permeation pathways have been simulated to identify and investigate "barriers" or "energetic wells" to such, with the hypothesis of an energetic barrier for polar molecules such as $Na^+$, $Cl^-$ ions, water and favourable pathways for more hydrophobic molecules such as methane and benzene through a hydrophobic pore.

### 4.3.2 Types of Simulation

To analyse the permeation pathway of these molecule classes and the model pores under conduction, equilibrium and various non-equilibrium methods are used to probe the energetics of transport of these molecules. These being-

- Equilibrium - used in the previous chapter and continued here as equilibrium simulations with the implementation of positional restraints on select ions and protein.

- Steered Molecular Dynamics (SMD) - a $Na^+$ ion is pulled through the pore of the STLLLTS Pore.
- Umbrella sampling - calculated a potential of mean force (PMF) profile for the conduction of ions through the protein pore.

#### 4.3.2.1 Equilibrium and Positional Restraints

So far, I have only measured water conductance through these model pores, considering this as a proxy for ionic conductance. I initiated the explorations of the behaviour of ions within the hydrophobic models by taking a dewetted state from a simulation of e.g. the STNLLNT model, and restraining a $Cl^-$ ion in the region of the dry central constriction. Whilst the ion was restrained in this position it resulted in persistent wetting of the central region of the pore. However, upon removing the restraint on the ion, the ion was quickly expelled from the central region of the pore, leading to pore dewetting (figures 4.3 and 4.4). This suggests that the de-wetted state of the channel in the absence of an ion is more stable, and that the pore is functionally closed.

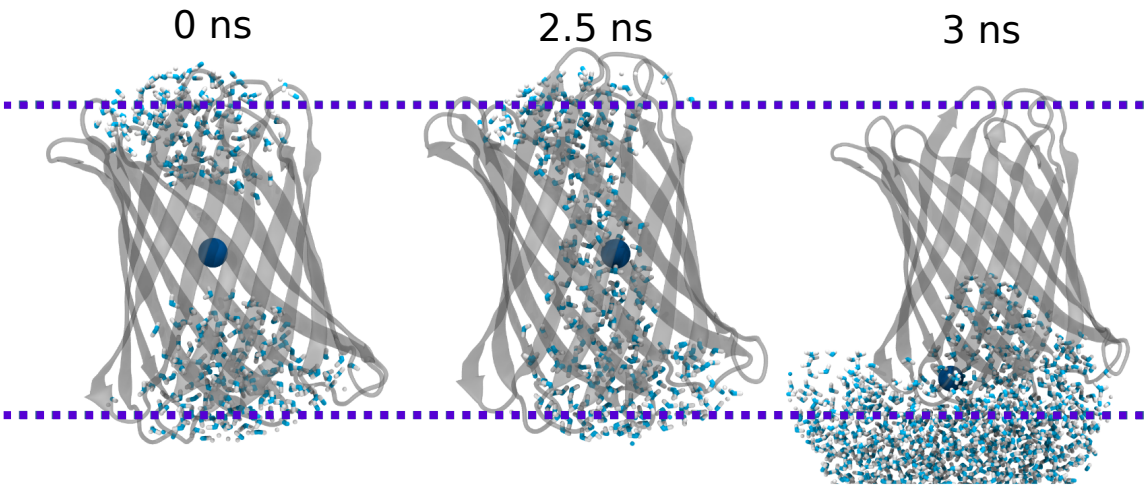


**Fig. 4.3:** Snapshots of ion restraint within the STNLLNT nanopore. $Cl^-$ ion (shown in dark blue sphere) within the nanopore and bilayer (DPPC phosphate particles indicated with dashes). At 0 ns, the ion is restrained within the LL region of the pore, within the hydrophobic gap. At 2.5 ns, the restraints upon the ion are removed, with wetting of the hydrophobic gap and the ion. After 0.5 ns, (3 ns), the ion is expelled from the pore and dewetting occurs.

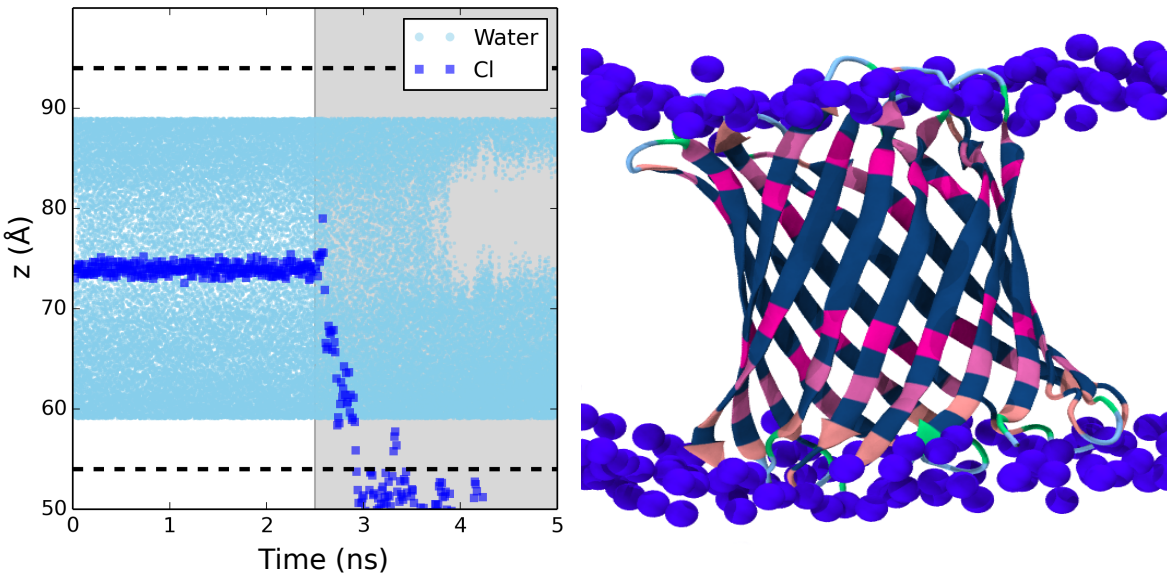


**Fig. 4.4:** Water around the ion within the STNLLNT pore during the restraint simulation. Represented in the z position of water (light blue points) within the volume of the pore, and restrained ion (blue). Shaded grey indicates region where restraints were removed. Cartoon on the right shows approximate position of the protein and bilayer (purple spheres). Dashes indicate phosphate z positions of the DPPC lipid.

This expulsion event suggests there is a barrier present, and this observation also argues for a more detailed analysis of the energy landscapes of permeation through these surprisingly complex model nanopores.

#### 4.3.2.2 Steered Molecular Dynamics

For this method, the force was applied to the (protein and) ion, which induced the "pulling" of a sodium ion through the lumen of the hydrophobic STLLLTS pore (figure 4.5). Complementary to the restrain simulations performed previously, the ion pathway was shown to be unfavourable. Positioning was very dependent on the ion being directly above the LLL-hydrphobic region and within the protein pore vicinity (if not, the ion would pass through the bilayer). A force of ~100 kj $mol^{-1}$ $nm^{-2}$ is observed (figure 4.5, B.) between ~75 and 80 Å within the the force profile. Nevertheless

no quantitative values can be actually obtained from such a "noisy" pull profile and possible limitations to the method itself. The change in pull force also suggests that there is a barrier in this region, therefore supporting the conclusion that more detailed analysis of such pores is needed for quantification of a barrier. This detailed analysis is performed using free energy calculations.

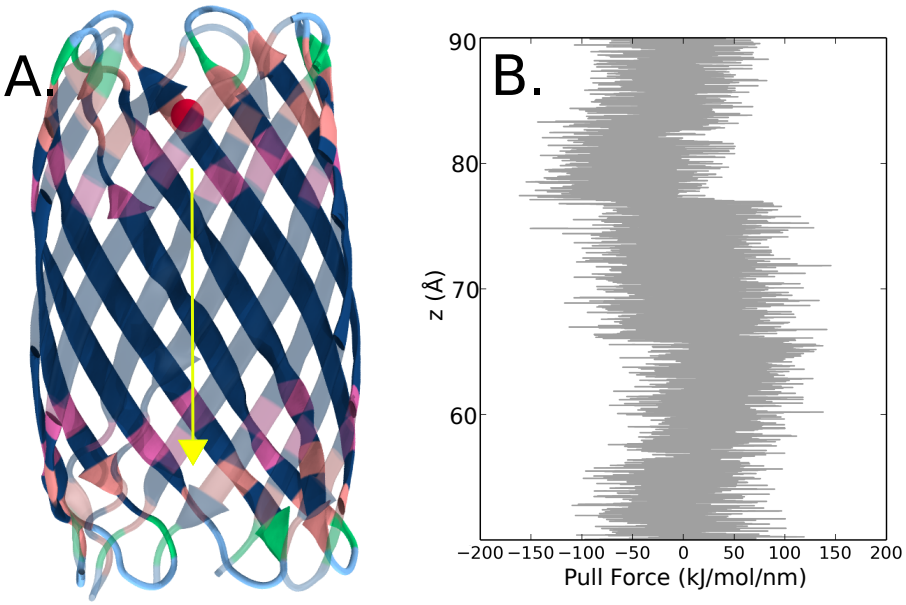


**Fig. 4.5:** Steered MD Simulation of ion translocation through STLLLTS pore. A. cartoon representation of STLLLTS pore in which a $Na^+$ shown at the top of the pore (red sphere) is pulled through the pore, direction shown by yellow arrow. B. Pull force profile from simulation. The height of the plot corresponds to the protein height.

### 4.3.3 Ions and Water Through Hydrophobic Barriers

#### 4.3.3.1 Ions

The PMF profile for a $Cl^-$ ion (figure 4.6) through the hydrophobic pores displays the expected behaviour based on previous simulations, of having an energetic barrier within the pore. These values calculated are comparable to other hydrophobic regions observed within such pores as the cationic nAChR (~26 kJ $mol^{-1}$ for $Na^+$ also ~18

kJ mol$^{-1}$ for Cl$^{-1}$) [72], the small mechanosensitive channel MscS (~40 to 80 kJ mol$^{-1}$ at its barrier) [303], the TWIK potassium channel (~20 kJ mol$^{-1}$ for K$^{+}$) [66], and a bacterial homologue such as the GLIC channel (~83 kJ mol$^{-1}$ is calculated for Na$^{+}$ ) [75]. Also other free energy calculations of the linear peptide of gramicidin A (~33 kJ mol$^{-1}$ for K$^{+}$) [323] show equivalent values to the calculated barrier.

The energetic barrier height observed in this chatper is also approximately equal to those for simple model nanopores, in which a barrier of ~19 kJ mol$^{-1}$ was calculated for a cation through a model hydrophobic pore [68], 24 kJ mol$^{-1}$ for Cl$^{-}$ transport through a 8.5 Å radius pore [203], and also CNT in which values ranged from 96 to 12 kJ mol$^{-1}$ for tubes ranging from 6.6 to 9.3 Å in diameter [94]. Based on diameter, the corresponding CNT to this protein model would have no barrier, however is has a differing in chemical nature and structure. Another model, based on larger dimensions of the nuclear porin complex (32 nm diameter pore and a 10 nm bead), indicate a barrier of ~23 kJ mol$^{-1}$ based on the hydrophobic particle type which also supports this theoretical value.

Therefore, the values calculated here for a theoretical pore constructed out of a theoretical $\beta$-barrel protein are equivalent to other models and proteins.

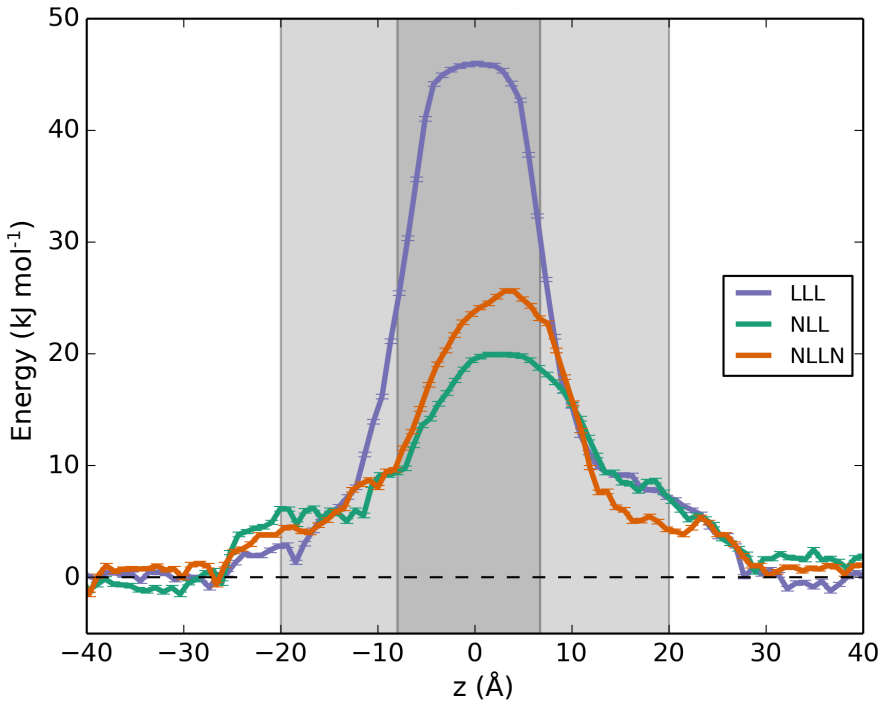


**Fig. 4.6:** Potential of mean force profile of a chloride ion through 3rd generation pores. Pore models have been aliased from STLLLTS to LLL, STNLLNT to NLLN, and STNLLTS to NLL. Plot represents the translocation pathway (on the x axis) which in this thesis is termed z, through the nanopore with calculated energy from that position (y). Barrier heights correspond to 46, 26 and 20 kJ $mol^{-1}$ for the LLL, NLLN, and NLL pores. Initial grey shade represents the z coordinate of the pore, with secondary inner shading indicates the central mutated region of the pore.

To determine firstly if the 1 Å positioning of the ion (and following molecules) is sufficient to provide enough overlap in the 1D pathway and 2D x-y space to accurately predict a free energy landscape, the gromacs code g_wham [325] was used to produce a histogram of the overlap of the simulation windows of a profile (figure 4.7, A). As can be seen, there is sufficient overlap between the histogram windows to ensure that there is adequate sampling with the pull force applied and with the z coordinate positioning. Also to be considered is whether the length of simulations used in each umbrella sampling windows is sufficient to allow convergence of the free energy (figure

4.7, B.). Convergence is observed after ca. 0.5 ns, with the PMF presented (in figure 4.6) based on data collected for the last 1.5 ns of each window.

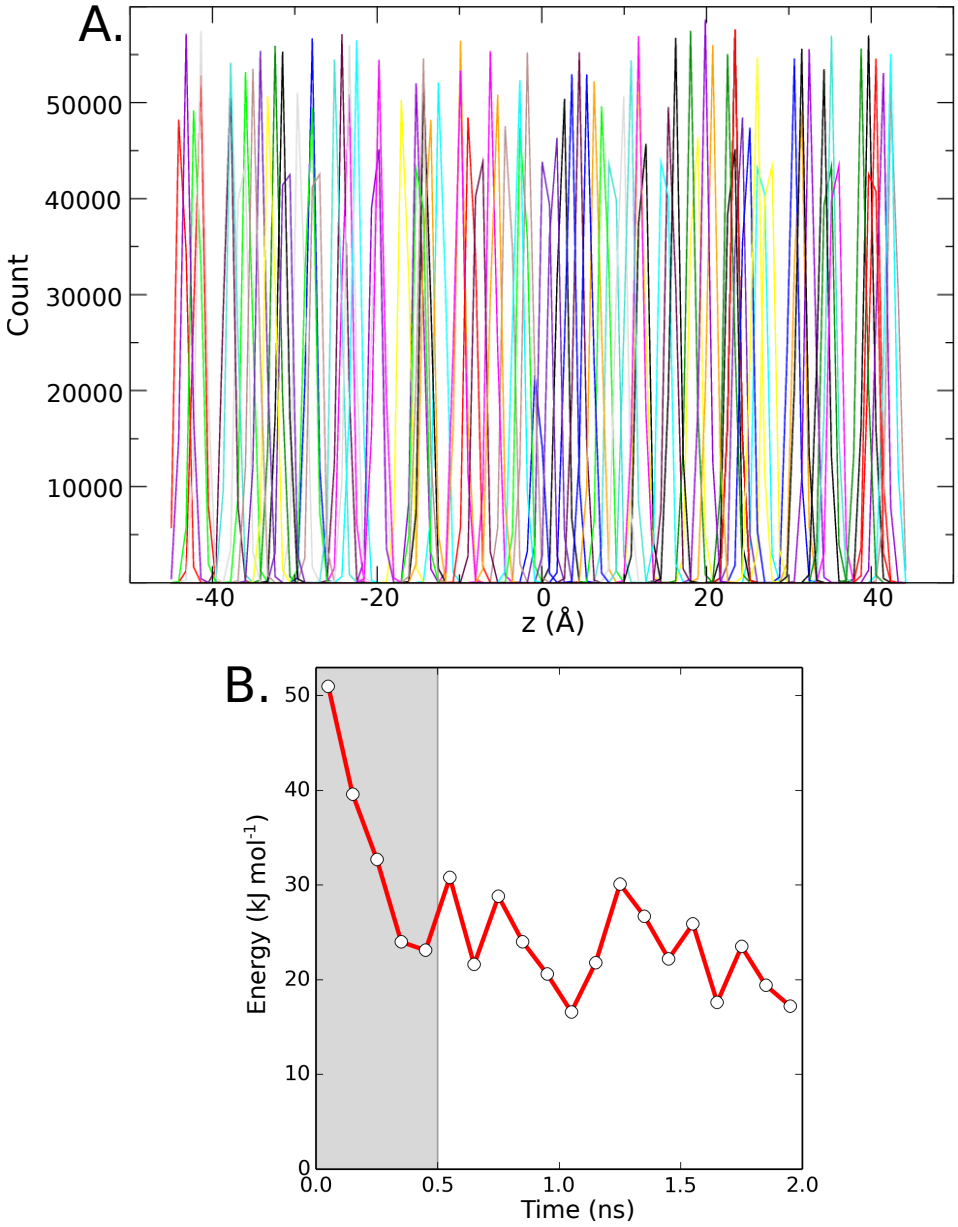


**Fig. 4.7:** Histogram and convergence profile for STNLLTS pore. A. Histogram of the count (how often a window falls into a specific peak) of the window overlay of chloride ion at varying z position within each simulation. B. Plotted is the maximum calculated free energy for incremental windows. i.e., 0 - 0.1 ns, 0.1 - 0.2 ns and so on until 1.9 -2.0 ns (point is plotted at 0.1 increments). Shaded grey region is the time which will be omitted from the final profile.

Another observation into an adequate length of simulation is the movement in the x and y plane of the solute. For windows that are too short in time scale, inadequate sampling of the x-y space would occur, thus not giving an accurate representation of the possible interacting groups within the structure. This is shown in the ion movement in the x and y plane (figure 4.8) for the ion within the solvent phase (B.) and within the protein pore (C.). For the simulation time scale used, based on the distribution and movement of the ion within the system for both phases, ample movement for the region is observed and gives proportional representation of movement within the system.

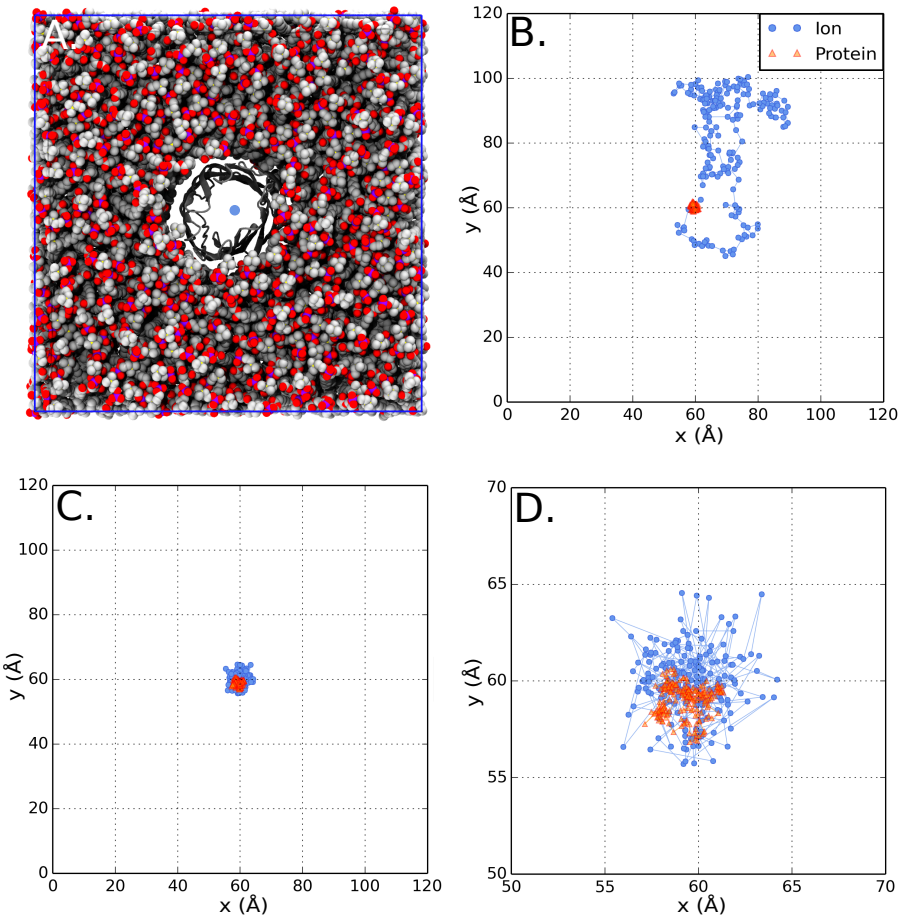


**Fig. 4.8:** Chloride ion movement within simulation windows for STLLLTS pore. A. The initial set up of ion (blue dot) within the lumen of the protein (grey cartoon) in which the z values are varied to explore the energy landscape in the pore lumen. DPPC lipid is shown in VdW representation. Water and other ions are omitted for clarity. Image is to scale in figures B and C in the x and y directions. B. Plot of protein and chloride ion c.o.m movement z value for the ion of 30 Å, where the ion is in the solvent phase of the simulation. C. Ion at z = 73 Å which is the center of the LLL motif of the pore. D. Zoom of C. Ion and protein colours are consistent throughout images.

It is of importance to probe the origin of the energetic barriers in the profile shown, which may be further elucidated by calculating the solvation numbers around the ion. This is based on the numbers of chloride ion-water contacts as a function of pore axis position during the simulations. Radial distribution function (rdf) analysis was conducted on both chloride and sodium ions (figure 4.9) to indicate the hydration

shell distances within these simulations. From this, the number of waters around the chloride ion of interest was calculated for both hydration shells (for $Cl^-$, 4.0 and 6.3 Å and $Na^+$, 3.1 and 5.4 Å) which will be used as distance cut-offs for chloride-water contacts through the model pores.

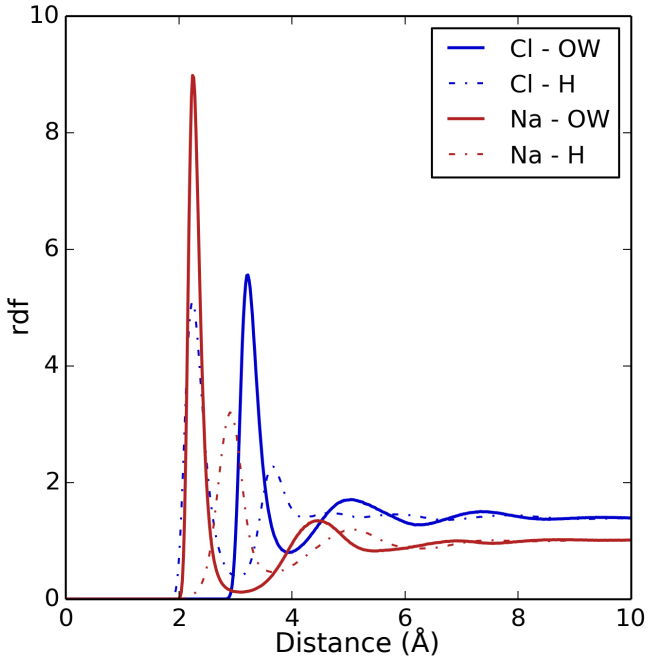


**Fig. 4.9:** Radial distribution function of water around a $Cl^-$ and $Na^+$ ion. Profile indicates distances between water-oxygen atom and water-hydrogen atom to the ion. Value used in this thesis are from the water-oxygen values, with values obtained from the base of the first and second corresponding peaks to include the entire shell.

Water contacts for chloride ion at both hydration shell distances are calculated for all three pores (figure 4.10). It can be noted for the chloride ions first solvation shell remains intact in translocation through the solvent and pore region. In contrast, a significant depletion of the second solvation shell occurs as the ion passes through the hydrophobic constriction. This suggests that the energetic barrier may reflect the large cost of hydration of the hydrophobic constriction and also the the cost of removal of (part of) the second hydration shell. This is noted especially for the LLL pore which

undergoes a 'double dip' of ion dehydration through the central region of the protein. This has also been simulated in varying radii channel-ion systems. In this study, a $Na^+$ ion is present most likely in the center of the pore where it can form the most complete solvation shell [326]. Based on the radius of the proteins shown previously, (chapter 3, figure 3.22, A.) all three of the pores have a minimum radius of ~5-6 Å which would interact with the outer hydration shell, and directly interact and contribute to the decrease in water. This has been noted in the study of the GLIC channel where it is suggested that the barrier to $Na^+$ permeation presented by the hydrophobic gate arises largely from the cost of hydrating the pore [75]. A similar analysis has been presented for anions passing through simple models of narrow hydrophobic nanopores [327]. Thus, looking at the solvation through the pore can give an insight into the gating mechanism in use.

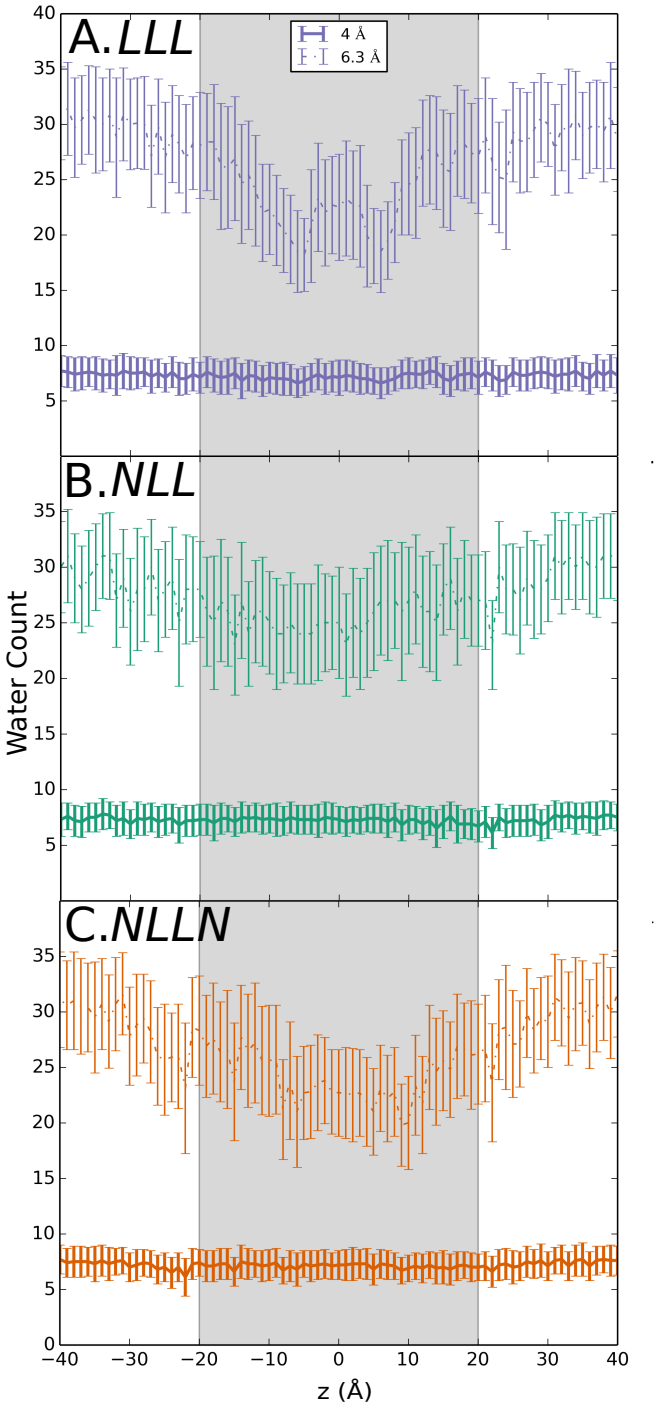


**Fig. 4.10:** Water hydration shells of a chloride ion through the 3rd generation pores. A. LLL model pore with z coordinate on the x axis and number of waters from calculated rdf (figure 4.9) shells on the y axis. B. NLL and C. NLLN pore. For both, shell radii is consistent with values shown in A. Grey region in plots represents protein region.

A more detailed inspection of the hydrophobic region within the model nanopores would be a free energy calculation and profile of selected 1$^{st}$ and 2$^{nd}$ generation pores. Within equilibrium simulation, they exhibited a change in water flux through the pore (chapter 3, figure 3.20) with mutation within only one ring of residues within the constriction region, from a complete hydrophobic pore to one with a glutamine residue constriction. From the free energy profile (figure 4.11), akin to the 3$^{rd}$ generation pores, the GAVLVAG complete hydrophobic pore has a higher barrier ca. 60 kJ mol$^{-1}$. In contrast, the hybrid model has no significant barrier and revealed a relatively flat permeation profile with a central minimum of ca. 2 kJ mol$^{-1}$. Based on water flux I have judged the GAVQ pore to be open (35 ns$^{-1}$) whilst the GAVL pore was closed (0.3 ns$^{-1}$). This relation of water flux and PMF calculation initially supports the assumption that calculations of water fluxes can be used as initial screen of models, as functionally open or closed. This assumption is also supported in the water-ion hydration shells of these model pores (figure 4.12).

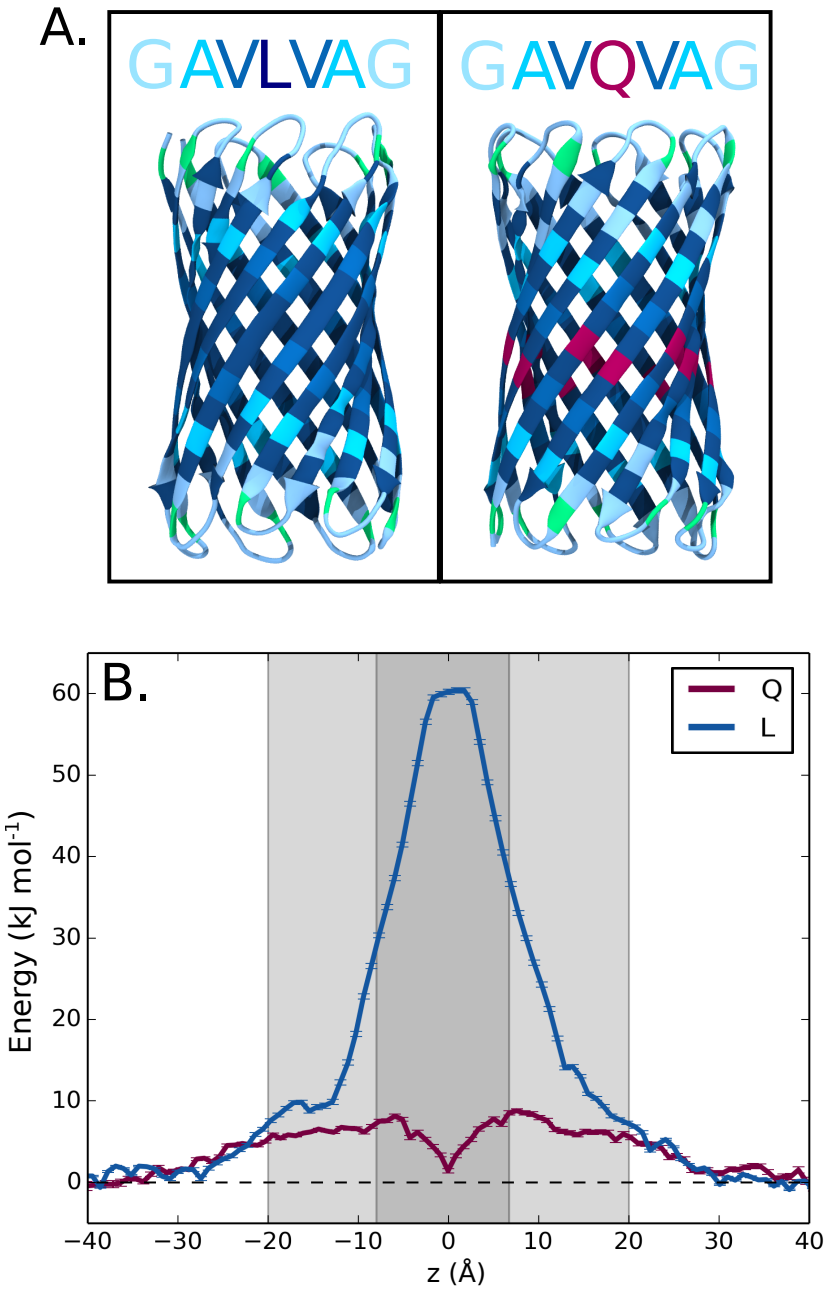


**Fig. 4.11:** Potential of mean force profile of $Cl^-$ through a 1st and 2nd generation pore. A. Cartoon of the 1st and 2nd generation pores from previous chapter. B. Potential of mean force profile of pores from A. In the legend, L denotes GAVLVAG pore and G, GAVQVAG. Grey region indicates the pore region, with darker grey showing the central three residues.

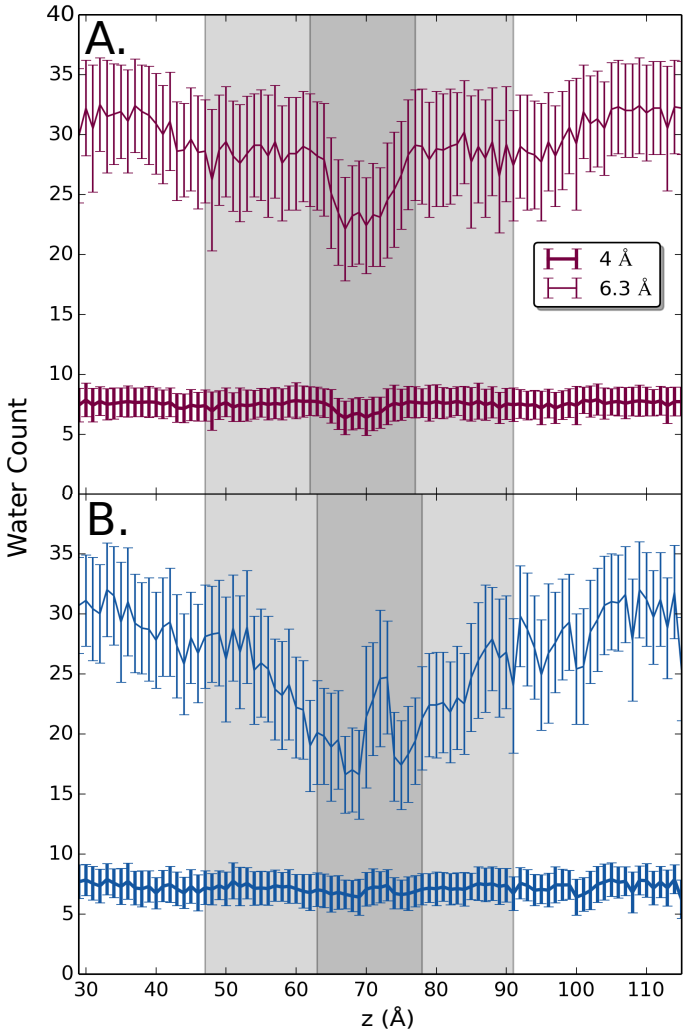


**Fig. 4.12:** Hydration shells of a $Cl^-$ ion through selected 1st and 2nd generation pores. A. GAVQVAG pore and B. GAVLVAG pore. For B, radius and representation is consistent with figure A. Grey indicates protein pore region.

#### 4.3.3.2 Water

The other important molecule to consider in terms of energetic transport from previous findings is that of water through these pores, based on the assumption that their transport can be related to that of ion transport. With the profiles generated for free energy calculations (figure 4.13), as anticipated from equilibrium simulations and $Cl^-$ ion free energy profiles, there is a clear correlation between the height of the

central energy barrier and the rate of water transport through the pores. Akin to the ion barriers, the water barrier and height are within the same region of the protein. Such as the STLLLTS pore, which in equilibrium simulations exhibited a very low conductance for water. In contrast, the two models with only a double ring of leucine residues at the central constriction, showed higher water conductance in simulation and had smaller free energy barriers. Comparable conductive values of water transport through pores are noted within $\alpha$-HL with a maximum calculated value of ~4 kJ mol$^{-1}$ [302], the mammalian "porins" Aqp1 and GlpF have water free energy transport values of ~4 kJ mol$^{-1}$ [328].

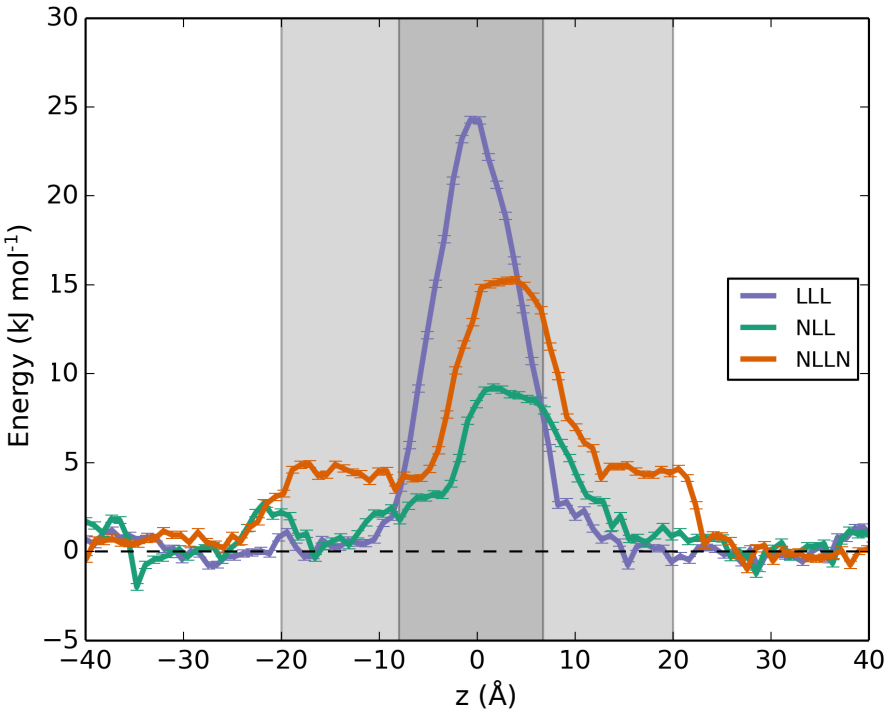


**Fig. 4.13:** Potential of mean force profile for water through 3$^{rd}$ generation pores. Pore models have been aliased from STLLLTS to LLL, STNLLNT to NLLN, and STNLLTS to NLL, with calculated barriers of 24, 15 and 9 kJ mol$^{-1}$ . Plot represents the translocation pathway (on the x axis) through the nanopore with calculated energy (y). Grey region represents the pore, with secondary shading to indicate the central mutated region of the pore.

As with the $Cl^-$ free energy calculations, there is also detailed information into the the origin of the energetic barrier within the profiles by calculating the hydration shell solvation numbers. Rdf analysis was conducted using a water molecule (figure 4.14 A.) within a 100 ns equilibrium simulation to estimate the distances of hydration shells. From this, the number of water molecules around the water of interest was calculated (4.8 Å, to encompass all molecules) and will be used for future calculations of water shell contacts.

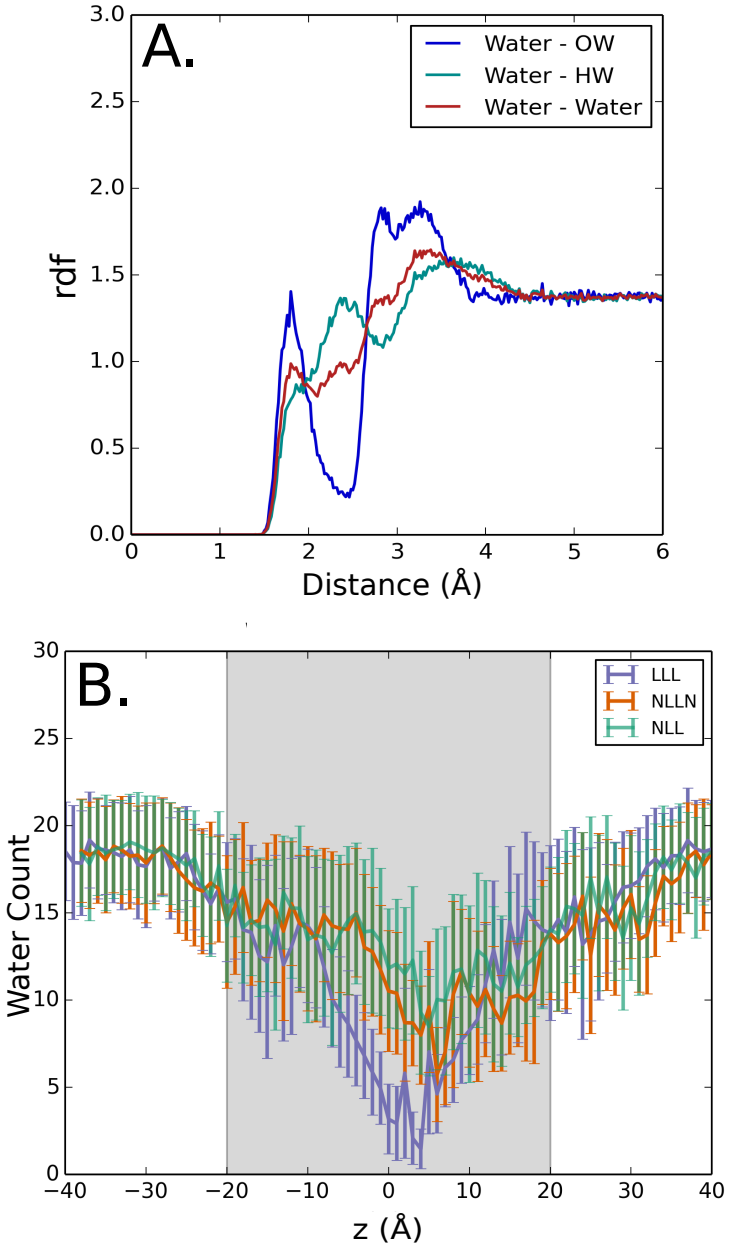


**Fig. 4.14:** Radial distribution function (rdf) of water around a selected water molecule and the water shell contacts through 3$^{rd}$ generation pores. A. Rdf profile indicates distance between water-oxygen and water molecule (blue), water-hydrogen and water molecule (light blue), and water-molecule and water-molecule (red line) within a 100 ns simulation. B. Water contacts within 4.8 Å of STLLLTS (lilac), STNLLNT (orange), and STNLLTS (green line, as denoted previously). Grey box indicates protein region.

Akin to the second hydration shell of chloride, all three nanopore systems indicate

a decrease in surrounding water, as the selected water molecule is moved through the protein. This is suggestive that hydration is a critical aspect to ion conduction through these pores as well as water flow, with the completely "dry" LLL pore having no water molecules (apart from restrained water) within the central hydrophobic region and no attempt of solvation as noted in the ion profiles. The rdf value is lower than that of the radius of the pore at the most constricted region and should not interact with the pore directly. Overall, both ion and water hydration radii suggests that the energetic barrier may reflect largely the cost of hydration of the hydrophobic constriction (as evidenced by the water PMF) plus the cost of removal of (part of) the second hydration shell.

To conclude this section, a PMF profile was also calculated for a $Na^+$ ion through the STLLLTS pore. Comparison of the three free energy profiles for the STLLLTS model (figure 4.15) shows those calculated for $Cl^-$ and $Na^+$ to be broadly similar, both with a higher and wider barrier than that for water, and with a symmetrical profile through the symmetrical pore as estimated.

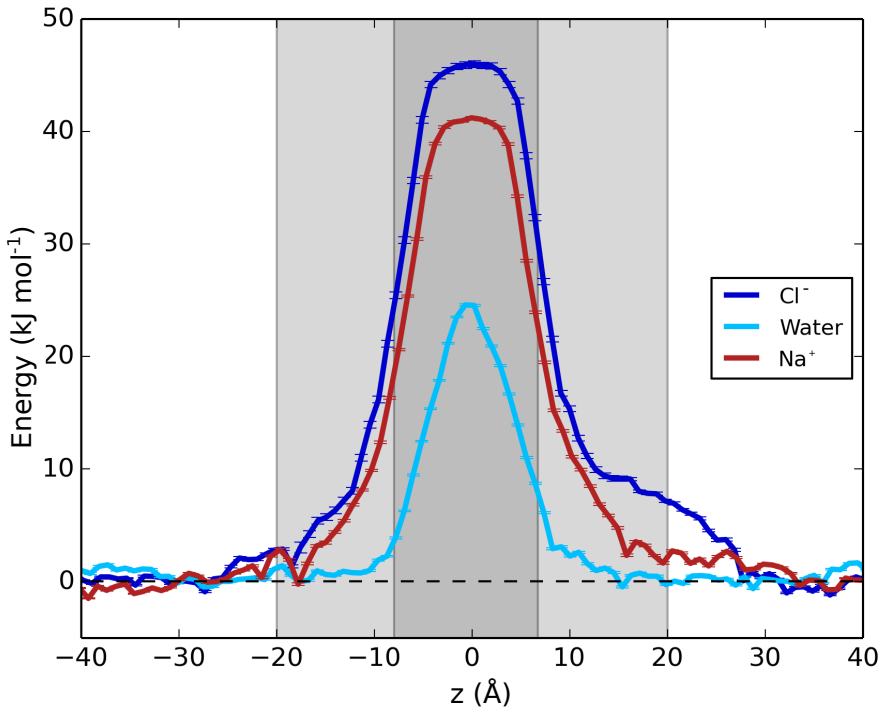


**Fig. 4.15:** PMF profile of $Na^+$, $Cl^-$, and water through STLLLTS pore. Plot is that of previously shown chloride and water, now including the sodium ion free energies of 46, 24 and 41 kJ $mol^{-1}$ through the pore. Representation is consistent with previous profiles with darker grey region of the LLL residues.

The energy profiles of water and ions through these pores are encouraging as it suggests water permeation may indeed be used as a proxy for ion permeation in designing hydrophobic gates or barriers into nanopores and for other hydrophobic residue containing membrane proteins. It is noted that the barriers are substantially higher for ions than they are for water, seen for simple models of nanopores [68], gramicidin A [323], and nAChR receptor [72].

Overall, the nanopore PMF profiles can be compared with those for a model (based on a relatively low resolution structure) of the closed state of much studied nAChR [72]. For the nAChR M2 helix bundle model, the barriers were somewhat lower barriers than for our hydrophobic barrier nanopores, reflecting that the nAChR channel is a

more polar pore and contains a single hydrophobic ring of leucine sidechains at the 9' position of the M2 helices, forming its central barrier. Within the related GLIC channel, the free energy barrier to ion permeation through the pore is estimated to be ca. 83 kJ $mol^{-1}$ in the closed state and ca.17 kJ $mol^{-1}$ when the channel is open [75]. These correspond to a change in radius in the pore focusing at the L9' position. The lower value of $Na^+$ in this in comparison to the higher GLIC value could be accounted for by the radius at position 9'on M2 of GLIC (~1.7 Å). Also more recently, with the publication of structures of similar pLGIC's, more protein structures are available for a comparison of hydrophobicity in constriction regions be it the $5HT_3$ receptor and GluCl channels. Recently calculated are the barriers to permeation for chloride through the chloride selective GluCl channel, where the closed structure barrier is estimated at 62 kJ $mol^{-1}$ and 21 kJ $mol^{-1}$ when open. These correspond to a change in pore radius at it's L9' position and also correspond and agreed to the values calculated here.

The barrier difference between $Na^+$ and $Cl^-$ has also been noted in other simulations on hydrophobic nanopores, with calculated values of 16 and 24 kJ $mol^{-1}$ for the ions, within a hydrophobic channel (radius of 8.5 Å and a length of 10 Å) [203]. The difference and change in barrier height has been correlated to the decrease in solvation free energy of the ions in a bulk SPC/E water model [326], which is similar to the one used in these simulations.

Comparison of the PMF profiles for water and for ions allows reflection on whether we can use water permeation as a (computationally cheaper) proxy for ionic conductance, in filtering out designs based on the former. For the STLLLTS model pore, it is evident that the energetic barriers for ions are higher than for water so a conclusion that the pore would be functionally closed based on the water permeation alone would be correct. This assumption has been verified in the $2^{nd}$ generation hydrophobic-x

pores.

### 4.3.4 Hydrophobic Transport

Lastly, I investigate the transport of hydrophobic molecules through model nanopores, which is of relevance to biological pores that selectively transport such molecules. Examples include the FadL porin which is known to transport long-chain fatty acids [329, 330] and the related porin TodX, which transports toluene across the bacterial outer membrane [331]. With biomimetic pores and the basic hydrophobic molecule available within the force field, it was of a final interest to calculate these energies and investigate possible favourable interactions.

Two hydrophobic molecules, methane and benzene, were used for umbrella sampling windows through the STLLLTS nanopore. Within the GROMOS forcefield, aliphatic hydrogen atoms are not included in the field, thus methane for this simulation is modelled as a hydrophobic bead. Benzene is modelled with all hydrogen atoms (figure 4.2, A.).

The free energy profile of both hydrophobic molecules are presented (figure 4.16), in which windows from 2.5 - 4.0 ns are used for methane and 4.0 - 9.0 ns for benzene. Profiles shown are normalised at zero (figure 4.16, A.) and also from the free energy of hydration for both (~8 kJ $mol^{-1}$ methane, -4 kJ $mol^{-1}$ benzene) [332]. For comparative values to ions and water, values corrected to zero will be considered. As initally expected, from the chemical nature of both species and the nature of the pore, when entering the protein hydrophobic region, free energy does decrease and to different degrees, however the profile is not symmetrical, as seen in ion and water profiles for this pore.

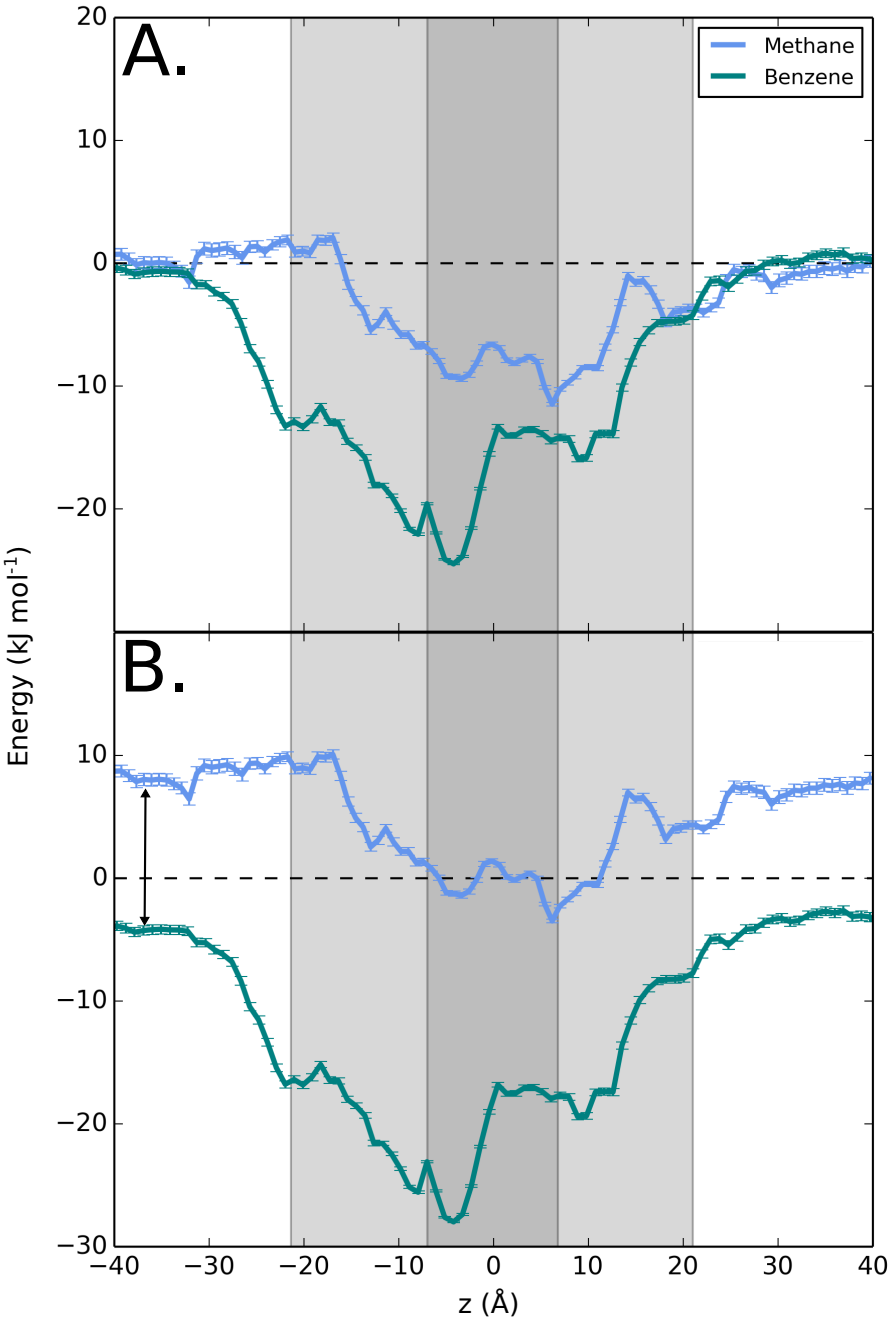


**Fig. 4.16:** PMF profile of methane and benzene through the STLLLTS pore. A. Profiles of both corrected to zero with minima of ~-12 and -25 kJ $mol^{-1}$ for methane and benzene. B. Profiles correct to the free energy of hydration for both species. Grey region indicates the protein region, with darker shade showing LLL region.

To repeat the previously mentioned protocol, convergence is calculated from the

simulation windows to gain an accurate representation of the free energy. The free energy is calculated for smaller regions of the simulation (figure 4.17) in order to assess the overall convergence of the window. Firstly, simulations for both these molecules were extended from the ion and water simulation lenth scales to 4 ns per windows for methane and 10 ns for benzene. Window "splitting" lead to varied profiles for both sets of hydrophobic molecules, which can be clearly seen especially in the 9-10 ns profile (black) for the benzene profile (B.). Thus, based on the lack of convergence of these profiles, the time scales used for these windows were not sufficient to allow a correct profile estimate. Longer simulations need to be considered, as in the case of free energy profiles of nucleotides through $\alpha$-HL and MspA [333, 334], where 150 to 250 ns were used for each window, with a sum of 40 $\mu$s in simulation for each nucleotide. This is not a fast, efficient method of estimating nanopore behaviour, thus a different free energy method should be considered if these molecular translocation pathways are to be considered in these biomimetic models.

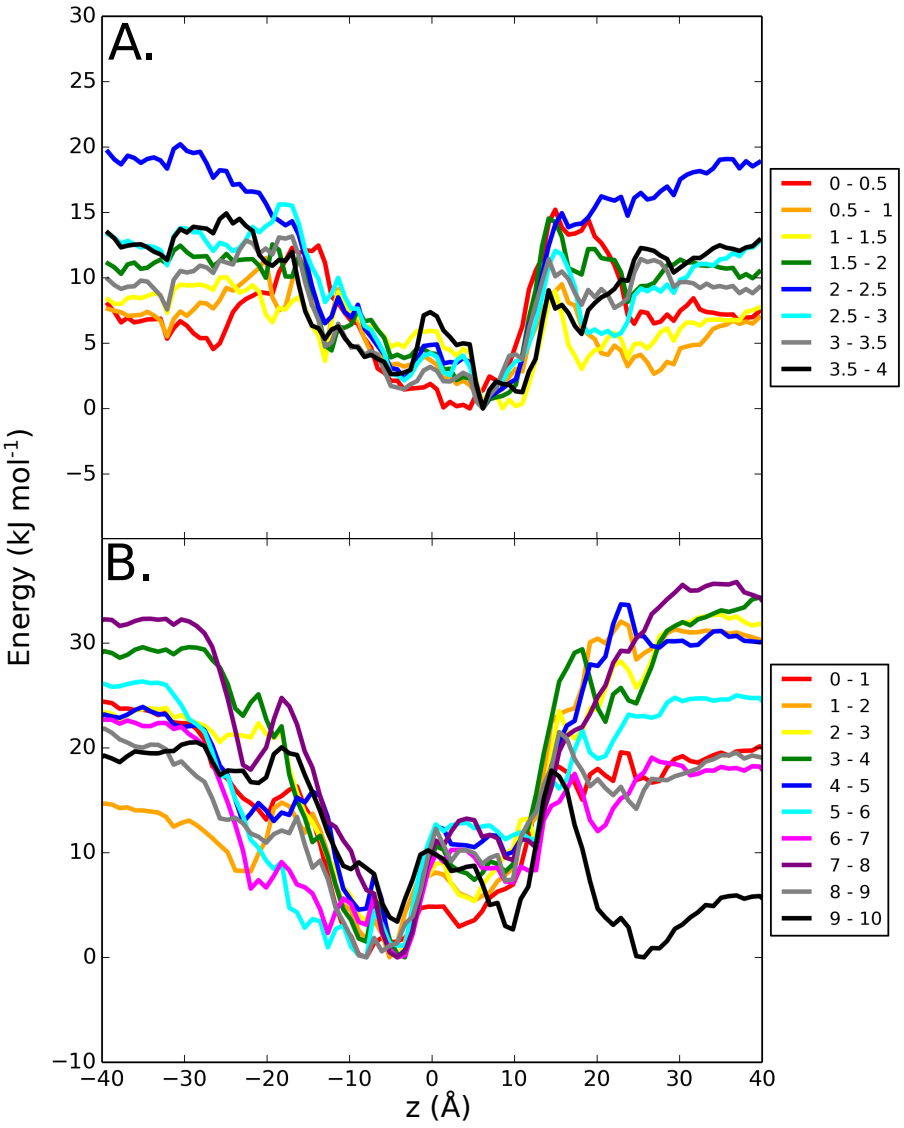


**Fig. 4.17:** Convergence PMF profiles for methane and benzene through the STLLLTS pore. A. Methane calculated PMF profile for every 0.5 ns increments to the end of simulation (at 4 ns). Colours and times are shown in the legend. B. Benzene calculated PMF profile for 1 ns increments to the end of the simulation at 10 ns.

As shown previously in this chapter, an estimate of whether the simulation time scale is adequate is by monitoring the movement of benzene within the 10 ns windows. As noted for the ion profiles, when windows are too short in time scale, inadequate sampling of the space would occur thus not giving an accurate representation of the

possible interacting groups within the system. This could be the origin for the poor convergence noted. Benzene movement within the x and y plane (figure 4.18) within the solvent (B.) and the protein pore (C.) is shown. Based on the distribution of the benzene movement within the system for both phases, ample movement for the region is observed and gives an anticipated proportional representation of movement within the system. Hence, lack of sampling in the x/y plane is not the main cause of an unconverged profile.

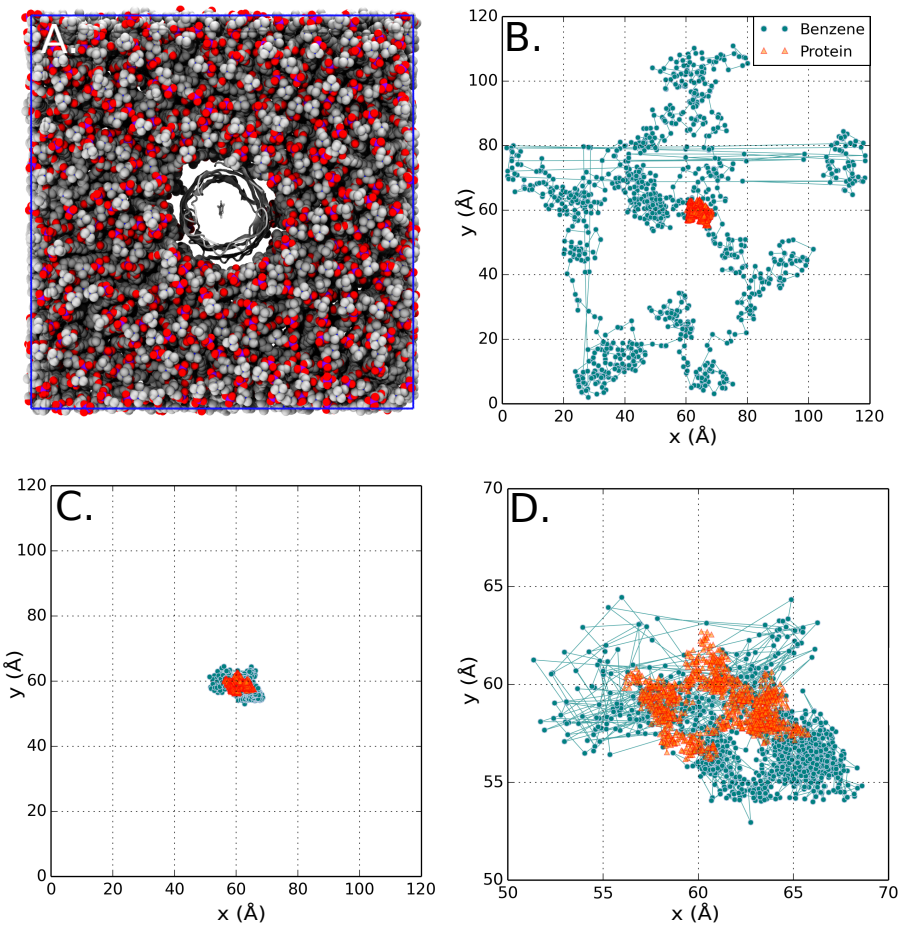


**Fig. 4.18:** Benzene movement within umbrella window simulations for STLLLTS pore. A. The molecule was placed within the c.o.m of the protein (grey cartoon) in which the z values are varied to explore the energy landscape through the protein pore. DPPC lipid is shown in VdW representation. Water and other ions in the system are omitted for clarity. Images are to scale in figures B and C in the x and y directions. B. Graph of protein and benzene c.o.m movement in the simulation in z value for the ion at 30 Å in which the ion is in the solvent phase. C. C.o.m of benzene at z = 71 Å which is the center of the LLL motif of the pore. D. Zoom in of C.

Even though the profiles are unexpected from initial anticipations, water shells around both molecules were investigated to assess their behaviour and possible contributions to the profiles. The rdf profiles were calculated based on 10 ns simulations of both molecules in solvent, with hydration shell values noted and used for water-shell counts (figure 4.19). The symmetrical decrease in the hydration shells is comparable

to that seen with the polar molecules. However unlike the polar species, both hydration shells are affected by the protein environment, with there being no water around either molecules within the center of the LLL region. Based on the hydrophobicity of the solute and the chemical nature of leucine, this is an expected behaviour in this region. However, it raises the discrepancy in relation to the water contacts and free energy barriers for this type of molecule.

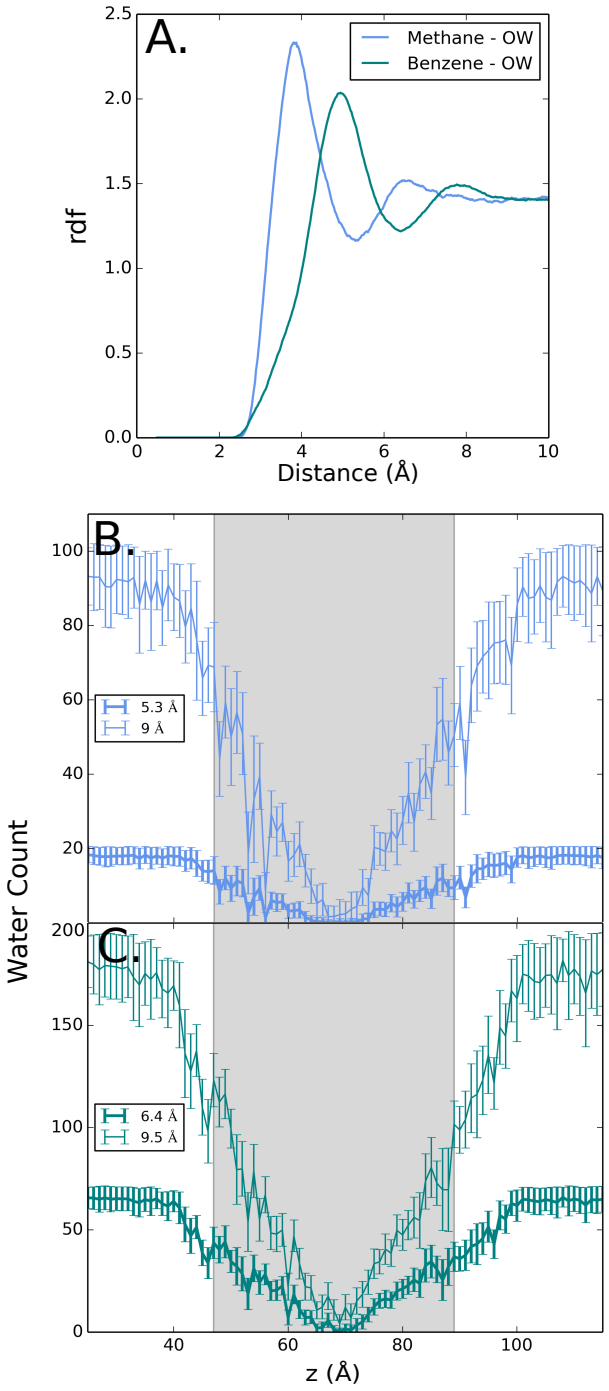


**Fig. 4.19:** Radial distribution function of water around methane and benzene and hydration shells within the STLLLTS pore. A. Rdf profile showing distance between water-oxygen to methane or benzene in a 10 ns simulation. B. and C. Water contacts shown within cut-off distance of the STLLLTS pore for B. Methane and C. Benzene. Grey box indicates protein pore z coordinates, where the center of the LLL pore is = 70 Å.

A possible reason for the "atypical" free energy profiles noted in this section could be down to the interactions with the protein and hydrophobic molecule. Porins which transport hydrophobic solutes, based on the structures and proposed mechanisms, a simple hydrophobic region is not sufficient for transport. Within FadL, diffusion of the transported fatty acid occurs from a low binding site to a high affinity binding site. From there, it is proposed that spontaneous conformational changes occur within the N terminus, resulting in a release from the high binding site. With this, conformational change is also expected in the hatch domain to open the channel and allow conduction [330, 335]. In the 14$\beta$-barrel TodX, there are similarities to the STLLLTS pore in terms of size and a continuous channel through the porin which transports toluene. However like FadL, affinity sites are needed for specificity and further inspection into the hydrophobic channel reveals polar and hydrophobic residues lining the pathway [331]. Thus, more specific and intricate pathways are needed for hydrophobic transport.

In simulations where an ion is placed and restrained within the hydrophobic region, sequential wetting of the ion occurs, allowing water into the region and providing a buffer between the ion and the pore. Within the hydrophobic restraint windows, presentation of benzene or methane within the region results in no hydration, thus keeping the molecule within the dry region. The pore radius of the hydrophobic porins is smaller than that of the STLLLTS model, thus the residues replace the void (present here) and directly interact with the hydrophobic solute. In the simulations presented here, structural changes occur within the nanopore which have not been noted in these types of simulations in this chapter (figure 4.20). From the figure, major deformation is occurring within the protein pore, as a possible compensation to size difference, and thus changing the chemical and structural relationship between the protein and molecule from the original protein design. Also noted is the change in

radius from a pore in which benzene is present (figure 4.20, B. water) in the solvent phase and within the LLL region (protein). This could explain the variation within the free energy profiles, but also suggests based on the negative free energy that this LLL motif could be a binding site for a hydrophobic molecule.

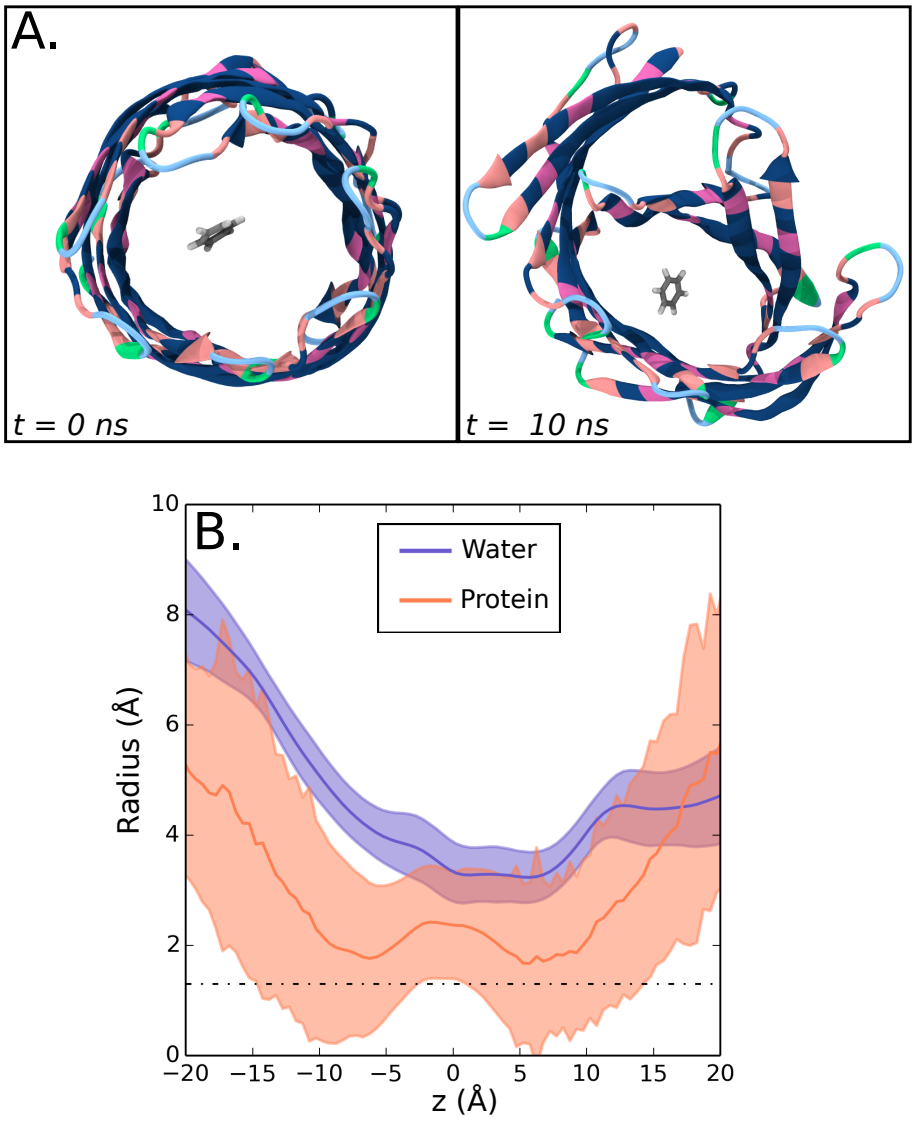


**Fig. 4.20:** Protein deformation and radius within benzene simulation windows. A. Benzene (grey, center of the image at 71 Å within the pore) and protein shown at 0 ns (start of simulation) and at 10 ns (end, right hand image). B. Radii profile of two windows mentioned in A. in which benzene is at ~30 Å (water) or in the middle of the pore (~71 Å, in the protein shown in A).

## 4.4 Conclusion

In this study, I have shown that there is a true hydrophobic barrier within the modelled STLLLTS nanopore (and also within the first generation GAVLVAG pore). Also based on the methods used, free energy estimates of translocation can be calculated, and accurately predicted for ions and water molecules going through hydrophobic regions. This therefore extends previously known studies on nanopore design and chemical behaviour as well as the energetics of hydrophobic nanopores/hydrophobic gating and their biomimicry.

In terms of free energy of biomimietic nanopores, the results do suggest that these motifs are indeed transferable and, as well as being dependent on radius, are also implemented by the height (in terms of number of rings in this case) of the hydrophobic region, leading to an idea that there may be certain 'aspect ratios' for such motifs. This can aid in the progression of possible transplantation into larger pores which may be above the 'critical' radius for such a motif.

The methods employed in this section may also be transferable to other possible proteins (be it nanopore or a channel) in which hydrophobic gating could be investigated, as a relatively quick way of establishing if such a gating form is present. With the assumption that short, small spaced windows can be used to explore the free energy will in theory not allow much protein movement, shown with the free energy calculations for the GluCl receptor [233].

Another outcome would be the use of water as a proxy for conductance of a pore. Shown in this chapter is that high water barriers to permeation do actually correspond to regions which are functionally closed to ions. In turn, allowing for the prediction of conductivity from shorter simulations without sufficient ion conduction events.

However, a downfall to this section would be the inability for accurate profiling of hydrophobic molecules through such biomimetic regions. As mentioned previously,

this could be down to the fundamental conduction pathway for hydrophobic molecules, which needs to be investigated more for accurate biomimicry. Another could be due to the lack of hydrogen atoms on the leucine and hydrophobic residues which may change and influence critical interactions. Further simulations could be used to investigate this type of interaction and system with the use of an all-atom force field to investigate such properties.

Umbrella sampling has been used in this chapter to investigate the free energy, however there are other methods available to estimate free energy of translocation through channels [336]. Umbrella sampling has been used in this case due to its previously implementation into hydrophobicity and barriers [72], and the manipulation of the time scale of simulation, which allowed for multiple "short" simulations to be used to calculate free energies. However, a newer method such as metadynamics [276, 337] could be used.

Based on the motif here, I predict (based on simulations of single file water in simple nanopores [69, 224]) that application of a sufficient voltage across a hydrophobic barrier would lead to voltage dependent wetting and functionally opening the pore. This will be investigated and simulated in the next chapter.

# Chapter 5

# Electrowetting of Biomimetic Pores

This chapter is based on following publication;
Electrowetting of a Hydrophobic Gate: Computational Electrophysiology of Voltage-Gating in a Biomimetic Nanopore. Trick et al, *in preparation.*

*"Darling I'm a nightmare dressed like a day dream"*

Taylor Swift

## 5.1 Introduction

Manipulation of hydrophobic gating within nanopore devices can be done with varying techniques such as light [338], pH [339], and pressure [205]. Most interesting in terms of utility is via voltage-gating, which was first noted in nanopores with broken symmetry [191], and more recently with the use of hydrophobic nanopores [70]. Conically shaped nanopores with pores ranging from of 4 to 30 nm in diameter at the narrower end and ~500 nm at the wider end are modified with (trimethylsilyl)diazomethane prepared in 12 $\mu$m thick polyethylene terephthalate (PET). Demonstrated in their work is that

measurements of these hydrophobic nanopores do indeed undergo a reversible wetting and dewetting transition under applied voltage (previously only pressure was applied to induced a change in conduction in such pores [205]).

Experimentally, the mechanism of reversible wetting and dewetting transition is considered to be an effect of capillary condensation [340, 341], in which above a few nm, reversible wetting and dewetting will be stalled due to a high activation barrier for evaporation within the compartment [205, 342–347]. Nanoscale water has differing properties to that of the bulk phase, allowing for different water densities near hydrophobic surfaces [342, 348]. This difference in water density enables spontaneous evaporation. Reversible filling in the absence of a field has been seen in nanopores simulated in this thesis driven by interfacial hydrogen bonding [342, 349, 350]. Filling in an electric field can be attributed to the orientation of the water dipole under such a field, and a change in water density in the hydrophobic regions of the nanopores, which results in a wetting event [69, 192, 203]. It has been noted that this is thermodynamically favourable for a range of nanopore diameters but may be only kinetically realistic in a small nanopore diameter [192].

Computationally this has been simulated by *Vaitheeswaran et al* [224], where conduction events were initiated and controlled in a CNT (in a so called (6,6) CNT with a diameter of ~10 Å) in a constant electric field. Modelled theoretical hydrophobic nanopores with two reservoirs of unequal cations have also been shown to induce wetting when the confined water undergoes strong electro-constriction [351] (which has also been noted experimentally [352]). Changes in the radius and length in this model gave qualitatively the same results; when the pore radius was larger than 5 Å, the pore would always be in a wet state [64]. For smaller hydrophobic nanopores the electric field strength that imitates water permeation is sensitive to length and pore radius, suggestive that ion channel hydrophobicity is dependent on geometry. Further MD

investigations have been conducted of wetting in cylindrical hydrophobic nanopores, with more focus on the pore radius and the electric field [203]. A theoretical hydrocarbon based nanopore, which is sufficiently wide to allow water infiltration but not to exceed the kinetic threshold for spontaneous water expulsion (therefore remaining filled) has also been simulated. Within this model, radius is varied to investigate water expulsion, and also a constant electric field is applied and overall wetting occurs. Characteristic water dipoles within the applied field and pore are noted in this model [226].

Based on the vast previous investigations it would be of interest to probe the possibility of such mechanism in the pores created in this thesis, especially the STLLLTS nanopore previously investigated to understand voltage induced wetting, and also consider other nanopores with different dimensions (be it diameter and width of hydrophobic region). Constant electric field and computational electrophysiology (CE) simulations are used to implement voltage within the hydrophobic nanopore models.

## 5.2 Methods

### 5.2.1 Models & Equilibrium Molecular Dynamics

Models simulated are formed from the same method as chapter 3. C$\alpha$ models were generated using idealized models for transmembrane $\beta$ barrels [279] and these templates were used as inputs for MODELLER 9v9 [280]. Atomistic models of designed pores were converted to a CG representation using procedures described previously with a locally modified version of the MARTINI force field [353]. CG MD simulations of 1 $\mu$s were used to position the nanopores within a bilayer, and at the end of the simulation the system was converted back to an atomistic system using CG2AT [267]. Systems were equilibrated for 1 ns. For CE simulations, this system was duplicated

and minimised for simulation.

### 5.2.2 Implementing Charge Imbalance

Charge imbalance was applied by either a constant electric field [354] or via computational electrophysiology (CE) [355].

#### Constant Electric Field

Due to the implication of the PBC and the mono-bilayer system where there is no defined compartmentalisation of systems as seen experimentally and physiologically, there is no explicit charge imbalance which would result in a potential difference across the bilayer. Therefore, the use of a constant electric field, perpendicular to the plane of the bilayer results in a potential difference. This is based on:

$$\Delta V \approx |\overrightarrow{E}| \cdot L_z \tag{5.1}$$

Where the change in potential difference is dependent on the field applied and the length of the box in simulation. This drives the ions and proteins directionally (z for the proteins in this chapter) [219, 356] and the conductions are simulated by imposing a force on all charged atoms within the system [199, 200, 357, 358].

$$\overrightarrow{F} = q_i \cdot \overrightarrow{E} \tag{5.2}$$

The force exerted on each particle depends on its charge and the strength of the applied field. This method results in a gradient which is linear of the z axis of the simulation box, therefore being an approximate of experimental conductions [221] and induce ion translocation [359]. The field itself within GROMACS is assumed as a linear field rather than a varied field based on what atoms are present in the system

thus is a basic approximation [235].

An electric change i.e. $Q_1$ is noted to produce an electric field in the space around itself and the field produced, exerts a force on any charge, $Q_2$. The strength at any point is defined at the electrical force per unit charge experienced by a test charge at point P.

$$\mathbf{E} \equiv \mathbf{F}/Q_{\mathrm{t}} \tag{5.3}$$

This equation associates a vector ($\mathbf{E}$) with each point in the system. Charge $Q_t$ may affect the surrounding charges thus E is dependent on the test charge. Rearrangement gives F = qE which in the SI units of newtons per coulomb (N $C^{-1}$) which is equivalent to volts per meter (V $m^{-1}$) which is how the field is interpreted in simulation (V $nm^{-1}$). Within this chapter this will range from 0.1 to 1.5 V $nm^{-1}$.

### Computational Electrophysiology

To simulate voltage caused by an ion asymmetry, the vacuum-buffer [359] or the double bilayer method [69, 360–362] with the implementation of an ion-swap method for longer simulations [355] can be used. All are based on direct charge imbalance from ions within the simulation system.

Used for this chapter is the a double bilayer system which has been created from a single bilayer simulation, via the duplication and the movement (within the z plane) of the initial pdb file. Formed is a system in which the central region (figure 5.1, C. region $\alpha$) is now enclosed to the rest of the system.

A charge imbalance is imposed to create region, $\alpha$, as a cathode or anode (and thus the $\beta$ as the opposite). An example from this piece of work is that is charge imbalance of 2 cations (779 in $\alpha$ , 781 in $\beta$ & 780 chloride ions in each) results in a voltage difference of 0.25 V (figure 5.2). As the system conducts and depletes an ion

for the cation or anion reservoir, this is followed by a randomly selected water molecule within the corresponding region being replaced with an ion to maintain the gradient and potential throughout simulation (the CE method) [355]. Variation in initial ion concentrations allows for variation in the potential simulated.

Within the gromacs code, and based on the theory above, the electrostatic potential ($\psi$) across a system can be computed using a double integral of charge density [235].

$$\psi(z) - \psi(-\infty) = -\int_{-\infty}^{z} dz' \int_{-\infty}^{z'} \rho(z^n) dz^n / \epsilon_0 \tag{5.4}$$

in which, $\psi$ (electrostatic potential), where the position of z = -$\infty$ is far enough from the bulk phase of the system so that the field experienced is zero. This method allows for the effective splitting into separate contributions from lipids, ions and water. Firstly in each slice (approximately 200 in a box), the sum of all charges is calculated. From there, it is integrated to give the electric field within the simulation. A second integral gives the potential.

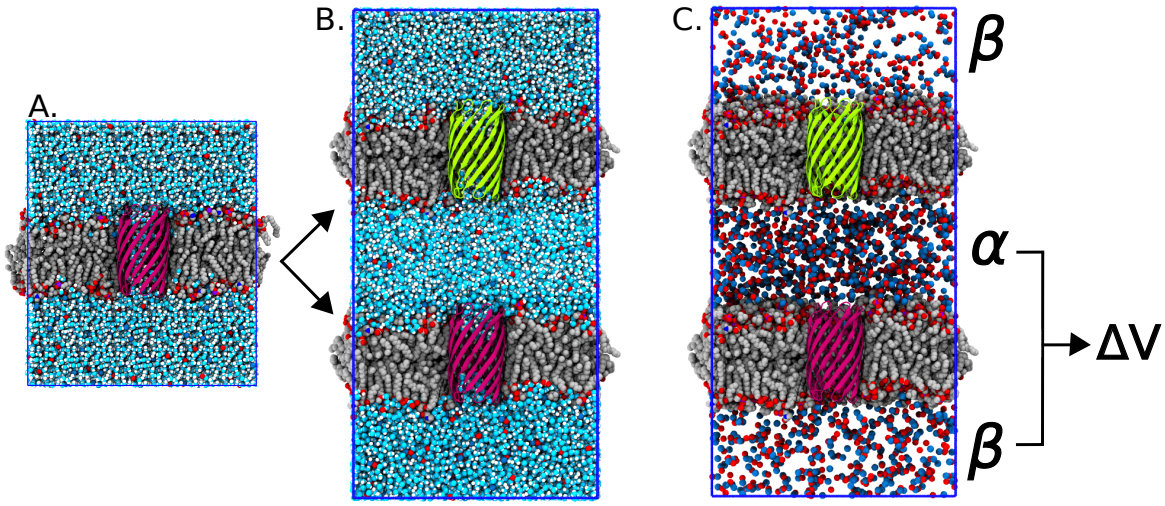


**Fig. 5.1:** Set up of double bilayer system used in the computational electrophysiology simulations. A. Standard bilayer system used within this thesis. B. System from A. is duplicated, original shown with pink protein. C. System is manipulated so that shown central region ($\alpha$) has a differing ion concentration to the $\beta$ region. Water is omitted for clarity.

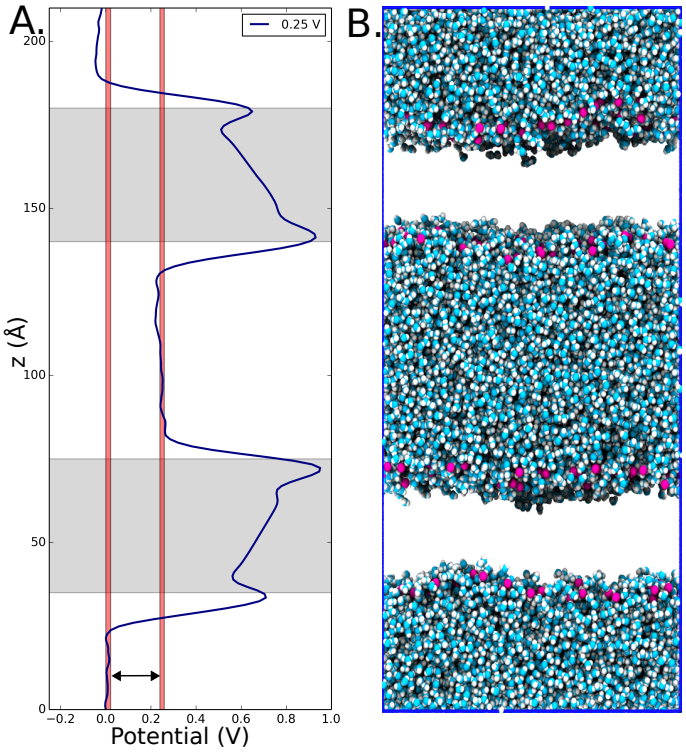


**Fig. 5.2:** Visualisation of CE voltage. A. Plot of the potential along the z axis of the system. Grey region indicates bilayer. Blue plot is the calculated potential. Red bars indicate voltage in both regions, with the difference (0 and 0.25) being the potential difference. B. Corresponding system to scale, water molecules in cyan/white and DPPC phosphate head groups in pink. Remaining lipid chains and ions omitted for clarity.

### 5.2.3 System Setup & Parameters

Atomistic simulations were performed using GROMACS version 4.6.5 [363] with the GROMOS96 43a1 forcefield [246, 247]. Long range electrostatic interactions were treated with the Particle Mesh Ewald method [240, 241] with a short range cut off of 1 nm and a Fourier spacing of 0.12 nm. The SPC model was used for water. Simulations were performed in the NPT ensemble with the temperature being maintained at 310 K with a v-rescale thermostat [256] and a coupling constant of $\tau_t = 0.1$ ps. Pressure was maintained semi-isotropically using the Parrinello-Rahman algorithm [255] at 1 bar

coupled at $\tau_p = 1$ ps. The time step for integration was 2 fs with bonds constrained using the LINCS algorithm [253]. Ion concentration is 1 M for all simulations, with ~400 lipids and ~44,000 water molecules simulated for constant electric field, and ~800 DPPC lipids and ~88,000 waters within the CE simulations. Simulations were conducted for 100 ns using constant electric field and 50 ns for CE. Analysis was conducted with GROMACS, CE implemented GROMACS, MDAnalysis [284], and locally written code. Water flux was calculated by counting the water molecules crossing through an x y area using the method described previously in chapter 3. Pore radii with an error estimate from simulation was calculated within an add-on of MDAnalysis [285]. Voltage was estimated using GROMACS code, and water count was estimated using VMD locally written code. Molecular graphic images were produced with visual molecular dynamics (VMD) [281].

## 5.3 Results & Discussion

### 5.3.1 Ascertaining Hydrophobic Ratios

Initial investigations into voltage induced wetting of hydrophobic nanopores requires protein nanopores of the correct diameter and height to allow for a voltage induced wetting event to be feasible. Based on models and designs from chapter 3, $\beta$ barrels with 16 and 18 $\beta$-strands were constructed with an increasing number of leucine rings within the central region of the protein, to test for a pore which was closed in terms of water flux (and also used as a measure of pore openness in this thesis). Previous calculation of the 14$\beta$-barrel pores indicate that 3 leucine residue rings are sufficient to omit water and cease conduction through the pore. For the 16 and 18 barrels, cumulative water fluxes and pore radii were evaluated for these models over the course of an equilibrium simulation (100 ns) to determine if any of the models behaved in a

similar manner to that of the 14-3L pore (figure 5.3) with fluxes in table 5.1.

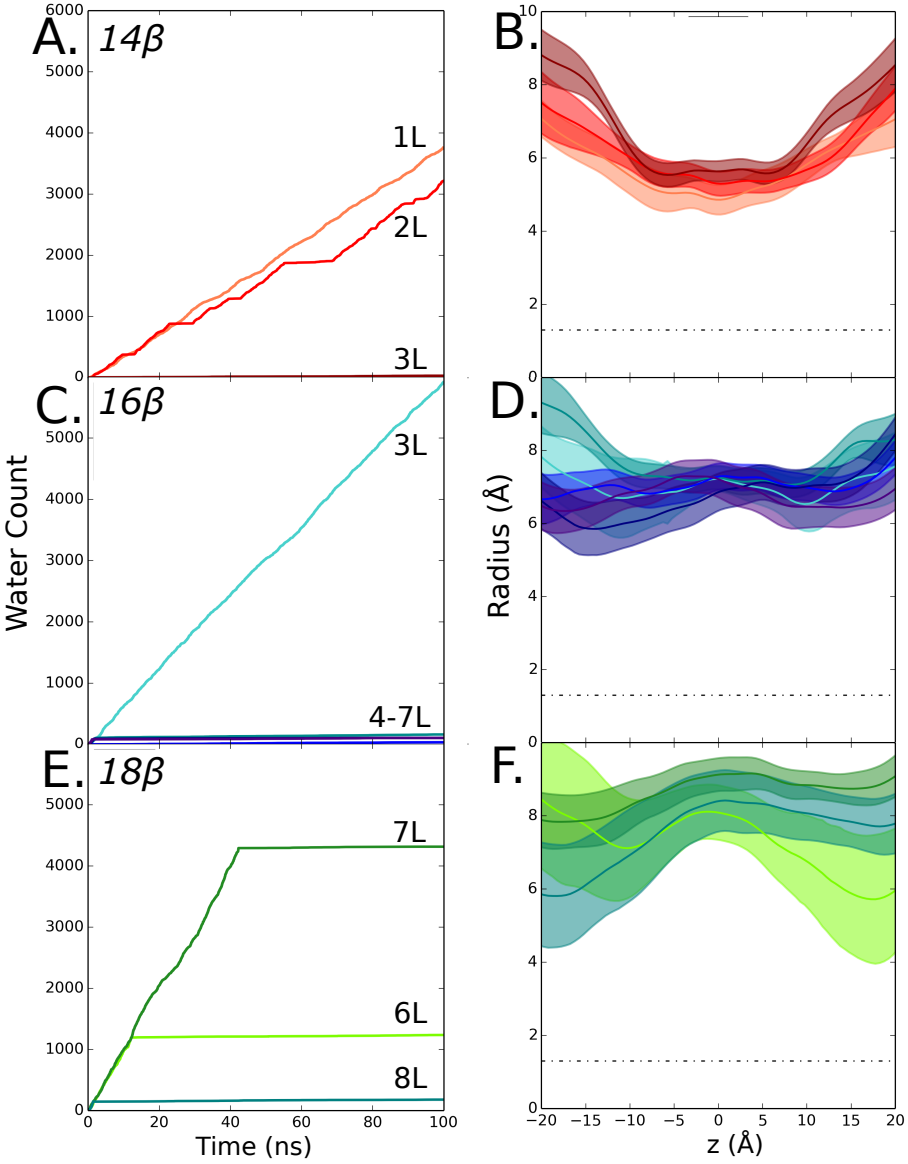


**Fig. 5.3:** Water flux and radii profiles for 14, 16 & 18 x-L $\beta$ pores. A,C & E. Water flux for 14, (A.), 16 (B.), & 18 (C.) $\beta$ barrels. Within each, the number of central leucine residue rings is varied from 1 ring (1L) up to 3 rings (3L). Only upward flux is shown for clarity. B, D & F. Radius profiles for corresponding pores in A, C & E. Colours are consistent with flux profiles. Dashed line indicates radius of water (1.9 Å). A & B results are repeated from previous chapters for comparison.

| Pore model | Flux ($ns^{-1}$) |
|---|---|
| 16-3L | 58.9 |
| 16-4L | 1.7 |
| 16-5L | 0.3 |
| 16-6L | 1.3 |
| 16-7L | 1.1 |
| 18-6L | 12.2 |
| 18-7L | 43.2 |
| 18-8L | 1.6 |

**Table 5.1:** Fluxes through 16$\beta$ & 18$\beta$ barrel hybrid pores under equilibrium simulation conditions. Pores with the lowest flux are considered for further simulation, larger fluxes calculated for 18$\beta$ 6 & 7 L due to longer water expulsion from the pore.

The outcome of the equilibrium simulations in comparison to the 14$\beta$ pore (A & B in figure 5.3), indicate that within the wider pores with the varied height-radius ratio (aspect ratio), there is a "leucine cut-off" in which a hydrophobic plug and no water flux is present. Due to lack of free energy calculations on these pores, it is unknown if they are indeed true hydrophobic barriers or a limitation of simulation timescale. However it is of interest to look at these models for the purpose of understanding how voltage can overcome hydrophobicity. Functionally, all pores have a radius that is sufficient to allow water transport but what can be observed from the fluxes in table 5.1, water flux does vary in simulation with minimal fluxes for the 16-5L model & 18-8L model noted. The 14-3L, 16-5L and 18-8L pores are investigated for voltage induced breaking of the hydrophobic gate via simulation. Images of all three protein pores are shown (figure 5.4).

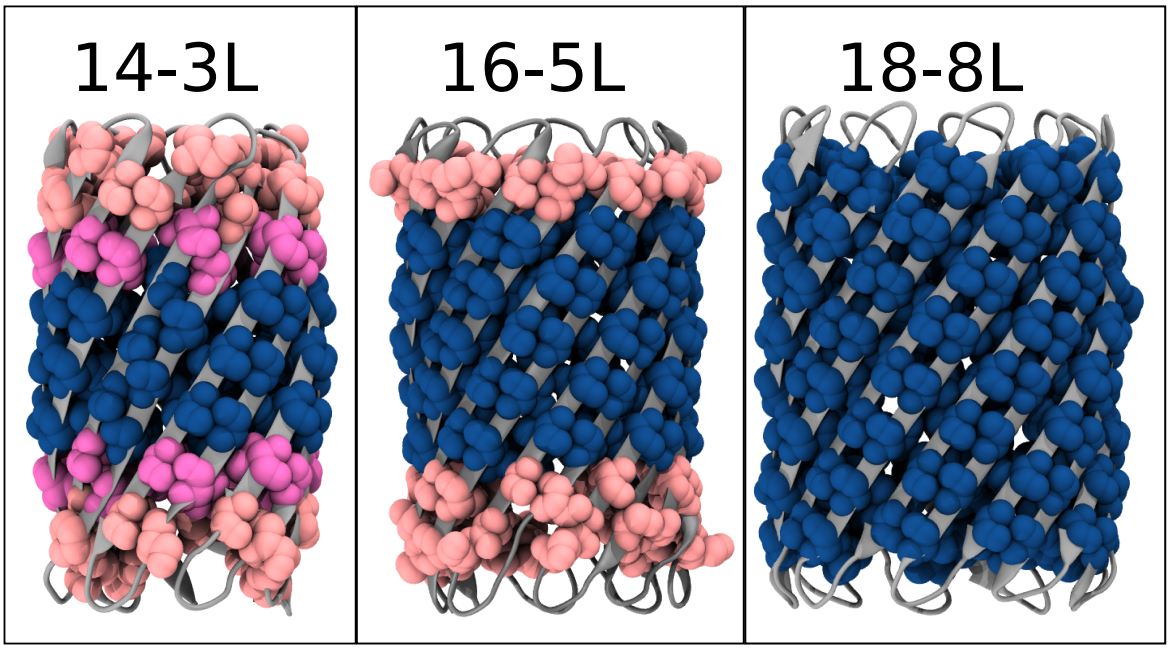


**Fig. 5.4:** Model pores simulated under voltage, using a constant electric field and CE. From investigations under equilibrium, the three pores are shown (backbone in cartoon. Inward, lumen facing residues only shown, in VdW representation) which are simulated. Pores are denoted by size (14, 16 or 18) and the number of leucine 'rings' (3, 5 or 8) in this case.

### 5.3.2 14$\beta$ Pore

#### Constant Electric Field Simulations

Voltage induced wetting of the hydrophobic hybrid 14-3L $\beta$ barrel pore was conducted with both voltage simulation methods. A constant electric field was used initially to test the system with a known computational method, which has been previously used to investigate hydrophobic barriers [203, 225, 226, 364]. Two states are detected in the nanopore with application of a lower, and higher electric field (figure 5.5).

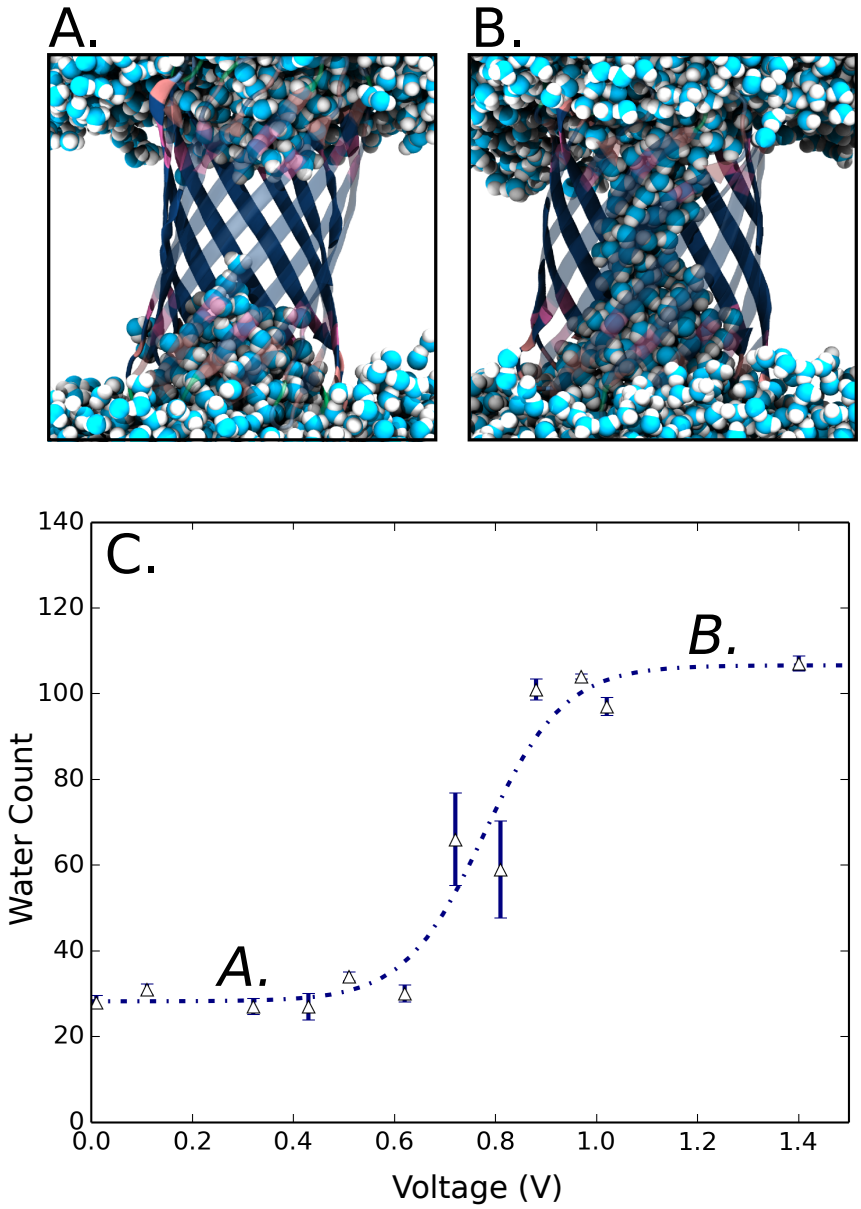


**Fig. 5.5:** Constant electric field filling of 14-3L$\beta$ pore. A. Dry, closed (no water within leucine region) pore. B. Wet, open pore. Water shown as VdW spheres and protein in cartoon with residues coloured to hydrophobic colouring scheme. Lipids and ions omitted. States are defined visually, but also by the number of waters within the pore. C. Plot of constant electric field voltage against the number of waters within the pore. Voltage calculated from gromacs [363], by measuring the voltage difference between the bilayer head groups. Water count is that of the number of waters within the pore volume, within the leucine region. Each point represents a separate simulation of differing constant electric field inputs. *A & B* indicates regions of the plot which correspond to A. and B. from the dry to wet transition. Curve fitted using a sigmoid function within matplotlib [286], $V_{½}$ ~0.77. Error is calculated from standard error of the mean from water count within the pore.

Water filling is seen within the nanopore upon application of higher constant electric fields (figure 5.5, B. and C.), therefore creating two discrete states, interpreted as the voltage induced break of the hydrophobic barrier. Wetting is induced when a voltage of $V_{½}$ ~0.8 V is applied across the bilayer. Higher errors can be noted for transient breaks (between 0.7 & 0.85 V) where the pore does not become water conducting at the start of the simulation unlike the higher voltages, lower error values which break within 2 ns.

#### 5.3.2.1 Computational Electrophysiology

Within the set up of this method, an arbitrary number of ions (cation or anions), are "swapped" from the $\alpha$ to the $\beta$ regions (figure 5.1) to create the voltage. Initially, an ion swap of 18 cations (1187 and 1205 within the respective regions) was simulated to implement a voltage. This created a voltage of 1.2 V through the simulation box (representation of a lower measured voltage in figure 5.2). Under this potential, conduction breaks were noted in the simulation from dry non-conductive, to water and ion conducting pores, akin to the higher voltage breaks seen with the constant electric field.

#### 5.3.2.2 Water

A more detailed inspection is required into the conduction breaking event of the pores under 1.2 V, specifically the initiation of the breakage event. Within the nanopore simulations conducted under applied field (images not shown) and within this CE breakage, the barrier is initially broken by water entry into the hydrophobic region of the pore (figure 5.6) rather than by a Coulombic ion event as seen in newer simulations of a potassium channel [365]. Previously hypothesised from crystal structures, experiments, and simulations [366–369] is the conduction event of water-ion-water within

the selectivity filter of the $K^+$ channel under a constant electric field. However, in the newer, CE method, a direct Coulomb knock-on is obtained in which no water is present in the ion conduction event within the selectivity filter. It would be of interest thus to observe if changes occur in water conduction within nanopores and hydrophobic pores of these models with comparison to simulations of hydrophobic nanopore models under a constant electric field [203]. The water and ion flow through the pores can be surveyed in more detail in figure 5.7. Within these pores, water breaks the hydrophobic barrier first, and is then followed by multiple ion conduction events.

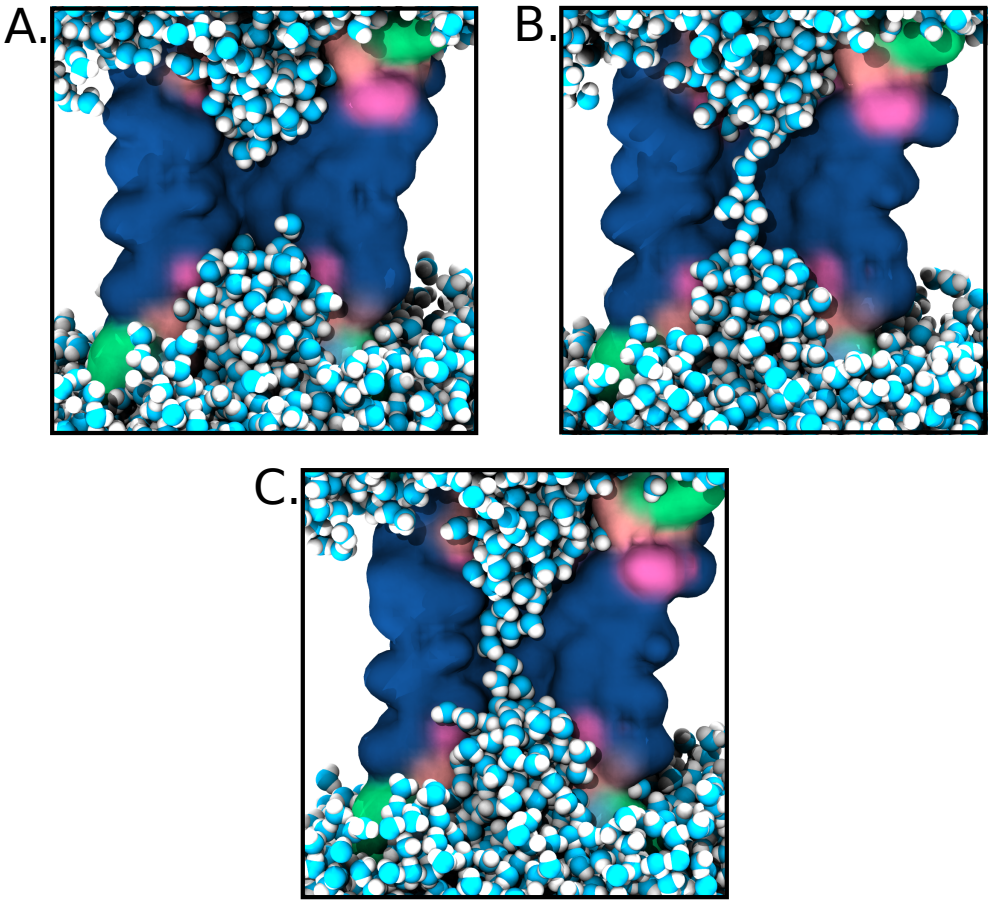


**Fig. 5.6:** Water entry in the 14-3L$\beta$ at 1.2 V. Ions and lipid omitted for clarity. Protein shown in a surface representation. A. Pore at 0.3 ns. B. First water chain transverses leucine barrier region forming a water wire (blue, middle of the pore) at 0.32 ns. C. Ordered and continued filling of the pore at 0.33 ns.

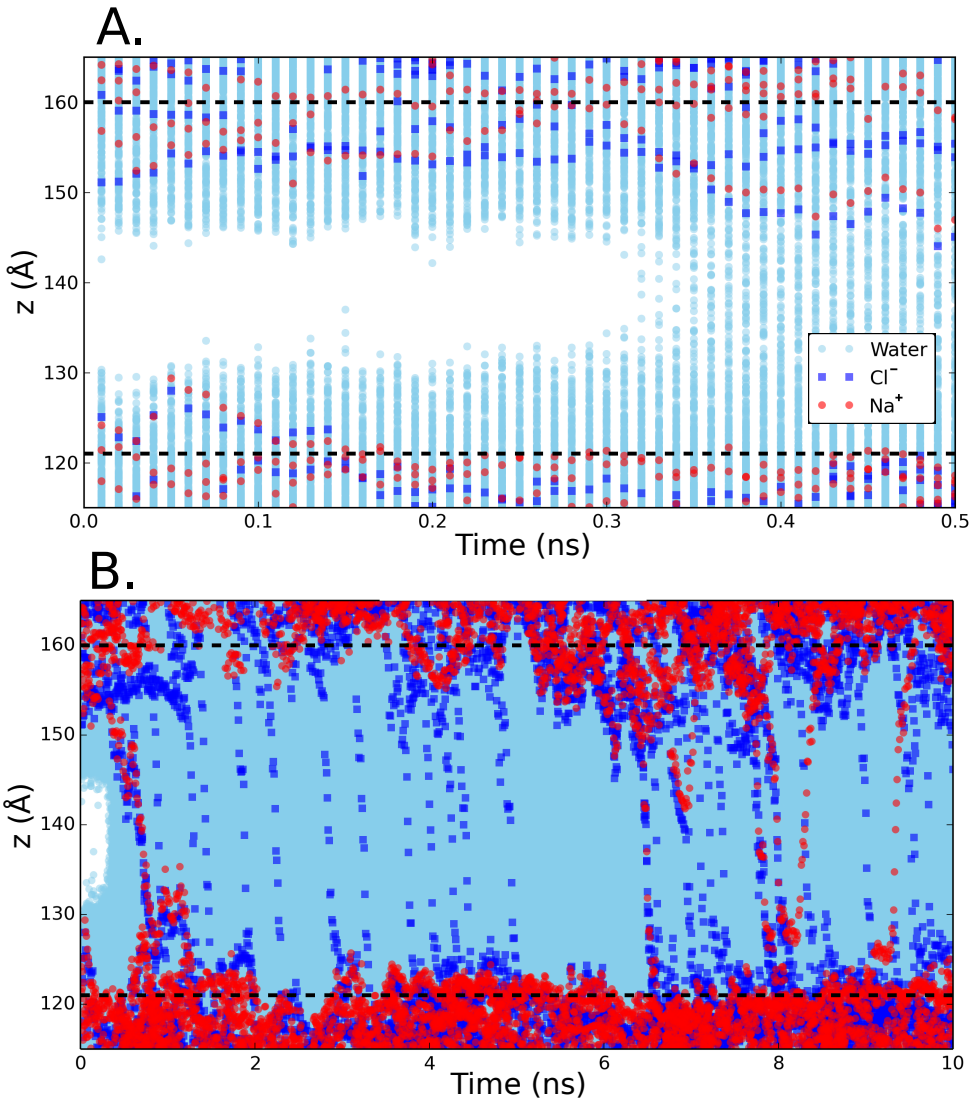


**Fig. 5.7:** Water filling of 14-3L$\beta$ pore at 1.2 V. A. Plot of the z position of a particle (water or ion species) over time. Dashed lines indicate average z position of the phosphate P8 atom to represent the lipid boundaries. White region until 0.3 ns indicates unfilled leucine region shown in figure 5.6, A. B. Extension of A up to 10 ns. Colours are consistent with A.

Water entry (with and without a voltage) into the hydrophobic regions of theoretical nanopores and CNT's has been studied extensively, however most studies are based on the older, constant field method and not on a potential difference created from ion asymmetry. Therefore, it would be of interest to verify is the same mechanism

is also present in these protein pores. Previous simulations of water and pores focus upon theoretical hydrophobic pores [61, 64] and CNT's [60, 319] which both exhibit radius/length dependent filling of the pore, and like this pore also exhibit water entry, before ion entry into the hydrophobic region.

Water densities and ordering (figure 5.8) within the ion-induced CE voltage are in agreement with other electro-simulation pore studies [203, 217, 370]. Within the no-voltage conducing pores previously simulated in this thesis, no orientation is noted within the water dipole moment, however orientation is seen within conduction events under voltage. Orientated water is noted in OmpF and OmpC porins [371] and within the aquaporin [328, 372] which has been studied in more detail [373–375]. The highly charged constriction of OmpF and the half helical dipoles with the Aqp1 (aquaporin) structure are assumed to influence the water structure within the pore. Hence in this simulation, the simulated voltage is influencing water in a similar same manner. Furthermore, there is also good agreement of the water and phosphate densities through the system as seen in other studies [376].

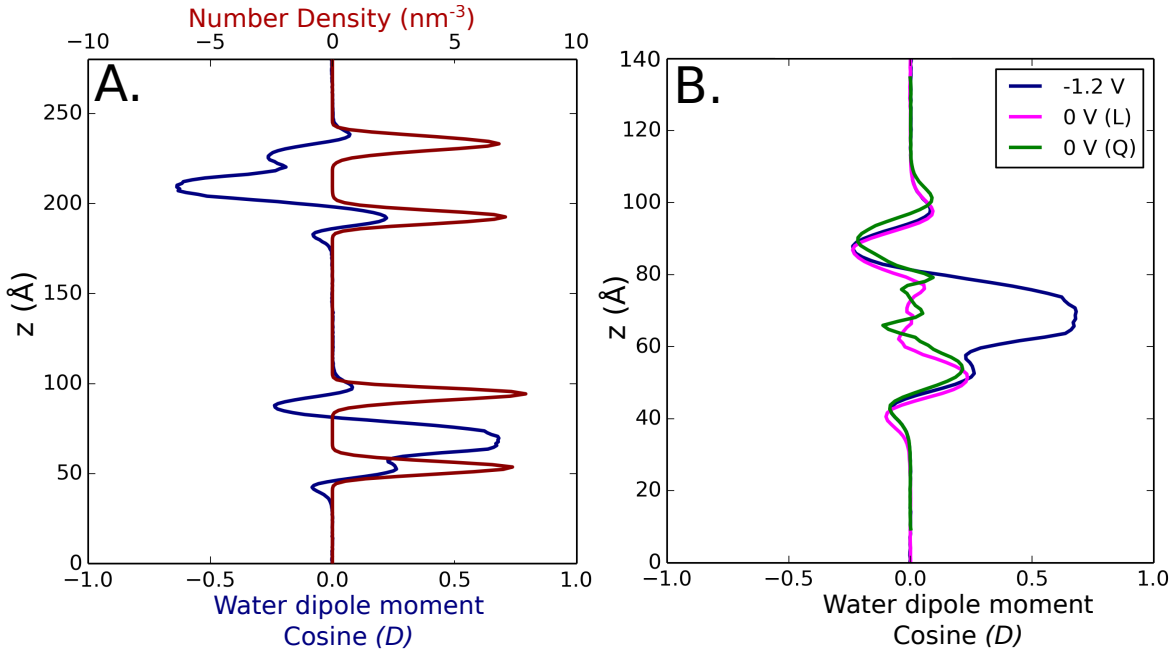


**Fig. 5.8:** Water ordering within 14-3L$\beta$ pore at 1.2 V. A. Double x-axis plot of water order (cosine of water dipole moment, navy) and phosphate density (dark red) through the double bilayer system B. Cosine of the water dipole moment through a single bilayer of three systems, the CE 1.2 V (navy), no-voltage equilibrium system of conducting STNLNTS pore (L, pink), and conducting STNQNTS pore (Q, green) from chapter 3.

## Reversibility of Electrowetting

A decrease in voltage below the threshold value of opening has been shown to expel water from hydrophobic solid state nanopores [70], computational models [226], and closed electropores [217, 377, 378]. To validate this hypothesis with this system, the CE element of the simulation was removed. After an ion permeation even, an ion swap would not occur and thus deplete the voltage (previously used method to simulate voltage [351, 377]). After a number of ion conduction events, there is a decrease in voltage and the system should return to an equilibrium. This was conducted for 14$\beta$ pore starting at 1.2 V (figure 5.9).

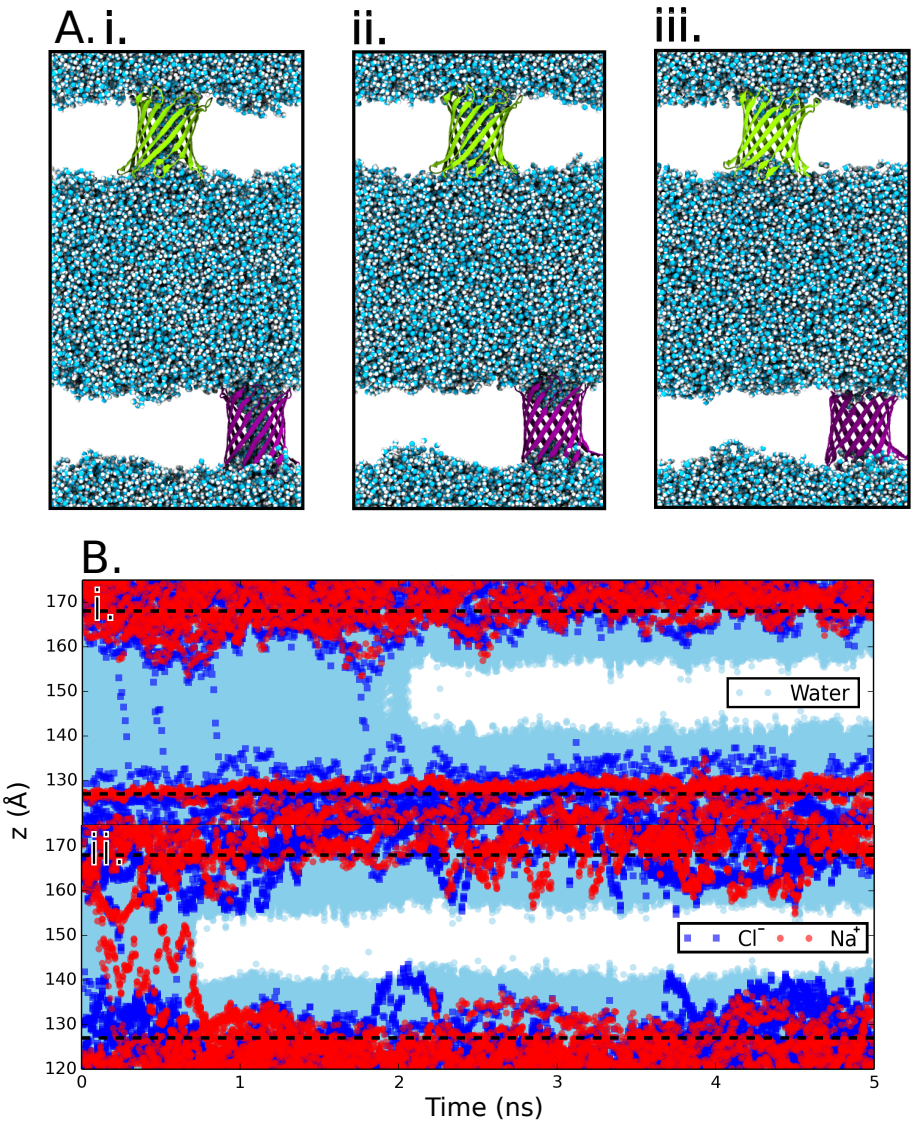


**Fig. 5.9:** CE system with depleted voltage from 1.2 V. A. Cartoon and VdW representation of the first 5 ns of simulation. Ions and lipids omitted for clarity. i. System at 0 ns in which both pores are saturated with water. ii. 1 ns into simulation in which bottom, purple pore is no longer water filled. iii. 3 ns, top yellow pore (as well as bottom pore) are both no longer filled. B. Graphical representation of drying. Top plot (i) corresponds to the yellow, top pore and (ii) to the purple. Each point represents the z position of either water, chloride or sodium ion within the indicated z plane. Black dashes indicate average DPPC phosphate position.

Within this system, a drying transition occurs for both pores within 2.5 ns of the simulation as the voltage decreases. For the remainder of the simulation they remain in a dry state (data not shown, simulation 50 ns in length). Ion conduction

events occur in the direction of the chloride ions migrating to the anode region and *vice versa*. Thus, in agreement with other hydrophobic pores and electroporation studies in which without voltage, water is expelled [70, 370]. Dewetting of nanopores is thermodynamically favourable but is only predicted to be feasible kinetically in nanopores with a diameters of several nanometers [50, 60, 379], which this pore falls into. It has been noted for solid state pores with a diameter greater than 20 nm that there is no expulsion of water after water-input stimulus (be it pressure, or field) with surface hydrophobicity restored. These pores are thought to be kinetically stalled due to a high activation barrier for dewetting [192, 205, 342–344, 346].

## Range of Voltages

With the establishment that this method is viable for simulation of hydrophobic gating within the 14-3L pore, simulations were conducted with varying voltages, akin to the constant electric field simulations. As anticipated, there is a similar trend to that of the constant electric field in the transition from a dry pore to a wet pore creating two differing pore states (figure 5.10). The voltage required for a transition between the dry and wet pore states is higher using this method, as opposed to the constant electric field method, with the transition voltage of $V_{½}$ ~1 V. Based on the difference of the two methods, this discrepancy is not significant as transition voltages to experimental values are firstly highly ranged and also a factor out, which are to be discussed further on.

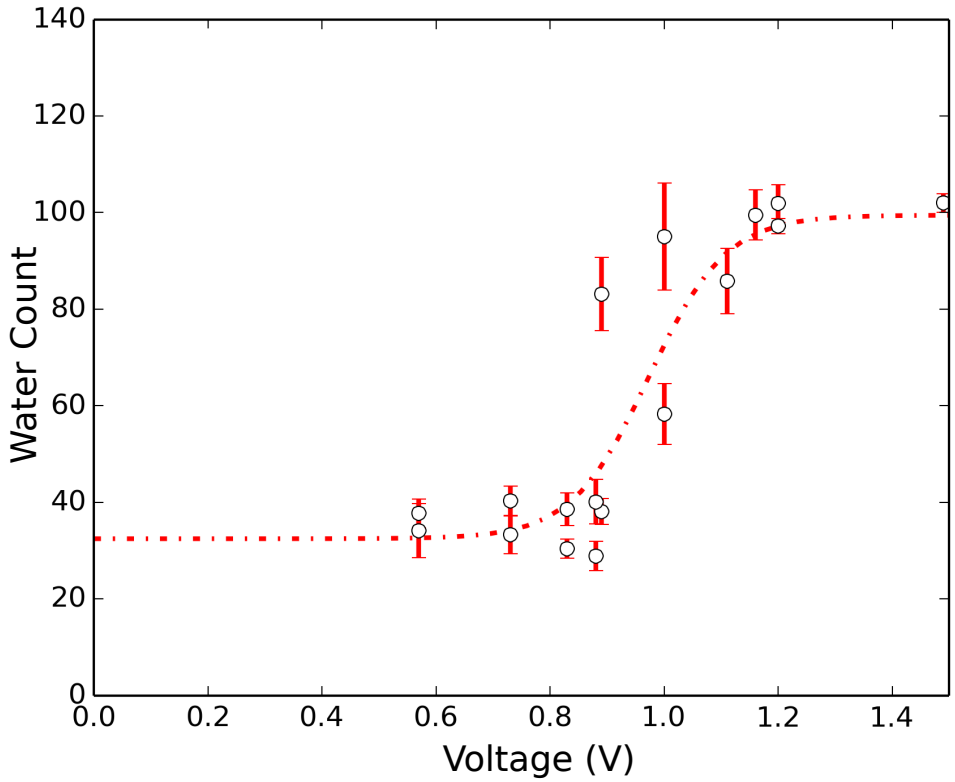


**Fig. 5.10:** CE simulations of the 14-3L $\beta$ pore at multiple voltages. Plot of the voltage (calculated within gromacs, [363]) with the water count. As with figure 5.5, states are defined by number of waters within the leucine region of the pore, with the dry pores being at the low voltages and wet at the high voltages. Curve fitted using a sigmoid function within matplotlib [286], $V_{½}$ ~0.97. Error is calculated from standard error of the mean from water count within the pore. Multiple points at each voltage position indicate conductive values for each of the pores (2 pores per simulation). 1 dot indicates only one stable conductive pore in simulation.

From the ion conduction events through the pores (figure 5.11), the current and conductance is calculated for the open pores (table 5.2). The experimentally calculated conductance of $\alpha$-HL is 720 pS [380], which is within range of the calculated values and relates to the size of the pore. However, variance in the protein structure under high voltages and the small time scale used could present an inaccurate estimate. Related conductance can be compared with the OmpF porin with a conductance of 800 pS,

and PhoE with a conductance of 600 pS [293]. In a model nanopore of 16$\beta$ based on its size, conductance is predicted to be 480 pS [279]. All are comparable and reasonable values to this non-biological pore.

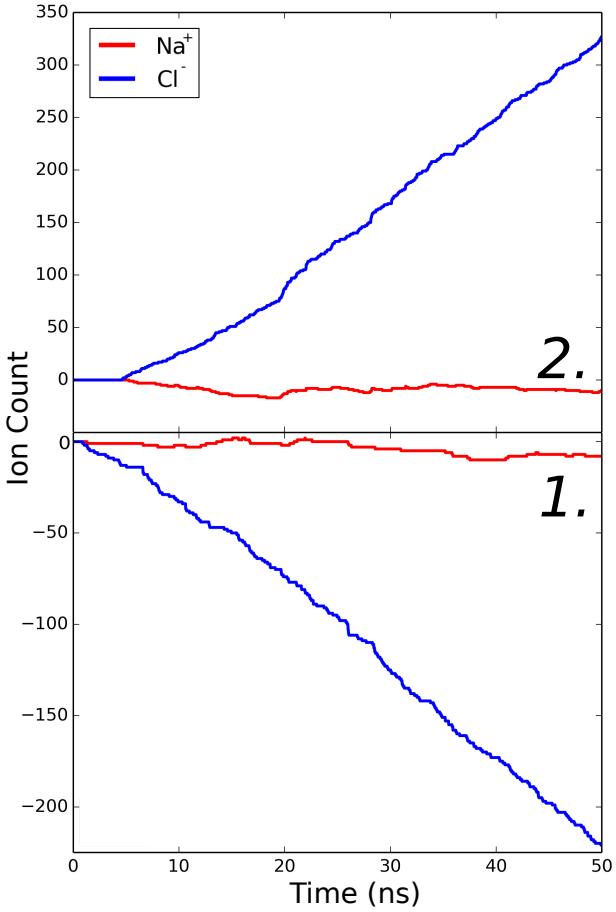


**Fig. 5.11:** Ion conductions through the 14-3L pores at 1.2 V. Shown are the difference in ion fluxes (up flux minus down flux) for both $Na^+$ and $Cl^-$ through both of the conducting pores. Chloride selectivity shall be discussed later on.

| Voltage (V) | Current (pA) | Conductance (pS) |
|---|---|---|
| 1.00 | 610 | 610 |
| 1.00 | 200 | 200 |
| 1.11 | 250 | 230 |
| 1.16 | 850 | 730 |
| 1.20 | 580 | 480 |
| 1.20 | 800 | 670 |
| 1.49 | 440 | 300 |

**Table 5.2:** Current and conductances of 14-3L$\beta$ pore under varying CE voltage.

## Lipid Stability

The effect of voltage on membranes has been looked at widely experimentally and computationally using the constant electric field [354, 376, 381, 382] and basic asymmetric ion concentrations [370] with high fields known to cause destabilisation and electroporation [383–385].

To assess stability of the lipid membrane, densities and bilayer thicknesses are assessed (figure 5.12). The data suggests that under higher voltages (1.49 V is the maximum simulated), induced via the CE method, the bilayer is still stable in terms of density, however is showing characteristic membrane thinning. This has been seen within droplet interface bilayers (DIB) where an applied potential difference ($\pm$ 100 mV) caused thinning of 0.44 Å within a DPhPC/hexadecane DIB [386] and is also seen in simulation [378]. With longer simulations at higher voltages, electropores may occur.

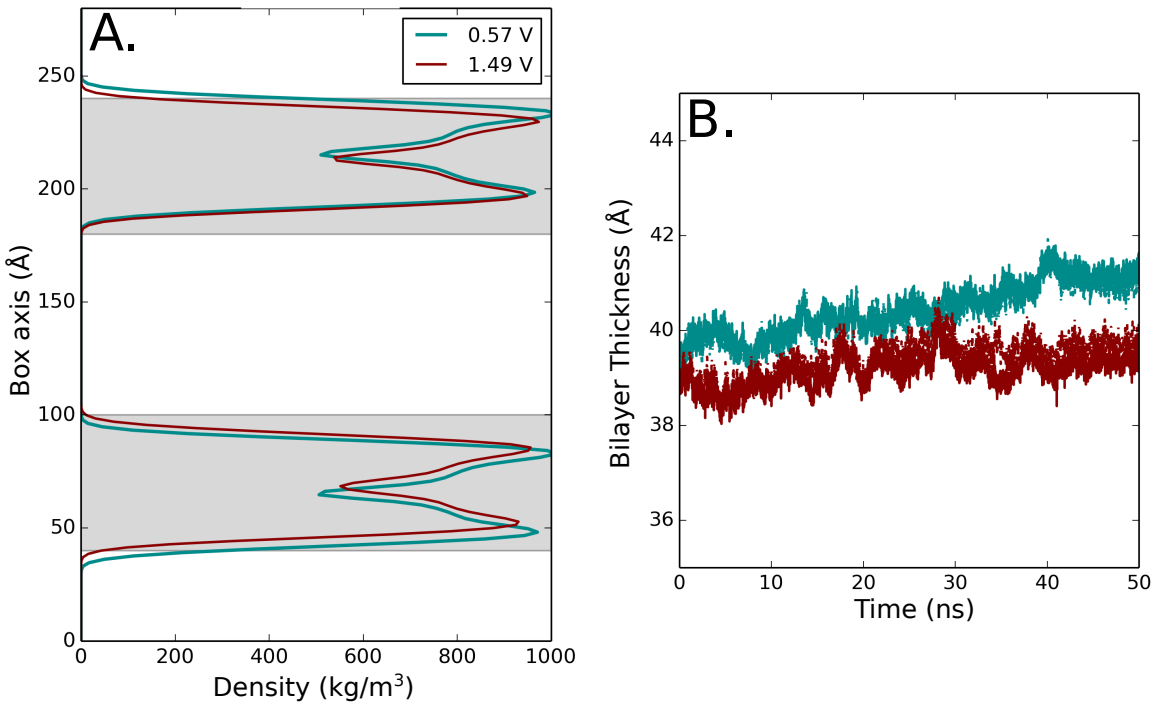


**Fig. 5.12:** Lipid density and thickness of CE 14-3L$\beta$ systems. A. DPPC density through the simulation system at two differing voltages. Shaded grey region represents bilayer region of the box. B. Bilayer thickness of both leaflets. Colours correspond to A. Dashed indicates lower leaflet, calculated by plotting average phosphate distance difference through simulation. Difference in thickness between the two bilayers at the end of simulation is ~2 Å.

## Protein Stability

To determine the stability of the biomimetic pores under the higher range of voltages (previously simulation only goes up to 0.3 V [355] for PorB and 0.2 V nm$^{-1}$ for gramicidin A [220], which in simulation, both were considered stable) the structure in terms of radius is used as a measure. In figure 5.10, it can be noted that as the voltage increases, the number of functional pores (white dots within the figure) decreases from two to one in some of the cases. In simulations at lower voltages, both pores remain in a functional state (open) however with an increase in voltage, pore closure is observed (figure 5.13). Complete pore collapse is not seen, however a change in the

lumen constriction results in a smaller pore and hence a decrease in water flux. This regulation of flux is noted as a possible form of gating in the VDAC anion pore [387].

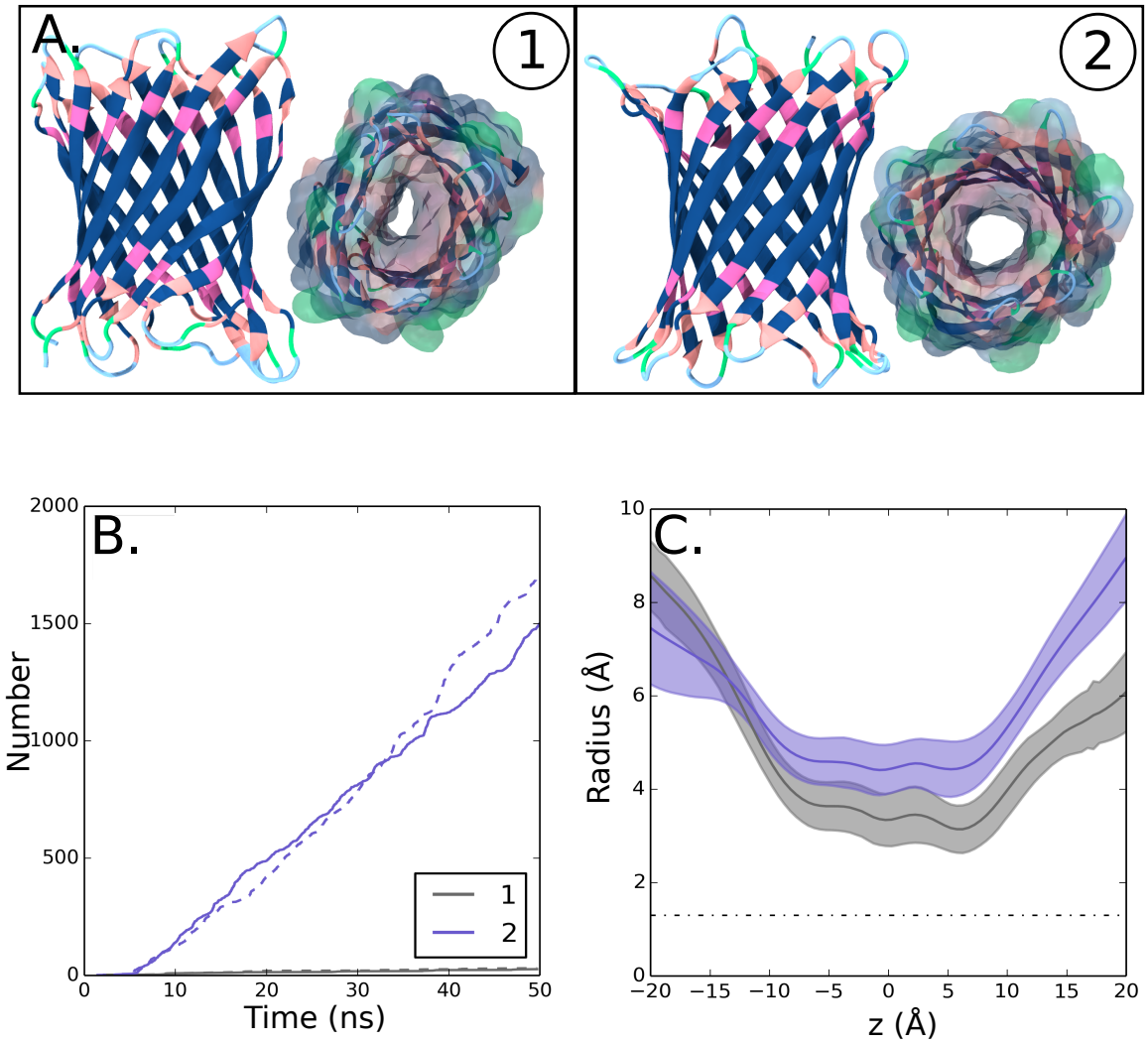


**Fig. 5.13:** Radius and flux under voltage of the 14-3L pore. A. Cartoon representation and surface of both 14-3L proteins (1 and 2) in the double bilayer CE system at 1.1 V. B. Water flux through pores 1 and 2 mentioned in A. Number corresponds to the protein. C. Radius of proteins 1 and 2. Dashed lined indicates radius of a water molecule.

Following from the electric field simulations and the utility of the CE method to control voltage, the CE method will now be used as the simulation technique to evaluate the possible wetting and dewetting events of other pores (figure 5.4, 16-5L

and 18-8L$\beta$).

### 5.3.3 16 & 18$\beta$ Pore

#### Water and Ion Conduction

As simulated under equilibrium conditions earlier in this chapter, both the 16-5L and 18-8L pores have the ability to expel water in simulation (100 ns). Thus, akin to the 14$\beta$ pores, they are simulated under the CE methodology to investigate whether they indeed undergo reversible wetting and dewetting. This is conducted in the same manner as the 14$\beta$ model with water count in the pore accounting for the state of the pore in varying voltages (figure 5.14).

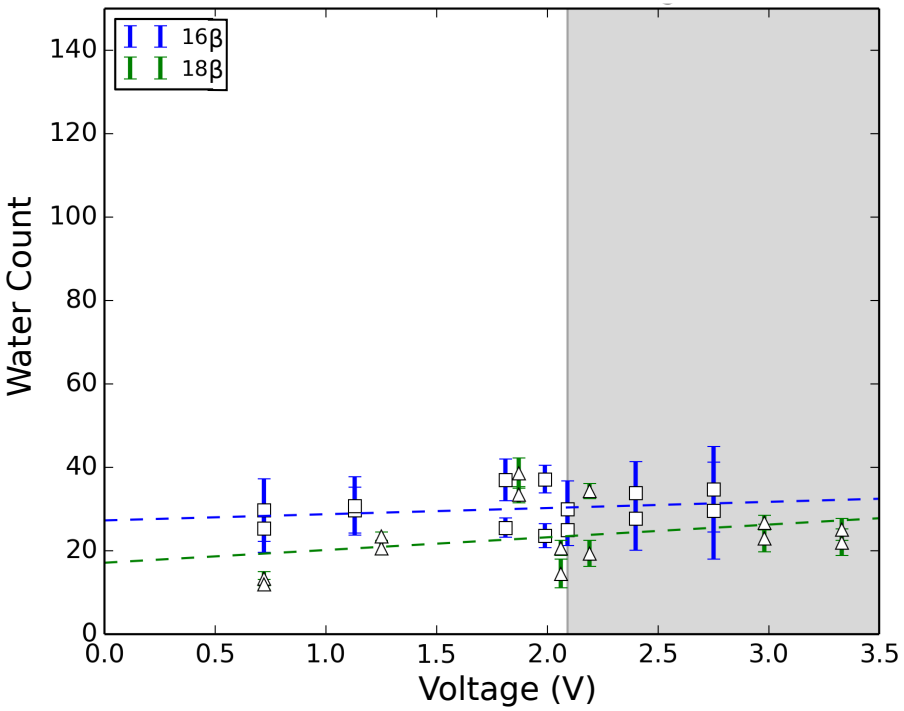


**Fig. 5.14:** CE simulations of the 16-5L and 18-8L$\beta$ pores at multiple voltages. Plot of the voltage (calculated within gromacs, [363]) with the water count (16 in squares, 18 in triangles). As with figure 5.5, states are defined by number of waters within the leucine region of the pore, with the dry pores being at the low voltages and wet at the high. Line fitted using matplotlib [286]. Grey region indicates voltages that resulted in pore formation within the DPPC bilayer. Error is calculated from standard error of the mean from water count within the pore. Multiple points at each voltage position indicate conductive values for each of the pores (2 pores per simulation).

Unlike the smaller, 14-3L $\beta$ pore, only one dry state is present under varying voltages for both sized models. Additional higher voltages are used to test whether this could be the limiting aspect. Resultant from the high voltages used (indicated as grey region in figure 5.14) is the electroporation of the bilayer and no conduction is observed through the respective pores. This has been seen in simulations of Gramcidin A in DMPC [220], in which electropores were formed with and without the protein at a field strength of 0.35 V $nm^{-1}$ (equivalent to ~1.4 V across the DMPC, thickness of

~40 Å [388]).

## Protein and Lipid Stability

To determine the stability of these pores under these (even) higher voltages, the radius and RMSD is considered. From figure 5.15, in contrast to the conducting 14-3L $\beta$ pore, the protein deformation and stability are more pronounced in both these larger pores. Deformation is apparent in the strand positioning across the pore lumen and also an increasing RMSD for both ranges of voltage. This could be due to the field strength or the 'high' hydrophobicity of the protein pore, intrinsically acting to destabilise the barrel. The apparent instability could be accountable for the lack of a break and hence a conduction event. However noted before, both pores are of a radius which is conducting, even with the protein destabilisation.

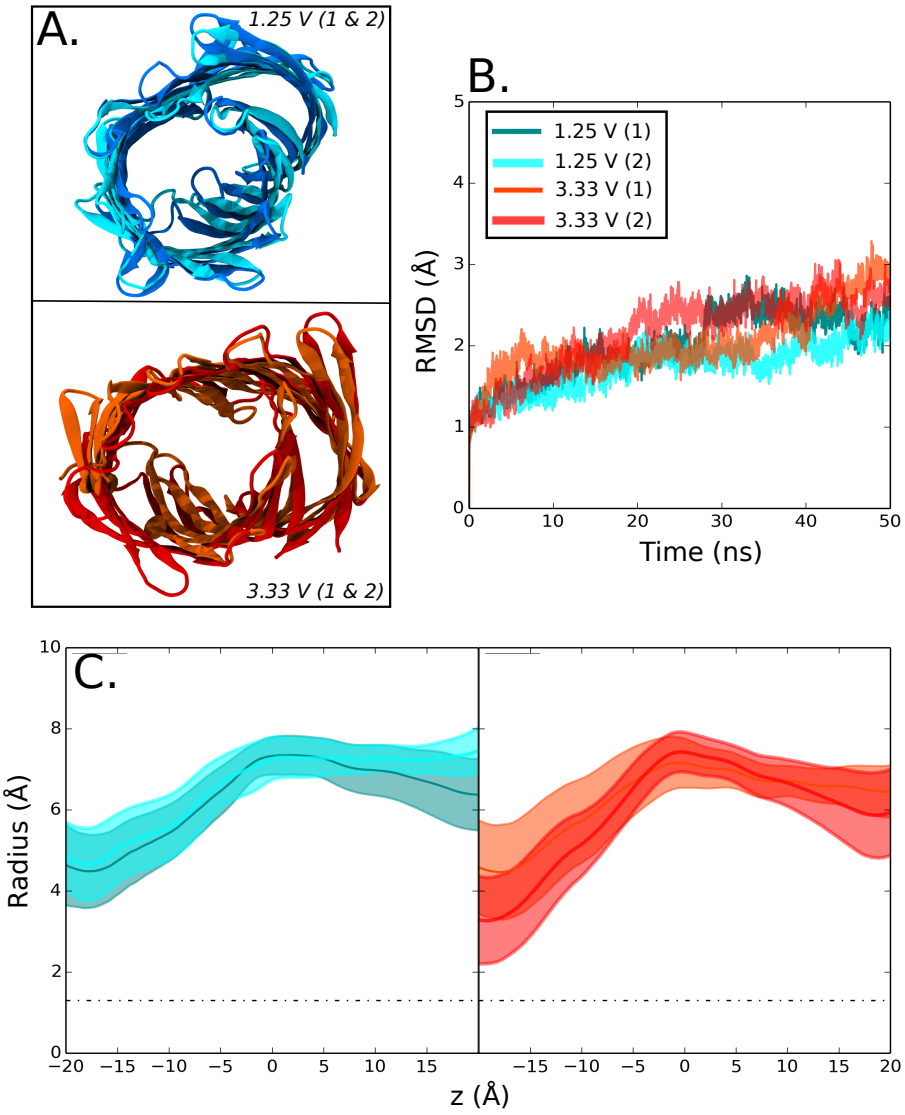


**Fig. 5.15:** Stability of 18-8L$\beta$ pores under CE voltage. A. Overlay of cartoon of both bilayer pores in simulations under 1.25 V and 3.33 V. B. RMSD of pores in figure A with voltages and number indicating the two pores within a simulation. C. Radius of pores. Colours correspond to figures A and B.

The increased voltages used to try to create a wetting transition in these pores can be viewed also in terms of membrane thickness (figure 5.16). The bilayer thickness is shown to decrease with a higher voltage, resulting in a thinner bilayer as seen before with the conducting 14$\beta$ pore, with a similar change in thickness noted between the "low" and "high" voltage bilayers, which also occurs within these simulated models.

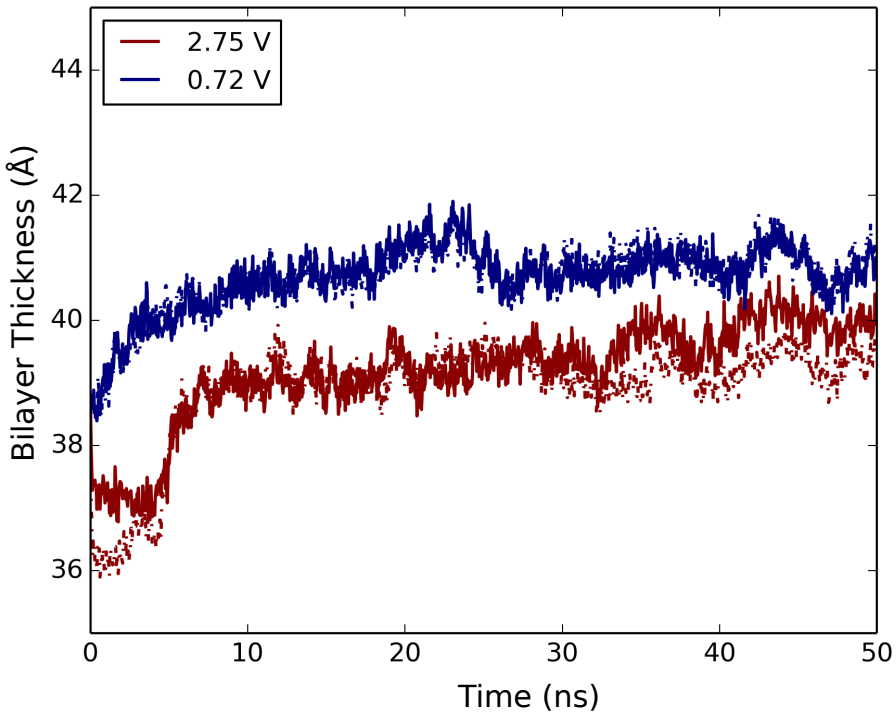


**Fig. 5.16:** DPPC Thickness under CE voltage for 16-5L$\beta$ pore. Bilayer thickness of both leaflets, dashed indicates lower membrane within simulation box. Calculated from the average phosphate P8 distances through simulation. Difference in thickness between the two bilayers of ~2 Å.

As previously demonstrated, higher voltages induce electroporation events within the bilayer. A more detailed view of this is to look at bilayer deformation in relation to the densities of the protein and the bilayer (figure 5.17).

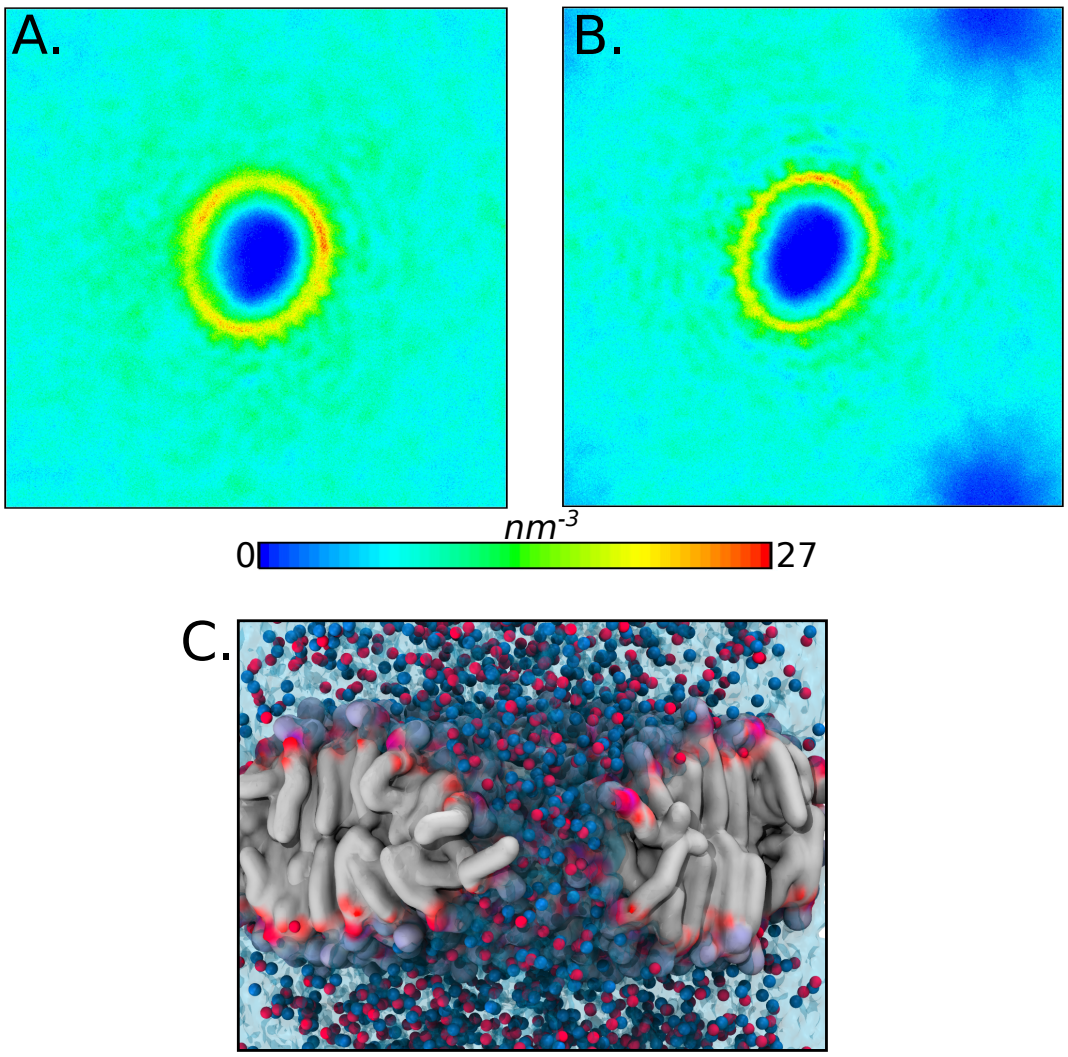


**Fig. 5.17:** Lipid and 16-5L$\beta$ pore density at high voltage (2.5 V). A & B. Density is of the membrane and of the protein (yellow circle) looking down the z coordinate at 0 ns (A.) and 50 ns (B.). Electropore formation is towards the top right and bottom right regions of B. C. Representation of electroporation of the bilayer. Ions are shown as blue and red spheres ($Cl^-$ & $Na^+$), water as transparent cyan and DPPC in grey surface.

Viewed from the density and pore structure is that of a characteristic electropore forming in the bilayer. Comparable to this are MD and electric field simulations on the water conduction pathway through gramicidin A in a DMPC bilayer. At high field strengths, there was the formation of electropores both near and far to that of the protein [220]. However, the protein is shown to have stabilised the membrane close to

it, up to distances of 20 to 30 Å from it. This could also be a form of stabilisation in this pore, explaining why the electropore forms at the furthest distance to the protein at the PBC.

Extensive simulation studies have been conducted showing pore formation within constant electric fields and with the application of mechanical stress in phospholipid bilayers [389] of which, the molecular basis is described in much detail [382, 390]. It is suggested from many a simulation, pore formation is driven by the electric field induced rearrangements and realignments of the water dipoles and charges at the membrane-water interface be it their dipoles at the water-liquid/water-vapour interface into an more energetically favourable configuration [223, 370]. The most likely candidate for the initiation of pore formation in this case is the water and head group dipoles as well as the enthalpy and entropic contributions at the membrane interface [391, 392]. Emphasis on the interface of the water dipole orientation and the charge density gradients during pore initiation have shown to be a factor [377, 382, 389] therefore provide a sequence of pore formation events that are apparent across many bilayer systems [215, 218, 377, 382, 389].

Electropores have been simulated and formed at ~3.1 V membrane potential in DOPC bilayers under double bilayer conditions [370], and varying minimum pore forming values have been established for phospholipid of varying tail lengths [390]. A field of 280 mV $nm^{-1}$ has been shown to induce pores in DPPC, with higher fields (380 mV $nm^{-1}$) reported for DOPC, with values corresponding to the thickness of the bilayer. In comparison to the breaking voltages seen for the 16 and 18$\beta$ pores within this study (2.1 V break) with a bilayer thickness of between 40 to 42 Å, all values simulated are higher than physiological recordings be it formation or pores on a black lipid membrane (0.25 - 0.5 V) [393]. A higher voltage is considered for these types of simulation due to the surface area under a potential. Hence for electropores to

occur in simulation, one must either increase the simulated area or simulation time (computationally infeasible) or by increasing transmembrane potential [383–385] which has been used in simulations in this thesis. It has been shown that pore formation induced at higher voltages in simulation still show the same characteristics as those seen experimentally [382].

Experimental evidence indicates that living cells in external fields have limited formation of conductive pores to a maximum of 1.5 V [394–396]. However, in MD all values appear to be higher [215, 377, 382, 397, 398]. Therefore, simulation can be used to assess the breaking point of hydrophobicity, however the breaking points may be higher as indicated from electroporation values. This also limits the lipid scaffold to an upper value.

DPPC breaks and forms electropores at 2.2 V [218], via a constant electric field, and at 2.1 V within this chapter, under a CE voltage. Once initiated, the pores become effectively hydrophilic, [381, 399], with phospholipid head group rearrangement along the water pathway, in a number of nanoseconds [400, 401], which is present in the electropores formed in the high voltage protein-lipid simulations. Ion conduction events through the electropore have also been noted in other studies [370].

## 5.4 Conclusion

### 5.4.1 Hydrophobicity and Water

Within this chapter, it is has been shown that electrowetting of a hydrophobic gate within a $\beta$-barrel nanopore is possible in simulation. Also based on current estimates, a larger barrier (be it in the 16-5L and 18-8L pore models) would require a higher membrane potential to break, which unfortunately due to the bilayer was not possible with this set-up. Interestingly, looking at the water properties within the hydrophobic

region here, they have similarities to other proteins with hydrophobicity under a voltage, for example the simulations of MscS [402]. The structure initially indicates an open protein pore, however with similar features to that of a hydrophobic gating mechanism. Simulations with a constant electric field were conducted on the MscS protein in a lipid bilayer in which current and water flow through the pore was visualized through the channel with comparable values to experiments. No current electric field simulations resulted in an occluded, dehydrated pore [403]. Lateral pressure applied in simulation resulted in a higher conducting pore and thus could be used in combination with this method to measure conductance events. Various water models and wetting energies of the hydrophobic pores of mechanosensitive channels were conducted [404]. Hydrophobic regions have also been noted in the TWIK channel [66] and nAChR [405]. Interestingly to this study is the $Cl^-$ selectivity of the pores under voltage. This has not been noted in other hydrophobic conducting pore studies thus selectivity remains elusive. Within this thesis, it has been shown that the 14-3L has a similar barrier to $Cl^-$ and $Na^+$ (chapter 4, free energy profile) therefore it is expected to be selective for both under a biasing potential. With further investigative simulations using varying anions and differing water models, an insight can be given as to their effect. However remains questionable in this thesis.

Based on these hydrophobic models it would be of interest to be able to acquire an 'aspect ratio' of hydrophobic length/width for an estimate into how much voltage is needed to break a certain degree of hydrophobicity. For example, a protein with a certain degree of hydrophobicity or a hydrophobically modified solid state nanopore, akin to those built in [70] it would be beneficial to predict how much of the solid state pore is chemically modified. An initial state to this could be the breaking of the larger pores, to establish that this method is indeed correct for these pores. This may be conducted using a lipid with a higher voltage capacitance, as shown in the higher

breakage points of ester and ether forms of DPhPC (2.7 V and 3.4 V in simulation) [218] or a possible scaling down of the models.

Water ordering is a critical part of hydrophobic wetting under voltage. In hypothetical models, simulations have shown intermittent filling above the critical radius, $R_c$, for a model hydrophobic nanopore under equilibrium conditions. Below the radius, filling was induced (into what was a 'dry' pore) with the application of an electric field generated by an ionic imbalance with the simulation which is replicated in the simulations presented here. Within the newly wetted region, the bulk water properties varied, to double of the mean calculated and a noted decrease in the dielectric permittivity due to variations in the hydrogen bonding network in water [203]. Bulk, dielectric and hydrogen bonding variations within the pores have not been assessed but assuming the same breaking trend, would be expected to display similar properties. A more physical chemistry approach could be taken with such models to assess such properties.

Field induced wetting of hydrocarbon like nanopores (separated at distances from 9 to 40 Å) also are shown to have a threshold break with the wetting pattern dependent on field direction, with a field parallel to the pore axis resulting in a wetting event (perpendicular fields resulted in no water-events through the pore region) [225]. However, fields induced perpendicular to the water surface edge enhance the evaporation [406]. Direction of the electric field and the roughness of the surface results in the directional pulling of water [407]. Thus, it may be of interest to other possible pore models to consider the directionality of the field and thus, the possibility of an off-center field which may enhance wetting or allow a different wetting pattern with differing protein functionality. This has also been noted in solid state hydrophobic nanopores, from the work noted in [408]. Hypothesised is the initial breaking factor which wets these pores, be it a menisci overlap event due to an increase in water

curvature at the water-vapour-hydrophobic interface or a pure electrowetting event in which the position of the menisci migrate towards the hydrophobic region (within a 100 nm diameter pore) [192]. For the water event here, due to the small size of the pore it is unclear which event is allowing the water initiation. This may be more clearly shown in larger pores if simulation conditions can be formed to allow such an event.

Within a CNT pore model, a 8.1 Å diameter (6,6) CNT is shown to fill under an electric field [224], akin to the 14$\beta$ pore in this study with its larger diameter. Energy of transfer depends on the water-tube interaction potential, Hence, the potential of a water-hydrophobic amino acid may be of a consideration to the cost of wetting and transfer to this system. Also under an applied electric field, the liquid to pore-liquid ('ice' due to its ordered hydrogen bonding) transition has been simulated. Seen in the lumen of (7,7), 9.3 Å diameter and (10,10) $>$ 1.1 Å diameter CNTs, with an increase the lifetime of the hydrogen bonds within the larger pores. This may indicate the initial equilibrium de-wetting events in which the larger pores, resulting in a slower de-wetting transition [364]. This is also seen in equilibrium systems in this chapter (figure 5.3 for the 16 and 18 models which displayed slower initial dewetting). Within the applied field, water dipoles are shown to direct themselves in a parallel direction to the pore which is observed in the electropores from this chapter. Also from simulation, ion dependence is analysed in a CNT model with an applied field simulation with varying ionic concentration. This results in no change of the water initiation within the CNT [409]. As a result, the ionic concentration used in these simulations would not affect the water initiation events, which have also been simulated and analysed in the applied field method of the work in this chapter, with no change in the water initiation event. However, noted in [410], varying salt concentrations were used for transport through modified solid state hydrophobic nanopores. Different gating was

noted with differing ion concentration.

Water entry into certain CNT's is shown to be thermodynamically favourable. The free energy decreases in a filled nanopore state to an unfilled one [411, 412]. The driving force changes with a diameter change within the nanopore. Filling is shown to be entropically driven in a small diameter tube due to the increase in transitions and rotations of the water within the confined pore compared to that of the bulk water. Also hydrogen bonding in the larger diameter CNT's impose a favourable enthalpic contributions to the system due to a rigid hydrogen bonding network within the pore lumen which may be transferable to the energetics of water entry into the model pores in this thesis. Such studies may be conducted with the pores created in this thesis. Water confined in hydrophilic 'SCNT's' (silicon carbide nanotubes) show the same filling trend to that of the hydrophobic form. Water molecules within SCNT's have structures and properties that resemble those in the hydrophobic single-walled carbon nanotube since both are controlled by the confinement and geometry allowed within the lumen of the pore [413]. Hence it may be expanded that the filling events noted in these nanotubes, solid state models and the protein models in this thesis may all be consequently analysed and theorised based on a geometry-confinement assumption as well as chemical character.

Shape is also an important factor when considering water translocation, as shown within the various shaped pores within this thesis, the theorised hourglass shape of aquaporins [373] and water flow rates within CNT is varied by the shape of the system and the field applied to the system [414]. Also functionality, with functionalised CNT's and graphene sheets [415] and also more complicated CNT junction shapes [416] and modelled charge regions within a CNT [417] may be of interest in further voltage simulations under this method to establish a correct water-entry route and conductivity through the pores.

### 5.4.2 Bilayers

The mechanism of biological membrane electroporation was first hypothesised for lipid bilayers in 1979 [381], with varying simulation methods used to model the breakdown of the bilayer itself. With lipid bilayers, a constant field method has been shown computationally to accurately study bilayers and pore initiation events [354]. Compartmentalised ion simulations have also been performed [370], however not with the ion-swap method used in this chapter, thus longer timescale simulations can be produced with the depletion of voltage. Physiologically, it is known that electroporation can also occur in a bilayer, when a cell is exposed to a long electrical pulse (ms) or a low AC signal (Hz to kHz) In this case, the energy is dissipated to the membrane, which has a capacity for charging [418]. Once capacitance is reached, the energy is dissipated in the formation of pores. Thus, in the double bilayers under low voltage in this chapter, we may see electropores in simulation but we would have to simulate for very long computational time scales, which is not feasible at this moment in time. Therefore, higher voltages have been used in this, and many other studies to observe such defects.

Again, akin to the hydrophobic pores under voltage, water in the newly formed electropores in this, and other findings are found to be orientated to the voltage (data not shown) [378, 390]. Previous simulations have shown that the pore is unstable if the field is returned to zero before the walls of the pore are fully assembled by head group reorientation, therefore a simulation of sufficient length is needed. This control was not conducted with the electropores formed in this chapter, however it may be of interest to conduct in the future under this method and with varying lipid head and tail groups.

Simulations with voltage have also been conducted on asymmetric bilayer systems [391, 392]. In an asymmetric bilayer, the water dipole orientation is reinforced at the

more positive side of the membrane (POPS and POPC compositions), thus directional pores are formed depending on the lipid composition. In an asymmetryic DOPS:DOPC bilayer, it was noted to break at an applied field of -450 mV $nm^{-1}$ (which regarding bilayer thickness corresponds to ~-3.4 V through the membrane) [419] which is higher than the values calculated in this thesis and is lipid-side dependent [420]. This may be of interest if trying to simulate voltage dependent proteins under asymmetric lipid compositions.

More to note for this system are previous simulations on the theory of electroporation under a high voltage [378], where membrane thinning under voltage occurs (as seen previously with the non-conducting pores under a high voltage). Again noted, this is due to the Maxwell stress generated (which occurs at two surfaces who have differing dielectrics). This event has been noted in membrane thinning by [421, 422] and also in membrane rupture [423, 424]. Based on the new DIB method [386], this could be investigated with such hydrophobic proteins using this manner which can be used to measure membrane thinning as well as a change in bilayer thickness under voltage.

Another aspect to the water-hydrophobic region transition is to note the electroporation with POPC and water-vacuum-water systems in simulation. At higher induced voltages, water bridges were noted through the vacuum and the bilayer. The water bridges had dipoles parallel to the field [222], which raises the possibility within the models of this thesis that induced voltage levels and water filling may be an issue of timescale within simulation. Thus, it may be of interest to conduct a long-low voltage simulation to check this aspect.

A direct comparison between MD and experiments may not be valid for this system. PME is used in this thesis, but is known to introduce artifacts (faster than direct calculation) in the charge profile and sensitive to the system length perpendicular

to the bilayer plane [425]. Therefore within the voltage and applied fields, precise electrostatic contributions may generate errors in potentials therefore exact values cannot be extrapolated. Another MD limitation is the water model used within these voltage simulations. Based on the various water models [257] and the influence on water dipoles on membrane and within hydrophobic regions, it would be of interest to compare such models. The basic SPC water model was used here and it would be of interest to also use a model which presents a lone pair electron charge, such as the TIP4P model [259]. However, it has been shown that the water model used did not affect the evaporation of water under a field [406] therefore changes (if any) may be slight.

# Chapter 6

# Conformational States of a Ligand Gated Ion Channel

This chapter is based on the the following publication;
Conformational State of the Ligand Gated Serotonin Receptor, A Simulation Study. Trick et al, *in preparation.*

*"Got a long list of Starbucks Lovers"*

Taylor Swift

## 6.1 Introduction

The Cys-loop receptor family of pentameric ligand-gated ion channels (pLGIC) have been resolved to multiple structures in recent years. The charge selectivity of pLGIC's is determined by the selectivity filter [426]. The constriction within the homology model of GlyR (based on nAChR) [427], $GABA_A$, $GABA_C$ [428], and GluCl channels [54] suggest that the transmembrane (TM) selectivity filter contributes to the conduction of the pore. However it is thought that the charge near the intracellular entrance

is also critical for selectivity [429].

Recently the x-ray crystal structure of another cys-loop cation selective pLGIC, the serotonin-gated 5-hydroxytryptamine type 3 ($5\text{-HT}_{3A}$) receptor has been solved [430], whose conformational state is in question (figure 6.1).

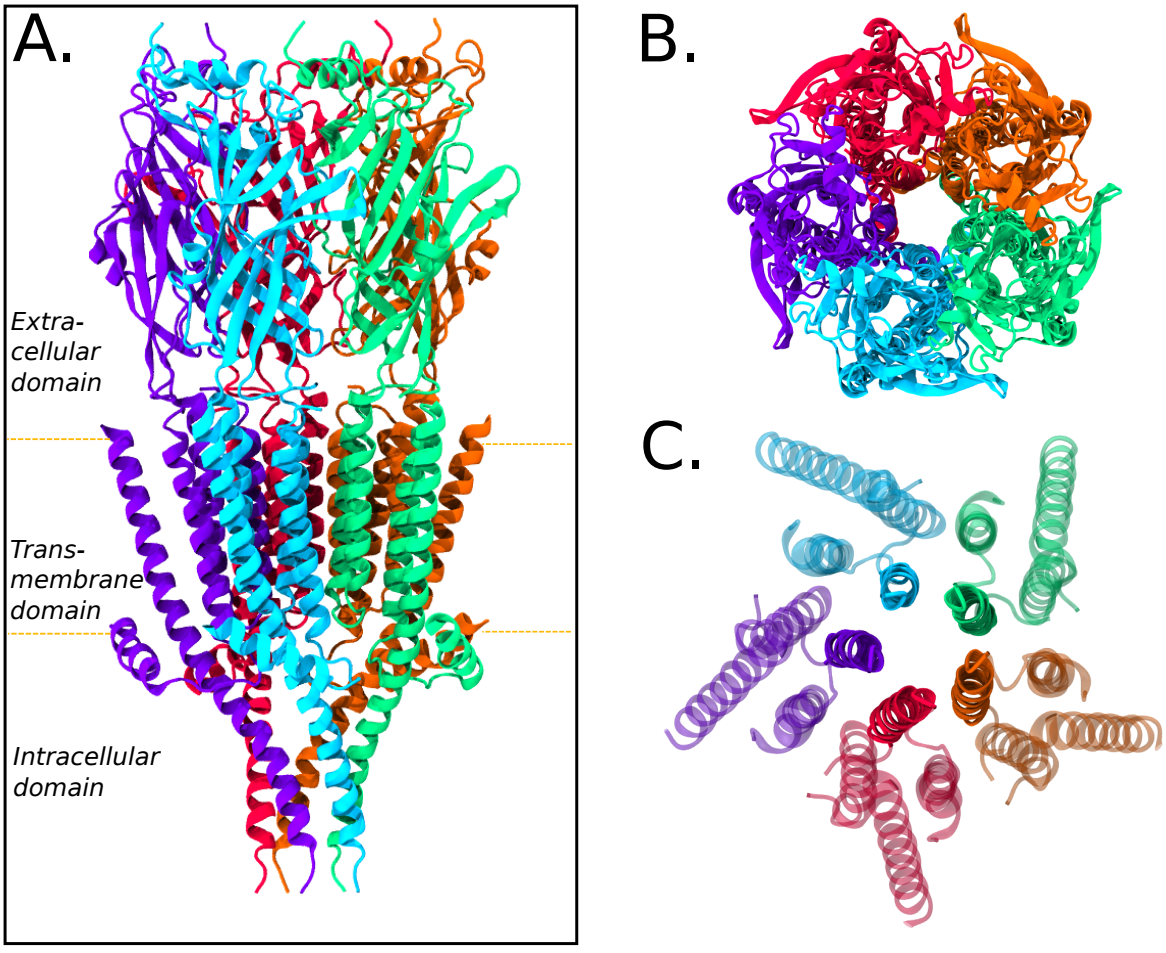


**Fig. 6.1:** Cartoon representation of the $5\text{-HT}_3$ receptor, (pdb: 4PRIR). A. Full receptor, transmembrane domain indicated with dashed yellow lines and orientation indicated. B. Top down view of A. C. Top down view of transmembrane region. Opaque, central helices indicate pore lining M2 helices. Protein is coloured according to chain.

Before the crystal structure was solved, it was known via experimental data and homology models that the central gate in the pore of the $5\text{-HT}_3$ involves the M2

region, discovered to be the pore lining pathway [431]. However, without a definitive structure at that moment in time, the position of the gate was in debate. Scanning cysteine accessibility method (SCAM) has been used extensively to determine the helical nature of the TMD. Within the open state 13 positions were modified, however only 3 positions were modified in the closed state, with the pattern of modification consistent with an $\alpha$ helix [432]. This method has also given an indication into which residues are pore facing (V291, L293, L287 and S280) for validation of homology models [433]. Pre-crystal structure homology-models estimated the F loop to be the key serotonin binding site with a total of 6 loops known to be involved in binding (A to F). Mutations in these loops results in the assumption that lateral movement is involved in the transduction of signal from agonist binding [434]. A summary of pre-crystal structure data is concluded in a recent minireview [435]. With the structure now available these elements can be studied more accurately and precisely.

The 5-$HT_3$ is homologous in structure to other pLGIC (unlike the G protein coupled receptor, 5-HT) however the conduction state of the pore cannot be concluded entirely from the structure. It was crystallised in complex with an inhibitor, which is expected to stabilise a non-conducting form of the channel, therefore it is expected to be a closed, or possibly a desensitised state. The dimensions of the constrictions are between those of an open and closed channel [436]. The M2 helices are similar to those seen in the GLIC and GluCl (open) structures, however they differ from previously seen closed forms of the many structures of GLIC and ELIC. The M2 helices and dimensions of 5-$HT_{3A}$ are shown in figure 6.2.

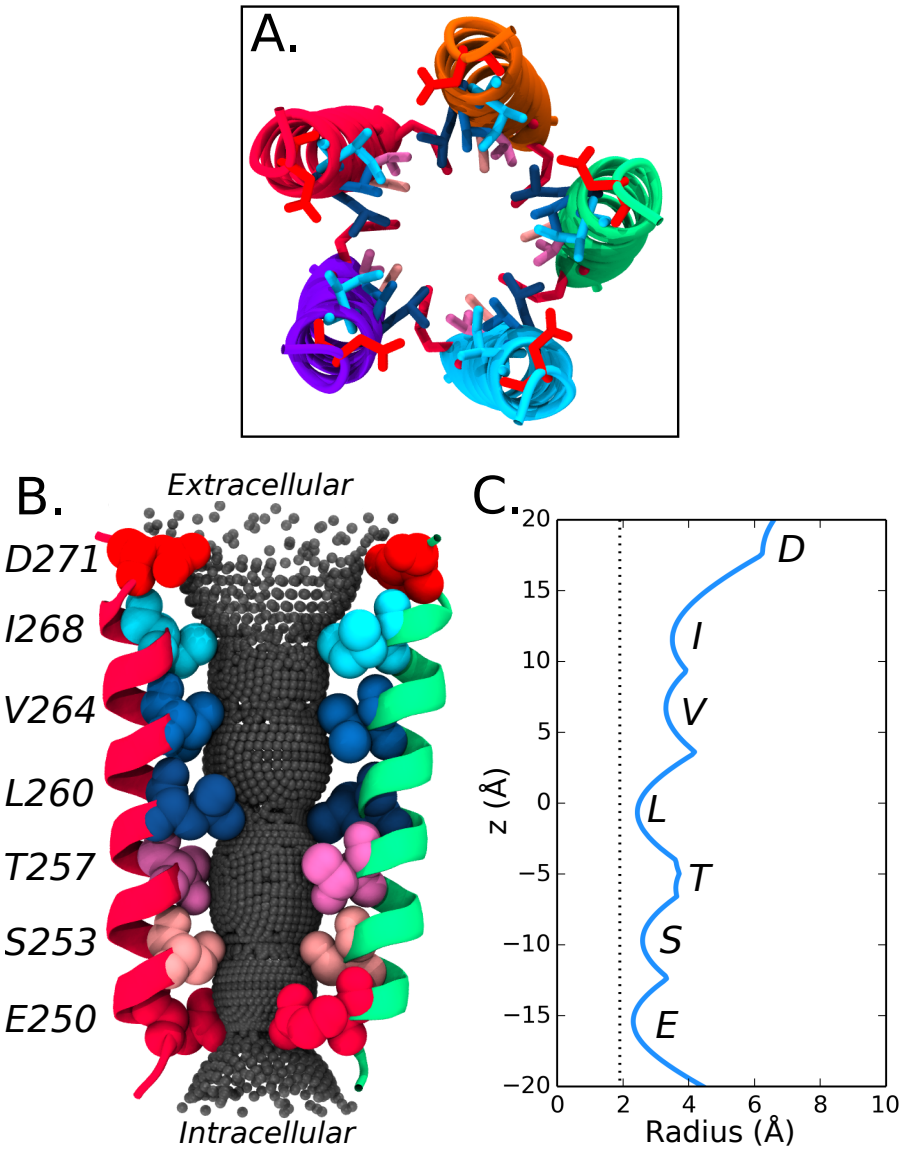


**Fig. 6.2:** M2 helices of 5-$HT_3$ receptor. A. Top down view of M2. Inward, pore facing residues are shown in stick form. B. Profile of 2/5 M2 helices with sphere representation of cavity, inward pointing residues are indicated again in VdW form and labelled to one letter code. C. Radius calculation of pore region from the crystal structure. Image to scale and corresponding to residue positions of B.

Based on the nature of other pLGIC's gating and the residues in the M2 helix, it is thought that there could possibly be a hydrophobic gating mechanism in the TMD of the 5-$HT_3$ channel, thus being of relevance to this thesis and also the conductive state itself. The structure shows a key leucine residues (L9') within the M2 helices,

seen in other pLGIC [48, 54, 437] which are known to be hydrophobically gated (and a radius of ~2-3 Å which is known from previous hydrophobic cut-off values to be of interest).

### Simulations of pLGIC's

Many simulations have been conducted on ion channels [438] and for this family of pLGIC's. Ion permeation has been simulated for nAChR which demonstrated a lower water density within the channel pore [72]. Simulations of the closed ELIC structure show there is complete dehydration in the pore, from the center to the extracellular side in the simulation [74], with the gate position closure point for the homologous GLIC at the L9' region [48, 426, 428, 439]. This L9' residue is also present in this 5-$HT_3$ structure (L260). Dehydration events around the L9' have also been simualted in GlyR, GLIC and GluCl [440–442].

MD utilising Brownian Dynamics (BD) have been used to calculate barrier heights for $Cl^-$ and $Na^+$ through the GLIC channel [228]. BD and hybrid MD/continuum electrostatics were used to calculate ion energies and barriers through the anion conducting GluCl. Most recently, *Yoluk et. al.* have simulated three different conformations of GluCl via umbrella sampling [233]. "Multiscale" simulations have also been conducted by *Zhu et al* [316] on GLIC where MD and a mixed elastic network model (ENM) were applied to the protein to induce a conformational change. Movement induced helical tilting and an iris like movement were accompanied by a drying transition. Multiple simulation studies have also noted that simulation of the open, GLIC protein resulted in spontaneous closing of the channel [316, 443, 444] and a change in the M2 helical tilt angle [54, 443].

Thus, MD can be used to look at permeation, gating and conductive states of many pLGICs. However, it is still computationally demanding to study the entire

channel when it is noted that the main gate is indeed in the the pore lining L9' position. Therefore the smaller M2 helical construct (figure 6.2) can be used with "short" umbrella sampling windows and free energy calculations could be used to look at the possible conductive state of the 5-$HT_3$ receptor by utilising previous methods used in this thesis (umbrella sampling) and adapted equilibrium simulations to deduce if this is a functionally closed or open form of the 5-$HT_3$ channel.

## 6.2 Methods

### 6.2.1 System Preparation

The transmembrane M2 helices were embedded in a self assembled lipid bilayer (POPC) in a CG martini representation [260]. After AT conversion [267], water molecules (~25,000 TIP4P [259]), the protein, lipids (~320), and counter ions were present in the system (ionic concentration of 0.15 M). For the umbrella sampling windows, either ion or a water molecule were placed at their respective positions. Water molecules or ions which overlapped with the molecule of interest were repositioned by energy minimization before simulation. Energy minimisation was run for 5000 steps. All simulations were carried out with GROMACS version 4.5.5 [288, 324] with the OPLS United-Atom forcefield [445].

Equilibrium simulations were conducted with long range electrostatic interactions treated with the Particle Mesh Ewald method [240] with a short range cut off of 1 nm, and a Fourier spacing of 0.12 nm. Simulations were performed in the NPT ensemble with the temperature being maintained at 310 K with a v-rescale thermostat [256] and a coupling constant of $\tau_t = 0.1$ ps. Pressure was maintained semi-isotropically using the Parrinello-Rahman algorithm [446] at 1 bar coupled at $\tau_p = 1$ ps. The time step for integration was 2 fs with bonds constrained using the LINCS algorithm [253]. Analysis

was conducted with GROMACS routines, MDAnalysis [284], and locally written code. Water flux was calculated by counting water molecules crossing through an xy plane centred on the protein within a 20 Å diameter shell from this centre. Water fluxes were evaluated over the full length of the simulations. Molecular graphic images were produced with visual molecular dynamics (VMD) [281] and PyMOL [282].

For the equilibrium MD Gaussian network model (GNM) simulations, an elastic mass-and-spring network are added [447] to all the C$\alpha$ residues between 7-9 Å within the structure. The distance was chosen based on C$\alpha$ distances, any shorter and they would not connect, and any longer the connections were made across the pore to opposite helices. The spring had a force constant of 1000 kJ mol$^{-1}$ nm$^{-2}$. Simulations were run with the same set up as previous equilibrium MD simulations in this thesis for up to 500 ns.

### 6.2.2 Umbrella Sampling

The starting system for the umbrella sampling was obtained from an energy minimised structure mentioned previously. The x and y coordinates for positioning were determined based on the center of mass of the channel. Visual analysis confirmed this was the center of the pore. The z axis coordinate for water was based on the position of the oxygen of the molecule (figure 6.3).

The reaction coordinate was defined as the z-axis, ranging from ~±40 Å with the bilayer centre at z = 0 Å This was used to define ~80 windows along the z axis, with a distance of 1 Å between successive windows. A harmonic biasing potential was applied to the z coordinate of one atom of the molecule with a force constant of 1000 kJ mol$^{-1}$ nm$^{-2}$ acting on the z coordinate only. Each window was simulated for 2 ns (5-HT$_3$) or 4 ns (GluCl), completely unrestrained (no position or distance restraints) with no external networks applied on the protein. Convergence was analysed by calculated

height of the central barrier as function of time intervals for consecutive 0.1 or 0.2 ns segments extracts from each window. PMFs were computed using the weighted histogram analysis method (WHAM). PMF profiles were tethered and errors were calculated by the bootstrapping method within the Grossfield wham script [448].

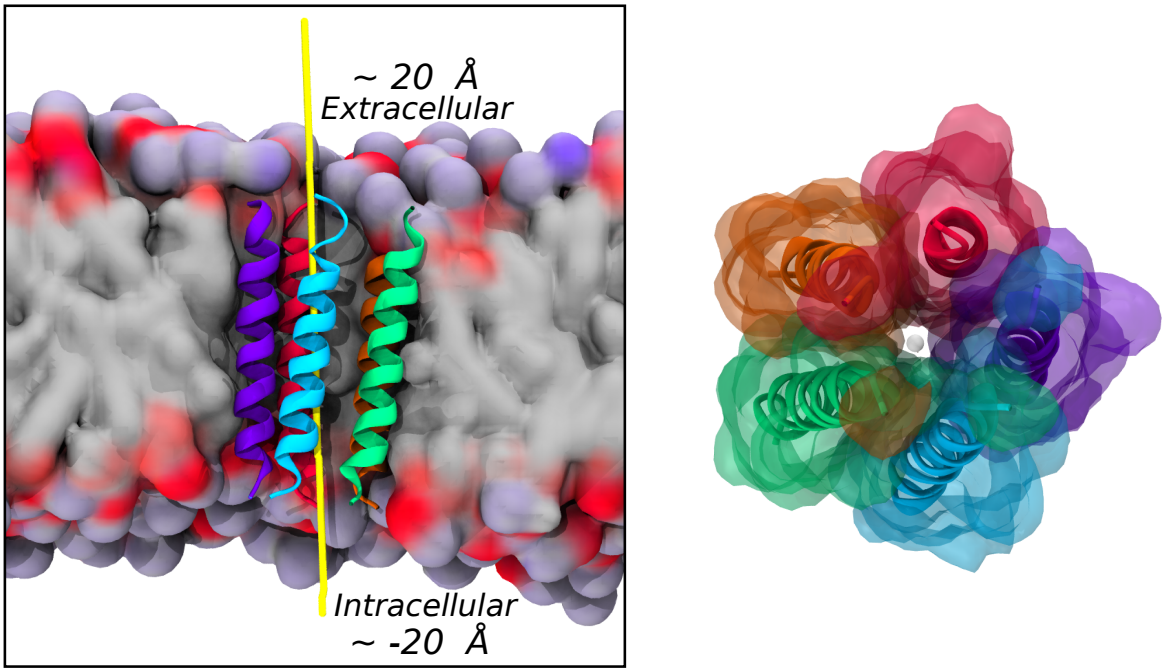


**Fig. 6.3:** PMF windows setup through M2 helices. Windows are calculated at every 1 Å through the pore lumen. x and y values are chosen from the c.o.m of the protein. Approximate pathway indicated by yellow line. Protein shown in POPC bilayer. Intracellular protein region corresponds to ~-20 Å in this image and following profiles.

## 6.3 Results and Discussion

## 6.4 5-HT$_3$ Serotonin Receptor

Free energy profiles for chloride, sodium and water pathway through the M2 helix bundle were constructed (figure 6.4).

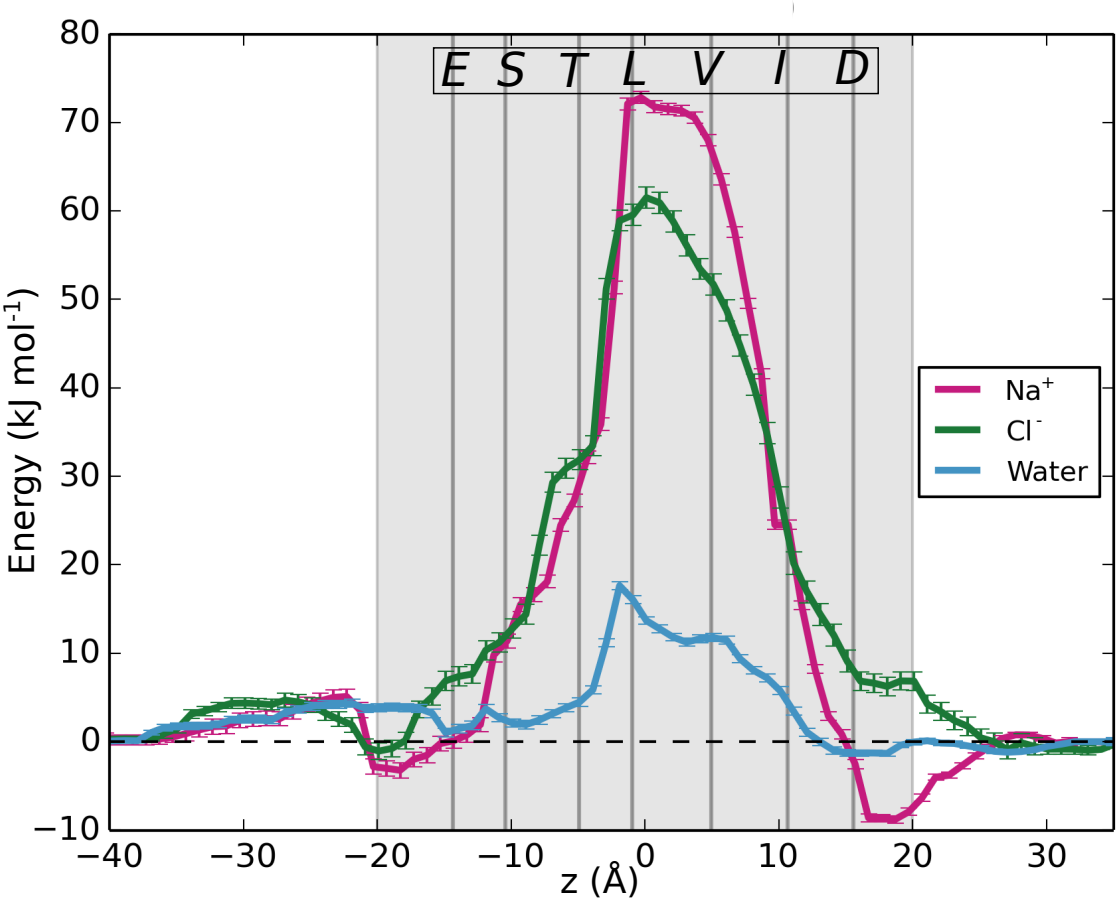


**Fig. 6.4:** Potential of mean force profile of ions and water through 5-HT$_3$ M2 helices. Plot represents the translocation pathway (on the x axis) through the helices with calculated energy from that position (y). Grey shade represents the z co-ordinate of the pore, with secondary vertical lines indicate approximate position of inward pointing residues (shown in one letter code). Intracellular region corresponds to the negative z region of the plot, with the extracellular on the right, positive hand side. Bootstrapping is used to calculate error.

As the profile shows, a high energy barrier to translocation is noted through the pore lumen. A barrier of ~72 and 61 kJ $mol^{-1}$ are noted for $Na^+$ and $Cl^-$ ions and 16 kJ $mol^{-1}$ for water. These correspond to other PMF values for related pLGIC's previously simulated. Such as the ELIC structure [75], $Na^+$ permeation was calculated at ~83 kJ $mol^{-1}$ with a barrier at the L9' position. Other studies for the open GLIC structure resulted in much lower values of 12.5 kJ $mol^{-1}$ for $Na^+$ [228] (and 17 kJ $mol^{-1}$ for $Na^+$ [229]) and with other values of 46 kJ $mol^{-1}$ for $Cl^-$ (barrier not at L9' but E-2' position within the pore) [449]. The structure of nAChR was assumed to be closed based on the free energy of translocation of sodium through the structure [72], in which a barrier of 25 kJ $mol^{-1}$ is calculated at L9' and of 37 kJ $mol^{-1}$ by others [450].

More recently, a PMF of chloride translocation through a closed MD structure of the GluCl channel had a barrier of 62 kJ $mol^{-1}$ [233]. Thus, based on the varying values of free energy in both closed and open forms of the pLGIC's indicate that it is in a closed form, and with the position of the barrier, indicate it could also be hydrophobically gated.

Firstly to interpret these profiles and determine again, if the proposed 1 Å positioning of the ion and water provides enough coverage in the 3D space to accurately predict a free energy landscape for this channel, the gromacs code g_wham [325] was used to produce a histogram of the overlap of the windows in all the simulations (figure 6.5, A). From the histogram, there is sufficient overlap between the histogram windows to ensure that there is adequate sampling with the pull force applied and with the z coordinate positioning. Also to be considered is the aspect of convergence, which needs to be checked to see if it is adequate for the length of simulations to be used in the calculation. In the figure (6.5, B), the convergence is considered after ca. 0.5 ns (where the maximum barrier calculated is no longer variable) of which, the PMF presented on the 5-$HT_3$ channel are based.

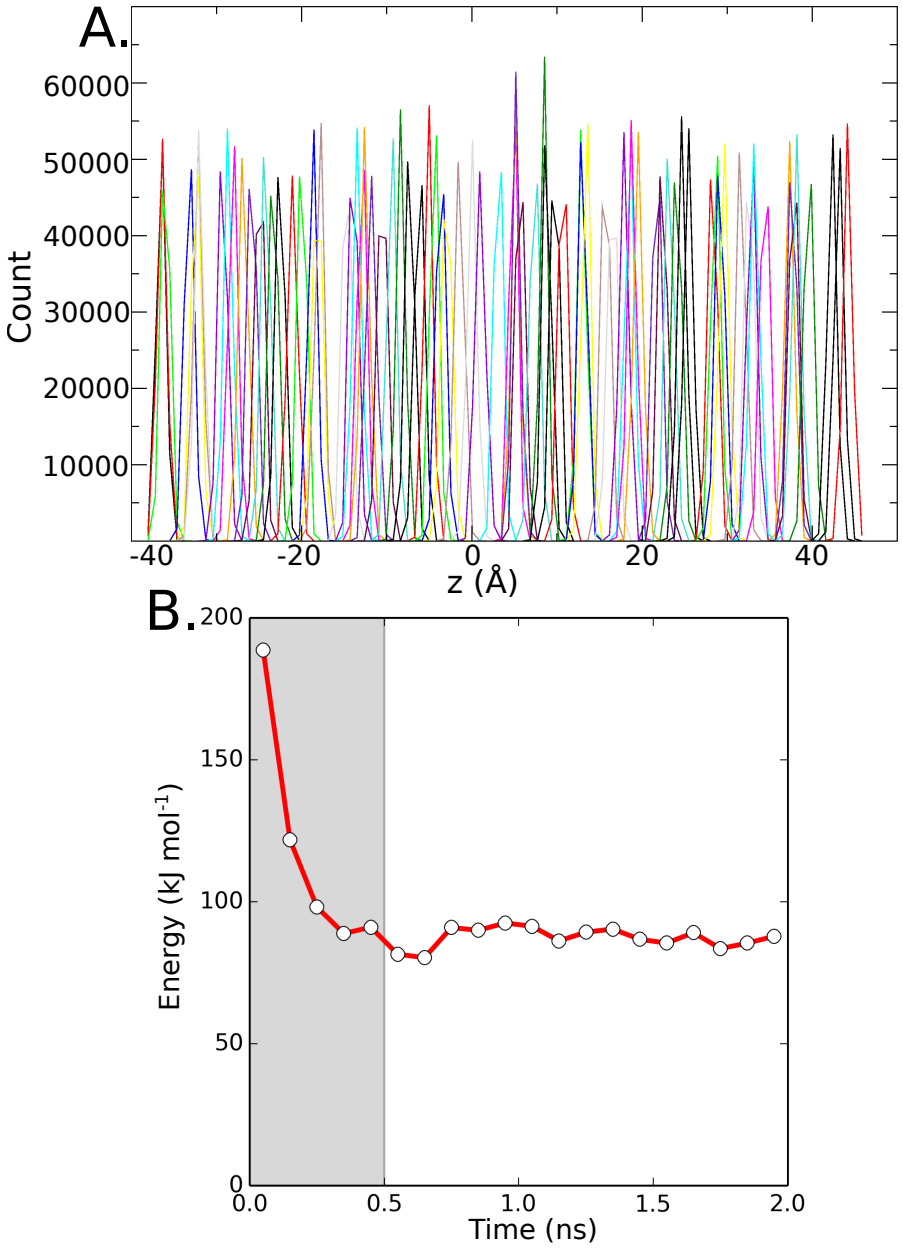


**Fig. 6.5:** Histogram and convergence profile for M2 helices of the 5-$HT_3$ channel. A. Histogram of window overlay of $Na^+$ ion positions within simulations. B. Plotted is the maximum calculated free energy for incremental windows. i.e., 0 - 0.1 ns, 0.1 - 0.2 ns and so on until 1.9 -2.0 ns (point is plotted at 0.05 increments) for a sodium ion. Shaded grey region is the time which will be omitted from the final shown profile.

To further validate the free energy calculations, and to assess whether the windows

are of an adequate length is the movement in the x and y plane of the ion or water molecule. This is shown by the ion movement in the x and y plane (and protein, figure 6.6) within the solvent phase of the simulation (B.) and within the L9' region of the alpha helical channel (C.). For the simulation time length used, based on the distribution of the ion within the system for both phases, ample movement for the region is observed in both phases, and is to be assumed gives a proportional representation of movement within this system.

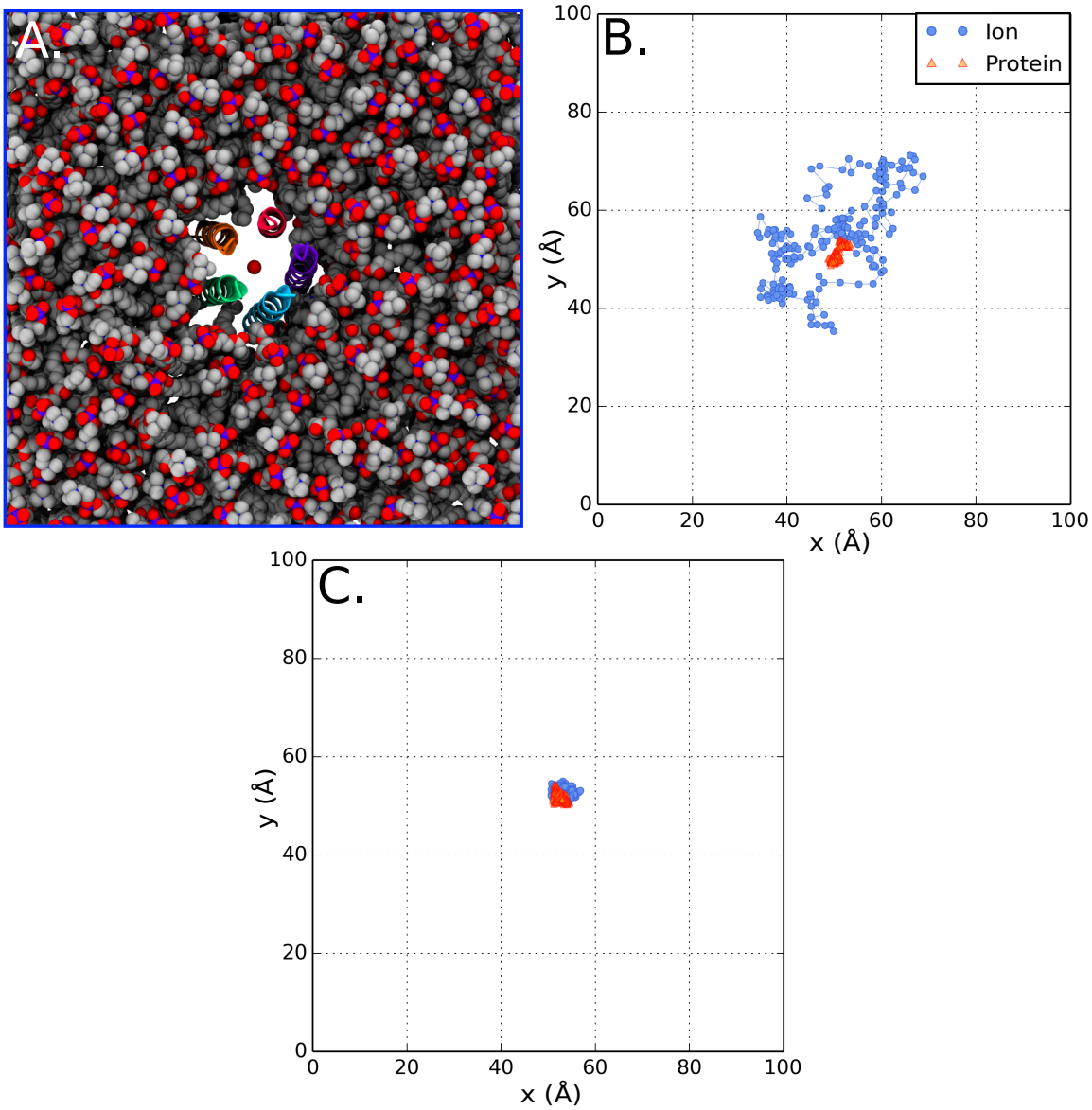


**Fig. 6.6:** Sodium ion movement within PMF windows for 5-$HT_3$ M2 Region. A. Set up of ion (pink dot) within the c.o.m of the protein (chain coloured cartoon) in which the z values are varied to explore energy landscape in the pore lumen. POPC lipid is shown in VdW. Water and other ions are omitted for clarity. Image is to scale in figures B and C in the x and y directions. B. Graph of protein and sodium ion c.o.m movement in the simulation for a z value for the ion of 23 Å where the ion is in the solvent phase of the simulation. C. C.o.m of ion in z = 58 Å which corresponds to the 9' leucine within the pore.

Hydration shells for $Na^+$, $Cl^-$ and water transversal through the pores has also

been calculated for the M2 channel based on rdf cut-offs from a previous chapter (figure 4.9, chapter 4). It can be noted for both $Na^+$ and $Cl^-$, the first solvation shell remains intact through translocation through the solvent and M2 helix. In contrast, depletion of the second solvation shell occurs as the ion passes through the channel, for all molecules, with a minima near 0 Å, which corresponds to the L9'(figure 6.7). As seen in other hydrophobic gated LGIC's such as GLIC where it is suggested the barrier to the hydrophobic region is present due to the cost of dehydration, and the barrier to $Na^+$ is due to the dehydration cost imposed by the region [327], the higher barrier observed for the hydrophobic pores modelled in this thesis may reflect firstly the large cost of hydration of the hydrophobic constriction and also the cost of removal of (part of) the second hydration shell. Again, this reinforces the views that looking at solvation through protein pores can give an insight into their gating mechanism as suggested in this thesis through hydrophobic $\beta$-barrels.

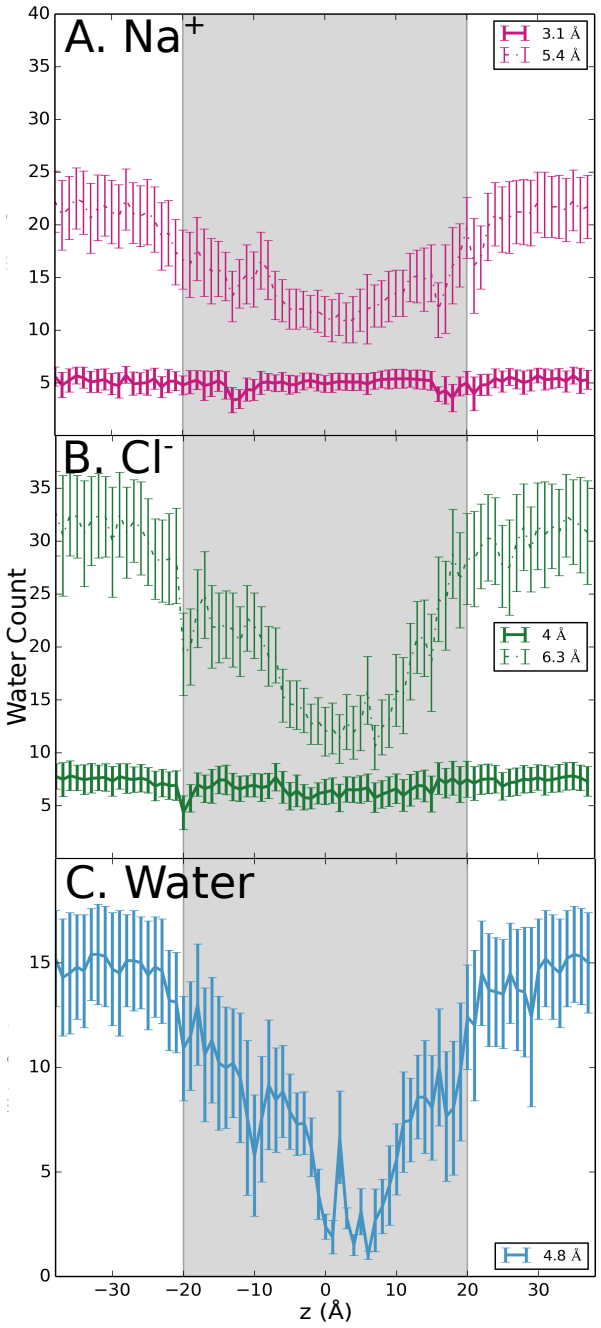


**Fig. 6.7:** Hydration shells for water and ions through M2 region. A. Number of water contacts around a sodium ion with z pathway on the x axis and number of waters within previously calculated rdf (figure 4.9, chapter 4) shells on the y axis. B. Chloride and C. Water contacts. For all, calculated radii is indicated. L9' is at ~-1 Å. Graph indicates from the intracellular (negative z region) to extracellular (positive z) regions.

## Open or Closed?

Based on the free energy calculations conducted here, and comparison to other free energy studies of cys-loop pLGIC's, the free energy profiles, the radius of the channel and the positions of the energy barriers indicate that this structure is closed in terms of ion translocation, and may be hydrophobically gated like other pLGICs. However, based on the radius of the pore and the barrier height calculated for water within the channel, it is possible that water is conductive through the pore. To look at this more, equilibrium simulations are conducted with the introduction of an adaptation of an elastic network model which has been used in previous pLGIC simulations.

### 6.4.1 Equlibrium MD and GNM

The application of an ENM (elastic network model) has been shown in previous MD simulation studies to improve channel stability, in an open or closed form [436, 442]. Therefore, to look at the MD conducting state of the pore via water and ion translocations, both a standard protein restraint (positional) and a Gaussian version of an elastic network model (termed GNM, figure 6.8) is used for comparison.

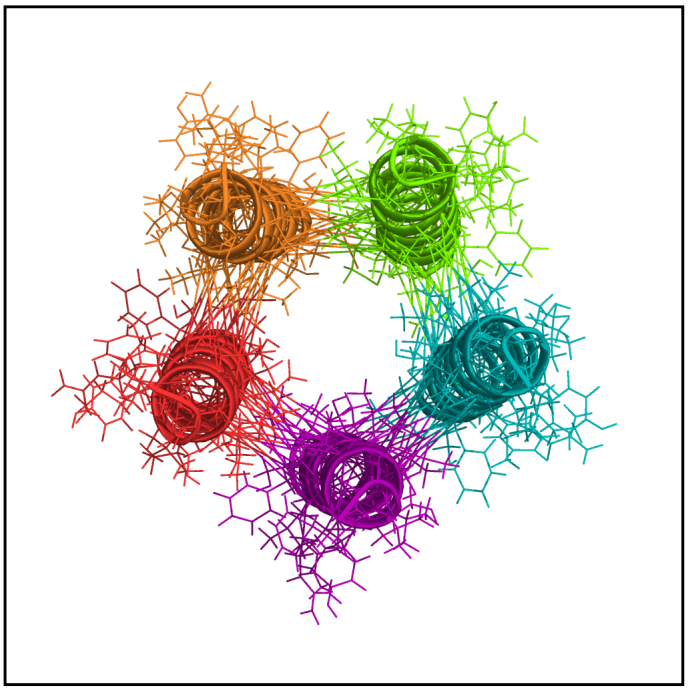

**Fig. 6.8:** GNM model of 5-$HT_3$ receptor M2 helices. Top view cartoon representation of M2 helices (coloured by chain) with harmonic springs indicated between the helices by lines, connections shown within 7 to 9 Å.

Within the 100 ns positional restraint simulation and the longer, 500 ns GNM simulation of the M2 helices, the radii and water flux were used to evaluate the conductive state of the helices (figure 6.9).

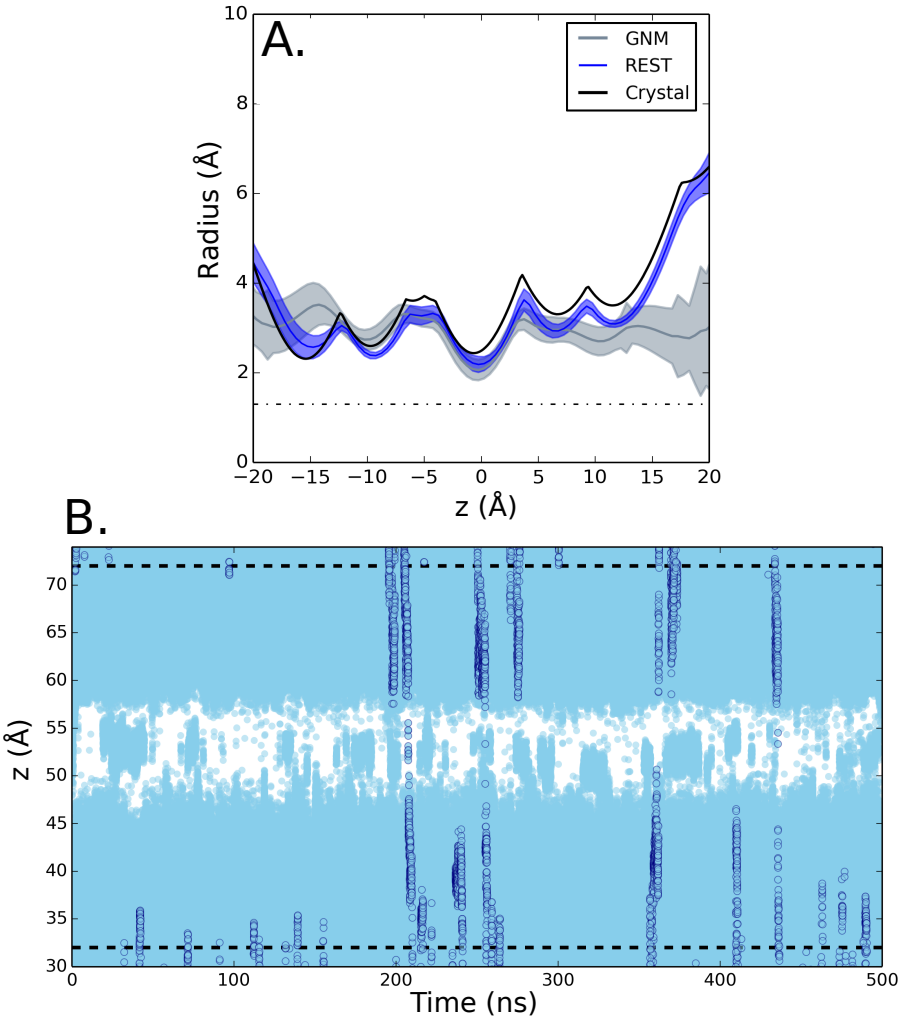


**Fig. 6.9:** Radius and water plot of 5-$HT_3$ M2 helices under GNM and positional restraints. A. Radius profile of M2 for GNM, positional restraints (REST) and the crystal structure. 0 Å indicates 9' leucine. B. Water molecules through the M2 helices under the GNM. Dashed lines indicate average phosphate headgroup position. Light blue spheres indicate water, with darker lines being individual waters through. z region shown corresponds to the protein position. White indicates a dry, L9' region at ~53 Å. 30 Å indicates the intracellular end of the protein.

With the application of a Gaussian network connecting the helices, more flexibility occurs towards the ends of the pore, noted in the shaded range of radii in simulation (figure 6.9. A), unlike the positional restrained pore. However, even with the two different restraint applications, at the 0 Å position (corresponding to the L9') remains

the minimum radius for both simulations and near to that of the crystal structure value. Based on the radius of the GNM (~2.0 Å), this suggests and supports the assumption from the free energy profiles that this is the hydrophobic gate within this protein.

In simulation, no ion flow is noted through either of the pores. This may be a problem of inadequate timescale for the restrained form, however based on the GNM having the same minima (and simulated for 500 ns), this is suggestive that an increase in time of the simulation would not result in an ion conduction event. Water flux is noted through each of the pores (~0.1 $ns^{-1}$) and is comparable to that of the closed, 14-3L $\beta$ barrel pore simulated in chapter 3. Therefore, supporting the assumption that the structure is in a closed conformation. The small water events noted could be due to the structure not being in a fully closed conformation, or the protein is partially water conductive in its closed state. Another possibility is that by using the M2 helices only introduces either side to the bulk and this is not physiological for this channel. The extracellular and intracellular domains disrupt the bulk water near the pore, thus they may not be even water accessible. However, even with no water or ion conduction and the high energy barriers calculated, it is suggestive that this channel is closed. A sufficient test for such a barrier would be the simulation under CE voltage, seen within chapter 5. Theoretically, this would take ~10 days to simulate and would give a firmer assumption to the channel state (and also an indication on the breaking voltage of such a motif).

## 6.5 GluCl - Glutamate Gated Chloride Channel

To test the methodology that short, small umbrella sampling windows on the M2 helices of this class of ion channels can give an accurate representation of the free energy landscape, simulations were run with two, molecule modulated states of the glutamate-

gated chloride receptor (GluCl). Agonist or antagonist bound crystal structures are common in the production of an open or closed crystal structure, thus it would be of interest if the removal of such a molecule (and not the characterisation, parametrisation and docking which would be time consuming in comparison) and the use of short simulation windows would an accurate representation of the conductive state of the channel. Simulated here are the partial agonist bound, potentially open ivermectin structure (pdb: 3RHW, [54]) and the allosterically modulated POPC bound channel (pdb: 4TNW, [55]) whose state is in question. A summary of both is in table 6.1.

| PDB ID | Ligand | r(L9') Å | State |
|---|---|---|---|
| 3RHW | Ivermectin | 3.6 | open |
| 4TNW | POPC | 2.1 | ? |

**Table 6.1:** Summary of GluCl channels simulated.

The 3RHW structure is thought to be in a partially open state based on the pore radius (open at L9' with minimum of 2.3 Å at the -2', Pro234). Ivermectin is a known partial agonist and comparison to the apo, closed form [54] there is a M2 tilt ~8 ° away and increased radius at L9'. The 4TNW structure is of more interest as it is thought to be an allosterically modulated form between the open and closed states due to the bound POPC, which is also in the same site as ivermectin. The pore is 'straighter' in comparison to 3RHW, and reported to be wider than that of the closed form.

Between 3RHW and 4TNW, there is a large relative movement seen in the extracellular and the transmembrane domain and a helical tilt of 8.7° (in 4TNW, from 3RHW). M2 helices and initial radius of both structures are shown (figure 6.10).

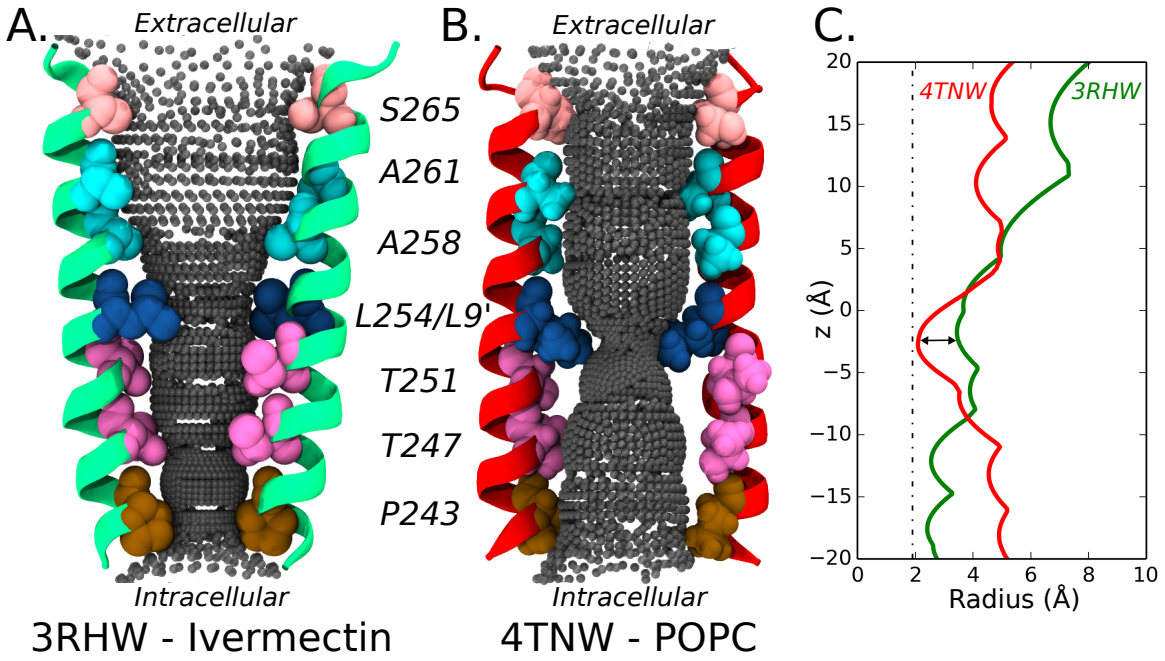


**Fig. 6.10:** M2 helices of GluCl receptor and radii A. and B. (A. pdb 3RHW, Ivermectin, B. 4TNW, POPC) Profiles of 2/5 M2 helices shown for clarity. colour of each will be consistent throughout this chapter. For both, inward, pore facing residues are shown in VdW spheres with corresponding one letter code. C. Radius calculation of pore region from the crystal structures. Image to scale, colour, and corresponds to residues positions in A. and B. Arrow indicates L9' positions with a difference of 1.5 Å between the helices.

Using the same simulation technique as the 5-$HT_3$ receptor, free energy profiles for chloride, sodium and water through the M2 helical lumen were conducted for both conformations of the GluCl receptor (figure 6.11) .

### 6.5.1 Ions and Water

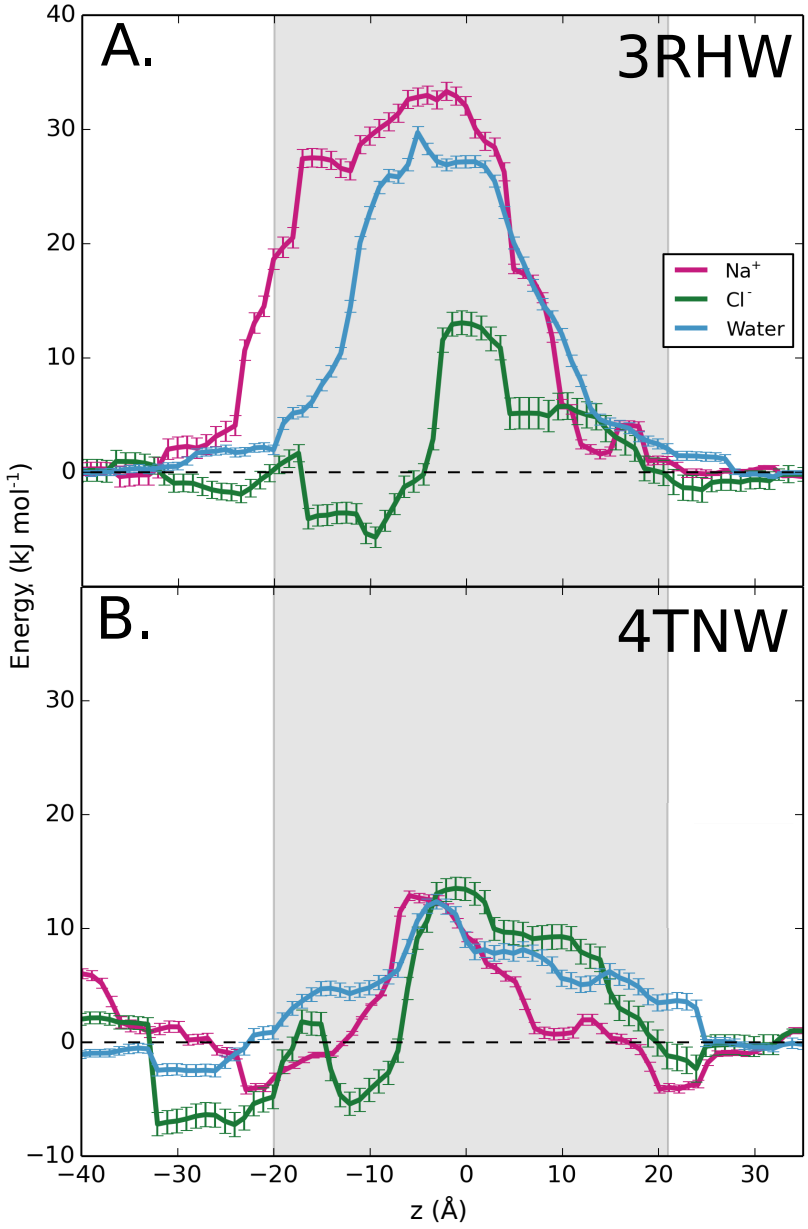


**Fig. 6.11:** Potential of mean force profile of ions and water going through both GluCl M2 structures. A. 3RHW. B. 4NTW from the intracellular (left) to the extracellular regions (right). Both graphs display the translocation pathway (on the x axis) through the helices with calculated energy from that position (y). Initial grey shade represents the z co-ordinate of the pore. Colour is consistent for B. as A. Bootstrapping is used to calculate error. Profiles shown were calculated using 1.5 to 3.5 ns of simulation.

The calculated potential of mean force for both proteins indicates multiple differences between the two. Within the 3RHW structure, high barriers are noted for both $Na^+$ and water of ~33 and 29 kJ $mol^{-1}$. In contrast, the free energy profile recorded for $Cl^-$ is indeed the lowest with a maximum barrier of 13 kJ $mol^{-1}$, and also a favourable free energy for the channels intracellular region. For a chloride channel, a lower free energy of translocation and favourable interactions for chloride is not surprising, however with the high water barrier, translocation in this state is questionable. In the 4TNW profile, all indicate a similar barrier height of 12, 13, and 11 kJ $mol^{-1}$ for sodium, chloride and water. With smaller barriers corresponding to the same region in both profiles for the $Cl^-$ ion.

These values are far lower than the previously calculated profiles for 5-$HT_3$ in this chapter and other profiles previously mentioned, suggesting that they are not a closed state which is initially assumed. However, the position of the barrier at L9' (L254), emphasises the role of the hydrophobic residue at this position in the helix. Looking at open pore PMF values for pLGIC's for the open GLIC structure [228] a barrier of 12.5 kJ $mol^{-1}$ and 17 kJ $mol^{-1}$ have been calculated for $Na^+$ [228, 229]. These values correspond to the 4TNW structure, thus suggesting it may be in a more "open" state. Comparison with 3RHW indicate values correspond to that of the nAChR closed form with a barrier of 25 kJ $mol^{-1}$ [72] at L9'. Free energy calculations of GluCl reported a barrier of 62 kJ $mol^{-1}$ for the closed form, ~42 kJ $mol^{-1}$ for a partially open/closed form and ~21 kJ $mol^{-1}$ for the open conformation (pdb: 4TNV) [233]. Based on these values (also conducted by short, umbrella sampling windows) and the varied values calculated in this chapter, the conductive state of these two proteins cannot be decisively deduced at present.

To determine if these profiles are indeed accurate in their representation of the free energy landscape, and that the 1 Å windows are sufficient within these channels,

convergence akin to the 5-$HT_3$ for the 4TNW structure is analysed (figure 6.12).

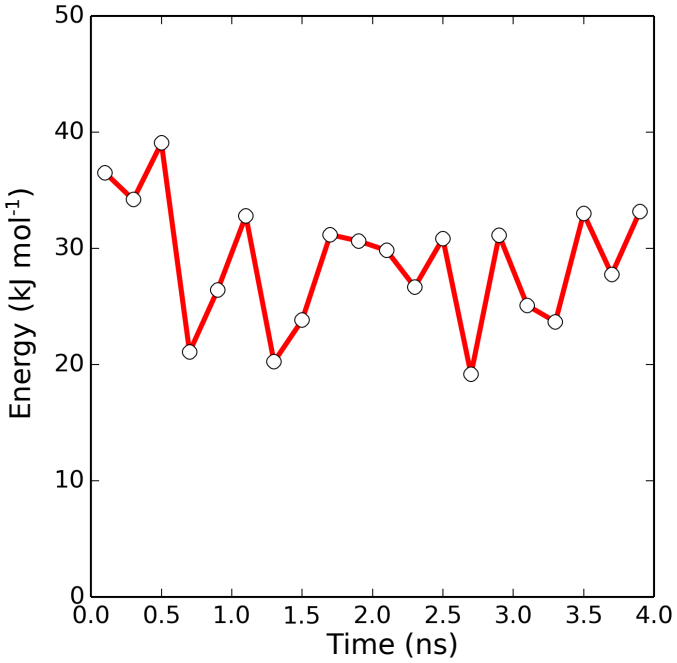


**Fig. 6.12:** Convergence profile for M2 helices of GluCl. Plotted is the maximum calculated free energy for incremental windows. i.e., 0 - 0.2 ns, 0.2- 0.4 ns and so on until 3.8 - 4.0 ns (points are plotted at 0.1 increments) for chloride ion within the 4TNW structure.

The convergence calculated is dissimilar to the profile for the 5-$HT_3$, since a decrease and then a plateau is not seen or reached within the simulation length. Even up to the 4 ns windows simulated, with variability seen through each of the time points indicated that the simulation is not converged. The same trend is seen for the 3RHW structure (data not shown). A longer time for each window could be used for convergence, however this negates the utility of a quick estimate method being investigated. Another possibility could be the stability of the protein itself, which will be questioned later. For comparison and consistency in this chapter, the PMF profile shown previously is between 1.5 and 3.5 ns of each simulation window.

Water hydration shells for $Na^+$, $Cl^-$ and water conducting through the pores have

been calculated for the M2 helices of the GluCl receptor (figure 6.13) based on rdf cut-off distances calculated within a previous chapter (figure 4.9, chapter 4). For both ions in both pores, there is a decrease in the second ion solvation shell through the protein region similar to the 5-$HT_3$ and previous hydrophobic nanopore simulations in this thesis. A larger change is seen for the $Cl^-$ ion shells, which may be related to its native chloride conductance. As before, there is no depletion from the first solvation shell. Unlike the 5-$HT_3$ receptor, there is no precise minima at the L9' residue, but highly variable water depletion through the pore. This could be due to the inconclusive conductive state of each of the structures.

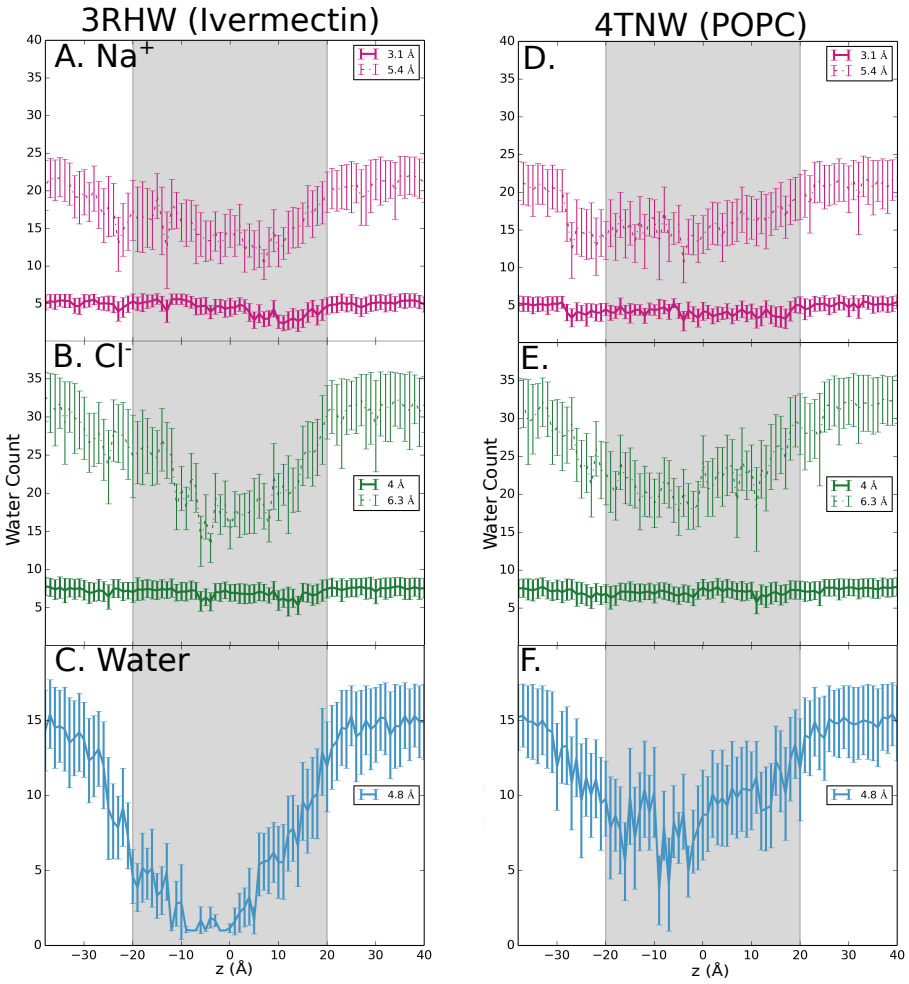


**Fig. 6.13:** Hydration shells for GluCl M2 helices. A. to C. Correspond to 3RHW and D. to F. 4TNW. A. and D. Number of water contacts with the positioned sodium ion (distances of 3.1 and 5.4 Å) with z pathway on the x axis and number of waters within previously calculated rdf (figure within chapter 4) shells on the y axis. B. and E. Chloride (4.0 and 6.3 Å) and C. and F. Water contacts (4.8 Å). For all, calculated radii is indicated. Profile is from intracellular (negative z) to extracellular (positive z).

Based on the utility of the application of a GNM to the channel previously studied in this chapter, similar connections were applied to 4TNW (400 ns) and 3RHW (100 ns), in which pore radius and flux were analysed for an indicated into their conductive states (figure 6.14).

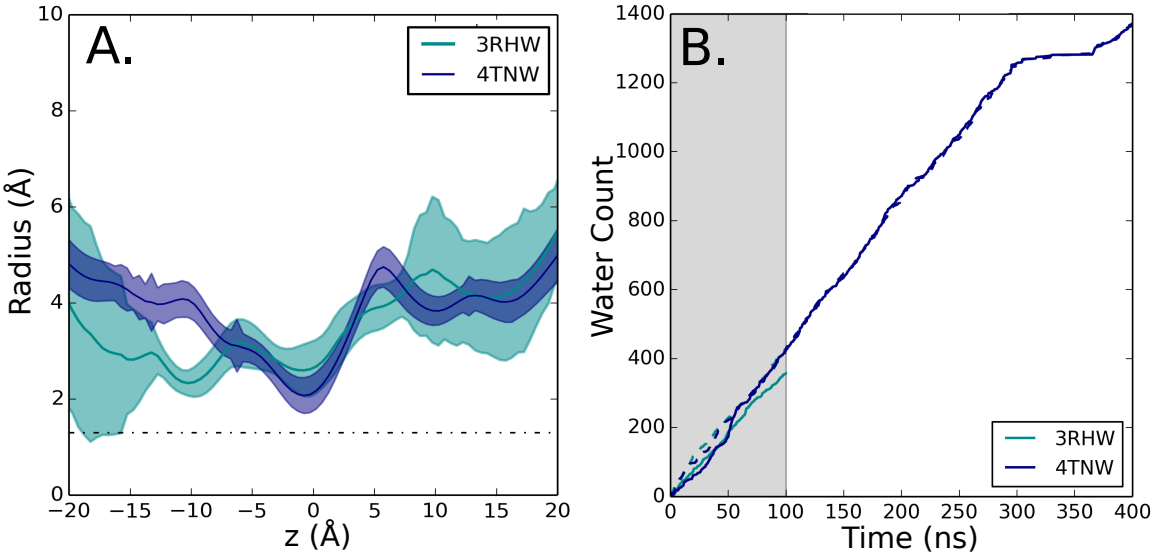


**Fig. 6.14:** Radius and flux of GNM M2 helices of GluCl. A. Radius profile of GNM model structures of GluCl. 0 Å indicates L9'. Dashed line indicateds radius of a water molecule. B. Water flux through the M2 helices under GNM simulation. Grey region indicates simulation length for 3RHW structure.

Pore radius, which is used as a measure of pore "openness" is varied between the two forms, which is to be expected based on the initial conformations. For the 3RHW structure (only simulated for 100 ns due to time constraints towards the end of this thesis), a trend comparable to the radius profile of the static structure (figure 6.10) is noted with a decreasing radius towards the intracellular region (negative) with the minimum corresponding to P243. However, highly variable regions are noted at the N and C termini. This could be due to the limitation of the positioning of the GNM in the model, with the constriction falling below the cut-off and the larger, extracellular region falling above. In the physiological form, the GNM would be continued in both directions by protein, thus the termini are expected to be less flexible than simulated here. Within the POPC modulated form, the constriction radius is that of the crystal structure (figure 6.10) and also highly conserved again at the L9' residue, re-emphasising the importance of this residue and its position in channel gating.

Seen in ENM simulation studies [442], is the decrease in radius at L9' position from 3.3 Å in the static, crystal structures down to 1.8 Å in the ENM of GluCl in an open conformation. This change it not seen in these structures, which could be down to the initial conformation of the helices. In relation to water and ion flow through the pores, based on the PMF profiles (figure 6.11), the conductive states of both suggest that ion flow could be possible through both structures. However, in each of the simulated models, no ion flow was noted through the pores, but higher water flows were observed (~3.5 $ns^{-1}$) than in the closed 5-$HT_3$ receptor, relating to their more open nature than that of the closed serotonin channel.

Unlike the 5-$HT_3$ receptor simulated, within umbrella sampling windows, major deformation has been noted in the M2 helices (5-$HT_3$ data not shown, figure 6.14). Within an umbrella sampling window, protein helical deformation and unfolding occurs within 2 ns of ion restraint within the protein region. This reflects a possible non-native physiological state of the helices and instability. Within the 4 ns window, helical deformation is noted throughout the structure, indicating that this may not be an accurate assumption for the free energy state of these proteins.

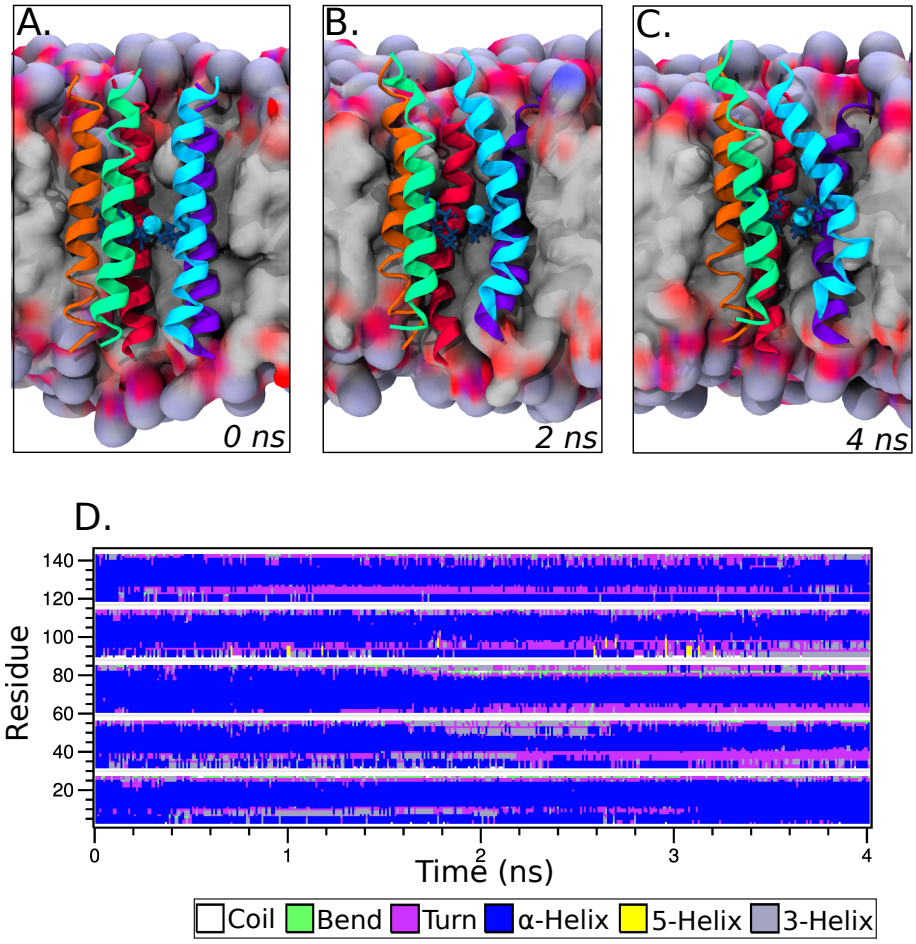


**Fig. 6.15:** Stability of M2 helices of 4TNW during sampling. A. to C. Snapshots of the protein (cartoon, chain coloured) in the bilayer (grey surface) during an umbrella sampling simulation of 4 ns. Chloride is positioned at 53 Å which is the same z value as L9'. A. 0 ns. B. 2 ns. C. 4 ns. D. Time evolution of secondary structure in simulation calculated by DSSP [451]. Blue region represents changing $\alpha$-helical regions of the structure.

Established from these simulations and free energy calculations for this type of protein structure, short, unrestrained, truncated umbrella sampling windows are not an accurate and predictable method for estimating conductive states based on free energy calculations. This could be due to the fact that these proteins are modulated by external molecules which are not included in simulation, and create a destabilising effect. Secondly, each state is not in a definite open or closed state, which could

also reflect on the stability of the protein. It would be interesting to simulate more via equilibrium methods to investigate the true nature of the pore and possibly the whole protein in MD. To predict more accurate, agonist/antagonists could be included, however time scales (and previously mentioned methods) could make this inefficient. Also to be considered are the roles of possible protein C$\alpha$ restraints or possibly the introduction of a GNM into the umbrella sampling windows, as done so by *Yoluk et al* [233].

## 6.6 Conclusion

From this chapter, I have revealed that the 5-$HT_3$ channel is in a closed conformation to cations and anions based on free energy calculations and is hydrophobically gated. The short windows and free energy windows on this stable structure established a possible protocol for looking at other ion channels, their conductivity and state. However, the method is limited to structures which are present in an anticipated stable form, shown by the variation in the GluCl calculations.

### M2 helices

The use of the M2 helices for simulation, and not simulating the entire protein has been shown to influence and be selectivity dependent, thus the estimate of selectivity and permeation can be estimated from this region. With it being suggested that within the 5-$HT_3$ receptor, a single ring of charged amino acids at the intracellular end of the pore (E250) can control the selectivity with mutation (E250A) resulting in a non selective channel [452]. Next to this pore facing glutamate is residue R251 (R0') which has been shown to be conserved in pLGICs, and a change in its charge state being associated with a change in pore selecitivty [453]. In the GlyR channel, mutations of

this conserved residue did not generate any functional channels [454], however within the $\alpha$7-GluCl$\beta$ chimera channel [455] and $\rho$1 $GABA_R$ [439] (both pLGIC's, at R0'), channels were functional and demonstrated lower, moderate changes in their selectivity ratio for both ions.

Therefore it is of interest to consider other, non-lumen facing residues. General mutations within the M2 helices of GlyR also change the selectivity from being anion to cation selective, (P250$\Delta$, A251E and T265V), with the corresponding three inverse mutations making the $\alpha$7 nAChR anion selective [456]. Within the 5-$HT_3$ pore simulated in this chapter, D247 is not included in the pore lining residues, therefore this may have an even larger reflection on the high energy barrier calculated.

## Remainder of the channel

However, use of the M2 region alone is thought not to be substantial enough to determine accurate conductivities, selectivity and even a possible gated state of the channel with various conformations of the extra- and intracellular domains of the protein are known to determine the state of the pore.

It is known that ion flow through the channels is dominated by the narrowest region, with emphasis on residues at the narrowest parts (M2 helices) and also the charged rings at the intracellular and extracellular regions [457], and the cytoplasmic domain [458]. Origin of the ion selectivity in the Cys-loop family of membrane proteins have been investigated with charged amino acids in the extracellular domain (ECD) aiding conductance and selectivity. Previous investigations using computational, structural and electrophysiology of nAChR concluded in negative residues in the ECD contributing to the cationic selectivity of the channel [459]. Also electrophysiology has been conducted on a heteropentameric nAChR channel with focus on the residues on the permeation pathway on the intracellular turn of the M2 channel, 4 Glu and 1 Gln of

the differing subunits at -1'contributing to the cationic conductance [460].

Single channel conductance and ion selectivity is not wholly to do with the M2 region in nAChR or 5-$HT_3$ channels. Experimentally it is shown that the intracellular domain of eukaryotic pLGIC's, especially the TM3-TM4 linker, are associated with conductance and gating of the proteins [461, 462], with simulation indicating key residues within the 5-$HT_3$ receptor within the M2-M3 loops [463]. Positive residue insertion in the extracellular loop region of the 5-$HT_3$ M2-M3 channel resulted in a non-functional construct (A24K, A275K) [452]. Considering the 5-$HT_{3A}$ isoform, rings of charges in the extracellular vestibule influence the ion permeation (D113 and D127). Neutralising mutations of these charges or reversal (*e.g.* D113K) changes the conductance of the channel, with complete loss of current with the D127K mutation [464].Therefore, even with the calculated barrier height within the M2 helices, within for example an open structure as simulated, selectivity cannot be assumed from free energy calculations of the M2 region alone.

Also seen within the nAChR channel, there is a suggested extracellular domain selectivity filter composed of a ring of lysine (K42) residues, 24 Å above the lipid membrane that is thought to act to stabilise ions in the extracellular vestibule of the channel [465]. That is similar feature is observed in the GluCl channel, with 3 layers of positive residues (lysine) within the ECD. It is thought these positive residues could act as an electrostatic well for $Cl^-$ ions, since free energy profiles have an energy minimum of ~10 kJ $mol^{-1}$ in this region [442].

Looking more closely at the different isoforms of the 5-$HT_3$ receptor, assembled as homomers of 5-$HT_{3A}$ (simulated in chapter) or heteromers of 5-$HT_{3A}$ and 5-$HT_{3B}$. In electrophysiology, the differing forms produce differing channel currents of 0.4 pS (A form) [466, 467] and 16 pS [468] (B form). Interestingly, the M2 helices of 5-$HT_{3B}$ appear not to be cation selective (or less selective than that of 5-$HT_{3A}$ [468]).

Now with the high resolution crystal structure being determined and with homology modelling for other conformational states, the investigation of the mechanism of the role of that mutation can be investigated. It is proposed that these arginine residues in the intracellular region of the 5-$HT_{3A}$ may cause electrostatic repulsion of cations [469], causing a lower conductance than that of the 5-$HT_{3AB}$ form. With similar arginine residues in the TM3/TM4 linker [458] and involved in cation repulsion [469].

This could be related to the gating conformational change of pLGIC, where ligand binding is proposed to cause a lateral twisting through the protein, resulting in a twist of the M2 pore changing it from an open to a closed state (or *vice versa*) thus changing their conductive state [279, 454, 470]. Twist motion has been associated with channel gating [471, 472] and seen within the well studied pLGIC, nAChR, changes between open and closed models indicate this twist motion, opening the M2 helices [436]. Targeted MD simulations of the $\alpha$7 nAChR have indicated that a change in the bottom ligand binding site, which is the region thought to allosterically translate motion to the pore domain. With substrate targeting, the channel partially opens within 4 ns with key charged residues involved in ligand binding [473]. Acetylcholine binding to nAChR resulted in ligand binding domain movement, with an ~1 Å outward displacement within the extracellular domain $\beta$ subunit. This resulted down to straightening within the M2 which changes the pore diameter [474] linking the ECD to motion within the helices and accounting for the different M2 helical tilt angles.

Within computational models of GluCl , a variety of pore sizes have been calculated [442], which have also been noted in other studies [427, 453, 456]. These models give variations in the open channel state noted via electrophysiology which could also be accountable for the states crystallised and simulated here. Five conductive states have also been observed for GlyR [426]. Therefore suggesting that there may be no definitive open state if for example, one is running free energy calculations on the

protein to analyse its conformational state.

Short (16ns) constant electric field simulations have also been applied to the cationic nAChR channel [**?** ]. A small voltage (100 mV) resulted in a conduction cation event with transient water in the pore region. A higher field caused more cations to traverse the pore, thus suggesting that it could be possible to simulate such pores, especially the 5-$HT_3$ under such voltage, and also using the CE implemented voltage shown in chapter 5.

With the structure of the 5-$HT_3$ solved, biochemical mutation data can be mapped onto the conductance and gating states of the channel, therefore an assumption of the whole protein may give more accurate barrier/accessibility results than looking at the M2 region only. However, there is computational limitation to the simulation of an entire channel of this size. Also with some of these mutational studies, it is unknown if they could be involved in the selectivity, conduction and gating pathways directly, which is what these type of computational studies examine.

## pH dependence

With the questioned role of charged residues in the selectivity and conductive states of these pores, it has been found that within a nAChR channel, 4 of the glutamate residues (at -1') are de-protonated within the pH range of 6-9, and that 2/4 of the residues contribute to the size of the current measured through the pore. Therefore they are thought to adopt positions which alter the current through the pore based on their protonation state [460].

pH has also been questioned in the GLIC crystal structure, was formed under acidic conditions [53]. In simulations in which the acidity was removed, to a pH of ~7, rapid channel closure at the hydrophobic leucine region occurred followed by a quaternary twist at the ECD region of the M2 helices [444] and is considered to be pH

gated [475]. Therefore, pH may be a factor to consider for the 5-$HT_3$ conductive state, not just the M2 helices but as an entire protein channel. The structure simulated in this thesis was crystalised at pH 7.4, however acidification for example could be used to assess key residues for conduction.

Several simulations have noted dehydration events around the L9' of LGIC's [440–442] however some note this could be down to imprecise protonation states of the channels, with others suggesting that with different protonation states result in a similar dehydration event [441, 442, 444] due to external factors, for example membrane potential and ionic current. Thus $pK_a$ needs to be established and considered for conductive states and gating of the pores, considering the charged residues within the lumen of the 5-$HT_3$ channel and also the influence of surrounding residues.

## Accuracy and other free energy methods

Comparison to other free energy calculations of pLGIC's is vast and varied. Brownian dynamics (BD) and hybrid MD/continuum electrostatics are used to calculate the free energy of $Na^+$ and $Cl^-$ through the channel with barriers noted at 9' L254 and 2' P243 for $Na^+$ of ~25 kJ $mol^{-1}$ and for $Cl^-$ ~15 kJ $mol^{-1}$ [442]. BD simulations also indicate permeability ratios for both ion species with $Cl^-$ being more permeable than $Na^+$. These values are comparable to the values calculated and indicate that 15 kJ $mol^{-1}$ is the appropriate value for an open, chloride ion channel.

Ion permeation barriers have also been calculated in the nAChR and GlyR pLGIC's. ABF calculations with both $Na^+$ and $Cl^-$ of both pores indicate a barrier corresponding to anion rejection of ~35 kJ $mol^{-1}$ for $Cl^-$ within nAChR with the barrier associated with the hydrophobic region. Within the GlyR model, a barrier of ~29 kJ $mol^{-1}$ is found for $Na^+$. However, no hydrophobic barrier akin to the nAChR channel is observed [450], therefore the various free energy methods used are all indicating similar

barriers within the open and closed structures.

The use of the ENM/GNM may be a useful direction for the study of these M2 helices. It is known from MD relaxation that closed state channels are often formed [316, 444]. This is undesirable if simulation involves a structure of a questionable state. Demonstrated in [442] is the use of such a ENM-protein method on maintaining channel stability and openness through a simulation, be it for the full receptor. Also simulated under ENM were hybrid MD/BD simulations and ABF calculations for free energy calculations [476, 477]. Due to the size of the system in this case, the TMD domain of the channel is an all atom form, however the extracellular region is at a lower resolution in a continuum electrostatic representation thus being more computationally and time efficient. I have tried to extrapolate this from the structure in this chapter with the use of just the M2 construct.

Recently, a free energy profile using umbrella sampling methods was constructed of an entire GluCl channel using varying conformations derived from simulation (with the removal and addition of agonist glutamate to induce conformational change) [233]. Within this study, short windows of 2 ns were run at every 0.5 Å through the lumen of three different conformations of the GluCl receptor, termed closed, half open/closed and open based on the radius of the M2 helices. Energy barriers for $Cl^-$ were reported through the pore at the L9' position of ~63 and 42 kJ $mol^{-1}$ and within the "open" structure ~21 kJ $mol^{-1}$. These results agree with the calculated closed state values for the 5-$HT_3$ profiled in this chapter, but also to the hydrophobic barriers calculated in the 14-$\beta$ stranded, three leucine hydrophobic pores within this thesis (and paper [299]).

# Chapter 7

# Conclusion

*"They tell you I'm insane"*

Taylor Swift

The work presented in this thesis addresses several aspects of the computational simulation of hydrophobic gating within nanopores and ion channels. Initially, the chemical nature of amino acids was varied and modelled in a number of biomimetic nanopore models to show any influence on water flow through (chapter 3). Building such motifs resulted in the energetic understanding of how hydrophobic residues in the models constructed are interacting with water, ions and hydrophobic molecules (chapter 4). It was found that the breaking of such barriers could be effected by external forces such as voltage (chapter 5). The underlying hydrophobic theme was then used to explore the functional state of the crystal structure of an ion channel (chapter 6).

## 7.1 Computational Design of Nanopores

Firstly, a computational approach to building and simulating $\beta$-barrel nanopores has been investigated in which a number of porin and lytic proteins were systematically

explored as mimics for the size of the barrels. Modeller derived barrels and equilibrium simulations of 100 ns in DPPC bilayers suggest that stable barrels can be formed in this manner for further investigations. Within the pores, the shape and chemical nature can also be modified; be it central or terminal construction, and polar or apolar residues, this can result in a different conductive state of the pore based on the size of the models. With the 14 strand $\beta$-pores, I have been able to computationally transplant a hydrophobic barrier to water and ions based on the dimensions of hydrophobic gates within channel proteins.

Based on this method, transplantation of other motifs that can influence gating and selectivity of their native proteins is seen to be the next reasonable direction. This could be a charged constriction as seen in *e.g.* OmpF and OmpC porins [298], a titrable residue observed in the protonation state of His37 in influenza M2 channel [478], or replication of the phenylalanine, tryptophan and leucine selectivity filter in the *Helicobacter pylori* urea transporter, which has been characterised computationally [479]. In the case of the latter two (and hydrophobic gating), protein conformation also contributes to the residue behaviour, and to replicate this change in dimensions, barrel size can also be modulated in terms of the number of strands to imitate a change in conductive radii.

## 7.2 Hydrophobic Gates

Secondly, a hydrophobic barrier has been characterised within a computational model nanopore. Free energy calculations have been used to estimate ion species and water molecules going through hydrophobic regions of this nature, extending previously studies on hydrophobic nanopores and the energetics of transport through them. Another outcome would be the use of water as a proxy for the ionic conductance of a pore. Shown in the work of this chapter is that high barriers to water permeation

do actually correspond to regions which are functionally closed to ions. In turn, this allowed for the prediction of conductivity from shorter simulations without sufficient ion conduction events. The nature of hydrophobic transport through such regions has also been investigated on longer time scale simulations, however still are not sufficient for an accurate estimate of such energies. The free energy simulation method used may also be transferable to other proteins or motifs in which hydrophobic barriers could be investigated, as a relatively quick way of establishing if such barriers are present. I have worked on the assumption that short, small spaced windows can be used to explore the free energy that will in theory not allow much protein movement, shown in previous free energy calculations [232].

Umbrella sampling has been used in this chapter to investigate the free energy, however there are other methods available [336]. Examples of this, thermodynamic integration or free energy perturbation, which can be used to calculate the maxima within the hydrophobic bands or regions. Metadynamics can also be used for permeation simulations, such as translocation of ions through potassium selectivity filters [480], in which a single simulation can be used instead of multiple, allowing for a more efficient method for free energy calculations on many molecule types.

## 7.3 Simulation of Voltage

Within chapter 5, it has been demonstrated that electrowetting of a hydrophobic gate within a $\beta$-barrel nanopore is feasible in a simulation using both constant electric field methods and a "computational electrophysiology" type protocol to implement a voltage. The conducting water within the hydrophobic region is similar to other proteins with hydrophobicity [402], CNTs [224], and theoretical nanopores [203, 351] under a simulation voltage and electroporation under higher voltages.

Higher voltages were applied to try and break the hydrophobic barrier within the

larger model nanopores, resulting in the breakdown of the bilayer around the protein. To allow higher voltages, simulations could be performed using a lipid with a higher voltage threshold to induce these breaks. These could include *e.g.* the branched chain archaeal lipid DPhPC and related species which are known in simulation to break at higher thresholds [218]. There is also (as mentioned throughout this thesis) scope for the use of various water models which could induce a differing dipole, and polarisability under a potential difference.

## 7.4 High-throughput Selection of Protein Gates

Finally, with the protocol for hydrophobic biomimetic pores devised, this was then utilised on a protein pore which possibly contained a hydrophobic gate. It has been shown that the 5-$HT_3$ channel is in a closed conformation to cations and anions, based on free energy calculations, and is hydrophobically gated. Short umbrella sample time scales, 1 Å windows, and simulation of only the M2 helices can give an accurate value, corresponding to other calculated values of closed state channels. This creates a possible protocol for looking at other ion channels, their conductivity and state. However, the method is limited to structures that are present in an anticipated stable form.

Use of harmonic restraints, in the form of an elastic or Gaussian network have been shown to modulate and stabilise closed and open forms of pLGICs [316, 444], and has been used in combination with free energy methods (ABF) [442] to predict accurate barriers. Use of only the M2 helix within this thesis, led to the observation of abnormal motion at the N and C termini and within the helices themselves. Incorporation of such networks into the M2 helices under umbrella sampling would reduce atypical protein movement, thus providing a more accurate measure of the free energy landscape.

### Limitations of Molecular Dynamics

When using MD to simulate a system, it is important to remember the limitations of the method. Problems can arise from the fact that force fields are imperfect, an example being the free energy of solvation of amino acids which often have an error of ~1 kJ $mol^{-1}$. As such, the error of the calculations within this thesis can be carried along. When considering polarisation within these force fields, water molecules can reorientate as shown here, however their partial charge is fixed [235]. Therefore, as repeated within this simulation, it would be advantageous to use a more detailed water model [257], however this would lead to a decrease in computational efficiency to a high degree. Other limitations include the simulation of pH and the inability of proton transfer in simulation, and also the general limitation in simulation timescale and size that can lead to low sampling problems.

# References


[1] S. Singer and G. Nicolson, "The fluid mosaic model of the structure of cell membranes," *Science*, vol. 175, pp. 720–731, 1972.

[2] M. Luckey, *Membrane Structural Biology: With Biochemical and Biophysical Foundations*. Cambridge University Press, 2008.

[3] M. C. Wiener, G. I. King, and S. H. White, "Structure of a fluid dioleoylphosphatidylcholine bilayer determined by joint refinement of x-ray and neutron diffraction data. I. Scaling of neutron data and the distributions of double bonds and water.," *Biophys. J.*, vol. 60, pp. 568–576, 1991.

[4] A. Parsegian, "Energy of an ion crossing a low dielectric membrane: solutions to four relevant electrostatic problems.," *Nature*, vol. 221, pp. 844–846, 1969.

[5] H. C. Gram, "Über die isolierte färbung der schizomyceten in schnitt- und trockenpräparaten," *Frotschritte der Mdeizin*, vol. 2, pp. 185 – 189, 1884.

[6] J. Parkin, M. Chavent, and S. Khalid, "Molecular Simulations of Gram-Negative Bacterial Membranes: A Vignette of Some Recent Successes," *Biophys. J.*, vol. 109, pp. 461–468, 2015.

[7] H. T. McMahon and J. L. Gallop, "Membrane curvature and mechanisms of dynamic cell membrane remodelling.," *Nature*, vol. 438, pp. 590–596, 2005.

[8] H. T. McMahon and E. Boucrot, "Membrane curvature at a glance," *J. Cell Sci.*, vol. 128, pp. 1065–1070, 2015.

[9] C. Sohlenkamp and O. Geiger, "Bacterial membrane lipids: diversity in structures and pathways," *FEMS Microbiol. Rev.*, pp. 1–27, 2015.

[10] P. Sperandeo, G. Dehò, and A. Polissi, "The lipopolysaccharide transport system of Gram-negative bacteria," *Biochim. Biophys. Acta - Mol. Cell Biol. Lipids*, vol. 1791, pp. 594–602, 2009.

[11] M. A. Ferrero, H. Martínez-Blanco, F. F. Lopez-Velasco, *et al.*, "Purification and characterization of GlcNAc-6-P 2-epimerase from Escherichia coli K92," *Acta Biochim. Pol.*, vol. 54, pp. 387–399, 2007.

[12] L. K. Tamm, "Structure and Assembly of $\beta$-Barrel Membrane Proteins," *J. Biol. Chem.*, vol. 276, pp. 32399–32402, 2001.

[13] J. P. Saenz, E. Sezgin, P. Schwille, and K. Simons, "Functional convergence of hopanoids and sterols in membrane ordering," *Proc. Natl. Acad. Sci.*, vol. 109, pp. 14236–14240, 2012.

[14] A. Krogh, B. Larsson, G. von Heijne, and E. L. Sonnhammer, "Predicting transmembrane protein topology with a hidden Markov model: application to complete genomes.," *J. Mol. Biol.*, vol. 305, pp. 567–580, 2001.

[15] J. L. Popot and D. M. Engelman, "Helical membrane protein folding, stability, and evolution.," *Annu. Rev. Biochem.*, vol. 69, pp. 881–922, 2000.

[16] D. J. F. Du Plessis, N. Nouwen, and A. J. M. Driessen, "The Sec translocase," *Biochim. Biophys. Acta - Biomembr.*, vol. 1808, pp. 851–865, 2011.

[17] I. Lasters, S. J. Wodak, P. Alard, and E. van Cutsem, "Structural principles of parallel $\beta$-barrels in proteins.," *Proc. Natl. Acad. Sci.*, vol. 85, pp. 3338–3342, 1988.

[18] A. G. Murzin, A. M. Lesk, and C. Chothia, "Principles Determining the Structure of $\beta$-Sheet Barrels in Proteins I. A Theoretical Analysis," *J. Mol. Biol.*, vol. 236, pp. 1369–1381, 1994.

[19] R. Hancock, "Role of Porins in Outer Membrane Permeability," *J. Bacteriol.*, vol. 169, pp. 929–933, 1987.

[20] W. C. Wimley, "The versatile $\beta$-barrel membrane protein," *Curr. Opin. Struct. Biol.*, vol. 13, pp. 404–411, 2003.

[21] G. E. Schulz, "The structure of bacterial outer membrane proteins.," *Biochim. Biophys. Acta*, vol. 1565, pp. 308–317, 2002.

[22] J. W. Fairman, N. Noinaj, and S. K. Buchanan, "The structural biology of $\beta$-barrel membrane proteins: a summary of recent reports.," *Curr. Opin. Struct. Biol.*, vol. 21, pp. 523–531, 2011.

[23] M. Bayrhuber and T. Meins, "Structure of the human voltage-dependent anion channel," *Proc. Natl. Acad. Sci.*, vol. 105, pp. 15370–15375, 2008.

[24] R. Ujwal, D. Cascio, J.-P. Colletier, *et al.*, "The crystal structure of mouse VDAC1 at 2.3 Å resolution reveals mechanistic insights into metabolite gating.," *Proc. Natl. Acad. Sci.*, vol. 105, pp. 17742–17747, 2008.

[25] J. P. Rosenbusch, "Characterization of Major Envelope Protein from *Escherichia- Coli*," *J. Biol. Chem.*, vol. 249, pp. 8010 – 8029, 1974.

[26] S. Schenkman, A. Tsugita, M. Schwartz, and J. P. Rosenbusch, "Topology of Phage Lambda Receptor Protein," *J. Biol. Chem.*, vol. 259, pp. 7570–7576, 1984.

[27] T. Schirmer, "General and specific porins from bacterial outer membranes.," *J. Struct. Biol.*, vol. 121, pp. 101–9, 1998.

[28] G. E. Schulz, "Porins: general to specific, native to engineered passive pores.," *Curr. Opin. Struct. Biol.*, vol. 6, pp. 485–90, 1996.

[29] J.-M. Pagès, C. E. James, and M. Winterhalter, "The Porin and the Permeating Antibiotic: A Selective Diffusion Barrier in Gram-Negative Bacteria.," *Nat. Rev. Microbiol.*, vol. 6, pp. 893–903, 2008.

[30] J. H. Lakey, "Voltage gating in porin channels.," *FEBS Lett.*, vol. 211, pp. 1–4, 1987.

[31] N. Liu, H. Samartzidou, K. W. Lee, J. M. Briggs, and a. H. Delcour, "Effects of pore mutations and permeant ion concentration on the spontaneous gating activity of OmpC porin.," *Protein Eng.*, vol. 13, pp. 491–500, 2000.

[32] N. Liu and a. H. Delcour, "The spontaneous gating activity of OmpC porin is affected by mutations of a putative hydrogen bond network or of a salt bridge between the L3 loop and the barrel.," *Protein Eng.*, vol. 11, pp. 797–802, 1998.

[33] C. M. Soares, J. Björkstén, and O. Tapia, "L3 Loop-Mediated Mechanisms of Pore Closing in Porin: A Molecular Dynamics Perturbation Approach.," *Protein Eng.*, vol. 8, pp. 5–12, 1995.

[34] M. Chen, S. Khalid, M. S. P. Sansom, and H. Bayley, "Outer Membrane protein G: Engineering a Quiet Pore for Biosensing," *Proc. Natl. Acad. Sci.*, vol. 105, pp. 6272–6277, 2008.

[35] C. P. Moon, N. R. Zaccai, P. J. Fleming, D. Gessmann, and K. G. Fleming, "Membrane Protein Thermodynamic Stability may serve as the Energy Sink for Sorting in the Periplasm.," *Proc. Natl. Acad. Sci.*, vol. 110, pp. 4285–4290, 2013.

[36] S. White, "Membrane Proteins of Known Structure," *http://blanco.biomol.uci.edu/mpstruc/*.

[37] P. J. L. Werten, H. W. Rémigy, B. L. De Groot, *et al.*, "Progress in the analysis of membrane protein structure and function," *FEBS Lett.*, vol. 529, pp. 65–72, 2002.

[38] R. Grisshammer and C. G. Tate, "Overexpression of integral membrane proteins for structural studies.," *FEBS Lett.*, vol. 504, pp. 94–98, 2001.

[39] M. Caffrey, "Crystallizing membrane proteins for structure determination: use of lipidic mesophases.," *Annu. Rev. Biophys.*, vol. 38, pp. 29–51, 2009.

[40] K. R. Vinothkumar, J. Zhu, and J. Hirst, "Architecture of mammalian respiratory complex I," *Nature*, vol. 515, pp. 80–84, 2014.

[41] J. Du, W. Lü, S. Wu, Y. Cheng, and E. Gouaux, "Glycine receptor mechanism elucidated by electron cryo-microscopy," *Nature*, 2015.

[42] M. Hiller, L. Krabben, K. R. Vinothkumar, *et al.*, "Solid-state magic-angle spinning NMR of outer-membrane protein G from Escherichia coli," *ChemBioChem*, vol. 6, pp. 1679–1684, 2005.

[43] S. Hiller, R. G. Garces, T. J. Malia, *et al.*, "Soloution Structure of the Integral Human Membrane Protein VDAC-1 in Detergent Micelles," *Science.*, vol. 321, pp. 1206–1210, 2008.

[44] F. Hagn and M. Etzkorn, "Optimized Phospholipid Bilayer Nanodiscs Facilitate High-Resolution Structure Determination of Membrane Proteins," *J. Am. Chem. Soc.*, vol. 135, pp. 1919–1925, 2013.

[45] C. N. Connolly and K. A. Wafford, "The Cys-loop superfamily of ligand-gated ion channels: the impact of receptor structure on function," *Biochem. Soc. Trans.*, vol. 32, pp. 529–534, 2004.

[46] H. A. Lester, M. I. Dibas, D. S. Dahan, J. F. Leite, and D. a. Dougherty, "Cys-loop receptors: New twists and turns," *Trends Neurosci.*, vol. 27, pp. 329–336, 2004.

[47] N. Unwin, "Acetylcholine receptor channel imaged in the open state.," *Nature*, vol. 373, pp. 37–43, 1995.

[48] A. Miyazawa, Y. Fujiyoshi, and N. Unwin, "Structure and gating mechanism of the acetylcholine receptor pore.," *Nature*, vol. 423, pp. 949–955, 2003.

[49] N. Unwin, "Refined structure of the nicotinic acetylcholine receptor at 4 Å resolution," *J. Mol. Biol.*, vol. 346, pp. 967–989, 2005.

[50] O. Beckstein, P. C. Biggin, P. Bond, *et al.*, "Ion channel gating: insights via molecular simulations," *FEBS Lett.*, vol. 555, pp. 85–90, 2003.

[51] N. Bocquet, H. Nury, M. Baaden, *et al.*, "X-ray structure of a pentameric ligand-gated ion channel in an apparently open conformation.," *Nature*, vol. 457, pp. 111–114, 2009.

[52] R. J. C. Hilf and R. Dutzler, "Structure of a potentially open state of a proton-activated pentameric ligand-gated ion channel.," *Nature*, vol. 457, pp. 115–8, 2009.

[53] R. J. C. Hilf and R. Dutzler, "X-ray structure of a prokaryotic pentameric ligand-gated ion channel.," *Nature*, vol. 452, pp. 375–379, 2008.

[54] R. E. Hibbs and E. Gouaux, "Principles of activation and permeation in an anion-selective Cys-loop receptor," *Nature*, vol. 474, pp. 54–59, 2011.

[55] T. Althoff, R. E. Hibbs, S. Banerjee, and E. Gouaux, "X-ray structures of GluCl in apo states reveal a gating mechanism of Cys-loop receptors," *Nature*, vol. 512, pp. 333–337, 2014.

[56] P. S. Miller and A. R. Aricescu, "Crystal structure of a human $GABA_A$ receptor.," *Nature*, vol. 512, pp. 270–275, 2014.

[57] S. Uysal, V. Vásquez, V. Tereshko, *et al.*, "Crystal structure of full-length KcsA in its closed conformation.," *Proc. Natl. Acad. Sci.*, vol. 106, pp. 6644–6649, 2009.

[58] M. Madeja, "Extracellular Surface Charges in Voltage-Gated Ion Channels," *News Physiol. Sci.*, vol. 15, pp. 15–19, 2000.

[59] Y. Zhou, J. H. Morais-Cabral, A. Kaufman, and R. MacKinnon, "Chemistry of ion coordination and hydration revealed by a $K^+$ channel-Fab complex at 2.0 Å resolution.," *Nature*, vol. 414, pp. 43–48, 2001.

[60] G. Hummer, J. C. Rasaiah, and J. P. Noworyta, "Water conduction through the hydrophobic channel of a carbon nanotube.," *Nature*, vol. 414, pp. 188–190, 2001.

[61] O. Beckstein, P. C. Biggin, and M. S. P. Sansom, "A Hydrophobic Gating Mechanism for Nanopores," *J. Phys. Chem. B*, vol. 105, pp. 12902–12905, 2001.

[62] O. Beckstein and M. S. P. Sansom, "The influence of geometry, surface character, and flexibility on the permeation of ions and water through biological pores.," *Phys. Biol.*, vol. 1, pp. 42–52, 2004.

[63] R. Allen, S. Melchionna, and J. Hansen, "Permeation of Nanopores by Water: The Effects of Channel Polarization," *J. Phys. Condens. Matter*, vol. 15, pp. S297–S302, 2003.

[64] R. Allen, J.-P. Hansen, and S. Melchionna, "Molecular dynamics investigation of water permeation through nanopores," *J. Chem. Phys.*, vol. 119, p. 3905, 2003.

[65] R. Roth, D. Gillespie, W. Nonner, and R. E. Eisenberg, "Bubbles, Gating, and Anesthetics in Ion Channels.," *Biophys. J.*, vol. 94, pp. 4282–4298, 2008.

[66] P. Aryal, F. Abd-Wahab, G. Bucci, M. S. P. Sansom, and S. J. Tucker, "A hydrophobic barrier deep within the inner pore of the TWIK-1 K2P potassium channel," *Nat. Commun.*, vol. 5, pp. 1–9, 2014.

[67] P. Aryal, M. S. P. Sansom, and S. J. Tucker, "Hydrophobic Gating in Ion Channels," *J. Mol. Biol.*, vol. 427, pp. 121–130, 2014.

[68] O. Beckstein, K. Tai, and M. S. P. Sansom, "Not ions alone: barriers to ion permeation in nanopores and channels.," *J. Am. Chem. Soc.*, vol. 126, pp. 14694–14695, 2004.

[69] J. Dzubiella, R. J. Allen, and J. P. Hansen, "Electric field-controlled water permeation coupled to ion transport through a nanopore," *J. Chem. Phys.*, vol. 120, pp. 5001–5004, 2004.

[70] M. R. Powell, L. Cleary, M. Davenport, K. J. Shea, and Z. S. Siwy, "Electric-Field-Induced Wetting and Dewetting in Single Hydrophobic Nanopores.," *Nat. Nanotechnol.*, vol. 6, pp. 798–802, 2011.

[71] J. L. Trick, P. Aryal, S. J. Tucker, and M. S. P. Sansom, "Molecular simulation studies of hydrophobic gating in nanopores and ion channels," *Biochem. Soc. Trans.*, vol. 43, pp. 146–150, 2015.

[72] O. Beckstein and M. S. P. Sansom, "A hydrophobic gate in an ion channel: the closed state of the nicotinic acetylcholine receptor.," *Phys. Biol.*, vol. 3, pp. 147–59, 2006.

[73] B. Corry, "An Energy-Efficient Gating Mechanism in the Acetylcholine Receptor Channel Suggested by Molecular and Brownian Dynamics," *Biophys. J.*, vol. 90, pp. 799–810, 2006.

[74] X. Cheng, I. Ivanov, H. Wang, S. M. Sine, and J. A. McCammon, "Molecular-dynamics simulations of ELIC - A prokaryotic homologue of the nicotinic acetylcholine receptor," *Biophys. J.*, vol. 96, pp. 4502–4513, 2009.

[75] F. Zhu and G. Hummer, "Drying transition in the hydrophobic gate of the GLIC channel blocks ion conduction.," *Biophys. J.*, vol. 103, pp. 219–227, 2012.

[76] F. Zhu and G. Hummer, "Theory and Simulation of Ion Conduction in the Pentameric GLIC Channel," *J. Chem. Theory Comput.*, vol. 8, pp. 3759–3768, 2012.

[77] P. Blount and P. C. Moe, "Bacterial Mechanosensitive Channels: Integrating Physiology, Structure and Function," *Trends Microbiol.*, vol. 7, pp. 420–424, 1999.

[78] K. Yoshimura, A. Batiza, M. Schroeder, P. Blount, and C. Kung, "Hydrophilicity of a Single Residue within MscL Correlates with Increased Channel Mechanosensitivity.," *Biophys. J.*, vol. 77, pp. 1960–1972, 1999.

[79] A. Anishkin, B. Akitake, K. Kamaraju, C.-S. Chiang, and S. Sukharev, "Hydration properties of mechanosensitive channel pores define the energetics of gating.," *J. Phys. Condens. Matter*, vol. 22, p. 454120, 2010.

[80] J. P. Birkner, B. Poolman, and A. Koçer, "Hydrophobic Gating of Mechanosensitive Channel of Large Conductance Evidenced by Single-Subunit Resolution.," *Proc. Natl. Acad. Sci.*, vol. 109, pp. 12944–12949, 2012.

[81] M. Ø. Jensen, D. W. Borhani, K. Lindorff-Larsen, *et al.*, "Principles of Conduction and Hydrophobic Gating in $K^+$ Channels.," *Proc. Natl. Acad. Sci.*, vol. 107, pp. 5833–5838, 2010.

[82] M. Ø. Jensen, V. Jogini, D. W. Borhani, *et al.*, "Mechanism of Voltage Gating in Potassium Channels," *Science.*, vol. 336, pp. 229–233, 2012.

[83] C. Neale, N. Chakrabarti, P. Pomorski, E. F. Pai, and R. Pomès, "Hydrophobic Gating of Ion Permeation in Magnesium Channel CorA," *PLOS Comput. Biol.*, vol. 11, p. e1004303, 2015.

[84] M. S. Ardejani, N. X. Li, and B. P. Orner, "Stabilization of a Protein Nanocage through the Plugging of a Protein-Protein Interfacial Water Pocket," *Biochemistry*, vol. 50, pp. 4029–4037, 2011.

[85] R. K. Singh, M. K. Tiwari, R. Singh, and J. K. Lee, "From protein engineering to immobilization: Promising strategies for the upgrade of industrial enzymes," *Int. J. Mol. Sci.*, vol. 14, pp. 1232–1277, 2013.

[86] J. M. Perez-Aguilar and J. G. Saven, "Computational design of membrane proteins.," *Structure*, vol. 20, pp. 5–14, 2012.

[87] H. Bayley, T. Luchian, S.-H. Shin, and M. Steffensen, "Single Molecules and Nanotechnology," in *Single Molecule Covalent Chemistry in a Protein Nanoreactor*, pp. 251–277, Springer, Heidelberg, 2008.

[88] O. Braha, B. Walker, S. Cheley, *et al.*, "Designed protein pores as components for biosensors.," *Chem. Biol.*, vol. 4, pp. 497–505, 1997.

[89] H. Bayley and P. S. Cremer, "Stochastic Sensors Inspired by Biology," *Nature*, vol. 413, pp. 226–30, 2001.

[90] C. Y. Lee, W. Choi, J.-H. Han, and M. S. Strano, "Coherence resonance in a single-walled carbon nanotube ion channel.," *Science*, vol. 329, pp. 1320–1324, 2010.

[91] T. a. Hilder, R. Yang, D. Gordon, A. P. Rendell, and S. H. Chung, "Silicon carbide nanotube as a chloride-selective channel," *J. Phys. Chem. C*, vol. 116, pp. 4465–4470, 2012.

[92] J. K. Holt, H. G. Park, Y. Wang, *et al.*, "Fast mass transport through sub-2-nanometer carbon nanotubes.," *Science*, vol. 312, pp. 1034–1037, 2006.

[93] M. Majumder and B. Corry, "Anomalous decline of water transport in covalently modified carbon nanotube membranes.," *Chem. Commun.*, vol. 47, pp. 7683–7685, 2011.

[94] B. Corry, "Designing carbon nanotube membranes for efficient water desalination.," *J. Phys. Chem. B*, vol. 112, pp. 1427–1434, 2008.

[95] S. a. Kosa, G. Al-Zhrani, and M. Abdel Salam, "Removal of heavy metals from aqueous solutions by multi-walled carbon nanotubes modified with 8-hydroxyquinoline," *Chem. Eng. J.*, vol. 181-182, pp. 159–168, 2012.

[96] J. Lee and N. R. Aluru, "Water-solubility-driven separation of gases using graphene membrane," *J. Memb. Sci.*, vol. 428, pp. 546–553, 2013.

[97] J. H. Park, S. B. Sinnott, and N. R. Aluru, "Ion separation using a Y-junction carbon nanotube," *Nanotechnology*, vol. 17, pp. 895–900, 2006.

[98] X. Diao, H. Chen, G. Zhang, F. Zhang, and X. Fan, "Magnetic carbon nanotubes for protein separation," *J. Nanomater.*, vol. 2012, pp. 1–7, 2012.

[99] G. M. Cherf, K. R. Lieberman, H. Rashid, *et al.*, "Automated Forward and Reverse Ratcheting of DNA in a Nanopore at 5-Å Precision," *Nat. Biotechnol.*, vol. 30, pp. 344–348, 2012.

[100] E. A. Manrao, I. M. Derrington, A. H. Laszlo, *et al.*, "Reading DNA at Single-Nucleotide Resolution with a Mutant MspA Nanopore and Phi29 DNA Polymerase.," *Nat. Biotechnol.*, vol. 30, pp. 349–353, 2012.

[101] E. Pennisi, "Search for Pore-fection," *Science.*, vol. 336, pp. 534–537, 2012.

[102] P. M. Ashton, S. Nair, T. Dallman, *et al.*, "MinION nanopore sequencing identifies the position and structure of a bacterial antibiotic resistance island," *Nat. Biotechnol.*, vol. 33, pp. 296–299, 2015.

[103] M. Jain, I. T. Fiddes, K. H. Miga, *et al.*, "Improved data analysis for the MinION nanopore sequencer," *Nat. Methods*, vol. 12, 2015.

[104] S. Fernandez-Lopez, H. Kim, and E. Choi, "Antibacterial agents based on the cyclic D, L-$\alpha$-peptide architecture," *Nature*, vol. 412, pp. 452–456, 2001.

[105] X. J. A. Janssen, M. P. Jonsson, C. Plesa, *et al.*, "Rapid manufacturing of low-noise membranes for nanopore sensors by trans-chip illumination lithography," *Nanotechnology*, vol. 23, p. 475302, 2012.

[106] S. Howorka and Z. Siwy, "Nanopore analytics: sensing of single molecules," *Chem. Soc. Rev.*, pp. 2360–2384, 2009.

[107] X. Hou, W. Guo, and L. Jiang, "Biomimetic smart nanopores and nanochannels.," *Chem Soc Rev*, vol. 40, pp. 2385–401, 2011.

[108] S. W. Kowalczyk, T. R. Blosser, and C. Dekker, "Biomimetic nanopores: learning from and about nature.," *Trends Biotechnol.*, vol. 29, pp. 607–14, 2011.

[109] D. H. Stoloff and M. Wanunu, "Recent trends in nanopores for biotechnology.," *Curr. Opin. Biotechnol.*, vol. 24, pp. 699–704, 2013.

[110] L. Song, M. R. Hobaugh, C. Shustak, *et al.*, "Structure of Staphylococcal $\alpha$-Hemolysin, A Heptameric Transmembrane Pore.," *Science.*, vol. 274, pp. 1859–66, 1996.

[111] J. J. Kasianowicz, D. L. Burden, L. C. Han, S. Cheley, and H. Bayley, "Genetically Engineered Metal Ion Binding Sites on the Outside of a Channel 's Transmembrane $\beta$-Barrel," *Biophys. J.*, vol. 76, pp. 837–845, 1999.

[112] L. Movileanu, S. Howorka, O. Braha, and H. Bayley, "Detecting protein analytes that modulate transmembrane movement of a polymer chain within a single protein pore.," *Nat. Biotechnol.*, vol. 18, pp. 1091–1095, 2000.

[113] L. Q. Gu, O. Braha, S. Conlan, S. Cheley, and H. Bayley, "Stochastic sensing of organic analytes by a pore-forming protein containing a molecular adapter.," *Nature*, vol. 398, pp. 686–690, 1999.

[114] X. Guan, L.-q. Gu, S. Cheley, O. Braha, and H. Bayley, "Stochastic Sensing of TNT with a Genetically Engineered Pore," *ChemBioChem.*, vol. 6, pp. 1875–1881, 2005.

[115] X. F. Kang, S. Cheley, X. Guan, and H. Bayley, "Stochastic detection of enantiomers," *J. Am. Chem. Soc.*, vol. 128, pp. 10684–10685, 2006.

[116] D. Branton, D. W. Deamer, A. Marziali, *et al.*, "The potential and challenges of nanopore sequencing.," *Nat. Biotechnol.*, vol. 26, pp. 1146–1153, 2008.

[117] M. Akeson, D. Branton, J. J. Kasianowicz, E. Brandin, and D. W. Deamer, "Microsecond time-scale discrimination among polycytidylic acid, polyadenylic acid, and polyuridylic acid as homopolymers or as segments within single RNA molecules.," *Biophys. J.*, vol. 77, pp. 3227–3233, 1999.

[118] H. Bayley and L. Jayasinghe, "Functional engineered channels and pores (Review).," *Mol. Membr. Biol.*, vol. 21, pp. 209–220, 2004.

[119] J. Clarke, H.-C. Wu, L. Jayasinghe, *et al.*, "Continuous base identification for single-molecule nanopore DNA sequencing.," *Nat. Nanotechnol.*, vol. 4, pp. 265–270, 2009.

[120] G. Maglia, M. R. Restrepo, E. Mikhailova, and H. Bayley, "Enhanced translocation of single DNA molecules through alpha-hemolysin nanopores by manipulation of internal charge.," *Proc. Natl. Acad. Sci.*, vol. 105, pp. 19720–19725, 2008.

[121] M. Rincon-Restrepo, E. Mikhailova, H. Bayley, and G. Maglia, "Controlled translocation of individual DNA molecules through protein nanopores with engineered molecular brakes," *Nano Lett.*, vol. 11, pp. 746–750, 2011.

[122] J. Sanchez-Quesada, M. R. Ghadir, H. Bayley, and O. Braha, "Cyclic peptides as molecular adapters for a pore-forming protein," *J. Am. Chem. Soc.*, vol. 122, pp. 11757–11766, 2000.

[123] T. Z. Butler, M. Pavlenok, I. M. Derrington, M. Niederweis, and J. H. Gundlach, "Single-molecule DNA detection with an engineered MspA protein nanopore," *Proc. Natl. Acad. Sci.*, vol. 105, pp. 20647–20652, 2008.

[124] I. M. Derrington, T. Z. Butler, M. D. Collins, *et al.*, "Nanopore DNA Sequencing with MspA.," *Proc. Natl. Acad. Sci.*, vol. 107, pp. 16060–5, 2010.

[125] A. B. Farimani, M. Heiranian, and N. R. Aluru, "Electromechanical Signatures for DNA Sequencing through a Mechanosensitive Nanopore," *J. Phys. Chem. Lett.*, vol. 6, pp. 650–657, 2015.

[126] D. Wendell, P. Jing, J. Geng, *et al.*, "Translocation of double-stranded DNA through membrane-adapted phi29 motor protein nanopores.," *Nat. Nanotechnol.*, vol. 4, pp. 765–772, 2009.

[127] J. Geng, S. Wang, H. Fang, and P. Guo, "Channel Size Conversion of Phi29 DNA-Packaging Nanomotor for Discrimination of Single- and Double-Stranded Nucleic Acids," *ACS Nano*, pp. 3315–3323, 2013.

[128] G. F. Schneider and C. Dekker, "DNA sequencing with nanopores," *Nat. Biotechnol.*, vol. 30, pp. 326–328, 2012.

[129] Y. Feng, Y. Zhang, C. Ying, D. Wang, and C. Du, "Nanopore-based Fourth-generation DNA Sequencing Technology," *Genomics. Proteomics Bioinformatics*, vol. 13, pp. 4–16, 2015.

[130] K. M. Halverson, R. G. Panchal, T. L. Nguyen, *et al.*, "Anthrax biosensor, protective antigen ion channel asymmetric blockade," *J. Biol. Chem.*, vol. 280, pp. 34056–34062, 2005.

[131] S. Hadi-Alijanvand, H. Mobasheri, and H. Hadi-Alijanvand, "Application of OmpF nanochannel forming protein in polynucleotide sequence recognition," *J. Mol. Recognit.*, vol. 27, pp. 575–587, 2014.

[132] M. M. Mohammad, K. R. Howard, and L. Movileanu, "Redesign of a plugged $\beta$-barrel membrane protein," *J. Biol. Chem.*, vol. 286, pp. 8000–8013, 2011.

[133] D. J. Niedzwiecki, M. M. Mohammad, and L. Movileanu, "Inspection of the Engineered FhuA $\Delta$c/$\Delta$4L Protein Nanopore by Polymer Exclusion," *Biophys. J.*, vol. 103, pp. 2115–2124, 2012.

[134] H. Killmann, R. Benz, and V. Braun, "Properties of the FhuA channel in the *Escherichia coli* outer membrane after deletion of FhuA portions within and outside the predicted gating loop," *J. Bacteriol.*, vol. 178, pp. 6913–6920, 1996.

[135] T. Zhuang and L. K. Tamm, "Control of the conductance of engineered protein nanopores through concerted loop motions," *Angew. Chemie - Int. Ed.*, vol. 53, pp. 5897–5902, 2014.

[136] A. Koçer, M. Walko, W. Meijberg, and B. L. Feringa, "A light-actuated nanovalve derived from a channel protein.," *Science*, vol. 309, pp. 755–758, 2005.

[137] M. R. Ghadiri, J. R. Granja, and L. K. Buehler, "Artificial Transmembrane Ion Channels from Self-Assembling Peptide Nanotubes.," *Nature*, vol. 369, pp. 301–304, 1994.

[138] T. D. Clark, K. Kobayashi, and M. R. Ghadiri, "Covalent Capture and Stabilization of Cylindrical $\beta$-Sheet Peptide Assemblies," *Chem. Eur. J.*, vol. 5, pp. 782–792, 1999.

[139] N. Sakai and S. Matile, "Synthetic ion channels," *Langmuir*, vol. 29, pp. 9031–9040, 2013.

[140] V. E. Carmichael, P. J. Dutton, T. M. Fyles, *et al.*, "Biomimetic Ion Transport: A Functional Model of a Unimolecular Ion Channel," *J. Am. Chem. Soc.*, vol. 111, pp. 767–769, 1989.

[141] L. Echegoyen, "Synthetic chemistry. Not through the usual channels.," *Nature*, vol. 369, pp. 276–277, 1994.

[142] X. Zhou, G. Liu, K. Yamato, *et al.*, "Self-assembling subnanometer pores with unusual mass-transport properties," *Nat. Commun.*, vol. 3, p. 949, 2012.

[143] X.-b. Hu, Z. Chen, G. Tang, J.-L. Hou, and Z.-t. Li, "Single-molecular artificial transmembrane water channels.," *J. Am. Chem. Soc.*, vol. 134, pp. 8384–8387, 2012.

[144] A. S. Verkman, "Aquaporins at a glance.," *J. Cell Sci.*, vol. 124, pp. 2107–2112, 2011.

[145] C. J. E. Haynes and P. a. Gale, "Transmembrane anion transport by synthetic systems.," *Chem. Commun.*, vol. 47, pp. 8203–8209, 2011.

[146] H. Cho and Y. Zhao, "Translocation of hydrophilic molecules across lipid bilayers by salt-bridged oligocholates," *Langmuir*, vol. 27, pp. 4936–4944, 2011.

[147] A. Liu, Q. Zhao, and X. Guan, "Stochastic nanopore sensors for the detection of terrorist agents: current status and challenges.," *Anal. Chim. Acta*, vol. 675, pp. 106–115, 2010.

[148] M. Barboiu and A. Gilles, "From Nature to Bioassisted and Biomimetic Artificial Water Channel Systems," *Acc. Chem. Res.*, vol. 46, pp. 2814 – 2823, 2013.

[149] N. Sakai, J. Mareda, and S. Matile, "Artificial $\beta$-Barrels," *Acc. Chem. Res.*, vol. 41, pp. 1354–1366, 2008.

[150] J. D. Lear, J. P. Schneider, P. K. Kienker, and W. F. DeGrado, "Electrostatic effects on ion selectivity and rectification in designed peptide channels," *J. Am. Chem. Soc.*, vol. 119, pp. 3212–3217, 1997.

[151] J. Montenegro, M. R. Ghadiri, and J. R. Granja, "Ion Channel Models Based on Self-Assembling Cyclic Peptide Nanotubes," *Acc. Chem. Res.*, vol. 46, pp. 2955–2965, 2013.

[152] M. R. Ghadiri, J. R. Granja, R. a. Milligan, D. E. McRee, and N. Khazanovich, "Self-assembling organic nanotubes based on a cyclic peptide architecture.," *Nature*, vol. 366, pp. 324–327, 1993.

[153] J. R. Burns, E. Stulz, and S. Howorka, "Self-Assembled DNA Nanopores That Span Lipid Bilayers.," *Nano Lett.*, vol. 51, pp. 9–14, 2013.

[154] N. a. W. Bell, C. R. Engst, M. Ablay, *et al.*, "DNA Origami Nanopores," *Nano Lett.*, vol. 12, pp. 512–7, 2012.

[155] H. W. Kroto, J. R. Heath, S. C. O'Brien, R. F. Curl, and R. E. Smalley, "C 60: buckminsterfullerene," *Nature*, vol. 318, p. 162, 1985.

[156] S. Iijima, "Helical microtubules of graphitic carbon," *Nature*, vol. 354, pp. 56–58, 1991.

[157] S. Garaj, W. Hubbard, a. Reina, *et al.*, "Graphene as a subnanometre trans-electrode membrane.," *Nature*, vol. 467, pp. 190–193, 2010.

[158] C. A. Merchant, K. Healy, M. Wanunu, *et al.*, "DNA Translocation Through Graphene Nanopores.," *Nano Lett.*, vol. 10, pp. 2915–2921, 2010.

[159] G. F. Schneider, S. W. Kowalczyk, V. E. Calado, *et al.*, "DNA Translocation Through Graphene Nanopores.," *Nano Lett.*, vol. 10, pp. 3163–3167, 2010.

[160] S. K. Min, W. Y. Kim, Y. Cho, and K. S. Kim, "Fast DNA sequencing with a graphene-based nanochannel device.," *Nat. Nanotechnol.*, vol. 6, pp. 162–165, 2011.

[161] L. Liang, P. Cui, Q. Wang, *et al.*, "Theoretical study on key factors in DNA sequencing with graphene nanopores," *RSC Adv.*, vol. 3, p. 2445, 2013.

[162] L. Liang, Q. Wang, H. Agren, and Y. Tu, "Computational studies of DNA sequencing with solid-state nanopores: key issues and future prospects.," *Front. Chem.*, vol. 2, p. 5, 2014.

[163] G. F. Schneider, Q. Xu, S. Hage, *et al.*, "Tailoring the hydrophobicity of graphene for its use as nanopores for DNA translocation.," *Nat. Commun.*, vol. 4, p. 2619, 2013.

[164] A. V. Titov, B. Wang, K. Sint, and P. Král, "Controllable synthetic molecular channels: biomimetic ammonia switch.," *J. Phys. Chem. B*, vol. 114, pp. 1174–1179, 2010.

[165] Y. He, M. Tsutsui, R. H. Scheicher, *et al.*, "Thermophoretic Manipulation of DNA Translocation through Nanopores," *ACS Nano*, vol. 7, pp. 538–546, 2013.

[166] F. Zhu and K. Schulten, "Water and proton conduction through carbon nanotubes as models for biological channels.," *Biophys. J.*, vol. 85, pp. 236–244, 2003.

[167] R. García-Fandiño and M. S. P. Sansom, "Designing Biomimetic Pores based on Carbon Nanotubes.," *Proc. Natl. Acad. Sci.*, vol. 109, pp. 6939–6944, 2012.

[168] J. Geng, K. Kim, J. Zhang, *et al.*, "lipid bilayers and live cell membranes," *Nature*, vol. 514, pp. 612–615, 2014.

[169] S. Pogodin and V. A. Baulin, "Can a Carbon Nanotube Pierce through a Phospholipid Bilayer?," *ACS Nano*, vol. 4, pp. 5293–5300, 2010.

[170] T. Kuila, S. Bose, A. K. Mishra, *et al.*, "Chemical functionalization of graphene and its applications," *Prog. Mater. Sci.*, vol. 57, pp. 1061–1105, 2012.

[171] S. Vardharajula, S. Z. Ali, P. M. Tiwari, *et al.*, "Functionalized carbon nanotubes: Biomedical applications," *Int. J. Nanomedicine*, vol. 7, pp. 5361–5374, 2012.

[172] C. Dekker, "Solid-state nanopores.," *Nat. Nanotechnol.*, vol. 2, pp. 209–215, 2007.

[173] U. F. Keyser, "Controlling molecular transport through nanopores Controlling molecular transport through nanopores," *J. R. Soc. Interface*, 2011.

[174] Z. Siwy and a. Fuliński, "Fabrication of a synthetic nanopore ion pump.," *Phys. Rev. Lett.*, vol. 89, p. 198103, 2002.

[175] A. T. Kuan and J. a. Golovchenko, "Nanometer-thin solid-state nanopores by cold ion beam sculpting," *Appl. Phys. Lett.*, vol. 100, pp. 2–5, 2012.

[176] A. J. Storm, J. H. Chen, X. S. Ling, H. W. Zandbergen, and C. Dekker, "Fabrication of solid-state nanopores with single-nanometre precision.," *Nat. Mater.*, vol. 2, pp. 537–40, 2003.

[177] J. Li, D. Stein, C. McMullan, *et al.*, "Ion-beam sculpting at nanometre length scales.," *Nature*, vol. 412, pp. 166–169, 2001.

[178] D. Fologea, M. Gershow, B. Ledden, *et al.*, "Detecting single stranded DNA with a solid state nanopore," *Nano Lett.*, vol. 5, pp. 1905–1909, 2005.

[179] A. J. Storm, J. Chen, H. Zandbergen, and C. Dekker, "Translocation of double-strand DNA through a silicon oxide nanopore," *Phys. Rev. E*, vol. 71, p. 051903, 2005.

[180] S. W. Kowalczyk, M. W. Tuijtel, S. P. Donkers, and C. Dekker, "Unraveling single-stranded DNA in a solid-state nanopore," *Nano Lett.*, vol. 10, pp. 1414–1420, 2010.

[181] G. M. Skinner, M. van den Hout, O. Broekmans, C. Dekker, and N. H. Dekker, "Distinguishing single- and double-stranded nucleic acid molecules using solid-state nanopores.," *Nano Lett.*, vol. 9, pp. 2953–2960, 2009.

[182] A. Han, G. Schürmann, G. Mondin, *et al.*, "Sensing protein molecules using nanofabricated pores," *Appl. Phys. Lett.*, vol. 88, pp. 16–19, 2006.

[183] D. S. Talaga and J. Li, "Single-molecule protein unfolding in solid state nanopores," *J. Am. Chem. Soc.*, vol. 131, pp. 9287–9297, 2009.

[184] C. R. Martin and Z. S. Siwy, "Chemistry. Learning Nature's Way: Biosensing with Synthetic Nanopores.," *Science.*, vol. 317, pp. 331–332, 2007.

[185] A. R. Hall, J. M. Keegstra, M. C. Duch, M. C. Hersam, and C. Dekker, "Translocation of Single-Wall Carbon Nanotubes Through Solid-State Nanopores," *Nano Lett.*, vol. 11, pp. 2446–2450, 2011.

[186] M. Wanunu, J. Sutin, and A. Meller, "DNA Profiling Using Solid-State Nanopores: Detection of DNA binding Molecules," *Nano Lett.*, vol. 9, pp. 3498–3502, 2009.

[187] X. Hou, W. Guo, F. Xia, *et al.*, "A Biomimetic Potassium Responsive Nanochannel : G-Quadruplex DNA Conformational Switching in a Synthetic Nanopore," *J. Am. Chem. Soc.*, vol. 131, pp. 7800–7805, 2009.

[188] Y. Tian, X. Hou, L. Wen, W. Guo, and Y. Song, "A biomimetic zinc activated ion channel," *Chem. Commun.*, vol. 46, pp. 1682–1684, 2010.

[189] Q. Liu, K. Xiao, L. Wen, *et al.*, "A Fluoride-Driven Ionic Gate Based on a 4-Aminophenylboronic Acid-Functionalized Asymmetric Single Nanochannel," *ACS Nano*, vol. 8, pp. 12292–12299, 2014.

[190] M. Wanunu and A. Meller, "Chemically Modified Solid-State Nanopores," *Nano Lett.*, vol. 7, pp. 1580–1585, 2007.

[191] Z. S. Siwy, "Ion-current rectification in nanopores and nanotubes with broken symmetry," *Adv. Funct. Mater.*, vol. 16, pp. 735–746, 2006.

[192] S. Smirnov, I. Vlassiouk, and N. Lavrik, "Voltage-Gated Hydrophobic Nanopores," *ACS Nano*, vol. 5, pp. 7453–7461, 2011.

[193] E. C. Yusko, J. M. Johnson, S. Majd, *et al.*, "Controlling protein translocation through nanopores with bio-inspired fluid walls.," *Nat. Nanotechnol.*, vol. 6, pp. 253–260, 2011.

[194] T. Jovanovic-Talisamn, B. T. Chait, and M. P. Rout, "NPC Mimics: Probing the Mechanism of Nucleocytoplasmic Transport," *Methods Cell Biol.*, vol. 122, pp. 379–393, 2014.

[195] F. Haque, J. Li, H.-C. Wu, X.-J. Liang, and P. Guo, "Solid-State and Biological Nanopore for Real-Time Sensing of Single Chemical and Sequencing of DNA.," *Nano Today*, vol. 8, pp. 56–74, 2013.

[196] S. Balme, J.-m. Janot, L. Berardo, *et al.*, "Confined into the Cylindrical Nanopore of a Solid-State Polymer .," *Nano Lett.*, vol. 11, pp. 712–716, 2010.

[197] C. Hall, AR; Scott, A; Rotem, D; Mehta, K; Bayley, H; Dekker, "Hybrid pore formation by directed insertion of $\alpha$-haemolysin into solid-state nanopores," *Nat. Nanotechnol*, vol. 5, pp. 874–877, 2010.

[198] B. K. Ziervogel and B. Roux, "The binding of antibiotics in OmpF porin," *Structure*, vol. 21, pp. 76–87, 2013.

[199] A. Aksimentiev and K. Schulten, "Imaging $\alpha$-Hemolysin with Molecular Dynamics: Ionic Conductance, Osmotic Permeability, and the Electrostatic Potential Map," *Biophys. J.*, vol. 88, pp. 3745–3761, 2005.

[200] D. B. Wells, V. Abramkina, and A. Aksimentiev, "Exploring Transmembrane Transport Through $\alpha$-Hemolysin with Grid-Steered Molecular Dynamics.," *J. Chem. Phys.*, vol. 127, p. 125101, 2007.

[201] Y. Luo, B. Egwolf, D. E. E. Walters, and B. Roux, "Ion Selectivity of $\alpha$-Hemolysin with a $\beta$-Cyclodextrin Adapter. I. Single Ion Potential of Mean Force and Diffusion Coefficient," *J. Phys. Chem. B*, vol. 114, pp. 952–958, 2010.

[202] O. Beckstein and M. S. P. Sansom, "Liquid-Vapor Oscillations of Water in Hydrophobic Nanopores.," *Proc. Natl. Acad. Sci.*, vol. 100, pp. 7063–7068, 2003.

[203] J. Dzubiella and J.-P. Hansen, "Electric-field-controlled water and ion permeation of a hydrophobic nanopore.," *J. Chem. Phys.*, vol. 122, p. 234706, 2005.

[204] C. Peter and G. Hummer, "Ion transport through membrane-spanning nanopores studied by molecular dynamics simulations and continuum electrostatics calculations.," *Biophys. J.*, vol. 89, pp. 2222–2234, 2005.

[205] S. Smirnov, I. Vlassiouk, P. Takmakov, and F. Rios, "Water Confinement in Hydrophobic Nanoporse. Pressure-Induced Wetting and Drying.," *ACS Nano*, vol. 4, pp. 5069–5075, 2010.

[206] E. Chiavazzo, M. Fasano, P. Asinari, and P. Decuzzi, "Scaling behaviour for the water transport in nanoconfined geometries.," *Nat. Commun.*, vol. 5, p. 4565, 2014.

[207] P. Pongprayoon, O. Beckstein, C. L. Wee, and M. S. P. Sansom, "Simulations of Anion Transport Through OprP Reveal the Molecular Basis for High Affinity and Selectivity for Phosphate.," *Proc. Natl. Acad. Sci.*, vol. 106, pp. 21614–21648, 2009.

[208] H. Rui, K. I. Lee, R. W. Pastor, and W. Im, "Molecular dynamics studies of ion permeation in VDAC.," *Biophys. J.*, vol. 100, pp. 602–610, 2011.

[209] N. Modi, R. Benz, R. E. W. Hancock, and U. Kleinekathöfer, "Modeling the Ion Selectivity of the Phosphate Specific Channel OprP," *J. Phys. Chem. Lett.*, vol. 3, pp. 3639–3645, 2012.

[210] N. Modi, I. Barcena-Uribarri, M. Bains, *et al.*, "Tuning the affinity of anion binding sites in porin channels with negatively charged residues: Molecular details for OprP," *ACS Chem. Biol.*, vol. 10, pp. 441–451, 2014.

[211] C. Song and B. Corry, "Intrinsic ion selectivity of narrow hydrophobic pores.," *J. Phys. Chem. B*, vol. 113, pp. 7642–7649, 2009.

[212] M. Thomas, B. Corry, and T. a. Hilder, "What Have We Learnt About the Mechanisms of Rapid Water Transport, Ion Rejection and Selectivity in Nanopores from Molecular Simulation?," *Small*, vol. 10, pp. 1453–1465, 2014.

[213] P. Pongprayoon, O. Beckstein, M. S. P. Sansom, and C. L. Wee, "Biomimetic design of a brush-like nanopore: simulation studies.," *J. Phys. Chem. B*, vol. 116, pp. 462–8, 2012.

[214] B. Corry, "Water and ion transport through functionalised carbon nanotubes: implications for desalination technology," *Energy Environ. Sci.*, vol. 4, p. 751, 2011.

[215] M. Tarek, "Membrane electroporation: a molecular dynamics simulation.," *Biophys. J.*, vol. 88, pp. 4045–4053, 2005.

[216] R. A. Böckmann, B. L. de Groot, S. Kakorin, E. Neumann, and H. Grubmüller, "Kinetics, statistics, and energetics of lipid membrane electroporation studied by molecular dynamics simulations.," *Biophys. J.*, vol. 95, pp. 1837–1850, 2008.

[217] L. Delemotte and M. Tarek, "Molecular dynamics simulations of lipid membrane electroporation," *J. Membr. Biol.*, vol. 245, pp. 531–543, 2012.

[218] A. Polak, D. Bonhenry, F. Dehez, *et al.*, "On the Electroporation Thresholds of Lipid Bilayers: Molecular Dynamics Simulation Investigations," *J. Membr. Biol.*, vol. 246, pp. 843–850, 2013.

[219] A. Suenaga, Y. Komeiji, M. Uebayasi, *et al.*, "Computational Observation of an Ion Permeation Through a Channel Protein.," *Biosci. Rep.*, vol. 18, pp. 39–48, 1998.

[220] S. W. I. Siu and R. a. Böckmann, "Electric field effects on membranes: Gramicidin A as a test ground," *J. Struct. Biol.*, vol. 157, pp. 545–556, 2007.

[221] B. Roux, "The membrane potential and its representation by a constant electric field in computer simulations.," *Biophys. J.*, vol. 95, pp. 4205–4216, 2008.

[222] M.-C. Ho, Z. A. Levine, and P. T. Vernier, "Nanoscale, electric field-driven water bridges in vacuum gaps and lipid bilayers.," *J. Membr. Biol.*, vol. 246, pp. 793–801, 2013.

[223] M. Tokman, J. H. Lee, Z. A. Levine, *et al.*, "Electric Field-Driven Water Dipoles: Nanoscale Architecture of Electroporation," *PLoS One*, vol. 8, 2013.

[224] S. Vaitheeswaran, J. C. Rasaiah, and G. Hummer, "Electric field and temperature effects on water in the narrow nonpolar pores of carbon nanotubes.," *J. Chem. Phys.*, vol. 121, pp. 7955–7965, 2004.

[225] D. Bratko, C. D. Daub, K. Leung, and A. Luzar, "Effect of field direction on electrowetting in a nanopore.," *J. Am. Chem. Soc.*, vol. 129, pp. 2504–2510, 2007.

[226] D. Vanzo, D. Bratko, and A. Luzar, "Dynamic Control of Nanopore Wetting in Water and Saline Solutions under an Electric Field," *J. Phys. Chem. B*, vol. 119, pp. 8890–8899, 2015.

[227] N. Calimet, M. Simoes, J.-P. Changeux, *et al.*, "A gating mechanism of pentameric ligand-gated ion channels.," *Proc. Natl. Acad. Sci.*, vol. 110, pp. E3987–96, 2013.

[228] M. H. Cheng, R. D. Coalson, and P. Tang, "Molecular Dynamics and Brownian Dynamics Investigation of Ion Permeation and Anesthetic Halothane Effects on a Proton- gated Ion Channel," *J. Am. Chem. Soc.*, vol. 132, pp. 16442–16449, 2010.

[229] F. Zhu and G. Hummer, "Theory and Simulation of Ion Conduction in the Pentameric GLIC Channel," *J. Chem. Theory Comput.*, vol. 8, pp. 3759 – 3768, 2012.

[230] S. Murail, B. Wallner, J. R. Trudell, E. Bertaccini, and E. Lindahl, "Microsecond simulations indicate that ethanol binds between subunits and could stabilize an open-state model of a glycine receptor," *Biophys. J.*, vol. 100, pp. 1642–1650, 2011.

[231] S. Murail, R. J. Howard, T. Broemstrup, *et al.*, "Molecular Mechanism for the Dual Alcohol Modulation of Cys-loop Receptors," *PLoS Comput. Biol.*, vol. 8, 2012.

[232] O. Yoluk, T. Brömstrup, E. J. Bertaccini, J. R. Trudell, and E. Lindahl, "Stabilization of the GluCl ligand-gated ion channel in the presence and absence of ivermectin," *Biophys. J.*, vol. 105, pp. 640–647, 2013.

[233] O. Yoluk, E. Lindahl, and M. Andersson, "Conformational gating dynamics in the GluCl anion-selective chloride channel," *ACS Chem. Neurosci.*, vol. 6, pp. 1459–1467, 2015.

[234] A. R. Leach, *Molecular Modelling: Principles and Applications*. 2001.

[235] E. Apol, R. Apostolov, H. J. C. Berendsen, *et al.*, "Gromacs User Manual version 4.5.4," 2013.

[236] H. M. Senn and W. Thiel, "QM/MM studies of enzymes," *Curr. Opin. Chem. Biol.*, vol. 11, pp. 182–187, 2007.

[237] H. M. Senn and W. Thiel, "QM/MM methods for biomolecular systems," *Angew. Chemie - Int. Ed.*, vol. 48, pp. 1198–1229, 2009.

[238] D. P. Tieleman, "Methods and Parameters for Membrane Simulations," in *Mol. Simulations Biomembr. From Biophys. to Funct.* (P. C. Biggin and M. S. P. Sansom, eds.), pp. 1–25, Royal Society of Chemistry, 2010.

[239] Y. Mo, "A critical analysis on the rotation barriers in butane," *J. Org. Chem.*, vol. 75, pp. 2733–2736, 2010.

[240] T. Darden, D. York, and L. Pedersen, "Particle mesh Ewald: An Nlog(N) method for Ewald sums in large systems," *J. Chem. Phys.*, vol. 98, pp. 10089–10091, 1993.

[241] U. Essmann and L. Perera, "A smooth particle mesh Ewald method," *J. Chem. Phys.*, vol. 103, pp. 31–34, 1995.

[242] P. P. Ewald, "The calculation of optical and electrostatic grid potential," *Ann. Phys.*, vol. 64, pp. 253–287, 1921.

[243] S. Piana, K. Lindorff-Larsen, and D. E. Shaw, "How robust are protein folding simulations with respect to force field parameterization?," *Biophys. J.*, vol. 100, pp. L47–L49, 2011.

[244] S. Piana, J. L. Klepeis, and D. E. Shaw, "Assessing the accuracy of physical models used in protein-folding simulations: Quantitative evidence from long molecular dynamics simulations," *Curr. Opin. Struct. Biol.*, vol. 24, pp. 98–105, 2014.

[245] W. L. Jorgensen, J. D. Madura, and C. J. Swenson, "Optimized intermolecular potential functions for liquid hydrocarbons," *J. Am. Chem. Soc.*, vol. 106, p. 6638, 1984.

[246] W. Scott, P. Hünenberger, I. G. Tironi, *et al.*, "The GROMOS Biomolecular Simulation Program Package," *J. Phys. Chem. A*, vol. 103, pp. 3596–3607, 1999.

[247] L. D. Schuler, X. Daura, and W. F. van Gunsteren, "An Improved GROMOS96 Force Field for Aliphatic Hydrocarbons in the Condensed Phase," *J. Comput. Chem.*, vol. 22, pp. 1205–1218, 2001.

[248] A. D. MacKerell, D. Bashford, M. Bellott, *et al.*, "All-atom empirical potential for molecular modeling and dynamics studies of proteins," *J. Phys. Chem. B*, vol. 102, pp. 3586–3616, 1998.

[249] J. M. Wang, R. M. Wolf, J. W. Caldwell, P. A. Kollman, and D. A. Case, "Development and testing of a general amber force field," *J. Comput. Chem.*, vol. 25, pp. 1157–1174, 2004.

[250] O. Berger, O. Edholm, and F. Jahnig, "Molecular Dynamics Simulations of a Fluid Bilayer of Dipalmitoylphosphatidylcholine at Full Hydration, Constant Pressure, and Constant Temperature," *Biophys. J*, vol. 72, pp. 2002–2013, 1997.

[251] R. Hockney, S. Goel, and J. Eastwood, "Quiet high-resolution computer models of a plasma," *J. Comput. Phys.*, vol. 14, pp. 148–158, 1974.

[252] J.-P. Ryckaert, G. Ciccotti, and H. J. Berendsen, "Numerical integration of the cartesian equations of motion of a system with constraints: molecular dynamics of n-alkanes," *J. Comput. Phys.*, vol. 23, pp. 327–341, 1977.

[253] B. Hess, H. Bekker, H. J. C. Berendsen, and J. G. E. M. Fraaije, "LINCS: A Linear Constraint Solver for Molecular Simulation," *J. Comput. Chem.*, vol. 18, pp. 1463–1472, 1997.

[254] S. J. Marrink and A. E. Mark, "Effect of Undulations on Sufrace Tension in Simulated Bilayers," *J. Phys. Chem. B*, vol. 105, pp. 6122–6127, 2001.

[255] M. Parrinello and A. Rahman, "Polymorphic transistions in single crystals: A new molecular dynamics method," *J. Appl. Phys.*, vol. 52, pp. 7182–7190, 1981.

[256] G. Bussi, D. Donadio, and M. Parrinello, "Canonical sampling through velocity rescaling," *J. Chem. Phys.*, vol. 126, 2007.

[257] M. Chaplin, "Water Models," *http://www1.lsbu.ac.uk/water/watermodels.html*, 2001.

[258] H. J. C. Berendsen, J. R. Grigera, and T. P. Straatsma, "The Missing Term in Effective Pair Potentials," *J. Phys. Chem.*, vol. 91, pp. 6269–6271, 1987.

[259] W. L. Jorgensen, J. Chandrasekhar, J. D. Madura, R. W. Impey, and M. L. Klein, "Comparison of simple potential functions for simulating liquid water," *J. Chem. Phys.*, vol. 79, p. 926, 1983.

[260] S. J. Marrink, H. J. Risselada, S. Yefimov, D. P. Tieleman, and A. H. de Vries, "The MARTINI force field: coarse grained model for biomolecular simulations.," *J. Phys. Chem. B*, vol. 111, pp. 7812–7824, 2007.

[261] A. Y. Shih, A. Arkhipov, P. L. Freddolino, and K. Schulten, "Coarse Grained Protein – Lipid Model with Application to Lipoprotein Particles," *J. Phys. Chem. B*, vol. 110, pp. 3674–3684, 2006.

[262] A. Arkhipov, P. L. Freddolino, and K. Schulten, "Stability and Dynamics of Virus Capsids Described by Coarse-Grained Modeling," *Structure*, vol. 14, pp. 1767–1777, 2006.

[263] J. J. Uusitalo, H. I. Ingólfsson, P. Akhshi, D. P. Tieleman, and S. J. Marrink, "Martini Coarse-Grained Force Field: Extension to DNA," *J. Chem. Theory Comput.*, p. 150723135724002, 2015.

[264] P. J. Bond and M. S. P. Sansom, "Insertion and assembly of membrane proteins via simulation.," *J. Am. Chem. Soc.*, vol. 128, pp. 2697–704, 2006.

[265] S. O. Yesylevskyy, L. V. Schäfer, D. Sengupta, and S. J. Marrink, "Polarizable water model for the coarse-grained MARTINI force field," *PLoS Comput. Biol.*, vol. 6, pp. 1–17, 2010.

[266] T. Carpenter, P. J. Bond, S. Khalid, and M. S. P. Sansom, "Self-assembly of a simple membrane protein: coarse-grained molecular dynamics simulations of the influenza M2 channel.," *Biophys. J.*, vol. 95, pp. 3790–3801, 2008.

[267] P. J. Stansfeld and M. S. P. Sansom, "From Coarse Grained to Atomistic: A Serial Multiscale Approach to Membrane Protein Simulations," *J. Chem. Theory Comput.*, vol. 7, pp. 1157–1166, 2011.

[268] P. Rotkiewicz and J. Skolnick, "Fast procedure for reconstruction of fullatom protein models from reduced representations," *J. Comput. Chem.*, vol. 29, pp. 1461–1465, 2008.

[269] S. Izrailev, S. Stepaniants, B. Isralewitz, *et al.*, "Steered molecular dynamics," in *Computational Molecular Dynamics: Challenges, Methods, Ideas* (P. Deuflhard, J. Hermans, B. Leimkuhler, *et al.*, eds.), pp. 39–65, Springer Berlin Heidelberg, 1999.

[270] B. Roux, "The calculation of the potential of mean force using computer simulations," *Comput. Phys. Commun.*, vol. 91, pp. 275–282, 1995.

[271] A. Grossfield, "WHAM: The Weighted Histogram Analysis Method. Version 2.0.9."

[272] R. W. Zwanzig, "High-Temperature Equation of State by a Perturbation Method. II. Polar Gases," *J. Chem. Phys.*, vol. 22, pp. 1420–1426, 1954.

[273] T. P. Straatsma and H. J. C. Berendsen, "Free energy of ionic hydration: Analysis of a thermodynamic integration technique to evaluate free energy differences by molecular dynamics simulations," *J. Chem. Phys.*, vol. 89, p. 5876, 1988.

[274] S. Park, F. Khalili-Araghi, E. Tajkhorshid, and K. Schulten, "Free energy calculation from steered molecular dynamics simulations using Jarzynski's equality," *J. Chem. Phys.*, vol. 119, p. 3559, 2003.

[275] G. Torrie and J. Valleau, "Nonphysical sampling distributions in Monte Carlo free-energy estimation: Umbrella sampling," *J. Comput. Phys.*, vol. 23, pp. 187–199, 1977.

[276] A. Laio and M. Parrinello, "Escaping free-energy minima.," *Proc. Natl. Acad. Sci.*, vol. 99, pp. 12562–12566, 2002.

[277] E. Darve and A. Pohorille, "Calculating free energies using average force," *J. Chem. Phys.*, vol. 115, pp. 9169–9183, 2001.

[278] J. H. Prinz, H. Wu, M. Sarich, *et al.*, "Markov models of molecular kinetics: Generation and validation," *J. Chem. Phys.*, vol. 134, 2011.

[279] M. S. P. Sansom and I. D. Kerr, "Transbilayer Pores Formed by $\beta$-Barrels: Molecular Modeling of Pore Structures and Properties Models Investigated," *Biophys. J.*, vol. 69, pp. 1334–1343, 1995.

[280] A. Sali and T. Blundell, "Comparative Protein Modelling by Satisfaction of Spatial Restraints," 1993.

[281] W. Humphrey, A. Dalke, and K. Schulten, "VMD: Visual Molecular Dynamics.," *J. Mol. Graph.*, vol. 14, pp. 33–38, 1996.

[282] Schrödinger, LLC, "The PyMOL molecular graphics system, version 1.3r1." August 2010.

[283] O. S. Smart, J. G. Neduvelil, X. Wang, B. A. Wallace, and M. S. P. Sansom, "HOLE: A Program for the Analysis of the Pore Dimensions of Ion Channel Structural Models.," *J. Mol. Graph.*, vol. 14, pp. 354–360, 1996.

[284] N. Michaud-Agrawal, E. J. Denning, T. B. Woolf, and O. Beckstein, "Software News and Updates MDAnalysis: A Toolkit for the Analysis of Molecular Dynamics Simulations," *J. Comput. Chem.*, vol. 32, pp. 2319–2327, 2011.

[285] L. S. Stelzl, P. W. Fowler, M. S. P. Sansom, and O. Beckstein, "Flexible Gates Generate Occluded Intermediates in the Transport Cycle of LacY.," *J. Mol. Biol.*, vol. 426, pp. 735–751, 2014.

[286] J. D. Hunter, "Matplotlib: A 2d graphics environment," *Computing In Science & Engineering*, vol. 9, pp. 90–95, 2007.

[287] H. Hong, D. R. Patel, L. K. Tamm, and B. van den Berg, "The Outer Membrane Protein OmpW Forms an Eight-Stranded $\beta$-Barrel with a Hydrophobic Channel.," *J. Biol. Chem.*, vol. 281, pp. 7568–7577, 2006.

[288] B. Hess, C. Kutzner, D. Van Der Spoel, and E. Lindahl, "GROMACS 4 : Algorithms for Highly Efficient, Load-Balanced, and Scalable Molecular Simulation," *J. Chem. Theory Comput.*, vol. 4, pp. 435–447, 2008.

[289] C. Wirth, G. Condemine, C. Boiteux, *et al.*, "NanC Crystal Structure, a Model for Outer-Membrane Channels of the Acidic Sugar-Specific KdgM Porin Family.," *J. Mol. Biol.*, vol. 394, pp. 718–731, 2009.

[290] K. Yamashita, Y. Kawai, Y. Tanaka, *et al.*, "Crystal Structure of the Octameric Pore of Staphylococcal $\gamma$-Hemolysin Reveals the $\beta$-barrel Pore Formation Mechanism by Two Components.," *Proc. Natl. Acad. Sci.*, vol. 108, pp. 17314–17319, 2011.

[291] J. A. Killian, "Hydrophobic Mismatch Between Proteins and Lipids in Membranes.," *Biochim. Biophys. Acta*, vol. 1376, pp. 401–415, 1998.

[292] P. J. Stansfeld, E. E. Jefferys, and M. S. P. Sansom, "Multiscale Simulations Reveal Conserved Patterns of Lipid iIteractions with Aquaporins.," *Structure*, vol. 21, pp. 810–819, 2013.

[293] S. W. Cowan, T. Schirmer, G. Rummel, *et al.*, "Crystal structures explain functional properties of two E. coli porins.," *Nature*, vol. 358, pp. 727–733, 1992.

[294] T. Schirmer, T. A. Keller, Y. F. Wang, and J. P. Rosenbusch, "Structural basis for sugar translocation through maltoporin channels at 3.1 A resolution.," *Science*, vol. 267, pp. 512–514, 1995.

[295] S. Biswas, M. M. Mohammad, L. Movileanu, and B. van den Berg, "Crystal Structure of the Outer Membrane Protein OpdK from Pseudomonas aeruginosa," *Structure*, vol. 16, pp. 1027–1035, 2008.

[296] M. Watanabe, J. Rosenbusch, T. Schirmer, and M. Karplus, "Computer Simulations of the OmpF Porin from the Outer Membrane of *Escherichia coli*," *Biophys. J.*, vol. 72, pp. 2094–2102, 1997.

[297] S. Khalid, P. J. Bond, S. S. Deol, and M. S. P. Sansom, "Modeling and Simulations of a Bacterial Outer Membrane Protein: OprF From Pseudomonas aeruginosa," *Proteins*, vol. 63, pp. 6 –15, 2006.

[298] A. Kumar, E. Hajjar, P. Ruggerone, and M. Ceccarelli, "Structural and Dynamical Properties of the Porins OmpF and OmpC: Insights from Molecular Simulations.," *J. Phys. Condens. Matter*, vol. 22, p. 454125, 2010.

[299] J. L. Trick, E. J. Wallace, H. Bayley, and M. S. P. Sansom, "Designing a Hydrophobic Barrier within Biomimetic Nanopores.," *ACS Nano*, vol. 8, pp. 11268–11279, 2014.

[300] M. Borgnia and S. r. Nielsen, "Cellular and Molecular Biology of the Aquaporin Water Channels," *Annu. Rev. Biochem.*, vol. 68, pp. 425–458, 1999.

[301] F. Zhu, E. Tajkhorshid, and K. Schulten, "Theory and simulation of water permeation in aquaporin-1.," *Biophys. J.*, vol. 86, pp. 50–57, 2004.

[302] J. Wong-ekkabut and M. Karttunen, "Molecular dynamics simulation of water permeation through the alpha-hemolysin channel," *J. Biol. Phys.*, 2015.

[303] A. Anishkin and S. Sukharev, "Water Dynamics and Dewetting Transitions in the Small Mechanosensitive Channel MscS.," *Biophys. J.*, vol. 86, pp. 2883–2895, 2004.

[304] J. Huang, P. E. M. Lopes, and A. D. Mackerell, "Recent Advances in Polarizable Force Fields for Macromolecules: Microsecond Simulations of Proteins Using the Classical Drude Oscillator Model," *J. Phys. Chem. Lett.*, vol. 5, pp. 3144–3150, 2014.

[305] J. Wong-ekkabut and M. Karttunen, "Assessment of Common Simulation Protocols for Simulations of Nanopores, Membrane Proteins, and Channels," *J. Chem. Theory Comput.*, vol. 8, pp. 2905–2911, 2012.

[306] C. N. Pace and B. a. Shirley, "Forces contributing to the conformational stability of proteins," *FASEB J.*, vol. 10, pp. 75–83, 1996.

[307] K. Zeth, K. Diederichs, W. Welte, and H. Engelhardt, "Crystal structure of Omp32, the anion-selective porin from *Comamonas acidovorans*, in complex with a periplasmic peptide at 2.1 Å resolution.," *Structure*, vol. 8, pp. 981–92, 2000.

[308] S. J. Kim, S. H. Ko, K. H. Kang, and J. Han, "Direct seawater desalination by ion concentration polarization.," *Nat. Nanotechnol.*, vol. 5, pp. 297–301, 2010.

[309] H. Y. Yang, Z. J. Han, S. F. Yu, *et al.*, "Carbon nanotube membranes with ultrahigh specific adsorption capacity for water desalination and purification.," *Nat. Commun.*, vol. 4, p. 2220, 2013.

[310] W. F. Chan, H. Y. Chen, A. Surapathi, *et al.*, "Zwitterion functionalized carbon nanotube/polyamide nanocomposite membranes for water desalination," *ACS Nano*, vol. 7, pp. 5308–5319, 2013.

[311] L. Liu and L. Zhu, "Thermally modulated biomolecule transport through nanoconfined channels," *Nanoscale Res. Lett.*, vol. 10, pp. 0–5, 2015.

[312] I. Vlassiouk, S. Smirnov, and Z. Siwy, "Ionic selectivity of single nanochannels," *Nano Lett.*, vol. 8, pp. 1978–1985, 2008.

[313] G. Pardon and W. Van Der Wijngaart, "Modeling and simulation of electrostatically gated nanochannels," *Adv. Colloid Interface Sci.*, vol. 199-200, pp. 78–94, 2013.

[314] H. Cao, J. O. Tegenfeldt, R. H. Austin, and S. Y. Chou, "Gradient nanostructures for interfacing microfluidics and nanofluidics," *Appl. Phys. Lett.*, vol. 81, pp. 3058–3060, 2002.

[315] K. E. Herold and A. Rasooly, eds., *Lab-on-a-chip Technology: Fabrication and Microfluidics*. Caister Academic Press, 2009.

[316] F. Zhu and G. Hummer, "Pore opening and closing of a pentameric ligand-gated ion channel.," *Proc. Natl. Acad. Sci.*, vol. 107, pp. 19814–19819, 2010.

[317] S. Bernèche and B. Roux, "Energetics of ion conduction through the $K^+$ channel.," *Nature*, vol. 414, pp. 73–77, 2001.

[318] P. W. Fowler, O. Beckstein, E. Abad, and M. S. P. Sansom, "Detailed Examination of a Single Conduction Event in a Potassium Channel.," *J. Phys. Chem. Lett.*, vol. 4, pp. 3104–3109, 2013.

[319] A. Waghe, J. C. Rasajah, and G. Hummer, "Filling and emptying kinetics of carbon nanotubes in water," *J. Chem. Phys.*, vol. 117, pp. 10789–10795, 2002.

[320] J. A. Garate, T. Perez-Acle, and C. Oostenbrink, "On the thermodynamics of carbon nanotube single-file water loading: free energy, energy and entropy calculations.," *Phys. Chem. Chem. Phys.*, vol. 16, pp. 5119–28, 2014.

[321] C. Y. Won and N. R. Aluru, "Water permeation through a subnanometer boron nitride nanotube," *J. Am. Chem. Soc.*, vol. 129, pp. 2748–2749, 2007.

[322] T. a. Hilder, D. Gordon, and S. H. Chung, "Salt rejection and water transport through boron nitride nanotubes," *Small*, vol. 5, pp. 2183–2190, 2009.

[323] T. W. Allen, O. S. Andersen, and B. Roux, "Molecular dynamics - Potential of Mean Force Calculations as a Tool for Understanding Ion Permeation and Selectivity in Narrow Channels.," *Biophys. Chem.*, vol. 124, pp. 251–267, 2006.

[324] H. Berendsen, D. V. D. Spoel, and R. Van Drunen, "GROMACS: A Message-Passing Parallel Molecular Dynamics Implementation," *Comput. Phys. Commun.*, vol. 91, pp. 43–56, 1995.

[325] J. S. Hub, B. L. De Groot, and D. Van Der Spoel, "G-wham. A free Weighted Histogram Analysis implementation including robust error and autocorrelation estimates," *J. Chem. Theory Comput.*, vol. 6, pp. 3713–3720, 2010.

[326] R. M. Lynden-Bell and J. C. Rasaiah, "Mobility and solvation of ions in channels," *J. Chem. Phys.*, vol. 105, p. 9266, 1996.

[327] L. a. Richards, A. I. Schäfer, B. S. Richards, and B. Corry, "Quantifying barriers to monovalent anion transport in narrow non-polar pores.," *Phys. Chem. Chem. Phys.*, vol. 14, pp. 11633–8, 2012.

[328] B. L. de Groot and H. Grubmüller, "Water permeation across biological membranes: mechanism and dynamics of aquaporin-1 and GlpF.," *Science*, vol. 294, pp. 2353–2357, 2001.

[329] B. van den Berg, P. N. Black, W. M. Clemons, and T. a. Rapoport, "Crystal structure of the long-chain fatty acid transporter FadL.," *Science*, vol. 304, pp. 1506–1509, 2004.

[330] H. Zou, M. Zheng, X. Luo, *et al.*, "Dynamic mechanism of fatty acid transport across cellular membranes through FadL: molecular dynamics simulations.," *J. Phys. Chem. B*, vol. 112, pp. 13070–13078, 2008.

[331] E. M. Hearn, D. R. Patel, and B. van den Berg, "Outer-membrane transport of aromatic hydrocarbons as a first step in biodegradation.," *Proc. Natl. Acad. Sci.*, vol. 105, pp. 8601–8606, 2008.

[332] M. H. Abraham, "Thermodynamics of solution of homologous series of solutes in water," *J. Chem. Soc. Faraday Trans. 1*, vol. 80, p. 153, 1984.

[333] R. M. Manara, E. Jayne Wallace, and S. Khalid, "DNA sequencing with MspA: Molecular Dynamics simulations reveal free-energy differences between sequencing and non-sequencing mutants," *Sci. Rep.*, vol. 5, p. 12783, 2015.

[334] R. Manara, S. Tomasio, and S. Khalid, "The Nucleotide Capture Region of Alpha Hemolysin: Insights into Nanopore Design for DNA Sequencing from Molecular Dynamics Simulations," *Nanomaterials*, vol. 5, pp. 144–153, 2015.

[335] B. Van Den Berg, "The FadL family: Unusual transporters for unusual substrates," *Curr. Opin. Struct. Biol.*, vol. 15, pp. 401–407, 2005.

[336] C. Domene and S. Furini, *Examining ion channel properties using free-energy methods.*, vol. 466. Elsevier Inc., 1 ed., 2009.

[337] E. Piccinini, M. Ceccarelli, F. Affinito, R. Brunetti, and C. Jacoboni, "Biased molecular simulations for free-energy mapping: A comparison on the KcsA channel as a test case," *J. Chem. Theory Comput.*, vol. 4, pp. 173–183, 2008.

[338] I. Vlassiouk, C. D. Park, S. a. Vail, D. Gust, and S. Smirnov, "Control of nanopore wetting by a photochromic spiropyran: A light-controlled valve and electrical switch," *Nano Lett.*, vol. 6, pp. 1013–1017, 2006.

[339] F. Rios and S. N. Smirnov, "pH valve based on hydrophobicity switching," *Chem. Mater.*, vol. 23, pp. 3601–3605, 2011.

[340] G. M. Sacha, a. Verdaguer, and M. Salmeron, "Induced water condensation and bridge formation by electric fields in atomic force microscopy," *J. Phys. Chem. B*, vol. 110, pp. 14870–14873, 2006.

[341] S. Gómez-Moñivas, J. J. Sáenz, M. Calleja, and R. García, "Field-induced formation of nanometer-sized water bridges.," *Phys. Rev. Lett.*, vol. 91, p. 056101, 2003.

[342] C. Y. Lee, J. a. McCammon, and P. J. Rossky, "The structure of liquid water at an extended hydrophobic surface.," *J. Chem. Phys.*, vol. 80, pp. 4448–4455, 1984.

[343] K. Lum and A. Luzar, "Pathway to surface-induced phase transition of a confined fluid," *Phys. Rev. E*, vol. 56, pp. R6283–R6286, 1997.

[344] K. Lum and D. Chandler, "Phase diagram and free energies of vapor films and tubes for a confined fluid," *Int. J. Thermophys.*, vol. 19, pp. 845–855, 1998.

[345] B. Lefevre, a. Saugey, J. L. Barrat, *et al.*, "Intrusion and extrusion of water in hydrophobic mesopores," *J. Chem. Phys.*, vol. 120, pp. 4927–4938, 2004.

[346] A. Luzar, "Activation barrier scaling for the spontaneous evaporation of confined water," *J. Phys. Chem. B*, vol. 108, pp. 19859–19866, 2004.

[347] B. Husowitz and V. Talanquer, "Nucleation in cylindrical capillaries," *J. Chem. Phys.*, vol. 121, pp. 8021–8028, 2004.

[348] D. a. Doshi, E. B. Watkins, J. N. Israelachvili, and J. Majewski, "Reduced water density at hydrophobic surfaces: effect of dissolved gases.," *Proc. Natl. Acad. Sci.*, vol. 102, pp. 9458–9462, 2005.

[349] A. Luzar, S. Svetina, and B. Zeks, "Consideration of the spontaneous polarization of water at the solid/liquid interface," *J. Chem. Phys.*, vol. 82, p. 5146, 1985.

[350] C. D. Daub, D. Bratko, K. Leung, and A. Luzar, "Electrowetting at the nanoscale," *J. Phys. Chem. C*, vol. 111, pp. 505–509, 2007.

[351] J. Dzubiella, R. J. Allen, and J.-P. Hansen, "Electric field-controlled water permeation coupled to ion transport through a nanopore Electric field-controlled water permeation coupled to ion transport through a nanopore," *J. Chem. Phys.*, vol. 5001, pp. 11–15, 2004.

[352] M. F. Toney, J. T. Howard, J. Richer, *et al.*, "Voltage-dependent ordering of water molecules at an electrode-electrolyte interface," *Nature*, vol. 368, pp. 444–464, 1994.

[353] P. J. Bond, J. Holyoake, A. Ivetac, S. Khalid, and M. S. P. Sansom, "Coarse-Grained Molecular Dynamics Simulations of Membrane Proteins and Peptides.," *J. Struct. Biol.*, vol. 157, pp. 593–605, 2007.

[354] J. Gumbart, F. Khalili-Araghi, M. Sotomayor, and B. Roux, "Constant electric field simulations of the membrane potential illustrated with simple systems.," *Biochim. Biophys. Acta*, vol. 1818, pp. 294–302, 2012.

[355] C. Kutzner, H. Grubmüller, B. L. De Groot, and U. Zachariae, "Computational electrophysiology: The molecular dynamics of ion channel permeation and selectivity in atomistic detail," *Biophys. J.*, vol. 101, pp. 809–817, 2011.

[356] D. P. Tieleman, H. J. Berendsen, and M. S. Sansom, "Voltage-dependent insertion of alamethicin at phospholipid/water and octane/water interfaces.," *Biophys. J.*, vol. 80, pp. 331–346, 2001.

[357] J. N. Sachs, P. S. Crozier, and T. B. Woolf, "Atomistic simulations of biologically realistic transmembrane potential gradients.," *J. Chem. Phys.*, vol. 121, pp. 10847–10851, 2004.

[358] P. S. Crozier, R. L. Rowley, N. B. Holladay, D. Henderson, and D. D. Busath, "Molecular dynamics simulation of continuous current flow through a model biological membrane channel," *Phys. Rev. Lett.*, vol. 86, pp. 2467–2470, 2001.

[359] L. Delemotte, F. Dehez, W. Treptow, and M. Tarek, "Modeling Membranes under a Transmembrane Potential," *J. Phys. Chem. B. Letts*, vol. 112, pp. 5547–5550, 2008.

[360] J. N. Sachs, P. S. Crozier, and T. B. Woolf, "Atomistic simulations of biologically realistic transmembrane potential gradients," *J. Chem. Phys.*, vol. 121, pp. 10847–10851, 2004.

[361] A. a. Gurtovenko, "Asymmetry of lipid bilayers induced by monovalent salt: Atomistic molecular-dynamics study," *J. Chem. Phys.*, vol. 122, 2005.

[362] E. J. Denning and T. B. Woolf, "Double bilayers and transmembrane gradients: a molecular dynamics study of a highly charged peptide.," *Biophys. J.*, vol. 95, pp. 3161–3173, 2008.

[363] D. van der Spoel, E. Lindahl, and B. Hess, "GROMACS User Manual version 4.6.5."

[364] Winarto, D. Takaiwa, E. Yamamoto, and K. Yasuoka, "Structures of water molecules in carbon nanotubes under electric fields," *J. Chem. Phys.*, vol. 142, p. 124701, 2015.

[365] D. a. Kopfer, C. Song, T. Gruene, *et al.*, "Ion permeation in $K^+$ channels occurs by direct Coulomb knock-on," *Science.*, vol. 346, pp. 352–355, 2014.

[366] Y. Zhou and R. MacKinnon, "The occupancy of ions in the $K^+$ selectivity filter: Charge balance and coupling of ion binding to a protein conformational change underlie high conduction rates," *J. Mol. Biol.*, vol. 333, pp. 965–975, 2003.

[367] C. Domene and M. S. P. Sansom, "Potassium channel, ions, and water: simulation studies based on the high resolution X-ray structure of KcsA.," *Biophys. J.*, vol. 85, pp. 2787–2800, 2003.

[368] C. Miller, "See potassium run.," *Nature*, vol. 414, pp. 23–24, 2001.

[369] J. H. Morais-Cabral, Y. Zhou, and R. MacKinnon, "Energetic optimization of ion conduction rate by the $K^+$ selectivity filter.," *Nature*, vol. 414, pp. 37–42, 2001.

[370] P. T. Vernier, M. J. Ziegler, Y. Sun, M. a. Gundersen, and D. P. Tieleman, "Nanopore-facilitated, voltage-driven phosphatidylserine translocation in lipid bilayers–in cells and in silico.," *Phys. Biol.*, vol. 3, pp. 233–247, 2006.

[371] S. Acosta-Gutierrez, M. A. Scorciapino, I. Bodrenko, and M. Ceccarelli, "Filtering with Electric Field: The Case of *E. coli* Porins," *J. Phys. Chem. Lett.*, pp. 1807–1812, 2015.

[372] E. Tajkhorshid, P. Nollert, M. O. Jensen, *et al.*, "Control of the selectivity of the aquaporin water channel family by global orientational tuning.," *Science*, vol. 296, pp. 525–530, 2002.

[373] S. Gravelle, L. Joly, F. Detcheverry, *et al.*, "Optimizing Water Permeability Through the Hourglass Shape of Aquaporins.," *Proc. Natl. Acad. Sci.*, vol. 110, pp. 16367–16372, 2013.

[374] D. Tang and D. Kim, "Study on the transport of water molecules under the geometry confinement of aquaporin-like nanopores," *Appl. Therm. Eng.*, 2014.

[375] C. Han, D. Tang, and D. Kim, "Molecular dynamics simulation on the effect of pore hydrophobicity on water transport through aquaporin-mimic nanopores," *Colloids Surfaces A Physicochem. Eng. Asp.*, 2015.

[376] M. J. Ziegler and P. Thomas Vernier, "Interface water dynamics and porating electric fields for phospholipid bilayers," *J. Phys. Chem. B*, vol. 112, pp. 13588–13596, 2008.

[377] P. T. Vernier, Y. Sun, M. J. Ziegler, and M. a. Gundersen, "Nanoelectropulse-driven membrane perturbation and permeabilization," *BMC Cell Biol.*, vol. 16, p. 52, 2006.

[378] Q. Hu, Z. Zhang, H. Qiu, M. G. Kong, and R. P. Joshi, "Physics of nanoporation and water entry driven by a high-intensity, ultrashort electrical pulse in the presence of membrane hydrophobic interactions," *Phys. Rev. E - Stat. Nonlinear, Soft Matter Phys.*, vol. 87, pp. 1–9, 2013.

[379] K. Leung, A. Luzar, and D. Bratko, "Dynamics of capillary drying in water.," *Phys. Rev. Lett.*, vol. 90, p. 065502, 2003.

[380] D. Wong, T.-J. Jeon, and J. Schmidt, "Single molecule measurements of channel proteins incorporated into biomimetic polymer membranes," *Nanotechnology*, vol. 17, pp. 3710–3717, 2006.

[381] I. Abiror, V. Arakelyan, L. Chernomordik, *et al.*, "246 - Electric breakdown of bilayer lipid membranes I. The main experimental facts and their qualitative discussion," *Bioelectrochemistry Bioenerg.*, vol. 6, pp. 37–52, 1979.

[382] D. P. Tieleman, "The molecular basis of electroporation.," *BMC Biochem.*, vol. 5, p. 10, 2004.

[383] L. Chernomordik, S. Sukharev, I. Abidor, and Y. Chizmadzhev, "Breakdown of lipid bilayer membranes in an electric field," *Biochim. Biophys. Acta - Biomembr.*, vol. 736, pp. 203–213, 1983.

[384] R. Nuccitelli, U. Pliquett, X. Chen, *et al.*, "Nanosecond pulsed electric fields cause melanomas to self-destruct," *Biochem Biophys rev Commun*, vol. 343, pp. 351–360, 2006.

[385] J. C. Weaver and R. A. Mintzer, "Decreased bilayer stability due to transmembrane potentials," 1981.

[386] L. C. M. Gross, A. J. Heron, S. C. Baca, and M. I. Wallace, "Determining membrane capacitance by dynamic control of droplet interface bilayer area," *Langmuir*, vol. 27, pp. 14335–14342, 2011.

[387] U. Zachariae, R. Schneider, R. Briones, *et al.*, "$\beta$-Barrel mobility underlies closure of the voltage-dependent anion channel," *Structure*, vol. 20, pp. 1540–1549, 2012.

[388] S. Tristram-Nagle, Y. Liu, J. Legleiter, and J. F. Nagle, "Structure of gel phase DMPC determined by X-ray diffraction.," *Biophys. J.*, vol. 83, pp. 3324–3335, 2002.

[389] D. P. Tieleman, H. Leontiadou, A. E. Mark, and S.-J. Marrink, "Simulation of Pore Formation in Lipid Bilayers by Mechanical Stress and Electric Fields," *J. Am. Chem. Soc.*, vol. 125, pp. 6382–6383, 2003.

[390] P. T. Vernier and M. J. Ziegler, "Nanosecond field alignment of head group and water dipoles in electroporating phospholipid bilayers," *J. Phys. Chem. B*, vol. 111, pp. 12993–12996, 2007.

[391] S. J. Marrink, M. Berkowitz, and H. J. C. Berendsen, "Molecular dynamics simulation of a membrane/water interface: the ordering of water and its relation to the hydration force," *Langmuir*, vol. 9, pp. 3122–3131, 1993.

[392] L. Saiz and M. L. Klein, "Electrostatic interactions in a neutral model phospholipid bilayer by molecular dynamics simulations," *J. Chem. Phys.*, vol. 116, pp. 3052–3057, 2002.

[393] K. C. Melikov, V. A. Frolov, A. Shcherbakov, *et al.*, "Voltage-induced nonconductive pre-pores and metastable single pores in unmodified planar lipid bilayer.," *Biophys. J.*, vol. 80, pp. 1829–1836, 2001.

[394] W. Frey, J. a. White, R. O. Price, *et al.*, "Plasma membrane voltage changes during nanosecond pulsed electric field exposure.," *Biophys. J.*, vol. 90, pp. 3608–3615, 2006.

[395] P. Marszalek, D. S. Liu, and T. Y. Tsong, "Schwan equation and transmembrane potential induced by alternating electric field.," *Biophys. J.*, vol. 58, pp. 1053–1058, 1990.

[396] Y. Tanaka and a. J. Schroit, "Calcium/phosphate-induced immobilization of fluorescent phosphatidylserine in synthetic bilayer membranes: inhibition of lipid transfer between vesicles.," *Biochemistry*, vol. 25, pp. 2141–2148, 1986.

[397] A. a. Gurtovenko and I. Vattulainen, "Pore formation Coupled to Ion Transport through Lipid Membranes as Induced by Transmembrane Ionic Charge Imbalance: Atomistic Molecular Dynamics Study," *J. Am. Chem. Soc.*, vol. 127, pp. 17570–17571, 2005.

[398] A. Polak, D. Bonhenry, F. Dehez, *et al.*, "On the electroporation thresholds of lipid bilayers: Molecular dynamics simulation investigations," *J. Membr. Biol.*, vol. 246, pp. 843–850, 2013.

[399] R. W. Glaser, S. L. Leikin, L. V. Chernomordik, V. F. Pastushenko, and a. I. Sokirko, "Reversible electrical breakdown of lipid bilayers: formation and evolution of pores.," *Biochim. Biophys. Acta*, vol. 940, pp. 275–287, 1988.

[400] I. P. Sugar and E. Neumann, "Stochastic model for electric field-induced membrane pores. Electroporation.," *Biophys. Chem.*, vol. 19, pp. 211–225, 1984.

[401] J. C. Weaver, K. T. Powell, and R. A. Mintzer, "The Electrical Capacitance of Bilayer Membranes. The Contribution of Transient Aqueous Pores," *Biochem. Bioenerg.*, vol. 12, pp. 393–404, 1984.

[402] S. a. Spronk, D. E. Elmore, and D. a. Dougherty, "Voltage-dependent hydration and conduction properties of the hydrophobic pore of the mechanosensitive channel of small conductance.," *Biophys. J.*, vol. 90, pp. 3555–3569, 2006.

[403] M. Sotomayor, V. Vásquez, E. Perozo, and K. Schulten, "Ion conduction through MscS as determined by electrophysiology and simulation.," *Biophys. J.*, vol. 92, pp. 886–902, 2007.

[404] A. Anishkin, B. Akitake, K. Kamaraju, C.-S. Chiang, and S. Sukharev, "Hydration properties of mechanosensitive channel pores define the energetics of gating.," *J. Phys. Condens. Matter*, vol. 22, p. 454120, 2010.

[405] H. L. Wang, X. Cheng, P. Taylor, J. A. McCammon, and S. M. Sine, "Control of cation permeation through the nicotinic receptor channel," *PLoS Comput. Biol.*, vol. 4, 2008.

[406] Y. Okuno, M. Minagawa, H. Matsumoto, and A. Tanioka, "Simulation study on the influence of an electric field on water evaporation," *J. Mol. Struct. THEOCHEM*, vol. 904, pp. 83–90, 2009.

[407] T.-H. Yen, "Investigation of the effects of perpendicular electric field and surface morphology on nanoscale droplet using molecular dynamics simulation," *Mol. Simul.*, vol. 38, pp. 509–517, 2012.

[408] S. Smirnov, I. Vlassiouk, and N. Lavrik, "Voltage-Gated Hydrophobic Nanopores," *ACS Nano*, vol. 5, pp. 7453–7461, 2011.

[409] J. Köfinger, G. Hummer, and C. Dellago, "Macroscopically ordered water in nanopores.," *Proc. Natl. Acad. Sci.*, vol. 105, pp. 13218–13222, 2008.

[410] L. Innes, D. Gutierrez, W. Mann, S. F. Buchsbaum, and Z. S. Siwy, "Presence of electrolyte promotes wetting and hydrophobic gating in nanopores with residual surface charges," *Analyst*, pp. 4804–4812, 2015.

[411] D. Lu, Y. Li, S. V. Rotkin, U. Ravaioli, and K. Schulten, "Finite-size effect and wall polarization in a carbon nanotube channel," *Nano Lett.*, vol. 4, pp. 2383–2387, 2004.

[412] T. a. Pascal, W. a. Goddard, and Y. Jung, "Entropy and the driving force for the filling of carbon nanotubes with water.," *Proc. Natl. Acad. Sci.*, vol. 108, pp. 11794–11798, 2011.

[413] R. Yang, T. a. Hilder, S.-H. Chung, and A. Rendell, "First-Principles Study of Water Confined in Single-Walled Silicon Carbide Nanotubes," *J. Phys. Chem. C*, vol. 115, pp. 17255–17264, 2011.

[414] Y. Wang, Y. J. Zhao, and J. P. Huang, "Giant pumping of single-file water molecules in a carbon nanotube.," *J. Phys. Chem. B*, vol. 115, pp. 13275–13279, 2011.

[415] A. Striolo, A. a. Chialvo, P. T. Cummings, and K. E. Gubbins, "Simulated water adsorption in chemically heterogeneous carbon nanotubes," *J. Chem. Phys.*, vol. 124, 2006.

[416] Y. Tu, P. Xiu, R. Wan, *et al.*, "Water-mediated signal multiplication with Y-shaped carbon nanotubes.," *Proc. Natl. Acad. Sci.*, vol. 106, pp. 18120–4, 2009.

[417] D. Lu, "Accelerating water transport through a charged SWCNT: a molecular dynamics simulation.," *Phys. Chem. Chem. Phys.*, vol. 15, pp. 14447–57, 2013.

[418] K. S. Cole, "Electric impedance of marine egg membranes," *Trans. Faraday Soc.*, vol. 33, p. 966, 1937.

[419] P. T. Vernier, M. J. Ziegler, Y. Sun, *et al.*, "Nanopore formation and phosphatidylserine externalization in a phospholipid bilayer at high transmembrane potential," *J. Am. Chem. Soc.*, vol. 128, pp. 6288–6289, 2006.

[420] A. a. Gurtovenko and A. S. Lyulina, "Electroporation of asymmetric phospholipid membranes.," *J. Phys. Chem. B*, vol. 118, pp. 9909–18, 2014.

[421] D. Needham and R. M. Hochmuth, "Electro-mechanical permeabilization of lipid vesicles. Role of membrane tension and compressibility.," *Biophys. J.*, vol. 55, pp. 1001–1009, 1989.

[422] M. Kummrow and W. Helfrich, "Deformation of giant lipid vesicles by electric fields," *Phys. Rev. A*, vol. 44, pp. 8356–8360, 1991.

[423] H. Isambert, "Understanding the Electroporation of Cells and Artificial Bilayer Membranes," *Phys. Rev. Lett.*, vol. 80, pp. 3404–3407, 1998.

[424] L. T. Gao, X. Q. Feng, Y. J. Yin, and H. Gao, "An electromechanical liquid crystal model of vesicles," *J. Mech. Phys. Solids*, vol. 56, pp. 2844–2862, 2008.

[425] E. Spohr, "Effect of electrostatic boundary conditions and system size on the interfacial properties of water and aqueous solutions," *J. Chem. Phys.*, vol. 107, pp. 6342–6348, 1997.

[426] J. W. Lynch, "Molecular structure and function of the glycine receptor chloride channel.," *Physiol. Rev.*, vol. 84, pp. 1051–1095, 2004.

[427] A. Keramidas, A. J. Moorhouse, K. D. Pierce, P. R. Schofield, and P. H. Barry, "Cation-selective mutations in the M2 domain of the inhibitory glycine receptor channel reveal determinants of ion-charge selectivity.," *J. Gen. Physiol.*, vol. 119, pp. 393–410, 2002.

[428] A. Keramidas, A. J. Moorhouse, P. R. Schofield, and P. H. Barry, "Ligand-gated ion channels: Mechanisms underlying ion selectivity," *Prog. Biophys. Mol. Biol.*, vol. 86, pp. 161–204, 2004.

[429] V. E. Wotring, T. S. Miller, and D. S. Weiss, "Mutations at the GABA receptor selectivity filter: a possible role for effective charges.," *J. Physiol.*, vol. 548, pp. 527–540, 2003.

[430] G. Hassaine, C. Deluz, L. Grasso, *et al.*, "X-ray structure of the mouse serotonin 5-$HT_3$ receptor," *Nature*, vol. 512, pp. 276–281, 2014.

[431] P.-J. Corringer, N. L. Novere, and J.-P. Changeux, "Nicotinic Receptors at the Amino Acid level," *Annu. Rev. Pharmacol. Toxicol.*, vol. 40, pp. 431–458, 2000.

[432] S. Panicker, H. Cruz, C. Arrabit, and P. A. Slesinger, "Evidence for a centrally located gate in the pore of a serotonin-gated ion channel.," *J. Neurosci.*, vol. 22, pp. 1629–1639, 2002.

[433] D. C. Reeves, E. N. Goren, M. H. Akabas, and S. C. R. Lummis, "Structural and Electrostatic Properties of the 5-$HT_3$ Receptor Pore Revealed by Substituted Cysteine Accessibility Mutagenesis," *J. Biol. Chem.*, vol. 276, pp. 42035–42042, 2001.

[434] A. J. Thompson, C. L. Padgett, and S. C. R. Lummis, "Mutagenesis and molecular modeling reveal the importance of the 5-$HT_3$ receptor F-loop," *J. Biol. Chem.*, vol. 281, pp. 16576–16582, 2006.

[435] S. C. R. Lummis, "5-$HT_3$ receptors," *J. Biol. Chem.*, vol. 287, pp. 40239–40245, 2012.

[436] E. J. Haddadian, M. H. Cheng, R. D. Coalson, Y. Xu, and P. Tang, "*In silico* models for the human $\alpha 4\beta 2$ nicotinic acetylcholine receptor.," *J. Phys. Chem. B*, vol. 112, pp. 13981–13990, 2008.

[437] N. Bocquet, H. Nury, M. Baaden, *et al.*, "X-ray structure of a pentameric ligand-gated ion channel in an apparently open conformation.," *Nature*, vol. 457, pp. 111–114, 2009.

[438] C. Ma, S. Bhattacharya, J. Yoo, D. Wells, and A. Aksimentiev, "Modeling and Simulation of Ion Channels," *Chem. Rev.*, vol. 112, pp. 6250–6284, 2012.

[439] M. H. Cheng, M. Cascio, and R. Coalson, "Homology Modeling and Molecular Dynamics Simulations of the $\alpha 1$ Glycine Receptor Reveals Different States of the Channel," *Proteins Struct. Funct. Bioinforma.*, vol. 68, pp. 58–593, 2007.

[440] S. Murail, B. Wallner, J. R. Trudell, E. Bertaccini, and E. Lindahl, "Microsecond Simulations Indicate that Ethanol Binds between Subunits and Could Stabilize an Open-State Model of a Glycine Receptor.," *Biophys J*, vol. 100, pp. 1642–50, 2011.

[441] D. N. LeBard, J. Hénin, R. G. Eckenhoff, M. L. Klein, and G. Brannigan, "General anesthetics predicted to block the GLIC pore with micromolar affinity," *PLoS Comput. Biol.*, vol. 8, 2012.

[442] M. H. Cheng and R. D. Coalson, "Energetics and ion permeation characteristics in a glutamate-gated chloride (GluCl) receptor channel," *J. Phys. Chem. B*, vol. 116, pp. 13637–13643, 2012.

[443] D. Willenbring, L. T. Liu, D. Mowrey, Y. Xu, and P. Tang, "Isoflurane alters the structure and dynamics of GLIC," *Biophys. J.*, vol. 101, pp. 1905–1912, 2011.

[444] H. Nury, F. Poitevin, C. Van Renterghem, *et al.*, "One-microsecond molecular dynamics simulation of channel gating in a nicotinic receptor homologue.," *Proc. Natl. Acad. Sci.*, vol. 107, pp. 6275–6280, 2010.

[445] W. L. Jorgensen, W. L. Jorgensen, D. S. Maxwell, *et al.*, "Development and Testing of the OPLS All-Atom Force Field on Conformational Energetics and Properties of Organic Liquids," *J. Am. Chem. Soc.*, vol. 118, pp. 11225–11236, 1996.

[446] M. Parrinello and A. Rahman, "Polymorphic transitions in single crystals: A new molecular dynamics method," *J. Appl. Phys.*, vol. 52, pp. 7182–7190, 1981.

[447] A. R. Atilgan, S. R. Durell, R. L. Jernigan, *et al.*, "Anisotropy of fluctuation dynamics of proteins with an elastic network model.," *Biophys. J.*, vol. 80, pp. 505–515, 2001.

[448] A. Grossfield, S. E. Feller, and M. C. Pitman, "A role for direct interactions in the modulation of rhodopsin by omega-3 polyunsaturated lipids.," *Proc. Natl. Acad. Sci.*, vol. 103, pp. 4888–93, 2006.

[449] S. Fritsch, I. Ivanov, H. Wang, and X. Cheng, "Ion selectivity mechanism in a bacterial pentameric ligand-gated ion channel," *Biophys. J.*, vol. 100, pp. 390–398, 2011.

[450] I. Ivanov, X. Cheng, S. M. Sine, and J. a. McCammon, "Barrier ion translocation in cationic & anionic receptor from the Cys-loop family," *J. Am. Chem. Soc.*, vol. 129, pp. 8217–8224, 2007.

[451] P. Carter, C. a. F. Andersen, and B. Rost, "DSSPcont: Continuous secondary structure assignments for proteins," *Nucleic Acids Res.*, vol. 31, pp. 3293–3295, 2003.

[452] A. J. Thompson and S. C. R. Lummis, "A single ring of charged amino acids at one end of the pore can control ion selectivity in the 5-$HT_3$ receptor.," *Br. J. Pharmacol.*, vol. 140, pp. 359–365, 2003.

[453] G. D. Cymes and C. Grosman, "Tunable pK(a) values and the basis of opposite charge selectivities in nicotinic-type receptors.," *Nature*, vol. 474, pp. 526–530, 2011.

[454] J. W. Lynch, S. Rajendra, K. D. Pierce, *et al.*, "Identification of intracellular and extracellular domains mediating signal transduction in the inhibitory glycine receptor chloride channel," *EMBO J.*, vol. 16, pp. 110–120, 1997.

[455] M. Sunesen, L. P. De Carvalho, V. Dufresne, *et al.*, "Mechanism of $Cl^-$ selection by a glutamate-gated chloride (GluCl) receptor revealed through mutations in the selectivity filter," *J. Biol. Chem.*, vol. 281, pp. 14875–14881, 2006.

[456] A. Keramidas, A. J. Moorhouse, C. R. French, P. R. Schofield, and P. H. Barry, "M2 pore mutations convert the glycine receptor channel from being anion- to cation-selective.," *Biophys. J.*, vol. 79, pp. 247–259, 2000.

[457] K. Imoto, C. Methfessel, B. Sakmann, *et al.*, "Location of a $\delta$-subunit region determining ion transport through the acetylcholine receptor channel.," *Nature*, vol. 324, pp. 670–674, 1986.

[458] S. P. Kelley, J. I. Dunlop, E. F. Kirkness, J. J. Lambert, and J. a. Peters, "A cytoplasmic region determines single-channel conductance in 5-$HT_3$ receptors.," *Nature*, vol. 424, pp. 321–324, 2003.

[459] S. M. Sine, H. L. Wang, S. Hansen, and P. Taylor, "On the origin of ion selectivity in the Cys-loop receptor family," *J. Mol. Neurosci.*, vol. 40, pp. 70–76, 2010.

[460] G. D. Cymes and C. Grosman, "The unanticipated complexity of the selectivity-filter glutamates of nicotinic receptors," *Nat. Chem. Biol.*, vol. 8, pp. 975–981, 2012.

[461] J. A. Peters, M. A. Cooper, J. E. Carland, *et al.*, "Novel structural determinants of single channel conductance and ion selectivity in 5-hydroxytryptamine type 3 and nicotinic acetylcholine receptors.," *J. Physiol.*, vol. 588, pp. 587–596, 2010.

[462] M. Moroni, J. O. Meyer, C. Lahmann, and L. G. Sivilotti, "In Glycine and $GABA_A$ Channels, Different Subunits Contribute Asymmetrically to Channel Conductance via Residues in the Extracellular Domain," *J. Biol. Chem.*, vol. 286, pp. 13414–13422, 2011.

[463] C. Melis, G. Bussi, S. C. R. Lummis, and C. Molteni, "Trans-cis switching mechanisms in proline analogues and their relevance for the gating of the 5-$HT_3$ receptor," *J. Phys. Chem. B*, vol. 113, pp. 12148–12153, 2009.

[464] M. R. Livesey, M. a. Cooper, J. J. Lambert, and J. a. Peters, "Rings of charge within the extracellular vestibule influence ion permeation of the 5-$HT_{3A}$ receptor," *J. Biol. Chem.*, vol. 286, pp. 16008–16017, 2011.

[465] S. B. Hansen, H. L. Wang, P. Taylor, and S. M. Sine, "An ion selectivity filter in the extracellular domain of Cys-loop receptors reveals determinants for ion conductance," *J. Biol. Chem.*, vol. 283, pp. 36066–36070, 2008.

[466] A. M. Brown, A. G. Hope, J. J. Lambert, and J. A. Peters, "Ion permeation and conduction in a human recombinant 5-$HT_3$ receptor subunit (h5-$HT_{3A}$)," *J. Physiol.*, vol. 507, pp. 653–665, 1998.

[467] N. Hussy, W. Lukas, and K. a. Jones, "Functional properties of a cloned 5-hydroxytryptamine ionotropic receptor subunit: comparison with native mouse receptors.," *J. Physiol.*, vol. 481.2, pp. 311–323, 1994.

[468] P. A. Davies, M. Pistis, M. C. Hanna, *et al.*, "The 5-$HT3_B$ subunit is a major determinant of serotonin-receptor function.," *Nature*, vol. 397, pp. 359–363, 1999.

[469] J. L. Kozuska, I. M. Paulsen, W. J. Belfield, *et al.*, "Impact of intracellular domain flexibility upon properties of activated human 5-$HT_3$ receptors," *Br. J. Pharmacol.*, vol. 171, pp. 1–31, 2013.

[470] N. Unwin, "Acetylcholine receptor channel imaged in the open state.," *Nature*, vol. 373, pp. 37–43, 1995.

[471] A. Taly, M. Delarue, T. Grutter, *et al.*, "Normal mode analysis suggests a quaternary twist model for the nicotinic receptor gating mechanism.," *Biophys. J.*, vol. 88, pp. 3954–3965, 2005.

[472] A. Taly, P.-J. Corringer, T. Grutter, *et al.*, "Implications of the quaternary twist allosteric model for the physiology and pathology of nicotinic acetylcholine receptors.," *Proc. Natl. Acad. Sci.*, vol. 103, pp. 16965–16970, 2006.

[473] X. Cheng, H. Wang, B. Grant, S. M. Sine, and J. A. McCammon, "Targeted molecular dynamics study of C-loop closure and channel gating in nicotinic receptors," *PLoS Comput. Biol.*, vol. 2, pp. 1173–1184, 2006.

[474] N. Unwin and Y. Fujiyoshi, "Gating movement of acetylcholine receptor caught by plunge-freezing," *J. Mol. Biol.*, vol. 422, pp. 617–634, 2012.

[475] M. H. Cheng, R. D. Coalson, and P. Tang, "Molecular dynamics and brownian dynamics investigation of ion permeation and anesthetic halothane effects on a proton-gated ion channel," *J. Am. Chem. Soc.*, vol. 132, pp. 16442–16449, 2010.

[476] E. Darve, D. Rodríguez-Gómez, and A. Pohorille, "Adaptive biasing force method for scalar and vector free energy calculations," *J. Chem. Phys.*, vol. 128, 2008.

[477] C. Chipot and J. Hénin, "Exploring the free-energy landscape of a short peptide using an average force," *J. Chem. Phys.*, vol. 123, 2005.

[478] T. A. Cross, H. Dong, M. Sharma, D. D. Busath, and H.-X. Zhou, "M2 protein from influenza A: from multiple structures to biophysical and functional insights.," *Curr. Opin. Virol.*, vol. 2, pp. 128–133, 2012.

[479] R. McNulty, J. P. Ulmschneider, H. Luecke, and M. B. Ulmschneider, "Mechanisms of molecular transport through the urea channel of Helicobacter pylori.," *Nat. Commun.*, vol. 4, p. 2900, 2013.

[480] C. Domene, M. L. Klein, D. Branduardi, F. L. Gervasio, and M. Parrinello, "Conformational changes and gating at the selectivity filter of potassium channels," *Journal of the American Chemical Society*, vol. 130, pp. 9474–9480, 2008.